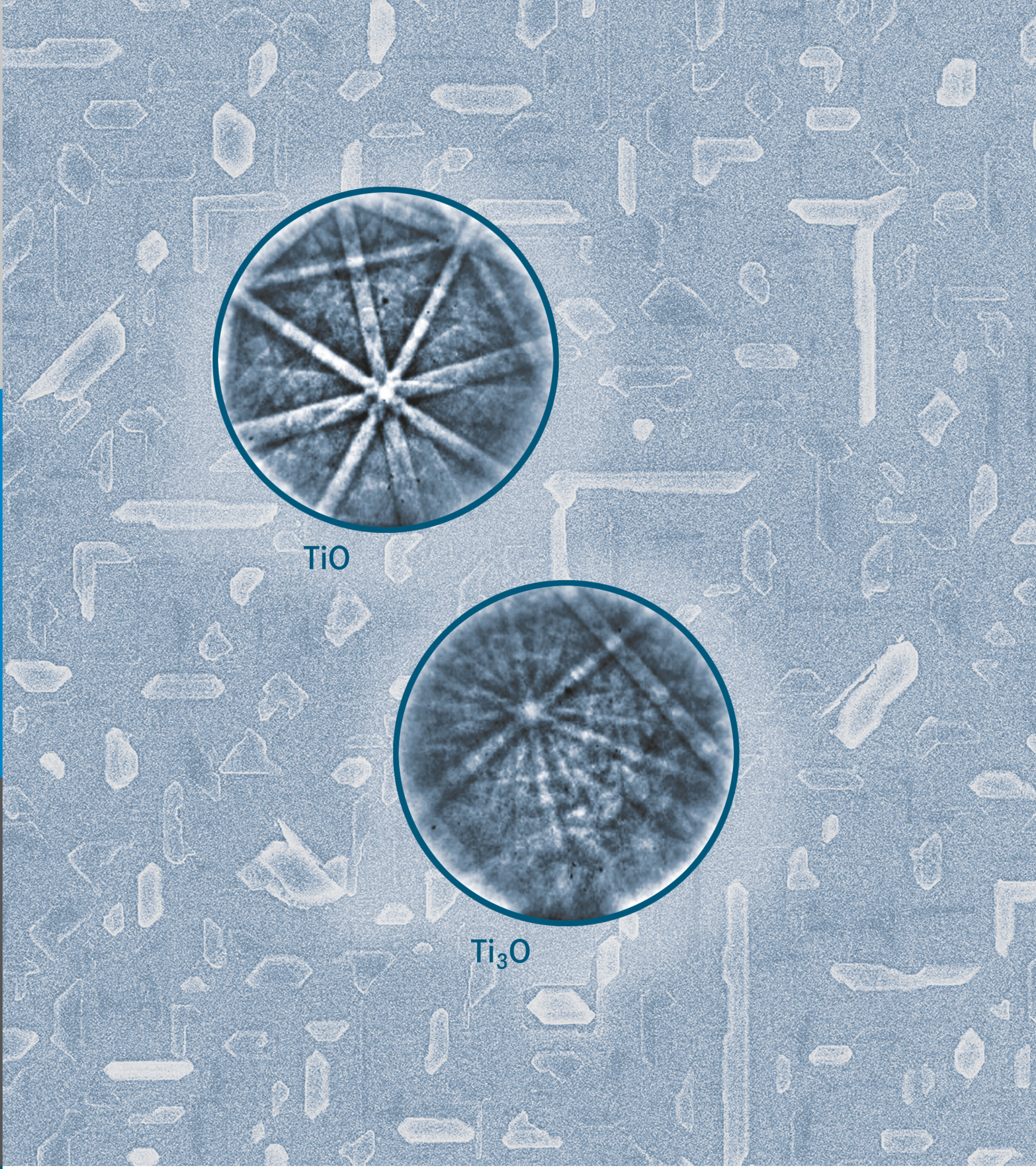

Resistive switching phenomena of extended defects in Nb-doped $SrTiO_3$ under influence of external gradients

Christian Rodenbücher

JÜLICH
FORSCHUNGSZENTRUM

Member of the Helmholtz Association

Schriften des Forschungszentrums Jülich
Reihe Information / Information Band / Volume 38

Forschungszentrum Jülich GmbH
Peter Grünberg Institute (PGI)
Elektronische Materialien (PGI-7)

Resistive switching phenomena of extended defects in Nb-doped $SrTiO_3$ under influence of external gradients

Christian Rodenbücher

Schriften des Forschungszentrums Jülich
Reihe Information / Information Band / Volume 38

ISSN 1866-1777 ISBN 978-3-89336-980-5

Bibliographic information published by the Deutsche Nationalbibliothek.
The Deutsche Nationalbibliothek lists this publication in the Deutsche Nationalbibliografie; detailed bibliographic data are available in the Internet at http://dnb.d-nb.de.

Publisher and Distributor:	Forschungszentrum Jülich GmbH Zentralbibliothek 52425 Jülich Tel: +49 2461 61-5368 Fax: +49 2461 61-6103 Email: zb-publikation@fz-juelich.de www.fz-juelich.de/zb
Cover Design:	Grafische Medien, Forschungszentrum Jülich GmbH
Printer:	Grafische Medien, Forschungszentrum Jülich GmbH

Copyright: Forschungszentrum Jülich 2014

Schriften des Forschungszentrums Jülich
Reihe Information / Information, Band / Volume 38

D 82 (Diss.,RWTH Aachen University, 2014)

ISSN 1866-1777
ISBN 978-3-89336-980-5

The complete volume is freely available on the Internet on the Jülicher Open Access Server (JUWEL) at www.fz-juelich.de/zb/juwel

Neither this book nor any part of it may be reproduced or transmitted in any form or by any means, electronic or mechanical, including photocopying, microfilming, and recording, or by any information storage and retrieval system, without permission in writing from the publisher.

Abstract

Redox-based memristive materials have attracted much attention in the last decade owing to their ability to change the resistance upon application of an electric field making them promising candidates for future non-volatile memories. However, a fundamental understanding of the nature of the resistive switching effect, which is indispensable for designing future technological applications, is still lacking.

As a prototype material of a memristive oxide, strontium titanate ($SrTiO_3$) has been investigated intensively and it was revealed that the valence change of a Ti "d" electron plays an important role during resistive switching related to insulator-to-metal transition. Such a transition can be induced by electrical gradients, by chemical gradients, by a combination of these gradients or by donor doping. Hence, $SrTiO_3$ doped with the donor Nb should have metallic properties and is used commonly as a conducting substrate for the growth of functional oxide thin films. Nevertheless, the resistive switching effect has also be observed in Nb-doped $SrTiO_3$. This paradoxical situation offers a unique opportunity to gain an insight into the processes during the insulator-to metal transition.

In this thesis, a comprehensive study of the influence of external gradients on $SrTiO_3$:Nb single crystals is presented. The focus is especially set on the investigation of the crystallographic structure, the chemical composition, the electronic structure, the lattice dynamics and the electronic transport phenomena using surface-sensitive methods on the macro- and nanoscale. On the as-received epi-polished single crystals, the evolution of a surface layer having a slight excess of strontium and – in contrast to the bulk of the material – semiconducting properties are observed. Hence, the key for understanding of the resistive switching effect is the knowledge of the nature of the surface layer. On the basis of systematic studies of the influence of external gradients on the physical and chemical properties of the surface layer it is demonstrated that a transformation between a Sr-rich and a Ti-rich surface layer can be induced easily illustrating the relevance of ionic movements and phase transformations for the resistive switching effect. On the nanoscale, the switching mechanism is investigated through the use of local conductivity atomic force microscopy with atomic resolution revealing the presence of conducting clusters with a size of 20-60 nm that can be switched independently between ON and OFF states. Since distinct inhomogeneities of the donor distribution are detected by various methods, it is assumed that the conducting clusters, which can be regarded as three-dimensional extended defects, are related to Nb segregation on the nanoscale, which already evolved during the crystal growth by the Verneuil method. In order to gain an insight into the processes taking place when switching the clusters, an emulation of switching is performed on the macroscale by applying extremal electrical gradients, resulting in an evolution of a phase transformation from strontium titanate to titanium oxide in the surface layer.

At the end of the thesis, a potential phenomenological model for resistive switching of $SrTiO_3$:Nb based on the experimental results as well as on *ab initio* and finite element simulations is presented. This is done after taking into account the formation of substoichiometric titanium oxide phases, which build up a switchable bridge between the conducting clusters, thereby illustrating that the resistive switching effect in oxides is a very complex phenomenon related to many different mechanisms that need to be considered.

Kurzfassung

Resistive Schaltphänomene ausgedehnter Defekte in Nb-dotiertem $SrTiO_3$ unter dem Einfluss von externen Gradienten

Redox-basierte memristive Materialien haben im letzten Jahrzehnt große Aufmerksamkeit erregt, da sie die Fähigkeit haben, ihren Widerstand durch den Einfluss eines elektrischen Feldes zu ändern, was sie zu aussichtsreichen Kandidaten für zukünftige nichtflüchtige Computerspeicher macht. Allerdings fehlt immer noch ein fundamentales Verständnis der Natur des resistiven Schalteffekts, welches für die Entwicklung zukünftiger technologischer Anwendungen unabdingbar ist. Als prototypisches Material eines memristiven Oxids wurde Strontiumtitanat ($SrTiO_3$) umfassend untersucht und es wurde gezeigt, dass die Valenzänderung eines Ti „d"-Elektrons eine große Rolle während des resistiven Schaltens verbunden mit einem Isolator-Metall Übergang spielt. Ein solcher Übergang kann durch elektrische Gradienten, chemische Gradienten, eine Überlagerung dieser Gradienten oder auch durch Donatordotierung induziert werden. Daher würden einerseits für $SrTiO_3$, das mit dem Donator Nb dotiert wurde, metallische Eigenschaften erwartet, weshalb es verbreitet als leitfähiges Substrat für das Wachstum funktionaler oxidischer Dünnschichten verwendet wird, aber andererseits wurde der resistive Schalteffekt auch in Nb-dotiertem $SrTiO_3$ beobachtet. Diese paradoxe Situation eröffnet die einmalige Möglichkeit, einen Einblick in die Prozesse, die während des Isolator-Metall Übergangs stattfinden, zu erhalten.

In dieser Arbeit wird eine umfassende Untersuchung des Einflusses externer Gradienten auf $SrTiO_3$:Nb-Einkristalle präsentiert. Im Besonderen liegt der Schwerpunkt auf der Analyse der kristallografischen Struktur, der chemischen Zusammensetzung, der elektronischen Struktur, der Gitterdynamik und der elektronischen Transportphänomene mittels oberflächenempfindlicher Methoden im Makro- und Nanobereich. Auf den gelieferten epi-polierten Einkristallen wird die Bildung einer Oberflächenschicht mit leichtem Strontiumüberschuss und – im Gegensatz zum metallischen Bulk des Materials – halbleitenden Eigenschaften beobachtet. Daher kann das Wissen über die Natur der Oberflächenschicht als Schlüssel für das Verständnis des resistiven Schaltens betrachtet werden. Basierend auf systematischen Untersuchungen des Einflusses äußerer Gradienten auf die physikalischen und chemischen Eigenschaften der Oberflächenschicht wird gezeigt, dass eine Transformation zwischen einer Sr-reichen und einer Ti-reichen Oberflächenschicht leicht herbeigeführt werden kann, was die Relevanz von Ionenbewegungen und Phasenumwandlungen für den Effekt des resistiven Schaltens verdeutlicht. Im Nanobereich wird der Schaltmechanismus durch Strom-Spannungs-Rasterkraftmikroskopie mit atomarer Auflösung untersucht. Dabei werden leitfähige Cluster mit einer Größe von 20-60 nm abgebildet, die unabhängig voneinander zwischen einem EIN- und einem AUS-Zustand geschaltet werden können. Da mittels verschiedener Methoden deutliche Inhomogenitäten der Donatordotierung nachgewiesen werden können, wird davon ausgegangen, dass die leitfähigen Cluster, die als dreidimensionale ausgedehnte Defekte angesehen werden können, mit einer Nb-Segregation im Nanobereich, die bereits während des Kristallwachstums durch die Verneuil-Methode entsteht, zusammenhängen. Um einen Einblick in Prozesse zu erhalten, die während des Schaltens der Cluster stattfinden, wird eine Emulation des resistiven Schaltens durchgeführt. Dazu werden extremale Gradienten im Makromaßstab angewendet, was das Auftreten einer Phasenumwandlung von Strontiumtitanat zu Titanoxid in der Oberflächenschicht zur Folge hat. Basierend auf den experimentellen Ergebnissen sowie auf Simulationen mit der *ab initio*- und der Finite-Elemente-Methode wird zum Abschluss dieser Arbeit ein mögliches phänomenologisches Modell des resistiven Schaltens von $SrTiO_3$:Nb vorgestellt, das die Bildung von substöchiometrischen Titaniumoxidphasen als schaltbare Brücken zwischen den leitfähigen Clustern in Betracht zieht, wodurch verdeutlicht wird, dass der resistive Schalteffekt in Oxiden ein sehr komplexes Phänomen ist.

Contents

List of Figures

List of Tables

1. Introduction

In recent years, the demand for computer memories with high storage density has increased in tandem with the ongoing miniaturization of electronic devices. According to Moore's law [Moo98], the components on integrated circuits doubled approximately every two years. At the same time, the sizes of single electronic elements such as transistors or capacitors decreased and reached their physical size limits preventing a further scaling of the storage units. Furthermore, the continuous increase in power consumption for electronics exacerbated the global energy crisis. These facts call for the investigation of novel materials and phenomena that can be used as cost- and power-efficient memory cells with greater performance than those used today.

Of all the key phenomena under investigation, the resistive switching effect in oxides has received the greatest attention due to its rather simple working principle and the availability of suitable materials. Basically, the term resistive switching describes the phenomenon whereby a material can change its resistance reversibly under external gradients, thus opening up the opportunity to use the different resistance states for storing information. Once a resistance state is written, no further power supply is needed to retain the state, thereby leaving the resistive switching effect as a promising candidate for a non-volatile memory. Hence, replacing conventional volatile random-access memories with redox-based random-access memories (ReRAM) would have the potential to save a significant amount of energy.

Although first reports on the resistive switching effect in oxides were published in the 1960s [Cho65, HH65], a more intense research on the resistive switching effect with respect to potential applications in memory devices started not until the year 2000 [BBG$^+$00]. Moreover, though there have been numerous studies on the resistive switching effect and as many models for it have been presented since then, a fundamental physical understanding of the origin of the effect as well as a feasible guideline for the production of reliable memory devices is still lacking. Among the models presented so far, two different types can be distinguished. On the one hand, there are interfacial models that attempt to explain the switching effect by a modulation of the Schottky barrier formed between oxide and metal electrodes under an electrical field. This could indicate that the surface or interface of the oxide is very sensitive to external gradients present during the resistive switching but a fundamental investigation of the surface layer was not presented in the literature so far. On the other hand, there are filamentary models assuming the formation of a conducting filament in the otherwise insulating oxide that can then be switched between different resistance states by a rupture and re-forming process [Saw08]. It is also assumed that extended defects serve as template for the formation of conducting filaments, which would allow predetermining the growth of the filaments if extended defects could be introduced artificially into the crystal structure in a controlled manner.

In order to gain an insight into the nature of the resistive switching effect, the ternary oxide strontium titanate ($SrTiO_3$) has been used as a model material owing to its ability to change the electrical resistance from insulator to semiconductor and even to superconductor under external gradients [SHC64]. The resistive switching effect was studied in $SrTiO_3$ thin films and single crystals on the macro- and nanoscale, following which a filamentary nature of resistive switching related to extended defects was found [SSBW06]. The change of the resistance between a high resistive ON state and a low resistive OFF state was attributed to a valence change of the Ti d electron leading to a local insulator-to-metal transition. In general, such an insulator-to-metal transition can be introduced by various external gradients as well as by doping the material with donors. While acceptor doped $SrTiO_3$ shows a "p"-type conductivity, donor doped $SrTiO_3$ doped with the donor Nb shows "n"-type or metallic conductivity depending on the donor concentration. Hence, the investigation of $SrTiO_3$ single crystals doped with Nb as presented in this thesis has the potential to reveal the mechanisms of the nature of the insulator-to-metal transition and the related resistive switching effect.

The resistive switching effect on $SrTiO_3$:Nb thin films and single crystals has been found by a number of researchers, a fact that poses a serious theoretical problem. Since the doping with the donor Nb leads to a valence change of the surrounding Ti atoms to a lower valence state, the system should already have metallic properties [TC67] raising the question

"How is it possible to switch a metallic material ?"

Despite numerous studies on resistive switching phenomena in $SrTiO_3$:Nb, this question has not been addressed in the literature so far. However, the investigation of this question has the potential to provide insights into the underlying insulator-to-metal transition under external gradients, thus serving as a guideline for the present thesis. As second problem to be investigated in this thesis, the question

"What is the switching mechanism on the nanoscale ? "

To date, many different models for the switching in $SrTiO_3$:Nb have been suggested, which are largely based on electrical measurements only. A group of researchers introduced interfacial models regarding the modulation of the Schottky barrier at the interface between $SrTiO_3$:Nb and a metal electrode while another group introduced local models related to filaments or clusters.

In order to further elucidate the resistive switching effect on $SrTiO_3$:Nb, a careful characterization of the influence of external gradients on the properties of single crystals is presented in this thesis. Particular emphasis is placed on the characterization of the surface layer using various surface-sensitive methods since the surface is the place where the crystal is in contact with external gradients. Since in Nb-doped $SrTiO_3$ thin films, a regular arrangement of clusters serving as switching blocks was found illustrating the relevance of the investigation of the conducting paths on the nanoscale [MDS+08], in this thesis, scanning probe microscopy (SPM) is applied on single crystals. Through analyses of the crystallographic structure, the chemical composition and the electronic structure, it is shown that on the surface of $SrTiO_3$:Nb single crystals grown by the Verneuil method, an intrinsic semiconducting Sr-rich surface layer is formed having significant different properties than the metallic bulk. Using electrical measurements of resistance and capacitance, this surface layer is identified as the place where resistive switching takes place.

Investigations of the electronic transport and resistive switching on the nanoscale using local conductivity atomic force microscopy (LC-AFM) show that resistive switching is related to conducting clusters with a size of 20-60 nm that are intrinsically present in the crystals. Since the chemical composition – particularly with respect to the distribution of the Nb dopants – is found to be rather inhomogeneous in the investigated crystals, the evolution of the conducting clusters is attributed to an Nb segregation on the nanoscale.

At the end of the thesis, an emulation of switching is performed by applying extremal electrical gradients on the macroscale, resulting in a phase transformation from $SrTiO_3$ to TiO_x in the surface layer. Based on these findings, a potential model for the origin of the cluster-like resistive switching is introduced describing the switching of the clusters through the formation of nanofilaments related to phase-change mechanisms.

The thesis is organized as follows.

Chapter 2 provides a general overview of the basis properties of $SrTiO_3$ with particular emphasis on the insulator-to-metal transitions and the resistive switching effect. Initially, the crystal preparation based on the Verneuil method and the crystallographic perovskite structure is described. The importance of defects in different dimensions, starting from point defects influencing the electronic structure to the extended defects such as disloca-

tions serving as potential easy diffusion path for oxygen in the surface layer as well as three-dimensional defects such as secondary phases, is illustrated. The electronic structure of undoped and doped $SrTiO_3$ and the special role of the surface layer is highlighted. Following a short description of the lattice dynamics, the electronic transport phenomena are focused and a detailed overview of the different models of resistive switching presented in the literature is given and their respective advantages and disadvantages are discussed.
In Chapter 3, the experimental methods are described. The various techniques of sample preparation as well as the characterization methods for the different properties of the crystal are presented.
In Chapter 4, the experimental results are discussed. Following the same guideline as in Chapter 2, investigations of the crystallographic structure and the chemical composition and the electronic structure are described. In particular, the influence of external gradients on the properties of the surface layer is presented prior to focusing on the electronic transport phenomena and resistive switching on the macro- and nanoscale. At the end of the chapter, a possible phenomenological model of resistive switching in $SrTiO_3$:Nb is derived based on the investigation of phase transitions of the surface layer showing that ionic movements due to the electrical and chemical gradients play an important role during switching leading to local electrochemical solid-state reactions.
In Chapter 5, the thesis is concluded and a short outlook is given.

2. Basics

2.1. Crystal growth

The production of artificial crystals has always been a challenging task and various methods were developed in the last century [Sch00]. In 1902, Verneuil succeeded in growing ruby crystals from a melt in a flame-fusion technique, which from then on was modified and improved to become the standard technique for growing oxide crystals. The Nb-doped $SrTiO_3$ crystals investigated in this work were also produced according to the Verneuil method. Compared to other techniques, this method is advantageous because no crucible, which could cause contaminations, is needed, thereby improving the quality of the grown single crystals. However, the method has the disadvantage that during the growth process, high temperature gradients are present in the sample. This could lead to the evolution of inhomogeneities, especially in doped crystals, and to the formation of dislocations. As reported by Bednorz [BS77], the dislocation density of $SrTiO_3$ crystals grown by Verneuil method is typically more than 10^6/cm.

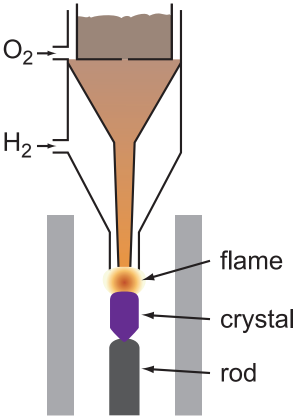

Figure 2.1.: Illustration of the crystal growth process using the Verneuil method.

A schematic of the Verneuil method is presented in Fig. 2.1. On top of the apparatus pure powders of the starting material are filled into a reservoir in an appropriate mixing ratio. In the case of Nb-doped $SrTiO_3$, the starting powders are SrO, TiO_2 and Nb_2O_5. Through an opening in the bottom of the reservoir, the powders fall into a tube where they are mixed with oxygen. Via a second tube, hydrogen is supplied leading to a combustion at the end of both tubes and resulting in the melting of the powders. The melted mass falls onto a support rod where it crystallizes. By slowly moving the rod downwards a pear-shaped crystal evolves. After cooling, the crystal is cut into slices (typical thickness 0.5 mm) along the crystal axes and the surfaces are polished.

Based on the Verneuil method, a number of other crystal growth techniques were developed for producing crystals from melt, as briefly summarized in the following for the sake of completeness [DBPD10].

In the Czochralski process, not only a small amount of powder like in the original Verneuil method but the whole starting material is molten in a crucible. By means of a cooled seed crystal, which is slowly pulled out of the melt, large crystals can be obtained. A modification of the Czochralski process is the Nacken-Kyropoulus process, in which the position of the seed crystal is fixed and the growth of the crystal is controlled by reducing the temperature of the melt.

In the Bridgman-Stockbarger process, the starting material is filled into a crucible moving through a temperature gradient in order to melt the material gradually. Owing to the special form of the crucible, the melt solidifies as single crystal. A similar technique is the floating zone process whereby only a small zone of a polycrystal is heated above the melting point. By moving the polycrystal, the floating zone travels through the material resulting in a recrystallization as single crystal.

A further approach of growing single crystals is the growth from solution. In the top seeded solution growth (TSSG), the starting material of the crystal is solved in a high-temperature solution and then the crystal is pulled out using a seed crystal similar to that in the Czochralski process. The solution growth technique was found to deliver $SrTiO_3$ crystals with the highest structural quality and having a density of dislocations below $100/\mathrm{cm}^2$, whereas the density of dislocations in Verneuil grown $SrTiO_3$ crystals is typically above $10^6/\mathrm{cm}^2$ [SC11].

2.2. Crystal structure

The band insulator $SrTiO_3$ belongs to the class of ternary oxides that crystallize in the perovskite structure. At room temperature, this structure is cubic and can be described by the space group $O_h^1 - Pm3m$. The lattice constant at room temperature of $SrTiO_3$

was measured with high precision and was found to be $a_0 = 3.905268(98)$ Å[SKS12]. The illustration of the unit cell structure shown in Fig. 2.2 reveals that the Sr atoms are

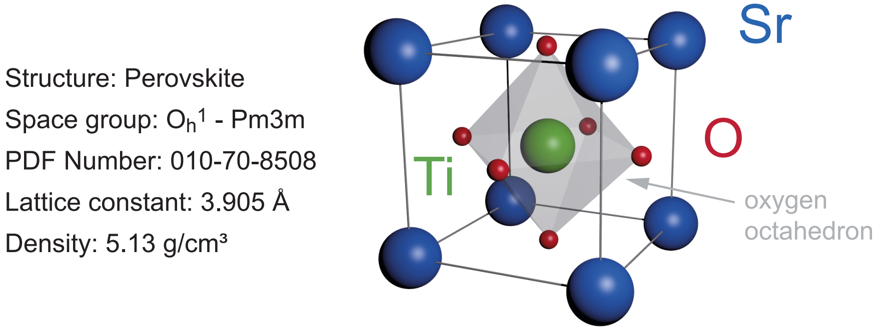

Figure 2.2.: The crystal structure of strontium titanate. [MRS].

positioned at the edges while the Ti atom occupies the centre position at (1/2,1/2,1/2). Each Ti atom is surrounded by six O atoms forming an octahedral TiO_6 cluster. Since the edge of each of these octahedra touches an octahedron in the neighbouring cell and thus being corner-sharing, the whole crystal can be regarded as a network of TiO_6 octahedra with the Sr atoms being positioned in the space between them. Owing to the crystallization in the perovskite structure, a regular arrangement of alternating SrO and TiO layers is present along the <100> directions. From the viewpoint of a classical ionic picture, the chemical bonding of $SrTiO_3$ is mixed covalent-ionic. Due to hybridization of the Ti3*d* and the O2*p* states, the nature of the bond in the octahedron between the Ti, which is in valence state 4+, and the O, which is in valence state -2, is covalent while the bonding to the Sr, which is in valence state +2, is mainly ionic [Mar09, LGF82].

Under the influence of external gradients, the perovskite structure can be distorted by a displacement of the cations and by a tilting of the oxygen octahedra which is of particular importance for the description of the structural phase transition between the cubic and the tetragonal phases taking place at 105 K [LSR11]. The low-temperature tetragonal phase of $SrTiO_3$ can be described according to the space group $\mathrm{D}_{4\mathrm{h}}^{18} - \mathrm{I4/mcm}$ with the lattice parameters $a \approx 2^{1/2}a_0$ and $b \approx 2a_0$ where a_0 is the lattice constant of the cubic phase [MRS].

The density at room temperature is 5.13 g/cm^3 [MRS] and the Mohs hardness is 6–6.5 [ABBN], making $SrTiO_3$ a denser but softer material than, for example diamond. The fracture of $SrTiO_3$ is conchoidal and the tenacity is brittle. In nature, $SrTiO_3$ can be found only rarely and was first discovered in 1982 in Siberia as a mineral, which was denominated tausonite.

2.3. Defects

In a solid, a variety of different defects can occur influencing the properties of the material significantly. Generally, they can be distinguished between point defects and extended defects and categorized by their dimension as follows.

- **Point defects**

  0 D: Vacancies, interstitials

- **Extended defects**

  1 D: Linear clusters, dislocations

  2 D: Stacking faults, grain boundaries, Wadsley defects, shear planes, surface

  3 D: Surface layer, voids, blocks, microdomains, intergrowth

2.3.1. Point defects

Point defects are distortions of the lattice in one single point and can be classified into intrinsic and extrinsic defects. Intrinsic defects can either be vacancies (Schottky disorder) or interstitials (Frenkel disorder) [Kit04]. If the crystal is doped unintentionally by impurities or by donor or acceptor doping for influencing the properties, these impurity atoms can form an extrinsic defect by occupying a regular lattice site by substitution or an interstitial site if their size is sufficiently small. In order to denominate the specific point defect, the so-called Kröger-Vink notation is used [KV56]

$$M_S^C . \tag{2.1}$$

In this notation, M specifies the species, which can be an atom like Sr or O, a vacancy V, an electron e, a hole h or an interstitial i. S denotes the site which the species occupies in the lattice and C denotes the charge. A negative charge is illustrated by the prime symbol ($'$) and a positive charge by a dot ($^{\cdot}$). Hence, $\mathrm{V}_{\mathrm{O}}^{\cdot\cdot}$ denotes an oxygen vacancy and $\mathrm{V}_{\mathrm{Sr}}''$ denotes an strontium vacancy, which are the predominant intrinsic defects in $\mathrm{SrTiO_3}$. Due to the need of charge neutrality in the crystal, a single charged point defect cannot be formed, but is associated with the generation of one or several defects having the opposite charge. The reactions leading to the formation of intrinsic defects in $\mathrm{SrTiO_3}$

can be expressed by the following equations [AAJC95].

$$\mathrm{SrTiO_3} \rightleftharpoons \mathrm{V_{Sr}''} + \mathrm{Sr_i^{\cdot\cdot}} \tag{2.2}$$

$$\mathrm{SrTiO_3} \rightleftharpoons \mathrm{V_{Ti}''''} + \mathrm{Ti_i^{\cdot\cdot\cdot\cdot}} \tag{2.3}$$

$$\mathrm{SrTiO_3} \rightleftharpoons \mathrm{V_{O}^{\cdot\cdot}} + \mathrm{O_i''} \tag{2.4}$$

$$\mathrm{SrTiO_3} \rightleftharpoons \mathrm{V_{Sr}''} + \mathrm{V_{O}^{\cdot\cdot}} + \mathrm{SrO(s.p.)} \tag{2.5}$$

$$\mathrm{SrTiO_3} \rightleftharpoons \mathrm{V_{Ti}''''} + 2\mathrm{V_{O}^{\cdot\cdot}} + \mathrm{TiO_2(s.p.)} \tag{2.6}$$

$$\mathrm{SrTiO_3} \rightleftharpoons \mathrm{V_{Sr}''} + \mathrm{V_{Ti}''''} + 3\mathrm{V_{O}^{\cdot\cdot}} + \mathrm{SrTiO_3} \tag{2.7}$$

The first three reactions describing the formation of Frenkel pairs are energetically very unfavourable owing to the close packing of the perovskite structure and can thus be neglected. The reactions in Eqs. 2.5 and 2.6 may be described as “Schottky-like” since they not only lead to the formation of Schottky pairs but also to the formation of secondary Sr-rich or Ti-rich phases. The formation of strontium vacancies according to Eq. 2.5 becomes relevant at temperatures above 1500 °C and the formation of a titanium vacancy according to Eq. 2.6 is rather unlikely due to the high formation energy.

Temperature dependence

Depending on the temperature, different defect reactions will take place in $\mathrm{SrTiO_3}$ that can be categorized in three temperature regimes [Hof10]. At low temperatures ($T < 500^\circ$ C), only the thermally activated generation and recombination of electron-hole pairs is relevant.

$$\mathrm{nil} \rightleftharpoons \mathrm{e}' + \mathrm{h}^{\cdot} \tag{2.8}$$

The equilibrium of this reaction is related to the thermally activated reaction constant K_I via the law of mass action

$$n \cdot p = K_I(T) = N_\mathrm{C}(T) \cdot N_\mathrm{V}(T) \cdot \exp\left(-\frac{E_g^0 - \alpha T}{kT}\right) \tag{2.9}$$

where N_C and N_V is the effective density of states as function of the temperature T at the bottom of the conduction band and at the top of the valence band respectively. $E_g^0 - \alpha T$ describes the temperature dependence of the band gap and k denotes the Boltzmann constant.

At higher temperatures ($500°\mathrm{C} \leq T \leq 800°\mathrm{C}$) under reducing conditions, oxygen atoms can leave their lattice sites leaving behind oxygen vacancies, which then become the dominant defect mechanism. It can be described by the following equation [Moo94, MH97, BE81]:

$$\mathrm{O_O^x} \rightleftharpoons \mathrm{V_{O}^{\cdot\cdot}} + 2\mathrm{e}' + \frac{1}{2}\,\mathrm{O_2} \tag{2.10}$$

In this case, the positive charge of the oxygen vacancy is compensated for by the generation of two electrons in the conduction band. The law of mass action of this reaction yields

$$[\mathrm{V_O}^{\cdot\cdot}] \cdot n^2 \cdot {p_{\mathrm{O}_2}}^{1/2} \quad = \quad K_{red}(T) \quad = \quad K^0_{red} \cdot \exp\left(-\frac{\Delta H_{red}}{kT}\right). \tag{2.11}$$

where n is the concentration of electrons, p_{O_2} the oxygen partial pressure and H_{red} the reduction enthalpy.

In the highest temperature regime ($T > 1000°$ C), all three elements can leave their lattice sites, resulting in the formation of vacancies according to the Schottky equilibrium.

$$\mathrm{nil} \quad \rightleftharpoons \quad \mathrm{V}''_{\mathrm{Sr}} + \mathrm{V}''''_{\mathrm{Ti}} + 3\mathrm{V}^{\cdot\cdot}_{\mathrm{O}} \tag{2.12}$$

The associated law of mass action reads

$$\left[\mathrm{V_{Sr}}''\right] \cdot \left[\mathrm{V_{Ti}}''''\right] \cdot [\mathrm{V_O}^{\cdot\cdot}]^3 \quad = \quad K_S(T) \quad = \quad K^0_S \cdot \exp\left(-\frac{\Delta H_s}{kT}\right). \tag{2.13}$$

Conductivity

Since the number of electrons n and holes p is related to the present mechanism of charge compensation via the specific reaction constants, the conductivity σ, which depends on the mobilities μ_n and μ_p and the elementary charge e, is a function of oxygen partial pressure and temperature. Since the temperature dependence of the mobilities is much weaker than that of the concentrations of n and p, it can be neglected in a first approximation.

$$\sigma \quad = \quad e\,(n\mu_n + p\mu_p) \tag{2.14}$$

With regard to the overall condition of charge neutrality depending on the concentration of single ionized donors $[D^{\cdot}]$ and acceptors $[A']$ and double ionized vacancies $[\mathrm{V}''_{\mathrm{Sr}}]$ and $[\mathrm{V}^{\cdot\cdot}_{\mathrm{O}}]$, it is possible to estimate the concentration of electrons and holes in specific oxygen partial pressure regimes.

$$n + 2[\mathrm{V}''_{\mathrm{Sr}}] + [A'] \quad = \quad p + 2[\mathrm{V}^{\cdot\cdot}_{\mathrm{O}}] + [D^{\cdot}] \tag{2.15}$$

Reducing conditions

Under reducing conditions with very low oxygen partial pressure, the formation of oxygen vacancies compensated for by electrons predominates independently on acceptor or donor doping leading to $n = [V^{\cdot\cdot}_{\mathrm{O}}]$. Hence, the following relation for the conductivity in this pressure regime can be extracted from Eqs. 2.15, 2.14 and 2.11.

$$\sigma \quad \propto \quad n \quad \propto \quad p_{\mathrm{O}_2}^{-1/6} \tag{2.16}$$

Intermediate regime

Within an intermediate oxygen partial pressure regime, the concentration of donors in donor doped $SrTiO_3$ is much greater than the concentration of vacancies $[V_O^{\cdot\cdot}] \ll [D^{\cdot}]$. In this so-called electronic compensation regime, the conductivity is constant and does not depend on the oxygen partial pressure.

$$\sigma_d \quad \propto \quad n \quad = \quad [D^{\cdot}] \quad = \text{const} \tag{2.17}$$

On the other hand, in an acceptor-doped system, the acceptors are compensated for by oxygen vacancies giving the charge neutrality equation $2[V_O^{\cdot\cdot}] = [A']$ and the conductivity

$$\sigma_a \quad \propto \quad n \quad = \quad p_{O_2}^{-1/4}. \tag{2.18}$$

Oxidizing conditions

Under oxidizing conditions, the concentration of strontium vacancies in donor-doped $SrTiO_3$ compensating for the negatively charged donors increases due to the Schottky equilibrium, thus leading to the charge neutrality equation

$$2[V''_{Sr}] \quad = \quad [D^{\cdot}]. \tag{2.19}$$

In this regime, the conductivity decreases in relation to increasing oxygen partial pressure according to

$$\sigma_d \quad \propto \quad n \quad = \quad p_{O_2}^{-1/4} \tag{2.20}$$

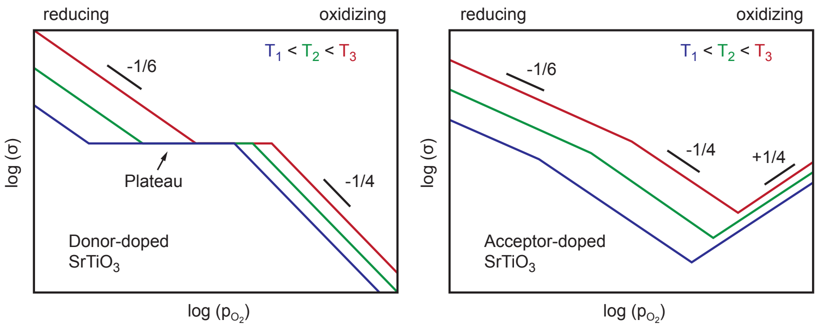

Figure 2.3.: Conductivity as function of oxygen partial pressure in donor-doped and acceptor-doped $SrTiO_3$ as predicted by point defect chemistry.

In acceptor-doped $SrTiO_3$, the compensation is still realized by oxygen vacancies as in the intermediate regime but the hole concentration exceeds the electron concentration.

Therefore, the conductivity is governed by the hole transport and increases as function of oxygen partial pressure.

$$\sigma_a \quad \propto \quad n \quad = \quad p_{\mathrm{O_2}}^{+1/4} \tag{2.21}$$

Nb doping

Following doping of $\mathrm{SrTiO_3}$ with the donor Nb, reactions get activated by the pentavalent Nb substituting the tetravalent Ti, thus leading to negatively charged point defects [BHH+08, BHWM09]. Under reducing conditions, this charge is compensated for by the generation of free electrons leading to metallic conductivity while the compensation mechanism changes under oxidizing conditions to the formation of strontium vacancies and the segregation of SrO as a secondary phase. The interplay between those two mechanisms is described by the redox equation

$$2\mathrm{Sr_{Sr}} + 2\mathrm{Nb^{\cdot}_{Ti}} + 6\mathrm{O_O} + 2\mathrm{e'} + \frac{1}{2}\mathrm{O_2(g)} \rightleftharpoons \mathrm{V''_{Sr}} + \mathrm{Sr_{Sr}} + 2\mathrm{Nb^{\cdot}_{Ti}} + 6\mathrm{O_O} + \mathrm{SrO(s.p.)}. \tag{2.22}$$

Hence, the chemical composition of the material can be expressed as $\mathrm{SrTi_{1-x}Nb_xO_3}$ under reducing conditions and $\mathrm{Sr}_{1-\frac{1}{2}\mathrm{x}}\Box_{\frac{1}{2}\mathrm{x}}\mathrm{Ti_{1-x}Nb_xO_3}$ under oxidizing conditions using the symbol $\Box$ for a vacancy. A further possibility of charge compensation would be the creation of a Ti vacancy resulting in the composition $\mathrm{SrTi}_{1-5/4x}\Box_{1/4x}\mathrm{Nb}_x\mathrm{O_3}$, which is however relatively unlikely due to the high formation energy of a Ti vacancy.

Diffusion

The properties of an oxide depend very sensitively on the concentration of the point defects. The reaction of the distribution of the point defects on a change of the ambient conditions is described by the diffusion equation [Phi91].

$$\frac{\partial}{\partial t}c(\mathbf{x},t) \; = D\nabla^2 c(\mathbf{x},t) \tag{2.23}$$

c is the concentration of the diffusing species, t is the time, D is the diffusion coefficient and x is the position. In this case, a random-walk diffusion in a homogeneous medium is taken into account while structural inhomogeneities or a drift due to electrical gradients is disregarded. In oxides such as $\mathrm{SrTiO_3}$, the interaction with oxygen influencing the distribution of oxygen vacancies is of particular interest. As a common method to probe the diffusion kinetics, an oxygen isotope exchange using $^{18}\mathrm{O}$ with a subsequent measurement of a depth profile using secondary ion mass spectroscopy is applied. As shown by DeSouza et al., the diffusion profiles obtained in this way in $\mathrm{SrTiO_3}$ can potentially be explained by the existence of a space charge layer on the surface leading to an depletion of oxygen vacancies [SMPW12].

2.3.2. Line defects

In $SrTiO_3$, two types of one-dimensional line defects are relevant – namely the agglomeration of point defects along a column and the dislocations [Szo10].

1D agglomeration of vacancies

As presented in section 2.3.1, the generation of vacancies in $SrTiO_3$ can be described in terms of point defect chemistry as statistically distributed defects in the crystal lattice. However, the assumption of such a statistical distribution with non-interacting point defects is only valid as long as the chemical composition is inside the stoichiometry width, which is only 0.1 at%, even at high temperatures [WDSS09, Smy84]. If the concentration of vacancies is large enough, they tend to form linear clusters oriented along the atomic columns in the perovskite lattice. For example, it has been reported based on investigations using high-resolution transmission electron microscopy that strontium vacancies V_{Sr}'' form linear clusters in the form of platelets oriented in the SrO planes in slightly Ti-rich $SrTiO_3$ thin films [TKO+11].

Dislocations

Dislocations are line defects related to distortions of the crystallographic structure [HB11]. In a solid, two types of dislocations can develop, namely edge dislocations and screw dislocations. As illustrated schematically in Fig. 2.4a, an edge dislocation can be generated if an extra half-plane is introduced in a perfect crystal lattice. Far away from the dislocation, the distance between the atoms correspond to the lattice parameter of the undistorted crystal, but close to the edge of the half plane, the atomic distances are increased altering the strength of bonding in this region and inducing a strain field close to the core of the dislocation. According to the theory of elasticity, the core of dislocation has a typical diameter of about 1 nm.

Due to the crystal structure of $SrTiO_3$, different types of edge dislocations can be present. If a half plane consisting of a double plane of SrO and TiO_2 is introduced into the crystal, an Sr- or Ti-terminated dislocation can evolve depending on the atomic configurations at the core of the dislocation, both of which have been found experimentally by HR-TEM investigations [ZSR02, WDSS09, JTU05].

The second type of dislocation, the screw dislocation, is illustrated in Fig. 2.4b. A screw dislocation can be visualized by cutting an imaginary incision into the crystal and reassembling the edges in a shifted manner. Depending on the sign of the shift, a left-handed or right-handed screw dislocation evolves.

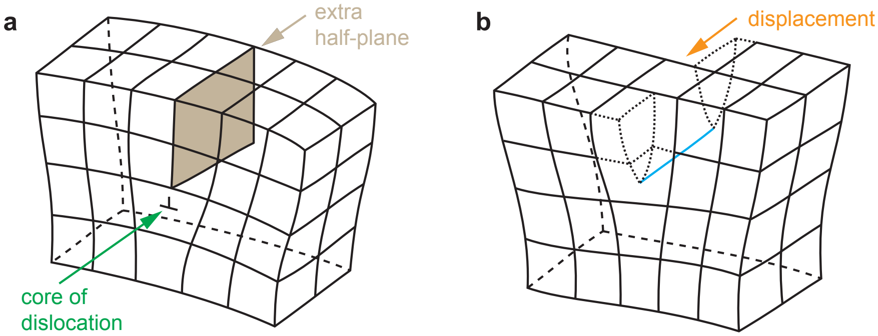

Figure 2.4.: Illustration of the two types of dislocations in a crystal. (a) Edge-dislocation. (b) Left-handed screw-dislocation. Adapted from [HB11].

Network of dislocations

Since the Burgers vector that describes the distortion of the lattice by the presence of a dislocation is a conserved quantity, a dislocation cannot end inside the crystal. It can only end at the surface or at grain boundaries, form a closed dislocation loop or branch into other dislocations [HB11]. Due to the high density of dislocations, especially in the surface layer (in $SrTiO_3$ values of $6 \cdot 10^9$ cm^{-2} were observed close to the surface after polishing, while the density in the of the as grown crystal was $\approx 4 \cdot 10^4$ cm^{-2}), a network of dislocations is present influencing the properties of the entire crystal [WZS98, SBS14]. For example, the conductivity at the core of Ti-rich edge dislocations is enhanced in relation to a shrinking of the band gap which opens up conducting paths in an insulating matrix [WDSS09].

2.3.3. Two-dimensional defects

Stacking faults

A stacking fault is a two-dimensional crystallographic defect related to a distortion of the sequence of planes in the lattice. In an ideal perovskite, having the formal composition ABO_3, where A is an anion like Sr and B is a cation like Ti, a regular sequence of AO and BO_2 planes is present: $AOBO_2AOBO_2AO$... If a stacking fault is generated, the sequence is changed to either $AOBO_2BO_2AO$... or $AOBO_2AOAOBO_2$... In the case of $SrTiO_3$, this would result in a double layer of SrO or TiO_2. In a real crystal, local stacking faults can occur if an additional plane is not extended over the whole crystal but ends at a dislocation [KWYZ09]. Due to the distortion of the lattice by the stacking fault, the local electronic structure changes affecting the electronic conductivity [Alb].

Shear planes

A crystallographic shear plane evolves if one part of the crystal (e.g. a block) is shifted relatively to the rest of the crystal leading to the presence of a two-dimensional defect at the boundary of the two parts. In a perovskite, a shear plane is related to a shift of half a unit cell, which causes a local increase in the density since the octahedra become corner-sharing leading to an agglomeration of oxygen [CF89]. In presence of a large number of blocks, shear planes can form regularly arranged structures or – if the size of the blocks varies significantly – build a non-periodic almost three-dimensional structure called Wadsley defect [GM80]. In the PbO-La_2O_3-TiO_2 system it was also found that disordered shear planes can accommodate a AO excess in an ABO_3 oxide [PG92]. The evolution of shear planes is also relevant for the formation of three-dimensional defects such as secondary phases since a deintercalation or dismantling of the crystal can start due to the weakening of the chemical bonds at the shear planes.

Grain boundaries

Grain boundaries are formed if different grains are present in the solid and thus are not expected to be present in a perfect single crystal. However, depending on the conditions during crystal growth, grain boundaries can be generated unintentionally.In particular, in $SrTiO_3$, where single crystals were grown by the Verneuil method, a mosaic structure related to the formation high and low angle grain boundaries between small crystallites was found [YYK00]. Similar to the one-dimensional dislocations, grain boundaries can serve as easy diffusion paths and influence the transport properties.

2.3.4. Secondary phases

Ternary oxides such as $SrTiO_3$ are very complex systems, in which the formation of secondary phases can occur easily. As predicted by Schmalzried *et al.*, there is a general tendency for kinetic demixing in multinary oxides in an potential gradient depending on the relative mobilities of the diffusing species [SL81]. Furthermore, an initial excess of Ti or Sr can lead to segregation effects and the formation of secondary phases as three-dimensional defects since the stoichiometry range of $SrTiO_3$ is relatively small. It was found that in $SrTiO_3$ the solubility of TiO_2 is less than 0.5 mol% and the solubility of SrO is even less than 0.2 mol% below 1400 °C [Rah04, WSP84], which demands a very careful adjustment of the starting materials for the crystal growth in order to obtain stoichiometric crystals. In Fig. 2.5, the high temperature phase diagram of the Sr-Ti-O system as derived by McCarthy *et al.*[MWR69] is shown illustrating the situation during crystal growth. It can be seen that at a low Sr content the formation of TiO_x as secondary phase takes place whereas at high Sr content Sr-rich phases evolve, which is in agreement with the phase diagram derived by Cocco and Massazza [CM63, BBP07]. However, these segregation effects cannot only take place at high temperatures but also at relatively low temperatures as described by Brandão *et al.* for the SrO-TiO_2-CO_2 system [BMK+11]. At low CO_2 partial pressures, which should be the case in most experiments under vacuum conditions, the formation of $SrCO_3$ can be neglected but – depending on the SrO/TiO_2 ratio – Ti-rich or Sr-rich phases evolve even at 500 K.

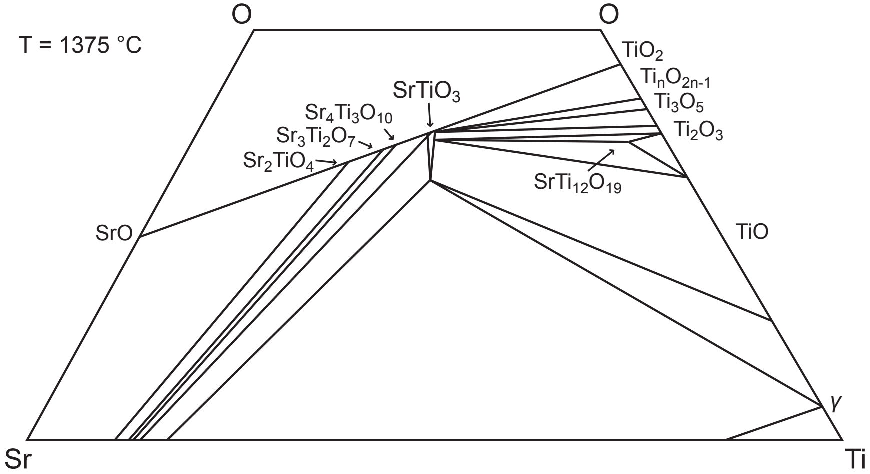

Figure 2.5.: The phase diagram of the Sr-Ti-O system according to McCarthy *et al.* [MWR69].

Ti-rich phases

As can be seen from the Sr-Ti-O phase diagram in Fig. 2.5, a formation of titanium dioxide (TiO_2) as secondary phase takes place in Ti-rich $SrTiO_3$. TiO_2 can crystallize in three polymorphic forms, namely rutile and anatase showing both a tetragonal crystal structure and brookite crystallizing in an orthorhombic structure [Car08]. Besides TiO_2, a variety of titanium suboxides exists as can be seen from the phase diagram of the Ti-O system depicted in Fig. 2.6. They can be created by a reduction of TiO_2.

$$\mathrm{TiO_2} \rightarrow \frac{1}{2}\mathrm{O_2} + \mathrm{Ti}_n\mathrm{O}_{2n-1} \tag{2.24}$$

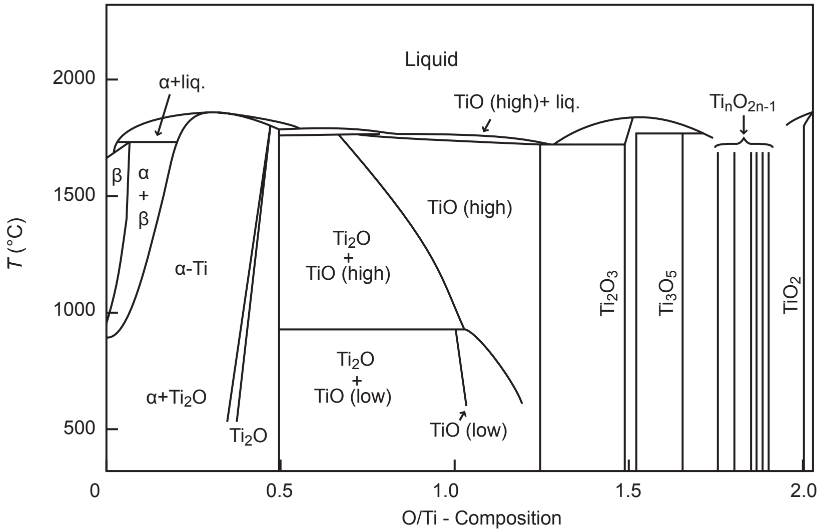

Figure 2.6.: The phase diagram of the Ti-O system according to Hayfield [Hay02].

In a wide range of composition, titanium monoxide (TiO) exists. At higher oxygen concentrations, the phases titanium sesquioxide (Ti_2O_3) and anosovite (Ti_3O_5) evolve. In a composition range having a O/Ti ratio between 1.75 to 1.90, an homologous series of suboxides with the chemical formula Ti_nO_{2n-1} ($4 \leq n \leq 10$) named Andersson-Magnéli phases exists [AM56]. They exhibit a triclinic shear structure, in which the oxygen octahedra are connected with each other in a complex manner. In non-stoichiometric Nb-doped $SrTiO_3$, the presence of such Andersson-Magnéli phases as three-dimensional defects has been proved experimentally [FW85, HY03]. At the other end of the phase diagram, Ti-rich oxides with a Ti/O ratio larger than one are present between titanium monoxide and metallic titanium, namely titanium hemioxide (Ti_2O) and trititanium oxide (Ti_3O), which was found to be a stable oxide, particularly in Nb-doped systems [DSDV77]. Table 2.1 gives an overview of the different titanium oxides.

Sr-rich phases

In Sr-rich Sr-Ti-O systems, excess strontium is compensated by a formation of a crystallographic shear structures of SrO and TiO_2 named Ruddlesden-Popper phases having the structural formula $Sr_{n+1}Ti_nO_{3n+1}$ [RP57, RP58, Nog00b, SS99]. As depicted in Fig. 2.7,

Name	**Formula**	**Crystal structure**
Titanium dioxide	TiO_2	Rutile, Brookite, Anatase
Andersson-Magnéli phases	$Ti_{10}O_{19}$ Ti_9O_{17} Ti_8O_{15} Ti_7O_{13} Ti_6O_{11} Ti_5O_9 Ti_4O_7	Triclinic structure
Anosovite	Ti_3O_5	Monoclinic structure
Titanium sesquioxide	Ti_2O_3	Corundum structure
Titanium monoxide	TiO	Rocksalt structure
Titanium hemioxide	Ti_2O	Cadmium iodide structure
Trititanium oxide	Ti_3O	Layered structure

Table 2.1.: Titanium oxides and their crystal structure

they are generated by intercalation of an SrO layer rock salt layer along the $\frac{1}{2}\,[111]$ direction between n $SrTiO_3$ perovskite layers leading to a change in the crystal symmetry from Pm3m to Immm.

$$n \cdot \mathrm{SrTiO_3} + \mathrm{SrO} \rightarrow \mathrm{Sr}_{n+1}\mathrm{Ti}_n\mathrm{O}_{3n+1} \tag{2.25}$$

Starting from $SrTiO_3$ ($n = \infty$) to SrO ($n = 0$), a series of different phases can be created that can be regarded as three-dimensional defects that influence the ionic and electronic transport properties of the crystal.

In donor-doped $SrTiO_3$, not only an overall non-stoichiometry with an Sr/Ti ratio larger than 1 but also the compensation mechanism of the donor dopant can lead to a formation of Sr rich phases. According to Eq. 2.22, the negatively charged Nb is compensated by strontium vacancies under oxidizing conditions leading to the formation of SrO as secondary phase.

Donor segregation

An additional mechanism forming three-dimensional defects in donor-doped $SrTiO_3$ can be the segregation of donors such as Nb. Depending on the conditions during sample fabrication, it is possible that Nb is not homogeneously incorporated into the crystal structure by substituting Ti atoms but segregates as clusters or secondary phases. While some groups succeeded in fabricating single-phase Nb-doped $SrTiO_3$ ceramics up to a Nb-content of 40% [ISW96], other researches reported an Nb segregation to grain boundaries or triple pockets [FG03, BZBH08]. Especially under reducing conditions, distinct Nb segregation at the grain boundaries has been observed, which was attributed to the negative charge of the grain boundary inducing a positively charged space charge region [CKD02]. Besides these substantial segregations taking place in ceramics, where a large number of grain boundaries as segregation sites is present, also in $SrTiO_3$:Nb thin films indications for Nb

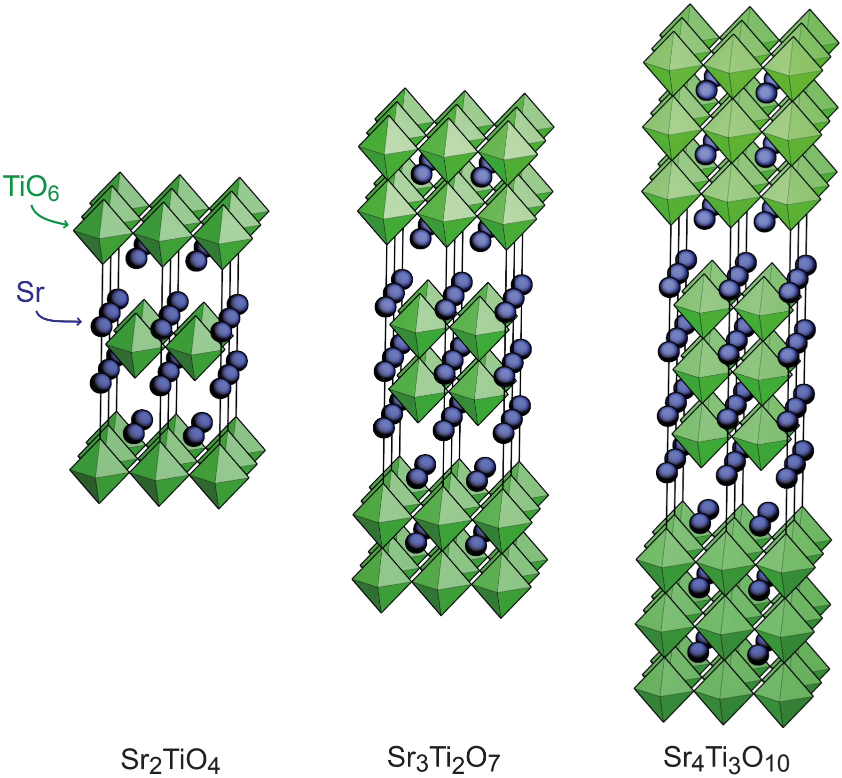

Figure 2.7.: Illustration of the crystal structure of Ruddlesden-Popper phases.

segregation on the nanoscale have been reported [ZML+05].

2.3.5. Structure of the surface

Surface charge

The most obvious extended defect of a crystal is the surface representing the boundary between the crystal and the surrounding. Depending on the crystallographic orientation, various surface structures can evolve with different electrostatic properties influencing the stability of the surface. Classically, three types of surfaces can be distinguished by their charge Q and their dipole moment $\vec{\mu}$ [Tas79, Nog00a]. A Type I surface is uncharged and unpolar($Q = 0$, $\vec{\mu} = 0$), whereas a type II surface has a dipole moment ($Q = 0$, $\vec{\mu} \neq 0$) and a type III surface is charged and polar ($Q \neq 0$, $\vec{\mu} \neq 0$).

Atomic structure

The atomic structure of the surface is determined by the surface termination and orientation. In (100) direction, which is the most stable surface of $SrTiO_3$, the crystal can be terminated by either a TiO_2 or an SrO layer due to the composition of the perovskite structure,. In this case, a surface Sr anion is surrounded by eight oxygen atoms instead of twelve in the bulk and also the coordination of a surface Ti is decreased from six-fold to five fold. [Nog96]. In this description, the surface is regarded as atomically flat, which however only the idealized case. A real crystal surface is the host of different kinds of surface defects [Nog96] as illustrated in Fig. 2.8. If an evolution of a terrace structure evolves, steps, ledges and kinks are formed, which have been investigated on $SrTiO_3$ by scanning probe microscopy [SS99, SSB+00, RC08, MNP+11]. The atomic resolution of the scanning tunnelling microscope (STM) even allows the direct investigation of the surface diffusion *in situ* leading to the formation of different surface terminations or nanostructures [MDS+06]. Surface defects with a point-like nature are ad-atoms, which are related to adsorption processes since the surface is the place where the crystal is in contact to the ambient. Depending on the chemical properties of the adsorbants, physisorption, which denotes the bonding of atoms or molecules to the surface via the van-der-Waals force, or chemisorption, which denotes a chemical bonding between the adsorbant and the dangling bonds on the surface, takes place. By removing oxygen from the lattice, either from the SrO or TiO_2 layer on top, surface oxygen vacancy (SOV) are created that influence the electronic surface structure [AKME09].

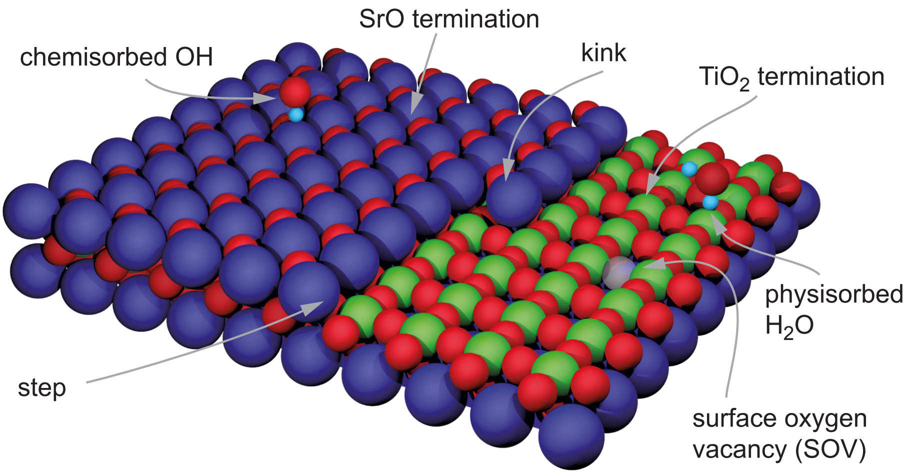

Figure 2.8.: Defects of the $SrTiO_3$ (100) surface. Adapted from [Szo10].

Distortion mechanisms

During the formation of the surface, the chemical bonds of the topmost atomic layers are broken resulting in the presence of dangling bonds[Nog96, Kit04]. In order to minimize the surface energy, the atoms of the surface rearrange and saturate the bonds, which results in a distortion of the lattice structure at the surface. Three distortion mechanisms can be distinguished, namely relaxation, rumpling and reconstruction as illustrated in Fig. 2.9.

Relaxation leads to the change of the spacing between the topmost atomic layer and the underlying layers. By an inward relaxation the spacing is contracted whereas by an outward relaxation the spacing is expanded.

Rumpling denotes a process, in which different atomic species of the topmost layer move in opposite directions. It often occurs simultaneously with relaxation. In oxides, it is generally observed that oxygen atoms move outwards whereas anions move inwards.

Reconstruction leads to a fundamental change of the periodicity of the surface structure, which can even be related to a change of the space group or the formation of a superlattice. It can be realized by an expansion of the original unit cell in one or several directions as well as by rotations giving rise to the existence of various reconstructions. By investigating $SrTiO_3$ (001) surfaces after reduction, eight different reconstructions have been found, which have been described predominately by models taking a double layer TiO_2

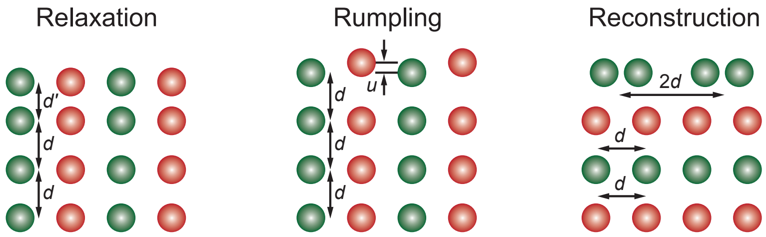

Figure 2.9.: Illustration of the three surface distortion mechanisms according to [Nog96].

structure into account [MNP+11]. The process of reconstruction is strongly influenced by the interaction with adsorbates, which can induce the formation of a new reconstruction or destroy a present reconstruction due to the binding to the dangling bonds.

Surface layer

It is well known that in metal oxides not only the direct surface, but also a surface layer can have different properties than the bulk. Extensive studies on $BaTiO_3$ revealed that the presence of such a surface layer strongly influences the ferroelectric properties of the material [Kän55, TI62]. Many oxides with perovskite structure were investigated and it was found that the chemical composition and the crystallographic structure of the surface layer differ from the bulk. Particularly in $KNbO_3$, an increased density of dislocations building up a network of dislocation was observed in the surface layer [SPH+96, SSC+96]. Upon heating the crystals, a solid reaction can be induced leading to a restructuring of the surface layer resulting in a layered structure of Ti-rich and Sr-rich phases [SSHF97], which is the first step before the formation of surface islands starts. Furthermore, it was reported that also in Nb-doped $SrTiO_3$ single crystals, a surface layer is present showing different properties and particularly a significantly higher resistance than the bulk [HIC+03].

Surface islands

As described above, the application of chemical gradients leads to the formation of secondary phases that can segregate as nanoscale surface islands. Upon prolonged heating of $SrTiO_3$ under reducing conditions, a formation of TiO [LPSR05, LSP05] and anatase TiO_2 [MC09] islands has been found. In $SrTiO_3$ donor-doped with La not only the formation of Ti_2O_3 islands under reducing conditions but also an segregation of the donor into these islands has been observed [GBF+03]. After donor-doped $SrTiO_3$ crystals were heated under oxidizing conditions, it was found that secondary SrO_x phases segregate as islands on the surface [GGB$^+$02, SSB$^+$00, MWHB02, Rah04, RFS$^+$05], which is related to the movement of SrO complexes along extended defects that serve as easy diffusion paths.

2.4. Electronic structure

The electronic structure of $SrTiO_3$ is of particular interest since it can change its resistance from insulator to metal and even to superconductor upon reduction or doping [SHC64]. In order to understand this insulator-to-metal transition and the related resistive switching effect, a detailed investigation of the electronic structure, which describes the energy states of the electrons, is of fundamental importance. Generally, the electronic structure of the crystal surface differs from that in the bulk since the break of the crystal symmetry by the surface leads to the evolution of special electronic surface states.

2.4.1. Electronic structure of the bulk

Undoped $SrTiO_3$

The energy levels of the electrons in a crystal differ from those in single atoms due to the overlap of the electron orbitals forming chemical bonds. Since the bond between Ti and O in the octahedron is of covalent character while the bond to Sr is mainly of ionic character as described in Chapter 2.2, a first insight into the electronic structure can be obtained by studying the electronic orbitals of a hypothetical TiO_6^{8-} molecule having an octahedral structure. In this symmetrical structure with the point group O_h, a Ti atom is surrounded by six O atoms distorting the Ti energy levels. The energy levels mainly involved into binding are the Ti$3d$, Ti$4s$, Ti$4d$ and O$2p$ levels. According to crystal-field-theory, a splitting of the Ti$3d$ orbitals into the triply generated t_{2g} and the doubly degenerated e_g orbital occurs [MJ04]. The O$2p$ levels are hybridized and can be distinguished by the type of binding in $2p_\sigma$ and $2p_\pi$ levels. As illustrated in Fig. 2.10, the further molecular orbitals can be obtained by combining the energy levels of the metal atom and the ligands [Nel63] resulting in the creation of bonding and anti-bonding molecular states. By filling the obtained orbitals with electrons, the ground state can be described revealing a HOMO-LUMO gap between the highest occupied molecular orbital and the lowest unoccupied molecular orbital corresponding to the band gap of the whole crystal. The highest occupied orbitals are mainly non-bonding t_{1g} and t_{2u} O$2p_\pi$ orbitals corresponding to the top of the valence band while the lowest occupied orbitals are mainly slightly anti-bonding t_{2g}^* Ti$3d$ states corresponding to the bottom of the conduction band.

In a real crystal, the energy levels will vary from those of the hypothetical TiO_6^{8-}

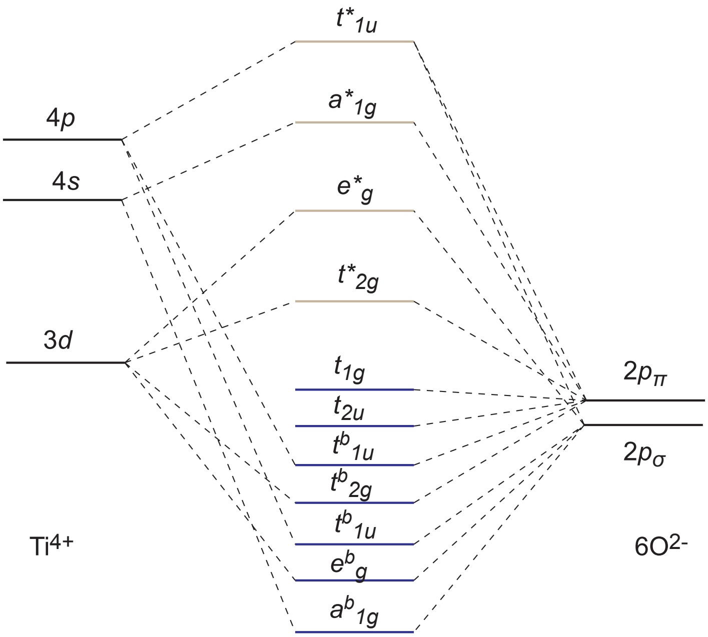

Figure 2.10.: Electronic structure related to the covalent bonding of the TiO_6^{8-} octahedron in O_h symmetry according to Radtke and Botton [RB11]

molecule due to the interaction with the other ions in the crystal leading to a change in the binding energy according to the Madelung constant. Hence, the binding and the electronic structure of a real crystals differs from the simple ionic model described in Sec. 2.2. In Table 2.2, a comparison between the nominal valency and the Born effective charge $Z^{*(T)}$ as calculated by Ghosez *et al.* [GMG98] using *ab initio* calculations is given. Specifically, the huge deviation of the Ti charge illustrates the strong covalent character of the binding.

In order to gain more insight into the complete band structure in dependence on the electron wave vector, a precise calculation using the method of linear combination of atomic orbitals (LCAO) were performed by Kahn and Leyendecker [KL64]. Since the symmetry group of the crystal structure determines the electron wave functions, the energy bands in the Brillouin zone are calculable [BSW36]. With regard to only Ti and O, the wave functions of the Ti3d electrons can be expressed by Bloch sums such as

$$(xy) \equiv \frac{1}{\sqrt{N}} \sum_i \mathrm{e}^{-i\vec{k}\cdot\vec{R}_i}\ \Phi_{xy}(\vec{r}-\vec{R}_i), \tag{2.26}$$

	$Z^{*(T)}_{\mathrm{Sr}}$	$Z^{*(T)}_{\mathrm{Ti}}$	$Z^{*(T)}_{\mathrm{O}_\parallel}$	$Z^{*(T)}_{\mathrm{O}_\perp}$
Nominal	2	4	-2	-2
Calculated	2.56	7.26	-5.73	-2.1

Table 2.2.: Comparison of nominal valences and Born effective charges as calculated by Ghosez *et al.* [GMG98].

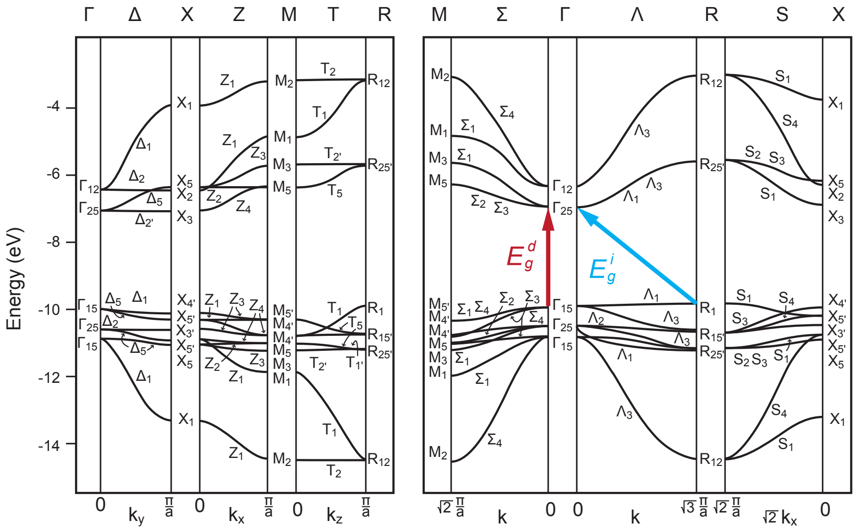

Figure 2.11.: Band structure of $SrTiO_3$ as calculated by Kahn and Leyendecker [KL64].

where $\vec{k}$ is the wave vector, Φ_{xy} is the wave function and the $\vec{R}_i$ over the primitive sides of the cubic lattice. For the O2p orbitals, the Bloch sums have the form

$$\frac{1}{\sqrt{2}}(y,-x,0) \equiv \frac{1}{\sqrt{2N}} \sum_{i,j} \mathrm{e}^{-i\vec{k}\cdot(\vec{R}_i+\vec{d}_1)}\, \Phi_y(\vec{r}-\vec{R}_i-\vec{d}_1) - \mathrm{e}^{-i\vec{k}\cdot(\vec{R}_i+\vec{d}_2)}\, \Phi_x(\vec{r}-\vec{R}_i-\vec{d}_2), \quad (2.27)$$

where x, y, z specifies the type of the orbital and the vectors $\vec{d}$ describe the relative position of the O atoms with respect to the Ti atoms. Following this approach, the energy values of the electronic states in the Brillouin zone can be calculated as shown in Fig. 2.11 revealing that $SrTiO_3$ is an insulator with a direct band gap of around 3 eV. In the simple cubic Brillouin zone, the Δ point lies in the [100] direction whereas the X point is the centre of the faces of the Brillouin zone. The M point is the midpoint of the edges and the R point lies at a corner of the Brillouin zone. In recent years, the simulation of the electronic structure and the density of states based on *ab initio* methods has been significantly improved due to the increasing computational power and optimization of the parameters used in the simulations [PHEB04].

A deeper insight in the electronic band structure of $SrTiO_3$ was also obtained from experiments addressing the optical transitions. By investigating reflectance spectra, various peaks were found that were related to transitions between the valence band and empty states in the conduction band in agreement to the calculated band structures [Car65, BBS+78].

A detailed study of the electronic structure by combining experimental methods such as electron energy loss spectroscopy, ultraviolet spectroscopy and spectroscopic ellipsometry with an *ab initio* calculation of the density of states was conducted by van Benthem *et al.* [vBEF01] revealing that the indirect band gap E_g^i between the Γ point and the R point [KP10] is 3.25 eV while the direct band gap E_g^d at the Γ point was found to be 3.75 eV. The conduction band was attributed to Ti3d and Sr4d states and free electron like states have been found above 15 eV. In agreement with the estimation described above it was found that the upper valence band filled with 18 electrons consists of O2p states being hybridized with Ti and Sr states whereas the lower valence band filled with 12 electrons consists of Sr4p and O2s states. Additionally, a further band with 8 electrons consisting of Sr4s and Ti3p states was found 233 eV below the top of the valence band.

Correlation effects

In the description of the electronic structure of the band insulator $SrTiO_3$ shown above, the electrons were treated as independent particles in an effective potential. This description works well if the screening of the mobile electrons is sufficient. However, in the case of very narrow bands and low electron concentration, correlation effects between the electrons become important and influence the electronic structure. In order to model such effects theoretically, the Mott-Hubbard model taking into account the Coulomb interaction U between the electrons was developed. It is modelled that the initially flat d-band of a band insulator splits off in two bands if the width W of the band is larger than the Coulomb interaction U resulting in a lower Hubbard band (LHB) and upper Hubbard band (UHB). As illustrated in Fig. 2.12, an overlap of the two energy bands occurs if $W > U$ takes place and the system is transformed into a metal.

In order classify transition metal oxides according to their electronic properties of oxides, a scheme regarding the energies of three electronic states close to the Fermi energy was developed by Zaanen, Sawatzky and Allan [ZSA86]. In Fig. 2.13a, a schematic illustration

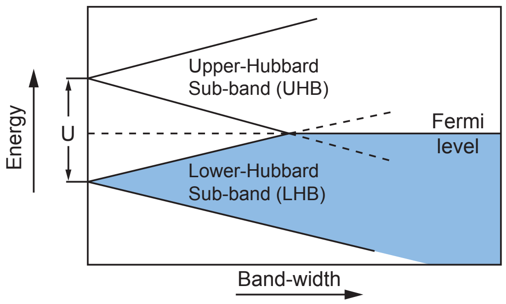

Figure 2.12.: Illustration of the band splitting of a *d*-band in two Hubbard bands due to correlation effects according to [Cox95].

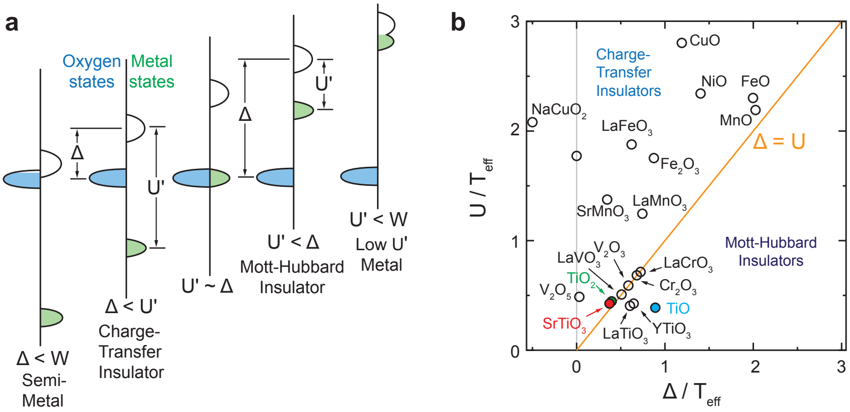

Figure 2.13.: The ZSA classification scheme. (a) Illustration of the overlap between the oxygen and metal bands for different situations. (b) ZSA-diagram for transition metal oxides according to [TLAM91] and [BMM^{+}96].

of the oxygen states on the left and for the metal states on the right is given for five examples. The difference of the energy of the highest occupied oxygen state and the lowest unoccupied metal state is labelled as Δ, while the difference between the lowest unoccupied metal state and the highest occupied metal state is labelled as U' [TLAM91]. If the bandwidth Δ is smaller than U' and Δ, the occupied orbitals do not overlap leading to insulating behaviour. In the framework of the ZSA-scheme, two different types of insulators can be distinguished, namely charge transfer insulators with $W < \Delta < U'$ and Mott-Hubbard insulators with $W < U' < \Delta$. In a charge transfer insulator, the band width is determined by Δ since the oxygen *p* band lies in between the two Hubbard bands of the metal while in a Mott-Hubbard insulator the bandwidth is determined by the Hubbard energy U'. The influence of the differences of the energies can be seen from a Zaanen-Sawatzky-Allan (ZSA) diagram, in which U is plotted versus Δ for different transition metal oxides as shown in Fig. 2.13b. In the ZSA diagram, the line $\Delta = U$ separates the class of charge transfer insulators from the class of Mott-Hubbard insulators. It can be observed from the graph that particularly if an insulator-to-metal transition taking place during electroforming or switching also complies a crystallographic phase change, correlation effects become important. As shown in this thesis, a transformation starting from the band insulator $SrTiO_3$ towards the Mott-Hubbard metal TiO can be induced by electrical gradients, which illustrates that the processes during resistive switching are very complex.

Nb doping

According to Chapter 2.3.1, Nb acts as a donor under reducing conditions, which strongly alters the electronic structure by a valence change of Ti from 4+ to 3+. Due to the high technological relevance of metallic oxides, the doping mechanism in $SrTiO_3$ has been subject of many experimental and theoretical studies. On lightly Nb-doped $SrTiO_3$, electronic donor states in the band gap depending on the Nb concentration have been found using X-ray absorption spectroscopy [HTK$^+$00]. The appearance of in-gap states also influences the optical properties by providing additional energy levels that can be addressed by optical transitions. Especially, it was found that blue luminescence related to a transition from an Nb-induced state 0.3 eV below the conduction band into the valence band can occur [YCHL11]. The same effect has not only been found for Nb-doped $SrTiO_3$ but also for $SrTiO_3$, which was donor-doped with oxygen vacancies by reduction. This indicates that the in-gap states are related to the valence change of Ti to 3+.

At higher Nb concentrations, the number of electrons due to the compensation mechanism increases accordingly leading to the presence of correlation effects inducing an insulator-to-metal transition as has been calculated using various methods. Using density functional theory (DFT) with a plane wave basis set it has been calculated that the substitution of Ti by Nb leads to a structural relaxation of the surrounding Ti atoms and the occupation of a conducting band state localized on the Ti ions [AB02]. Based on the calculations using full-potential linearized augmented plane waves (FLAPW), the similarities of the insulator-to-metal transition induced by donor doping with Nb or oxygen vacancies have been addressed [Ham09]. A detailed calculation of the density of states integrated over the whole Brillouin zone was performed by Guo *et al.* using a semi-relativistic linear muffin-tin orbital method with atomic sphere approximation (LMTO-ASA) [GCS$^+$03]. As

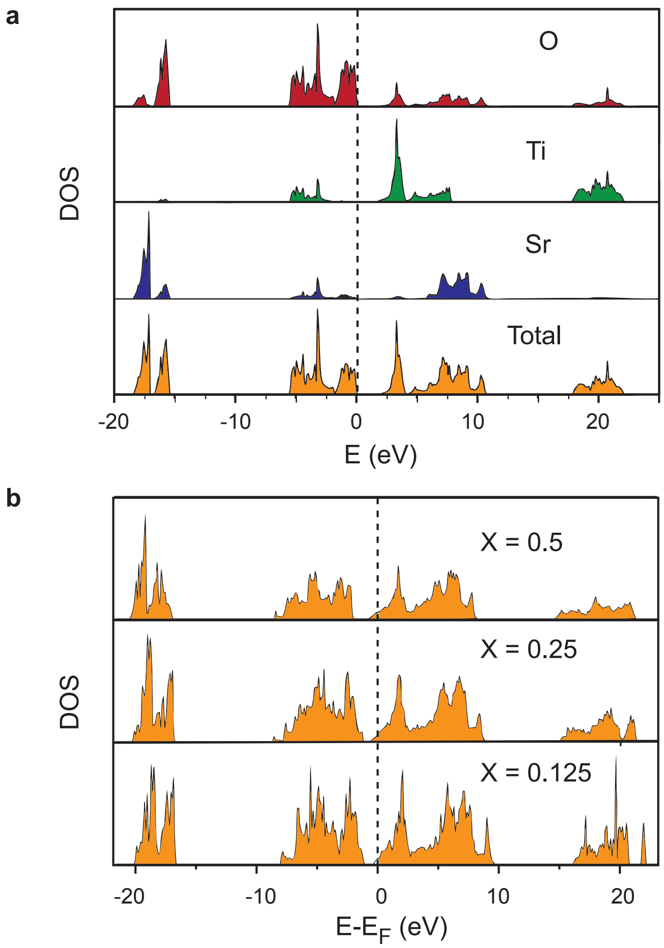

Figure 2.14.: Density of states of (a) undoped and (b) Nb-doped $SrTi_{1-x}Nb_xO_3$ with different donor concentration x as calculated by Guo [GCS$^+$03].

shown in Fig. 2.14, the total density of states of undoped $SrTiO_3$ composed of the density of states of O, Sr and Ti reveals an insulating behaviour whereas the Fermi energy moves into the bottom of the valence band if the crystal is doped with Nb expressed by the formula $SrTi_{1-x}Nb_xO_3$. Furthermore, Hartree-Fock (HF) calculations have been performed indicating that Nb is a shallow donor with a donor level 0.25 eV below the conduction band [EK10]. The consideration of different Nb concentration revealed that the Nb doping also induces a large distortion of the top of the valence band due to the charge impurity potential [ZWL+08].

2.4.2. Electronic structure of the surface

The electronic structure of crystal surfaces can differ from that in the bulk due to the existence of intrinsic or extrinsic surface states with energies in the bulk band gap. In ionic oxides, intrinsic surface states can evolve due to the lack of the crystal symmetry at the surface leading to a reduced local coordination of surface ions related to the reduction of the Madelung potential [AKWO98, LM66]. Furthermore, the surface is the place where external gradients influence the crystal, which can lead to surface defects or changes in the chemical composition according to Chapter 2.3.5 altering the electronic structure by extrinsic surface states.

Intrinsic surface states

In order to investigate intrinsic surface states, a clean and stoichiometric surface is needed, which can be obtained by *in situ* fracturing of single crystals under ultra high vacuum conditions. Based on theoretical calculations by Wolfram and Ellialtoğlu [WE77], the existence of empty surface states in the conduction band was predicted. However, some researchers claimed that no intrinsic surface states could be found experimentally in donor-doped and undoped $SrTiO_3$ using surface sensitive methods such as ultraviolet or X-ray photoemission spectroscopy (UPS/XPS) [AKWO98, RBM+84, KML+77]. Only after reduction or due to residual surface defects, a small amount of surface states in the band gap were detectable [HDZ78, PS76] and it has been calculated that those states are no intrinsic surface states [PV98]. On the other hand, Santander-Syro *et al.* reported on the observation of a two-dimensional electron gas on the surface of vacuum-cleaved $SrTiO_3$ [SSCK+11], illustrating the high sensibility of the surface layer on external influences. Calculations based on the Hartree-Fock method revealed that despite the absence of deep-gap surface states, a split-off of the surface states from the valence band or from the conduction band depending on the surface termination occurs leading to the presence of so-called Tamm states, which could stimulate the electron or hole migration [HEK+02]. Furthermore, it was calculated that the covalency of the Ti-O bond is increased at the surface influencing the electronic structure of surface defects and the adsorption and surface diffusion mechanisms [VZB10].

Extrinsic surface states

In contrast to intrinsic surface states, the existence of extrinsic surface states has been proven by various experiments. In order to induce these states, reduction, which leads to the loss of oxygen from the surface, or bombardment of the surface with Ar^+ ions was investigated. In agreement with calculations of the local density of states of an oxygen vacancy-rich surface [EWH78], and an additional band of the surface defect states was found in the bulk band gap by Henrich *et al.* that were assumed to be related to Ti^{3+}-$V_O^{\cdot\cdot}$ complexes [HDZ78]. The evolution of the in-gap states is related to a chemical instability of the $SrTiO_3$ surface as can not only be caused by Ar^+ bombardment but also by electron irradiation or metal deposition [PSPS09]. A detailed investigation of the in-gap states induced by Ar^+ bombardment revealed the existence of Ti^{3+} states around 11.6 eV and in Nb-doped $SrTiO_3$ an additional peak in the photoemission spectra was found around 1.4 eV related to Nb^{4+} states [AKWO98] affecting the electrical and optical properties [KTK⁺05]. This effect is also highly relevant for technological applications by offering the possibility of producing thin conducting surface layers as transparent metals having the properties of a two-dimensional electron gas [RB05, HCG+10, RKR+13].

Insulating surface layer of $SrTiO_3$:Nb

As described in Chapter 2.3.5, surface layers having different properties than the bulk are known to exists in oxides and particularly on Nb-doped $SrTiO_3$, the presence of a high resistive surface layer has been proven experimentally [HIC+03]. In order to clarify the origin of this surface layer, the electronic structure of the $SrTiO_3$ (100) surface obtained by cleaving in the vacuum at low temperatures and the influence of the exposure to oxygen was investigated by Haruyama *et al.* [HAB+97]. On the freshly cleaved surface it was found that the Nb doping leads to the appearance of a metallic peak at the Fermi energy as expected for a metallic material accompanied by a broad peak in the band gap at 1.3 eV. After exposing to oxygen gas, the metallic peak vanished already at very low oxygen doses below 1 L and a shift of the in-gap state closer to the Fermi energy was observed. Hence, the reduced metallicity was assumed to be related to the evolution of a depletion layer formed due to the electron transfer from the surface to the oxygen adsorbates.

The existence of an insulating surface layer on a nominally metallic material is of vital importance for technological applications such as the growth of oxide thin films with $SrTiO_3$:Nb crystals being used as a metallic substrate or the resistive switching phenomenon itself. Hence, a careful investigation of the properties of the $SrTiO_3$:Nb surface layer is needed, which will be investigated intensively in the present thesis.

2.5. Lattice dynamics

The investigation of the lattice dynamics is of high relevance for the understanding of the diffusion mechanisms, which are related to the lattice vibrations since statistic fluctuations in the oscillation frequency can occasionally lead to a displacement of the ions, which is large enough to activate the movement of the ions within the lattice. According to the Einstein equation, such a movement is directly related to the diffusion [Meh07].

$$D = \mu k_{\mathrm{B}} T \tag{2.28}$$

Here, D is the diffusion constant, μ is the mobility, k_{B} is the Boltzmann constant and T is the temperature. In the perovskite structure, displacements of the ions along different axes can occur leading to the appearance of different vibrational modes, which are determined by interatomic forces between nearest neighbours as well as by long-range electrostatic forces. For example, a movement of the TiO_6 octahedra against the Sr ions is described by the TO1 mode, while a movement of the O against the Ti ions is described by the TO2 mode. In Fig. 2.15a, the lowest transversal optical (TO) and the highest longitudinal optical (LO) modes are illustrated. Based on experiments using neutron spectroscopy, phonon dispersion curves were measured by Cowley, who presented the correlation between the lattice dynamics and ferroelectricity as well as phase transformations [Cow64]. Trautmann and Falter calculated the phonon dispersion based on an *ab initio* rigid ion model (RIM) shown in Fig. 2.15b revealing that not only stable but also unstable vibrational modes exist that are related to a rotation of the oxygen octahedra about one of the cubic axis leading to an antiferrodistortive (AFD) transition.

In order to investigate the behaviour of the different vibrational modes experimentally, intensive investigations using Raman-spectroscopy were performed making use of the inelastic interaction between light and lattice vibrations. The complete Raman spectrum of $SrTiO_3$ was measured by Nilsen and Skinner and the characteristic peaks could be attributed to optical transitions between the vibrational modes [NS68]. At room temperature, the Raman spectrum was found to be second order in agreement with the selection rules of the perovskite structure and it was found that the polarizability of oxygen, especially its intra-ionic anisotropy, strongly influences the vibrational properties [MRFB76]. In the low-temperature tetragonal phase, first-order peaks as well as additional peaks attributed to impurities were recorded illustrating the sensitivity of the physical properties on distortions of the chemical composition [BE82]. At higher temperatures, it was reported by Barbosa and Dos Santos that in the background of the one-phonon processes an additional relaxation mode is present [BS81]. Since the relaxation time of this mode decreases linearly with temperature, it was concluded that this mode is associated with

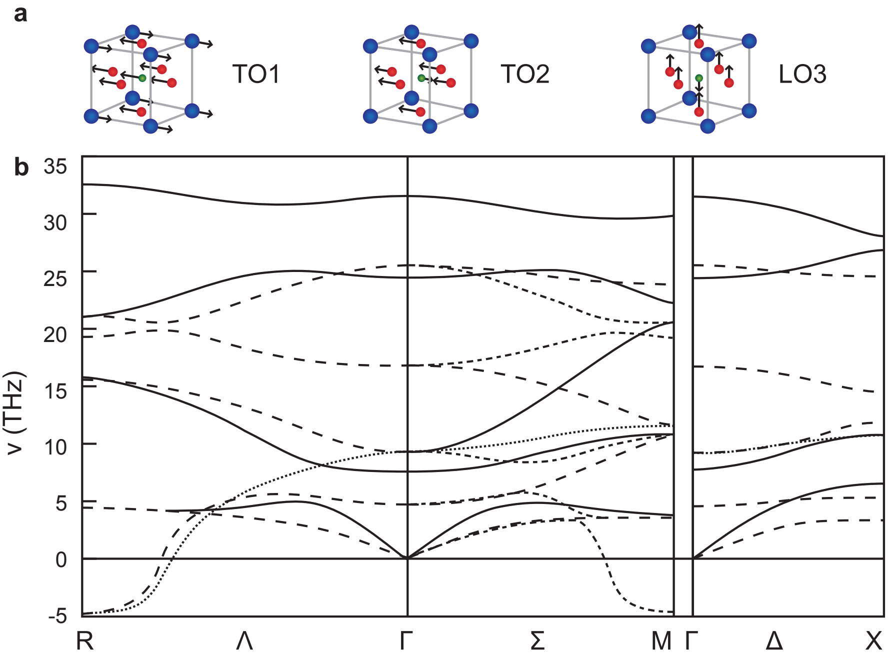

Figure 2.15.: (a) Illustration of the lowest TO and highest LO mode. (b) Phonon dispersion in $SrTiO_3$ as calculated by Trautmann and Falter [TF04].

melting mechanisms, indicating that even at relatively moderate temperatures, lattice movements are present that can lead to a transformation of the crystal.

2.6. Transport properties and resistive switching

2.6.1. Electronic transport

$SrTiO_3$ has become a model material for the investigation of the resistive switching effect due to its unusual electronic transport properties. Starting from undoped $SrTiO_3$ with semiconducting properties, metallic transport can be introduced by doping with donors or oxygen vacancies as described in Chapter 2.4.

Boltzmann equation

In general, the description of the electronic transport is related to the description of the statistical distribution of charge carriers. While the carriers are in a thermodynamical equilibrium without the presence of external gradients, the application of such gradients will lead to a non-equilibrium distribution of the carriers. Mathematically, the distribution of the charge carries such as electrons is expressed by the non-equilibrium distribution function $f(\vec{k}, \vec{r}, t)$ describing the electrons having the wave vector $\vec{k}$ in a unit volume near the point $\vec{r}$ at time t [Ask94]. The temporal change of this function, which is influenced by diffusion due to chemical gradients, by drift in an electric field and by collisions with phonons or other lattice defects, is described by the Boltzmann equation.

$$\frac{\partial f}{\partial t} = \left(\frac{\partial f}{\partial t}\right)_{\text{diff}} + \left(\frac{\partial f}{\partial t}\right)_{\text{field}} + \left(\frac{\partial f}{\partial t}\right)_{\text{coll}}. \tag{2.29}$$

By considering the influences of diffusion and of an electromagnetic field separately, the Boltzmann equation can be transformed into its explicit form.

$$\frac{\partial f}{\partial t} + \vec{v}(\vec{k})\vec{\nabla}_{\vec{r}} f - \frac{e}{\hbar}\left(\vec{E}_0 + \frac{1}{c}\left[\vec{v}(\vec{k})\vec{H}\right]\right)\vec{\nabla}_{\vec{k}} f = \left(\frac{\partial f}{\partial t}\right)_{\text{coll}} \tag{2.30}$$

In this equation, $\vec{E}_0$ is the electric field, $\vec{H}$ is the magnetic field, $\vec{v}(\vec{k})$ is the velocity of the electrons, e is the electron charge, $\hbar$ is the reduced Planck constant and c is the speed of light.

The Boltzmann equation illustrates that the electronic transport phenomena are very complex and a detailed knowledge about the material system is needed in order to gain an insight into these phenomena. Moreover, the appearance of effects such as resistive switching and related insulator-to-metal transitions, which strongly influence the transport properties, introduces additional complexity into the problem thus making the proper understanding of the resistive switching effect a very challenging task.

2.6.2. Electroformation

The application of electrical gradients to a switching material can introduce ionic movements and related redox reactions leading to a local transformation of the material. This process, which is called electroforming, electroreduction or electrodegradation is a necessary pretreatment step in order to activate filamentary resistive switching in a switching material [JTK$^+$12]. During this step, a conducting filament is assumed to be created or modified in an otherwise insulating matrix due to the application of electrical gradients related to ionic movements and local solid state reactions. The formation of the filament decreases the local resistance of the material and thus defines the place where the subsequent resistive switching takes place. During the electroforming step, usually a current compliance has to be activated in order to avoid a breakdown, which would irreversibly turn the filament to the ON state. Instead, during a controlled soft breakdown, a filament is formed, which can be ruptured and re-formed depending on the electrical gradients.

2.6.3. Resistive switching

The possibility to influence the electric resistance by the application of a voltage or by current flow has been discovered in a lot of materials based on various physical effects such as phase change mechanisms between amorphous and crystalline states, electrostatic and ferroelectric effects or redox-related processes. The redox-related processes can be distinguished in three different mechanisms, namely the electrochemical metallization mechanism (ECM), the thermochemical mechanism (TCM) and the valence change mechanism (VCM) [WDSS09].

Resistive switching in oxides

Starting from the 1960's, the increasing interest in oxides as material for electronic devices gave rise to the discovery of the resistive switching effect in various binary oxides such as TiO_2, Nb_2O_5, VO_2, or FeO [Cho65, HH65, Arg68, Hic69, COPS96, SRS$^+$11]. But even in ternary oxides, such as $SrTiO_3$, $SrZrO_3$, $BaTiO_3$ or $LaMnO_3$, the resistive switching effect was found and investigated intensively [BBG$^+$00, LWW$^+$05, WK08, XJG$^+$12].

Oxides, which are categorized in the class of valence change mechanism, generally exhibit bipolar resistive switching with at least two different resistance states [WDSS09]. In order to fabricate a resistive switching device, a layer consisting of one or several oxide materials is sandwiched between two metal electrodes serving as anode and cathode. When applying a voltage sweep to the device, the resistive switching effect becomes manifest in the IV-curve as illustrated in Fig. 2.16. Assuming that the device is in the high-resistive OFF state at the beginning of the sweep, the application of a positive voltage leads to the change into the low-resistive ON state via a SET process. Once the system has switched into the ON state, it remains in this state even when the voltage is turned off. Only upon application of a voltage with opposite polarity, a RESET process takes place and the device switches back to the high-resistive OFF state. Depending on the sense of the rotation, in which the switching loop is run through, two types of switching behaviour can be distinguished, namely “eightwise” and “counter-eightwise”, based on the number “8” [MMDW10]. In the “eightwise” case, which is illustrated in Fig. 2.16, the SET voltage is positive and the RESET voltage is negative, where as in the “counter-eightwise” case, the SET voltage is negative and the RESET voltage is positive.

The possibility of switching between two clearly distinguishable resistive state in a reproducible manner has great potential to serve as mechanism for the storage of information. Since no permanent application of the voltage is needed to conserve the specific resistance state, a memory device consisting of oxide materials would have less power consumption

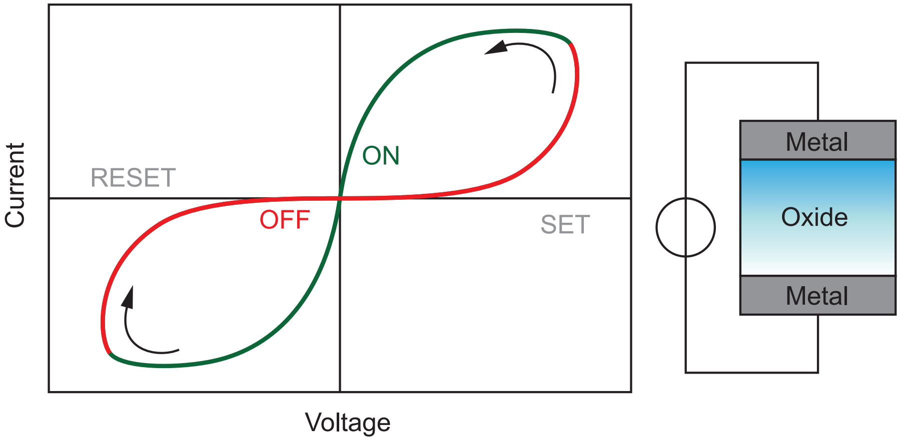

Figure 2.16.: Illustration of an IV-curve showing bipolar resistive switching with two resistance states and illustration of a resistive switching device.

but at high storage density than the memory devices used nowadays. Hence, intensive research activities were performed in order to develop a redox based random access memory (ReRAM) as a storage device that can be implemented in existing computer architectures.

Nanoscale models of resistive switching

The understanding of the origin of the resistive switching effect is the decisive step in order to design memory devices with bespoke characteristic. However, the actual switching mechanism is still under debate and various models based on experimental observation of the switching characteristics have presented that still need to be proven. In general, the developed models of the switching mechanism on the nanoscale distinguish between two types – namely the filamentary and the interfacial type as illustrated in Fig. 2.17 [Saw08].

In the oxides belonging to the class of filamentary type, resistive switching is related to the formation of a conducting filament or a modification of an intrinsic filament such as an extended defect in an otherwise insulating matrix. Therefore, generally an electroforming step is needed as first step of resistive switching, which forms a conducting filament by a soft local breakdown as described above. The switching itself then occurs by a rupture and re-formation of the filaments. In oxides showing bipolar switching as described above, the driving force of the evolution of the filament is assumed to be the electrochemical migration of oxygen ions or vacancies leading to a local valence change of the transition metal oxide [SSBW06, WDSS09]. The switching process can also be related to a distinct modification

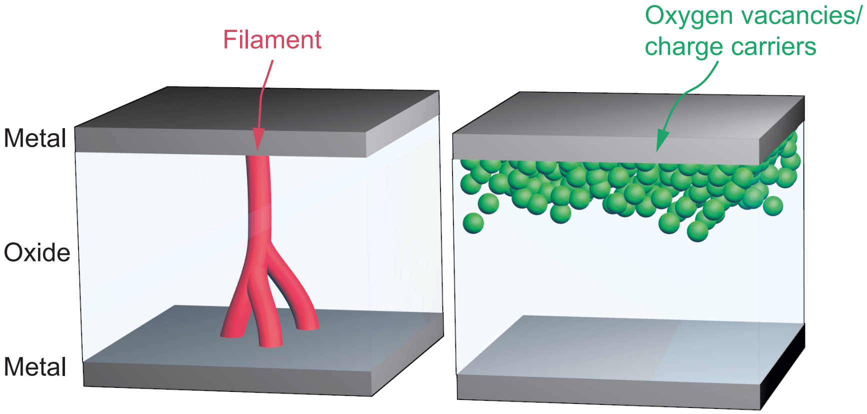

Figure 2.17.: Two types of conducting paths responsible for resistive switching according to Sawa [Saw08]. Left: Filamentary type. Right: Interfacial type.

of the chemical composition inside the filament if the change of the oxygen content exceeds the stoichiometric limit of the oxide. In addition, the filamentary switching type was found to be responsible for resistive switching in electrochemical and thermochemical memory materials, in which a thermal redox process or a so-called anodization in the region between the electrode and the oxide causes the rupture and formation of the filament [KTA+06, WA07]. In this context, the filamentary switching does not have to be related to bipolar switching but can also be present in cells showing unipolar switching, in which the polarity of the SET and RESET process is identical.

The second type of resistive switching is the interfacial type, in which resistive switching takes place in an spatially extended area at the interface between electrode and oxide. This mechanism has been related to the bipolar switching, which is present in perovskite oxides as shown above. Although the physical processes that could be responsible for the observation of switching phenomena that indicate the presence of interface-type switching are rather unidentified, it is generally assumed that the electrochemical migration of oxygen vacancies or the trapping of electrons and holes or charge-induced Mott-transition at the active interface enables the switching of the resistance [TBC+04, SJLH07, SFKT05, RIS04].

$SrTiO_3$ as model material for resistive switching

$SrTiO_3$ has become a prototypical oxide material for the investigation of resistive switching related to the valence change mechanism since numerous studies were conducted providing information not only about the fundamental physical properties but also about point defects and extended defects that have been found to play a decisive role in resistive switching [WDSS09]. Since the first report of resistive switching in Cr-doped $SrTiO_3$ by Watanabe *et al.* in 2001 [WBB$^+$01], the switching characteristics of $SrTiO_3$ doped with further dopants such as Nb, Fe, La [SCL$^+$05, MMD$^+$09, PS12] as well as of oxygen vacancy doped $SrTiO_3$ [CLS$^+$06, SZS$^+$10] have been investigated.

Also in undoped $SrTiO_3$ single crystals and thin films the resistive switching effect on the nanoscale has been found by Szot *et al.* [SSBW06, SDSW07]. Using local conductivity atomic force microscopy (LC-AFM) it was shown that the switching is locally extremely confined to areas on the surface with a diameter of only a few nanometres that could be switched between ON and OFF state by applying an appropriate switching voltage to these areas via the AFM tip. It was concluded that the switchable areas correspond to the exits of dislocation and a model was presented considering the movement of oxygen along the dislocations, which were supposed to serve as easy diffusion path, as the driving force for resistive switching. Hence, the resistive switching mechanism in undoped $SrTiO_3$ can be regarded to be of filamentary type.

In general, the resistive switching effect in $SrTiO_3$ can be regarded as an insulator-to-metal transition induced by external gradients leading to a valence change of the Ti "*d*"-electron from d^0 to d^2 and d^3 [RSB$^+$13]. This "*d*"-electron can be generated by various external gradients such as

- by a chemical gradient (reduction in low p_{O_2})
- by an electrical gradient (electroreduction)
- by a convolution of these gradients
- by donor doping.

2.6.4. Resistive switching in $SrTiO_3$:Nb

The resistive switching phenomena of $SrTiO_3$:Nb single crystals and thin films were investigated in numerous studies and various models for the explanation of the switching effect were presented. Some attribute resistive switching to the interfacial type, but for others local models prove the existence of filamentary-type switching. This illustrates that the resistive switching mechanism is very complex and not completely understood. In general, the observation of resistive switching in donor-doped $SrTiO_3$, which is supposed to exhibit metallic properties[TC67], raises the question how it is possible to switch a metallic material. However, this problem has not been addressed so far in literature. Furthermore, most of the models presented in literature are based on electrical measurements only and a potential change of the crystallographic structure and chemical composition during switching is often not taken into account.

Schottky models

Since a resistive switching device consist of an semiconducting or insulating oxide and a metal electrode, various models were presented taking into account the potential barrier formed between the different materials. According to the Schottky model, a bending of the energy bands at the interface occurs in order to level the Fermi energy, if a n-doped semiconductor is brought in contact with a metal leading to the formation of a space charge layer at the interface [Böe92]. This model however describes an idealized situation with the two contacting materials having homogeneous bulk properties. In case of the presence of surface defects, the Fermi level is pinned at the interface forming a so-called Bardeen barrier and cannot be adjusted by band bending [Bar47]. This illustrates that the electronic structure of a metal-semiconductor interface is very complex and many parameters should be taken into account to model it correctly.

One of the first reports of resistive switching in $SrTiO_3$:Nb was given by Sim *et al.*, who investigated the IV-characteristics of an $SrTiO_3$:Nb single crystal contacted with Pt electrodes [SCL$^+$05]. A distinct correlation between the resistances in ON and OFF state with the area of the electrode was observed, indicating the presence of an interface-type mechanism. Hence, the resistive switching effect was attributed to a modulation of the

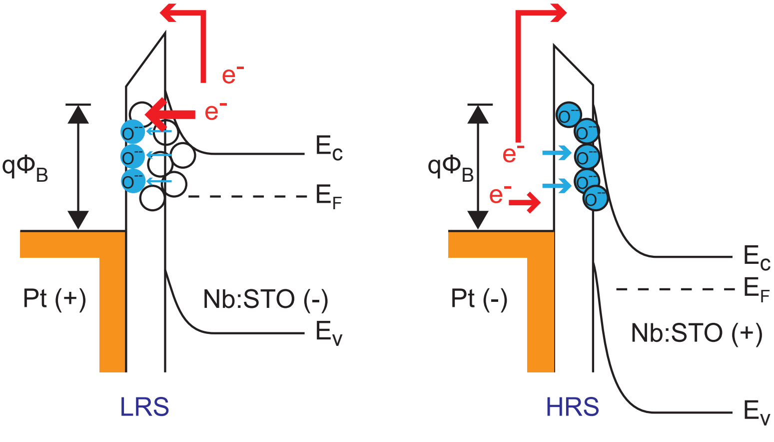

Figure 2.18.: Illustration of the energy diagram in the high resistance and low resistance state according to the Schottky model as presented by Seong *et al.* [SLP$^+$08].

Schottky barrier by the applied voltage. It was found that annealing of the samples in hydrogen atmosphere improved the switching characteristics, leading to a model considering the relevance of oxygen vacancies that could form tunnelling paths at the interface between electrode and oxide [SJLH07, SLP$^+$08]. Lee *et al.* excluded a filamentary model and regarded the migration and ionization of oxygen vacancies as the origin of resistive switching [LBS$^+$10].

Comparing the IV-characteristics of $SrTiO_3$:Nb contacted with Ag and Au, Chen *et al.* found that only the Au-contacted devices exhibit resistive switching [CMY$^+$11]. Similarly, Shen *et al.* demonstrated the suitability of Au electrodes in contrast to Ti electrodes [SQW$^+$13]. Since it was assumed that Ag forms an ohmic contact while Au forms a Schottky contact, it was concluded that the modulation of the Schottky barrier is the dominant effect when switching the resistance [CMY$^+$11]. However, this conclusion has to be viewed critically since other researchers also found resistive switching in $SrTiO_3$:Nb contacted with Ag [ZYYL10, DFC$^+$13]. In this context, Sun *et al.* showed that the characteristic of the contact does not necessarily depend on the material but on the electrode preparation. Using In, they found that a Schottky contact was formed when sputtering the electrode while an ohmic contact evolved when building the In electrode by pressing [SJLZ12].

A detailed investigation of the performance of devices contacted with different electrode materials revealed that also electronic interface states have to be taken into account when modelling resistive switching since they could induce charge trapping at the interface [PSJK08, LPK10]. This was supported by a study of the annealing atmosphere dependence, indicating that an insulating layer building up at the interface may also influence the switching behaviour [ZC13]. It was found that resistive switching characteristics were significantly enhanced in vacuum compared to air. Hence, it was concluded that the influence of oxygen on the interface modulates the resistance state [BGG$^+$12, BK13]. The importance of the interface for resistive switching was also illustrated by analysis of the thermoelectric properties of $SrTiO_3$:Nb. It was found that the largest fraction of an applied electric potential drops at the interface while the bulk is not affected by resistive switching [ZML$^+$12].

The influence of the Nb doping on resistive switching was addressed by the investigations of crystals having different doping concentrations. Gwon *et al.* observed on Pt/$SrTiO_3$ structures an improvement of the switching characteristics with increasing dopant and they suggested a relation to ionic movements or charge trapping [GLS$^+$10]. In agreement to this observation, Rana *et al.* reported that resistive switching can only be observed above a certain dopant concentration by investigation Au-contacted crystals [RKB12].

Although the conclusions about the origin of resistive switching described above were to some extent successful to model the specific measured data, their big drawback is that they are mainly based only on investigations of the macroscopical electrical characteristics. Hence, these models did not succeed in identifying a general mechanism of resistive switching. The consideration of the changes of other physical parameters especially on the nanoscale indicated that the resistive switching effect has a more local nature as will be described in the following.

Local models

In order to determine if the modulation of the Schottky barrier between electrode and oxide plays an important role, Shang *et al.* investigated the photoresponse of a Au/$SrTiO_3$:Nb junction during resistive switching [SSSS08]. Since the photocurrent in different resistive states was found to be the same, they concluded that the Schottky barrier is not affected by resistive switching, indicating the existence of filamentary conduction channels. This conclusion was supported by measurements of area dependence of current and capacitance of Pt/$SrTiO_3$:Nb contacts [KIS10]. Since only a dependence of the capacitance and not of the current on the electrode area could be observed, Kan *et al.* concluded that local conducting channels exist intrinsically in the crystal due to inhomogeneities leading to an only local modification of the Schottky barrier. In a similar way, Wang *et al.* deduced from investigations of Au/$SrTiO_3$:Nb heterostructures that conducting filaments are present since the Schottky barrier profile was found to be kept unchanged during the resistance switching [WZS$^+$13].

In order to gain an insight in the actual nanoscale conduction mechanisms, local conductivity atomic force microscopy (LC-AFM) investigations on $SrTiO_3$:Nb thin films were performed by Münstermann *et al.* revealing that resistive switching is related to clusters with a diameter of 30 nm that can be switched independently [MDS$^+$08]. Also in single crystals, similar conducting and switchable clusters were found using scanning tunnelling microscopy (STM) [CWX$^+$12] as well as by LC-AFM [RSB$^+$13]

These findings indicate that the switching mechanism is neither purely filamentary as in undoped $SrTiO_3$ nor purely interfacial but has to be categorized as a further type of resistive switching. Therefore, in this work, detailed nanoscale investigations of the resistive switching effect combined with measurements of the reaction of the material on the exposure to external gradients will be presented in Chapter 4.

3. Experimental methods

3.1. Preparation

Since in this thesis the fundamental properties of $SrTiO_3$:Nb were focused, single crystals were characterized. The majority of measurements were conducted without further preparation on as-received single crystals that were grown, cut and epi-polished by the manufacturers Mateck, Crystec and Surfacenet. In order to investigate the behaviour of the crystals under external gradients, additional preparation steps were performed as listed in the following.

3.1.1. Cleaving

As dedicated method in order to gain an insight in the structural properties of the crystal, cleaving planes were analysed [SJB94]. Therefore, the classical mechanical cleaving method was applied. An epi-polished single crystal was positioned in a brazen holder and then a sharp blade was aligned along the crystal axis. With a well-directed blow with a hammer on top of the blade the crystal was divided in different pieces. Due to the strong chemical bonds in the perovskite structure, such a cleaving experiment usually does not result in a cleavage along a defined plane but rather in a fracturing determined by extended defects being the weak points of the crystal.

3.1.2. Etching

In order to measure the density of dislocations in the surface layer of the crystals, etching was performed. The crystals were heated in a buffered hydrofluoric acid (12.5 %) at a temperature of 90 °C. During this treatment, etch pits evolve preferentially at the exits of dislocations due to the distortion of the lattice close to the dislocation. By monitoring the etch-pits by optical microscopy or atomic force microscopy, the density of dislocations can be estimated by counting the etch-pits in a defined area.

3.1.3. Ar^+ bombardment

The influence of ion bombardment on the surface layer was investigated by analysing the change of the chemical composition and electronic structure by X-ray photoelectron spectroscopy during sputtering with Ar^+ ions *in situ*. In order to correlate these changes with the electronic properties a dedicated set-up being capable to perform four-point-measurements using retractable probes was developed as illustrated in detail in Appendix A. The bombardment itself was performed by a Physical Electronics ion gun with an energy of 2 keV and an emission current of 15 mA in a scanning-beam modus.

3.1.4. Electrodegradation

In order to understand the processes during electroforming and resistive switching on the nanoscale, an emulation of switching was performed by electrodegradation due to DC self heating on the macroscale. A piece of an as-received crystal was contacted with Pt paste that was hardened by heating to 100 °C for 10 minutes. Then the sample was attached to a sample holder with two clamps serving as electric contacts. Under vacuum conditions ($p < 10^{-6}$ mbar), a voltage was applied to the sample leading to a direct heating and electrodegradation. By measuring the molecules inside the chamber by a mass spectrometer during the treatment, a correlation between electrodegradation and effusion was obtained. The changes of the surface layer that occurred during the electrodegradation were analysed ex situ by various methods such as scanning electron microscopy, X-ray photoelectron microscopy, electron back scattering diffractometry and transmission electron microscopy.

3.2. Characterization

In order to understand the origin of the resistive switching phenomena of $SrTiO_3$:Nb, a careful analysis of the behaviour of the physical properties under external gradients is inevitable. Therefore, a variety of methods was applied as illustrated in Fig. 3.1 to investigate the morphology, the crystallographic properties, the chemical composition, the electronic properties, the electronic transport phenomena and the lattice dynamics. In particular, surface-sensitive methods were applied since the surface is the place where external gradients act on the sample and where resistive switching is supposed to take place. In the following, an overview about the working principles of the used methods is given.

3.2.1. Hardness measurement

In order to determine the hardness of solids, an indentation measurement is performed. A diamond indenter with pyramidal shape in the so-called Vickers geometry is pressed onto the surface. The force is increased up to a maximum value, which is hold for a defined

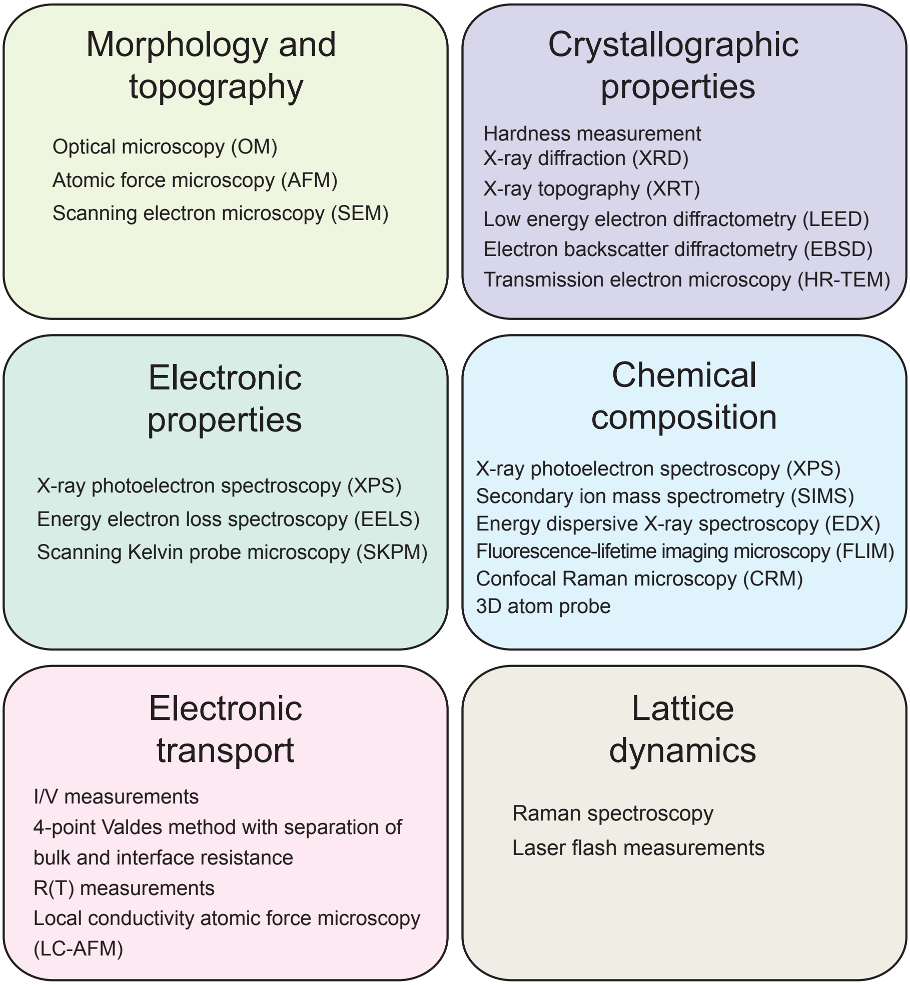

Figure 3.1.: Overview of method used for the investigation of the properties of $SrTiO_3$:Nb.

time period. By determine the indentation depth, the hardness value is calculated and converted into the Vickers hardness value (HV) [CSS06, Mal03].

3.2.2. X-ray diffraction (XRD)

The X-ray diffraction method is used in order to investigate the crystallographic structure of solids. This technique is based on the elastic scattering of X-rays on atoms which are aligned regularly in a crystal. Electromagnetic waves which are scattered at different planes of atoms interfere constructively if their respective phase shift is a multiple of 2 π which is described by Bragg's law

$$n\lambda = 2d_{hkl}\sin\theta \tag{3.1}$$

Here n is the order of diffraction, λ is the wavelength of the X-rays, d is the distance of lattice planes labelled by the Miller indices hkl in the crystal and θ is the angle of incidence related to the scattering planes [SN98]. Depending on the symmetry of a crystal, parallel planes exist in different directions of the crystal resulting in the evolution of a complex spatial diffraction pattern. By a careful refinement analysis of this pattern measured by a scanning detector in the plane of incidence and a comparison with pattern collected in databases it is possible to determine the lattice constant and the space group of the crystal. The XRD measurements in this thesis were obtained in cooperation with the Central Institute for Engineering, Electronics and Analytics (FZJ-ZEA-3) using a monochromatized X-ray source and a detector with high angular resolution.

3.2.3. X-ray topography (XRT)

In order to estimate the quality of single crystals with respect to structural defects, X-ray topography is applied [Bal74]. The entire crystal is irradiated with X-rays leading to the evolution of a topographic diffraction pattern containing information about the crystallographic orientation within the crystals. The XRT measurements presented in this thesis were obtained in reflection mode using a photographic plate to record the diffracted images of the crystals. The topograms showing the highest contrast and resolution were selected in order to analyse the quality with respect to mosaicity of the crystals. In a perfect crystal, a constructive interference between the lattice planes will occur resulting in a topogram imaging the sample geometry. In the case of a defective crystal structure, the presence of dislocations or other structural defects will locally change the Bragg condition (Eq. 3.1) due to strain fields resulting in a distorted topogram making the XRT technique a useful tool in order to monitor defects in a crystal. The XRT measurements presented in this thesis were obtained in cooperation with the Institut für Kristallographie der RWTH-Aachen (XTAL).

3.2.4. Low energy electron diffraction (LEED)

The low energy electron diffraction technique is based on the same principle as XRD respectively Laue diffraction, namely the elastic scattering of waves on crystal planes. In order to determine the crystallographic structure at the surface of a crystal, monochromatized electron waves induced by an electron gun are used since the penetration depth of electrons with low energy is much lower than that of X-rays. This implies that only the backscattered electrons interfere with each other resulting in a symmetrical diffraction pattern. By means of a fluorescent screen [Lüt10] the electron diffraction pattern is made visible and recorded by a camera as illustrated in Fig. 3.2 showing a schematic diagram of the LEED experiment. Additionally, an infrared filter is installed to avoid a perturbation of the recorded image by thermal radiation from the sample heater.

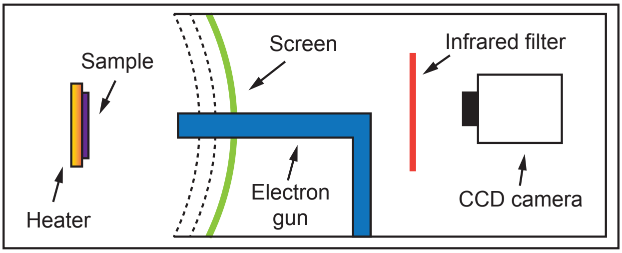

Figure 3.2.: Schematic of the LEED set-up

The symmetry of the points of highest intensity indicating the interference of the electrons represent the crystallographic symmetry of the surface of the crystal corresponding to diffraction pattern obtained by the Laue method for the entire crystal. Hence, the space group and lattice constant of the surface can be determined by an analysis of the LEED pattern. Due to the limited penetration depth of the electrons, LEED is an advantageous tool for the analyse of the crystallographic structure of surface layers but it is also very sensitive for surface contaminations implying that great care has to be taken in order to obtain a clean surface. Therefore, the LEED measurements presented in this thesis were conducted in UHV conditions ($p < 2 \cdot 10^{-8}$ mbar) using a Omicron Spectaleed instrument and the sample was mounted on a heatable sample holder to remove adsorbates from the surface by thermal desorption.

3.2.5. Archimedes method

The Archimedes method is a technique used for the determination of the density of solids. It is based on the fact that a solid, which is immersed into a solid, has a lower apparent mass than in are due to the buoyant force. This allows the density of a solid to be determined by weighing its apparent mass in air m'_a and in the liquid m'_l, if the density of the liquid ρ_l is known [Sar99].

$$\rho \;=\; \frac{m'_a \cdot \rho_l}{m'_a - m'_l} \tag{3.2}$$

3.2.6. Laser flash analysis

In order to measure the thermal conductivity of a solid, the laser flash method is applied. One side of a symmetric sample is irradiated by a short laser pulse leading to a local increase in the temperature. Using a sensitive temperature detector, the evolution of the temperature at the backside of the sample is measured as function of time allowing for the estimation of the thermal diffusivity α if the thickness of the sample is known. The thermal conductivity λ can then be calculated from the thermal diffusivity α by using literature values for the density ϱ and the temperature dependent specific heat c_p [dR96].

$$\lambda \;=\; \alpha \cdot \varrho \cdot c_p \tag{3.3}$$

The laser flash measurements presented in this thesis were obtained in cooperation with the hot materials lab (FZJ-HML).

3.2.7. Atomic force microscopy (AFM)

The atomic force microscope is the most prominent tool to investigate surfaces of solids with highest spatial resolution. It was invented in the year 1986 based on the development of the scanning tunnelling microscope [BQG86]. The fundamental concept of an AFM is to measure the force between a sharp needle and the surface of the sample in order to obtain information about the topography. The tip is attached on a cantilever, which reacts according to the topography when it is scanned over the sample.

When approaching the tip to the sample, different forces are present [TG11]. At first, the electrostatic force acts on the tip from a distance of 100 nm. Below 10 nm, the van-der-Waals interaction leads to an attractive force between tip and sample. Close to the surface, the Pauli repulsion related to the overlap of the electron wave functions of tip and sample instead results in a repulsive force. Theoretically, analysis of the Lennart-Jones potential between two molecules gives a first insight in the interaction between tip and sample

$$V = 4\varepsilon\left[\left(\frac{\sigma}{r}\right)^{12} - \left(\frac{\sigma}{r}\right)^{6}\right]. \tag{3.4}$$

ε is the depth of the potential well and σ is the distance where the potential is zero. The first term describes the attractive van-der-Waals potential and the second term describes the repulsive potential close to the surface. In order to analyse the forces between a real tip and a sample, it is necessary to calculate the van-der-Waals interaction between macroscopic bodies. This problem can be approximated by studying the interaction between a sphere representing the tip and a plane representing the sample. In this case the force between sphere with radius R at a distance D above a plane reads [BCK05]

$$F = -\frac{A_{\mathrm{H}}R}{6D^2}. \tag{3.5}$$

In this formula, all physico-chemical information is included in the Hamaker-constant A_{H}. Following an approach developed by Lifshitz, the Hamaker-constant can be estimated by assuming the macroscopic bodies as continuum with certain dielectric properties [Lif56, BCK05]. For the interaction between tip and sample through a third medium having different dielectric functions ϵ and refractive indices n, the Hamaker-constant yields

$$A_{\mathrm{H}} = \frac{3}{4}k_{\mathrm{B}}T\frac{\epsilon_1-\epsilon_3}{\epsilon_1+\epsilon_3}\frac{\epsilon_2-\epsilon_3}{\epsilon_2+\epsilon_3}\frac{\frac{3h\nu_e}{8\sqrt{2}}\cdot(n_1^2-n_3^2)(n_2^2-n_3^2)}{\sqrt{|n_1^2-n_3^2|}\sqrt{|n_2^2-n_3^2|}\left[\sqrt{|n_1^2-n_3^2|}+\sqrt{|n_2^2-n_3^2|}\right]} \tag{3.6}$$

Here, k_{B} is the Boltzmann-constant, T is the temperature, h is the Planck constant and ν_e is the Plasma frequency.

Taking into account the repulsive and attractive forces, a typical force-distance curve between tip and sample can be obtained as illustrated in Fig. 3.3. Depending on the

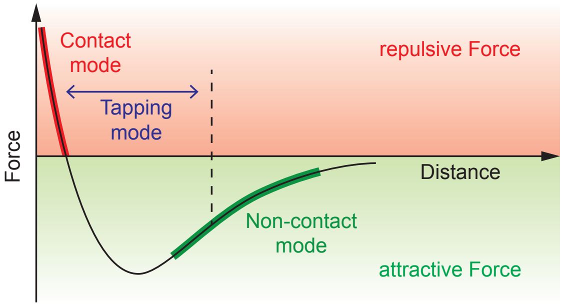

Figure 3.3.: Force-distance diagram between AFM-tip and surface

distance between tip and sample during measurements, different measurement modes can be realized, namely the contact mode, the non-contact mode and the intermediate tapping mode.

Contact mode

In the contact mode, the tip is approached to the surface until the repulsive force dominates. When scanning the tip across the surface, the cantilever bends following the topography. Since the differences in the topography are supposed to be measured with extremal high resolution, it is necessary to record very small movements of the cantilever which is realized by means of optical amplification. As illustrated in Fig. 3.4, a laser beam is directed on the backside of the cantilever, which reflects the beam towards a four segment photodiode. The signal, which is provided by the photodiode, depends on the position where the laser beam hits the diode and is therefore a measure of the deflection of the cantilever. Using a feedback loop, the deflection of the cantilever measured as difference in the photovoltage between the four segments can be hold on a fixed value by moving the sample in z-direction via a piezo element according to the signal of the photodiode and topographic images can be recorded. When using a conductive Pt/Ir coated cantilever, additionally information about the electrical conductivity can be obtained. This measurement technique called local-conductivity atomic force microscopy (LC-AFM) is based on the measurement of the current flowing between tip and sample when a voltage is applied to the tip as illustrated in Fig. 3.4. It is well suited for the investigation of resistive switching phenomena on the nanoscale since the resistance can be switched and read out

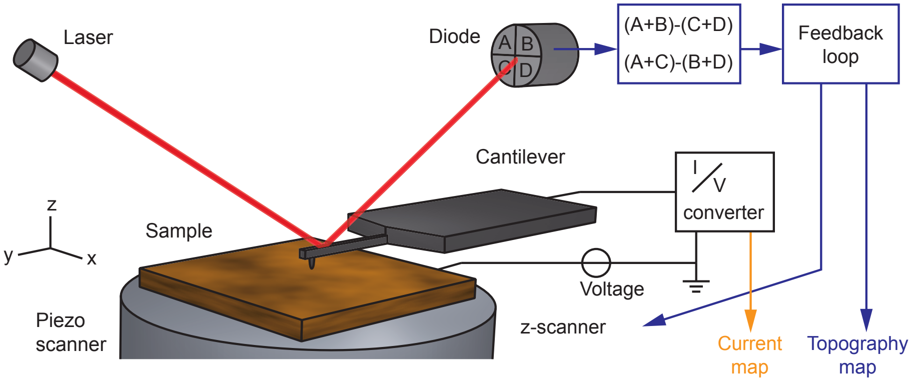

Figure 3.4.: Schematic of an LC-AFM measuring maps of topography and current simultaneously using the optical lever method .

by varying the voltage applied to the tip acting as mobile electrode. In comparison to the scanning tunnelling microscope (STM), which is also able to measure the conductivity spatially resolved, the advantage of the LC-AFM is that the current measurement is independent from the feedback loop, which allows the investigation of inhomogeneous and partially insulating samples. Although the diameter of the conducting tip is in the range of 20 nm [WSW11], the contact area where the current between tip and sample flows is much smaller [FBKS07] allowing the measurement of the local conductivity with atomic resolution. In Fig. 3.5, a finite element simulation of the distribution of the electric potential in the sample during an LC-AFM measurement by a conducting tip with a contact area of 2 nm is shown. It can be seen that the majority of the potential drops in the region close to the tip. Hence, a LC-AFM measurement allows the investigation of the local conductivity of very confined regions on the nanoscale. Furthermore, the simulation illustrates that a local resistive switching can be easily induced by the LC-AFM tip due to the high electric fields [LH11].

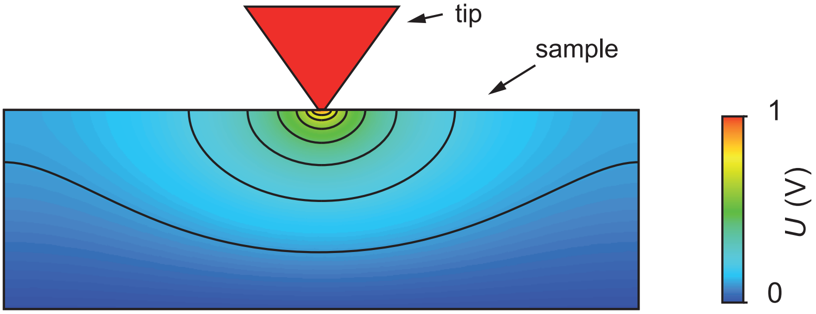

Figure 3.5.: Finite element simulation of the potential distribution during a LC-AFM measurement calculated by the ANSYS program.

Non-contact mode

In the non-contact mode, the distance between tip and sample is kept in a regime, in which the attractive van-der-Waals force plays the dominant role. In order to measure the force between tip and sample, the cantilever is oscillated at its resonance frequency by a piezoelectric drive. Upon approach to the surface, the force to the tip changes modifying the frequency of the vibration of the cantilever. This frequency shift is detected by analysing the signal measured by the photodiode and is then used to control the distance between tip and surface by the feedback loop.

In non-contact mode, the AFM can additionally be used as scanning Kelvin probe microscope (SKPM) providing information about the surface potential by measuring the local contact potential difference, which is caused by the different work functions of tip and sample.

$$V_{CPD} = \frac{\Phi_{sample}}{q} - \frac{\Phi_{tip}}{q} = \frac{\Delta\Phi}{q} \tag{3.7}$$

In order to measure the change in the contact potential difference in the non-contact mode, additionally an AC voltage is applied to the tip, which results in an electrostatic force[HHL$^+$96, GLSS$^+$07]. Using a feedback loop, this force is minimized by applying a voltage, which is proportional to the contact potential difference. The detailed operation of the SKPM method is described in Sec. 4.7.1.

Tapping mode

The tapping mode can be regarded as combination between contact and non-contact mode. Similar as in the non-contact mode, the cantilever is brought to oscillation with high amplitude. If the tip is approached to the surface, it hits the surface in the maxima of the oscillation, which changes the amplitude compared to the free oscillation. By using the modulation of the amplitude as feedback parameter, the distance between tip and sample can be controlled.

3.2.8. X-ray photoelectron spectroscopy (XPS)

In order to obtain information about the electronic structure and the stoichiometry, X-ray photoelectron spectroscopy is used. The XPS method is based on the photoelectric effect, which leads to the excitation and emission of electrons from a solid upon irradiation with photons [MSSB95] as shown exemplary in Fig 3.6a. The measured binding energy of the core electrons is characteristic for each element and hence allows the determination of the chemical composition with highest precision (< 0.1 at%). In order to calculate the stoichiometry from the measured count rate of the spectrum, the knowledge of the photoionization cross section, which describes the probability that an ion is ionized by a photon is highly important. This cross section depends on the energy of the incoming X-rays and the atomic number of the atoms [WD94]. By analysing the shapes of the peaks of the core line spectra, the electronic structure with respect to oxidation states and chemical bonds can be investigated providing a comprehensive insight in the properties of surface layers.

The schematic set-up is shown in Fig. 3.6b. A X-ray source using the monochromatized Al-K$_\alpha$ line generates photons with an energy of $E_\gamma = 1486.6$ eV, which irradiate the sample

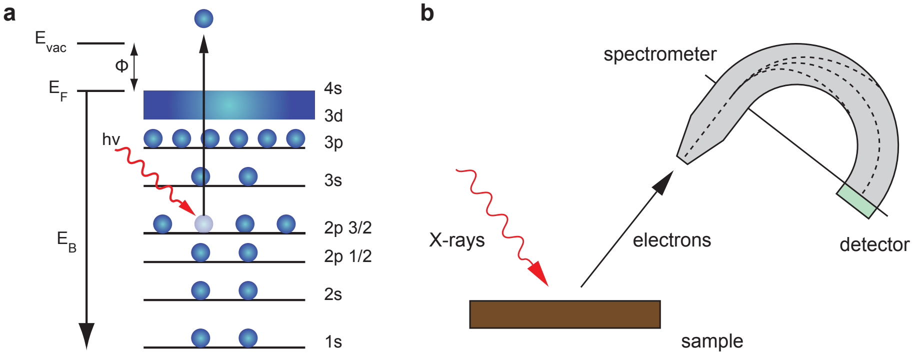

Figure 3.6.: a) Photoexcitation of an electron from the energy level $2p_{3/2}$ in copper upon X-ray irradiation. b) Schematic of the XPS spectrometer. Adapted from [BK99].

mounted on a heatable holder. Inside the sample, electrons are excited by the X-rays and can leave the sample if their kinetic energy is high enough. Due to scattering, most of the exited electrons lose their energy limiting the mean free path and only electrons close to the surface can reach the analyser. Hence, XPS is a very surface sensitive technique with an information depth up to several nanometres. Only electrons, which have not lost their kinetic energy, contribute to the characteristic photoelectron peaks while electrons, which lost a part of their energy contribute to the background signal. The kinetic energy E_{kin} of the emitted electrons is measured by a spectrometer and the binding energy E_B can be estimated taking into account the work function of the spectrometer Φ_s and the energy of the X-rays E_γ

$$E_B = E_\gamma - E_{kin} - \Phi_s - (R_{in} \cdot I_{ph})\, e. \tag{3.8}$$

Additionally, a shift of the measured binding energy can be generated due to the potential at the sample surface determined by the photocurrent I_{ph} and the resistance of the sample R_{in} [SPP$^+$09]. In order to avoid charging effects in insulating samples that would lead to a shift of the measured photoemission peaks on the energy scale, an additional float gun is used, which compensates the charge on the sample surface by electron irradiation. As presented in the cross section of Fig. 3.6b, the electrons entering the spectrometer are deflected by a voltage applied to two semicircular capacitor plates, which ensures that only electrons with particular energy can reach the detector. Hence, a whole spectrum can be measured by tuning the voltage between the plates. By varying the angle between sample and analyser, electrons from different depth of the surface layer can be analysed opening up the possibility of recording non-destructive depth-profiles up to a depth of 6 nm.

3.2.9. Mass spectrometry

Mass spectrometry is applied to investigate the chemical composition of a sample with respect to stoichiometry and contaminations by additional elements such as adsorbates or inclusions in voids. Therefore, the atoms are dissolved from the sample and ionized in order to accelerate them in an electric field allowing the determination of the ratio between mass and charge in a quadrupole mass spectrometer.

Effusion

In order to determine the contamination of single crystals by adsorbates or gases enclosed in voids, heating under vacuum conditions is performed while the atmosphere is monitored by a mass spectrometer. By correlating the detected ions to the heating temperature, it is possible to determine the evaporation temperature of the adsorbates. In the present theses, the effusion was not only monitored during external heating but also during direct heating and electroreduction by applying a AC or DC voltage to a crystal.

Secondary ion mass spectrometry (SIMS)

The secondary ion mass spectrometry is a characterization technique, which measures the chemical composition of the surfaces of solids with highest lateral and chemical resolution. The sample is bombarded with pulses of Bi ions, which dissolves particles from the sample as illustrated in Fig. 3.7a. Although most of them are uncharged atoms or molecules, the small fraction of charged so-called secondary ions can be used to determine the composition using a time of flight spectrometer, in which the ions are accelerated by an electric field and then the time is measured until they reach a detector [VG09]. In order to obtain depth profiles of the chemical composition up to the micrometre range, a second ion beam is used, which increases the abrasion by sputtering the sample with Cs ions. The calibration between the sputter time and the analysed depth is realized by measuring the depth of the sputter crater using a profilometer.

3D atom probe

The 3D atom probe allows the investigation of the chemical composition with three-dimensional resolution. This technique has a similar working principle as the SIMS method but is capable to measure the three-dimensional distribution of elements in a sample with

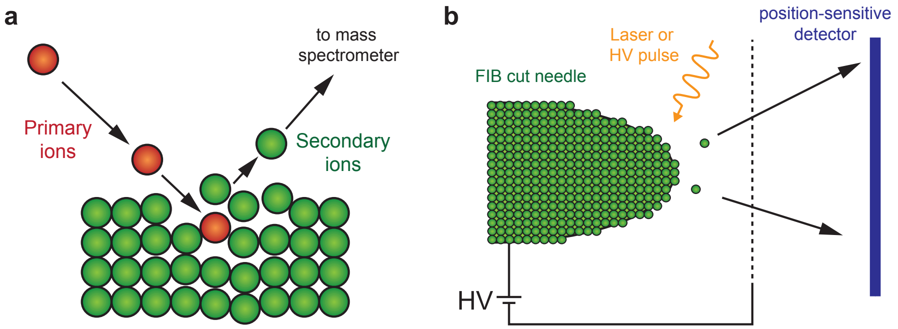

Figure 3.7.: Working principle of SIMS (a) and 3D atom probe (b).

quasi-atomic resolution. To dissolve ions from the sample in order to investigate them by a mass spectrometer, a sharp needle is formed out of the material under investigation using a focused ion beam. Then a high voltage is applied to this needle resulting in the presence of an extremely high electric field at the tip of the needle. By applying a laser or high voltage pulse to the needle, the electric field is increased for a short time leading to the dissolution of atoms from the tip. Using a position sensitive detector with single atom sensitivity and a time of flight mass spectrometer, the evaporated ions are detected and thus it is possible to reconstruct a chemical map of the atoms in the sample [RS10] as illustrated in Fig. 3.7b.

The SIMS and 3D atom probe measurements presented in this thesis were obtained in cooperation with the Central Institute for Engineering, Electronics and Analytics (FZJ-ZEA-3).

3.2.10. Fluorescence-lifetime imaging microscopy (FLIM)

The fluorescence microscope is a widely used tool especially in life science, which can image the spatial distribution of fluorescent atoms or molecules [DSW90]. In the present work, this technique is used to get an insight in the distribution of defects and donors in the $SrTiO_3$ single crystals. In order to emit fluorescence light, the electrons of the sample have to be excited into a higher energy level E_2 as depicted in the energy scheme in Fig. 3.8. In order to bridge the band gap E_G between valence band (VB) and conduction band (CB) of $SrTiO_3$, in this work two-photon excitation is used. The sample is irradiated with femtosecond laser pulses, which enhances the probability that two photons can transfer their energy to an electron at the same time. If the electrons are in the excited state, they undergo a radiationless decay to a slightly lower energy level E_3, from which they finally decay in a lower state e.g. the ground state E_1 under emission of fluorescent light. Due to the use of a two-photon experiment, the emitted light has a higher energy than the absorbed light. In order to record a map of the fluorescence intensity, the laser beam is scanned over the sample and the fluorescence light is recorded as a function of position and time by a single photon detector. Additionally, a map of the fluorescence lifetime can be calculated by measuring the decay of the fluorescence signal after the excitation while scanning the sample with the laser beam. The FLIM measurements presented in this thesis were obtained in cooperation with the Institute of Complex systems (FZJ-ICS-4).

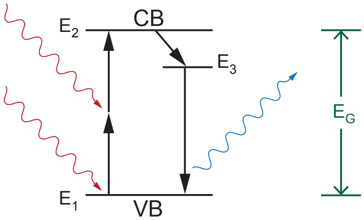

Figure 3.8.: Illustration of the two-photon excitation.

3.2.11. Raman spectroscopy

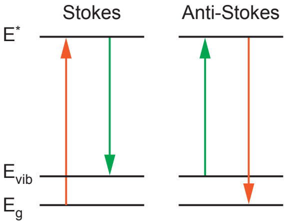

Figure 3.9.: Illustration of Stokes-Raman and Anti-Stokes-Raman scattering.

The Raman spectroscopy provides access to the lattice dynamics of solids using an optical method. It is based on the Raman effect, which describes the inelastic scattering of light on atoms [RK28]. In Fig. 3.9, a sketch of the relevant energy transitions is shown. At first an electron is excited to a higher virtual energy level E^* by a laser beam. Since this energy level is not stable, it immediately decays to a lower state, which can be a vibrational exited state E_{vib} representing lattice vibrations. Furthermore, also the opposite case can occur, in which an electron is excited from a vibrational state and decays into the ground state E_g. In both cases, which are called Stokes and Anti-Stokes, an energy shift between the absorbed and emitted light is measured and can be attributed to the mode of lattice vibration. Recently, the Raman spectroscopy was combined with confocal microscopy which allows the mapping Raman spectra, which can be used in order to obtain information about the spatial distribution of elements in the sample [DHT11]. In this work, the Raman microscopy performed by the company WITec GmbH was used for the investigation of the evolution of inhomogeneities due to donor doping in $SrTiO_3$.

3.2.12. Electrical four point measurements

In order to investigate the transport phenomena and resistive switching on the macroscale, the electric properties are characterized. Especially the resistance of the sample after the application of different treatment methods was measured in this work using the four point method in a modified Valdes geometry. In Fig. 3.10, the schematic set-up is depicted. Four electrodes are positioned along the sample and a current is fed in through the outer electrodes while the potential is measured between the inner electrodes. In order to avoid a perturbation of the potential distribution by the geometry of the crystal, the larger outer electrodes were positioned in a sufficient distance from the edges of the sample. The electrodes used in this work consisted of Pt, which was sputtered or manually pasted on the surface. In comparison to a two point measurement, the separation of current and voltage measurement can overcome the problem of the influence of the contact resistance at the electrodes. Since the measurement of the potential between the inner electrodes is nearly current free and the contact resistance of the electrodes is much smaller than the resistance of the voltage meter [Chu10], the total resistance R_{tot} of the sample can be estimated using the measured current I and voltage V_i by Ohm's law.

$$R_{tot} = \frac{V_i}{I} \tag{3.9}$$

Furthermore, the four point method allows to investigate inhomogeneous samples with different resistances of surface and bulk. In this case, the potential is not only measured between the inner electrodes but additionally between outer and inner electrodes. The resistance calculated from the potential between the inner electrodes corresponds to the bulk, while the voltage drop at the outer electrodes is determined by contact resistance and surface resistance. Due to this possibility, the four point method is a useful tool for the investigation of the influences of external gradients on the surface. In this work, especially the influence of the bombardment by Ar^+ ions was considered. Since solid electrodes would prevent the surface from being bombarded completely, a new set-up was designed and constructed which is equipped with four electrodes that can be pressed on the sample after bombardment *in situ*. The details of this set-up can be found in Appendix A.

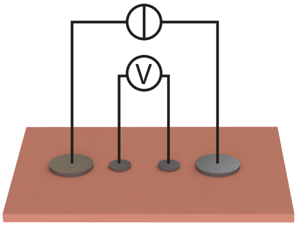

Figure 3.10.: Illustration of an electrical four-point measurement in Valdes geomety.

3.2.13. Resistance and capacitance measurements

The measurement of the capacitance is applied to investigate the dielectric properties of the single crystals. In order to measure the resistance and the capacitance of a sample simultaneously, a dedicated electrical set-up was designed and build as illustrated in Fig. 3.11. The basic idea of this set-up is to apply a slowly alternating quasi-DC voltage in order to observe the resistance switching effect superposed by a small AC voltage. The quasi-DC voltage is realized as triangular voltage sweep with low frequency (<1 Hz) while the sinusodial AC voltage has a smaller amplitude (100 mV) but higher frequency (1-10 kHz). The current flowing through the sample is analysed by a current-to-voltage converter. The DC component of the current is recorded directly by an analogue-to-digital converter (ADC) serving as low-pass filter while the AC component is filtered by a lock-in amplifier (LIA) with respect to the frequency f_{ref} of the AC voltage and the real and imaginary parts of this component are recorded. Hence, the resistance R of the sample can be calculated using the DC component of the current I_{DC} using Ohm's law.

$$R = \frac{U}{I_{\mathrm{DC}}} \tag{3.10}$$

The series capacitance C of the sample can then be extracted from the real part I'_{AC} and the imaginary part I''_{AC} of the AC current caused by the AC voltage U_{AC} with the frequency ω [GHH85].

$$C = \frac{(I'_{\mathrm{AC}})^2 + (I''_{\mathrm{AC}})^2}{\omega \cdot U_{\mathrm{AC}} \cdot I''_{\mathrm{AC}}} \tag{3.11}$$

The measurement of the capacitance can be used to determine the thickness d of a surface layer being present on a metallic material. If the dielectric function ε_r of the material and the area A of the electrodes building up a plate capacitor is known, the thickness can be calculated as follows.

$$d = \varepsilon_0 \varepsilon_r \frac{A}{C} \tag{3.12}$$

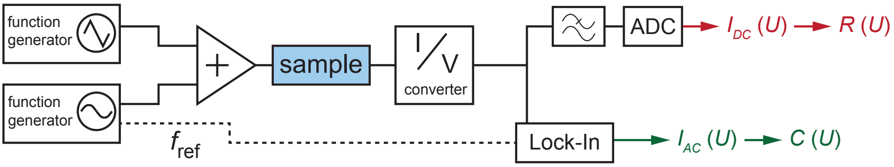

Figure 3.11.: Schematics of the set-up being capable to measure resistance and capacitance as function during resistive switching simultaneous.

3.2.14. Electron microscopy

The electron microscope is a valuable tool in order to image small features of solid state samples with highest resolution [AvDvLvT08]. The working principle of an electron microscope is similar to a conventional light microscope but electron waves are used instead of visible light. This requires the use of magnetic fields as lenses that are able to focus the electron beam. If the electron beam hits a sample, a part of the beam is transmitted and another part is reflected or interacts with the electrons in the material leading to the emission of secondary electrons. All parts can be used for obtaining information about the sample as realized in a transmission electron microscope and in a scanning electron microscope respectively.

Scanning electron microscopy (SEM)

In a scanning electron microscope, the secondary electrons emitted from a sample due to the interaction with the primary electron beam are recorded by a detector. Since the kinetic energy of the secondary electrons is relatively small, only those excited close to the surface can leave the sample making SEM a very surface sensitive technique. By scanning the electron beam across the sample, an image of the morphology of the surface can be obtained with a resolution in the nanometre range.

Additionally to the morphology, information about the crystallographic structure of the surface layer can be obtained by an SEM using the diffracted electron beam. The principle of this technique, which is called electron Backscatter diffraction (EBSD), is similar to the LEED method however using electrons with higher energy. Due to the interference of electron waves diffracted on planes such that the Bragg condition holds, a diffraction pattern showing so-called Kikuchi lines can be recorded, which is characteristic of the crystal symmetry. The EBSD measurements presented in this thesis were obtained in cooperation with the Gemeinschaftslabor für Elektronenmikroskopie der RWTH Aachen (GFE).

Transmission electron microscopy (TEM/HR-TEM)

In a transmission electron microscope, the sample is irradiated by the electron beam and image of the sample created by the transmitted beam is recorded. Since the reaction of the electrons with the atoms of the sample depends on the charge of the atoms, it is possible to identify different elements by their atomic number. By means of a TEM it is possible to image the arrangement of atoms in the crystal directly in the high resolution mode (HR-TEM). In order to obtain a sufficient intensity of the transmitted electron waves, the TEM technique requires the preparation of thin foils of the material of interest with a thickness below several tens of nanometres by a focused ion beam.

Due to the various interactions between the electron beam and the sample, additional information about the chemical composition and electronic structure can be obtained by a TEM. In order to get information about the chemical composition of a sample, the X-ray radiation that is generated if an electron hits an electron of an inner orbital of an atom leading to the decay of an electron from a higher energetic state under emission of a photon is analysed. This technique which requires an additional photodetector in the TEM system is called energy dispersive X-ray spectroscopy (EDX). Since the energies of the emitted photons are characteristic for the element, a quantitative analysis of the chemical composition is possible.

Another spectroscopic method that can be combined with a TEM is the energy loss spectroscopy (EELS) providing information about chemical composition and electronic structure. In this technique, the electrons that had interacted with the electrons of the sample due to inelastic scattering leading to a loss of the energy are analysed. Since the energy loss reflects the electronic structure of the sample, a spectrum with characteristic peaks is obtained that can be related to specific electron orbitals and valence states.

The TEM measurements presented in this thesis were obtained in cooperation with the Peter Grünberg Institute 5 (FZJ-PGI-5) using a microscope with a correction of the spherical aberration in order to obtain HR-TEM images with highest spatial resolution.

4. Results

In this chapter, the experimental results of the investigation of Nb-doped $SrTiO_3$ single crystals are described and discussed. Starting from a careful characterization of the fundamental properties of the as-received crystals such as crystallographic structure, chemical composition and electronic structure, the emphasis of the experimental investigation is placed on the influence of external gradients on the crystals, which is inevitable in order to understand the processes during resistive switching. At the end, resistive switching under electrical gradients itself is focused and a hypothetical model of the nanoscale origin of resistive switching in $SrTiO_3$:Nb surface layers is introduced.
Parts of this chapter have been published before:

> C. Rodenbücher, K. Szot, and R. Waser, How can we switch the resistivity of a metallic perovskite ($SrTiO_3$:Nb) by electrical stimuli? In: *Frontiers of Electronic Materials*, Wiley-VCH (2012), ISBN 978-3-527-41191-7
>
> C. Rodenbücher, S. Wicklein, R. Waser, and K. Szot, Insulator-to-metal transition of $SrTiO_3$:Nb single crystal surfaces induced by Ar^+ bombardment *Appl. Phys. Lett.*, 102:101603 (2013), `DOI:10.1063/1.4795611`
>
> C. Rodenbücher, W. Speier, G. Bihlmayer, U. Breuer, R. Waser, and K. Szot, Cluster-like resistive switching of $SrTiO_3$:Nb surface layers *New J. Phys.*, 15:103017 (2013), `DOI:10.1088/1367-2630/15/10/103017`
>
> C. Rodenbücher, T. Gensch, W. Speier, U. Breuer, M. Pilch, H.Hardtdegen, M. Mikulics, E. Zych, R. Waser, and K. Szot, Inhomogeneity of donor doping in $SrTiO_3$ substrates studied by fluorescence-lifetime imaging microscopy *Appl. Phys. Lett.*, 103:162904 (2013), `DOI:10.1063/1.4825367`
>
> C. Rodenbücher, A. Jauß, V. Havel, R. Waser, and K. Szot, Fast mapping of inhomogeneities in the popular metallic perovskite Nb:$SrTiO_3$ by confocal Raman microscopy *Phys. Status Solidi RRL*, 1-4 (2014), `DOI:10.1002/pssr.201409221`

4.1. Basic properties of the crystals

4.1.1. Colour and shape

In this work, Nb-doped $SrTiO_3$ single crystals with different donor concentration were investigated. In order to get an insight in the influence of the Nb doping on the properties of the crystals, three different concentrations (0.1 wt%, 0.7 wt%, 5.0 wt %) were chosen. The single crystals were grown using the Verneuil method [SBD76, Sch00] and were epi-polished with an accuracy of $< 0.5°$ after cutting pieces of 10 mm x 10 mm x 0.5 mm or 10 mm x 10 mm x 0.5 mm oriented along the (100) axes out of the crystal boule. In Fig. 4.1, a photograph of crystals obtained using the reflected light with different Nb concentration is shown. While undoped $SrTiO_3$ is transparent, introduction of Nb results in a change to a violet colour which gets darker with increasing Nb doping indicating distinct changes in the electronic structure. According to Section 2.4.1, the valence change of Ti from 4+ to 3+ leads to the appearance of occupied electronic states in the band-gap that can be made responsible for a change in the optical properties.

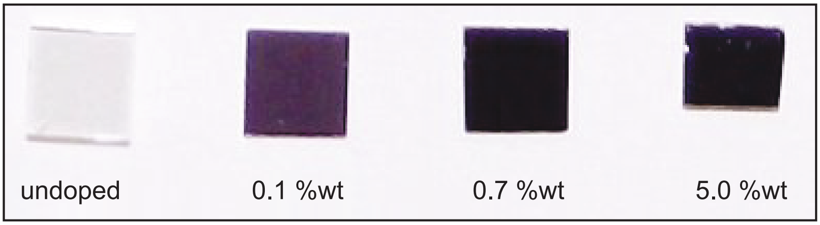

Figure 4.1.: Photograph of the investigated $SrTiO_3$ crystals with different Nb doping concentration.

4.1.2. Cleaving

Cleaving the crystal is a dedicated method in order to gain an insight into the structural properties of the crystal. As shown in the optical microscopy images (Fig. 4.2a) of the faces of the crystals after cleavage, the crystals did not cleave precisely along a crystal axis but revealed a conchoidral structure as expected from section 2.2. The magnifications measured by atomic force microscopy (Fig. 4.2b) on three crystals with different Nb concentration illustrate that all samples fractured conchoidrally but the lower doped crystals showed a more defined structure of the facets. In general, it can be seen that the roughness and inhomogeneity of the surface increased with the doping concentration, indicating that the introduction of Nb as dopant induced structural imperfections into the crystal.

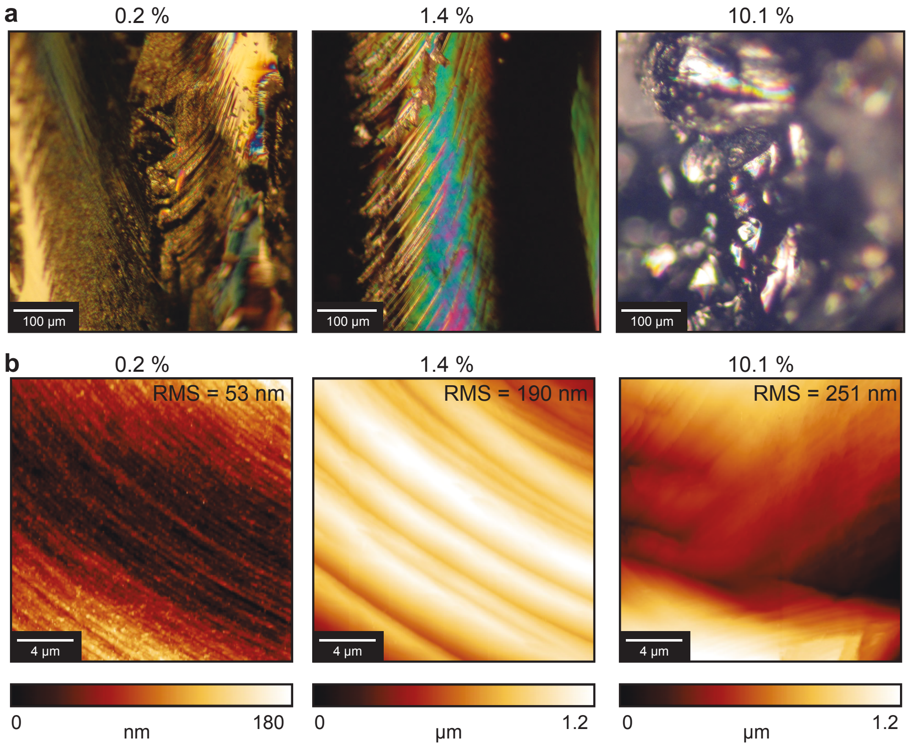

Figure 4.2.: Cleaving of the crystals. (a) Images obtained by optical microscopy on the crystal doped with 1.4 at%. (b) AFM topography maps obtained on crystals with different Nb concentration.

4.1.3. Hardness

The hardness of the crystals was measured using an indentation method. A pyramidal diamond indenter was pressed onto the crystals with a force of 1000 mN. The force was increased linearly for 30 s, while the maximum force was held for 20 s. In Fig. 4.3a, the photographs of the involved indents obtained by optical microscopy are shown. It can be seen that starting from the centre of the indent, cracks evolved due to the induced stress. The hardness values extracted from the indentation of the $SrTiO_3$ crystals with different Nb content are shown in Fig. 4.3b revealing that the hardness decreased systematically with the Nb concentration. This indicates that the higher doped crystals had a higher amount of extended defects and thus could be easily mechanically transformed.

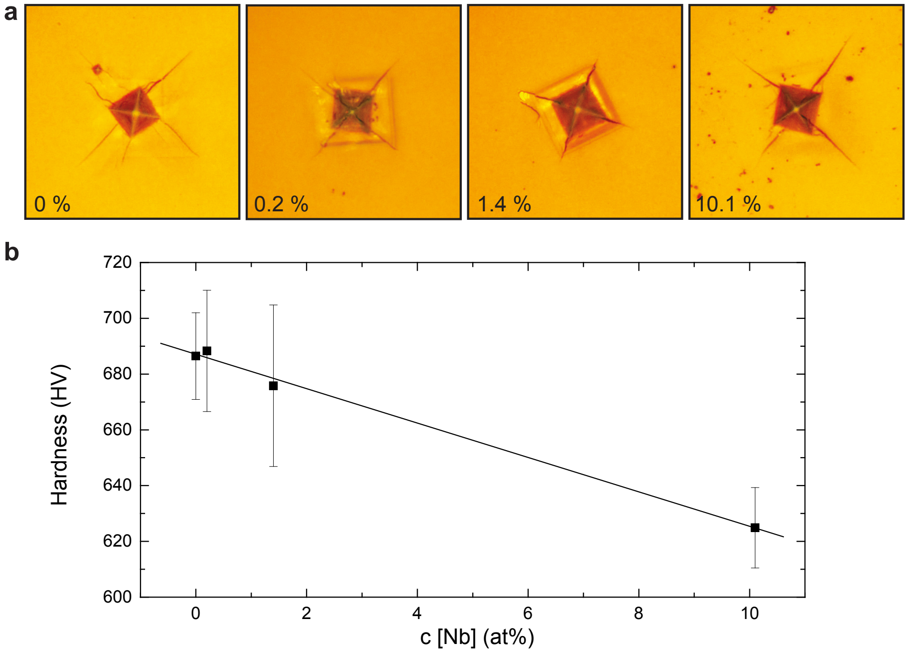

Figure 4.3.: Hardness measured by the Vickers method on crystals with different Nb concentration.

4.2. Crystallographic structure

4.2.1. Lattice constant

One of the most important factors for the estimation of the crystal quality is the crystallographic structure, which was investigated at first by powder diffraction measurements using the XRD technique after milling the samples in a mortar. To eliminate an eventual zero-shift, a reference Si standard (NIST 640a) was added. The diffraction pattern of the three crystals with different Nb content are presented in Fig. 4.4. By comparison with known pattern from the *powder diffraction file* database [Kar], an agreement with the pattern of the cubic perovskite structure with the space group Pm3m (No. 221) and the powder diffraction file (PDF) number 010-70-8508 was found. Using a Rietveld refinement procedure, the position of the peaks of the pattern was determined precisely allowing the lattice constants to be estimated. As can be seen in Fig. 4.4, the lattice constant increased linearly with the Nb content, which is consistent with the assumption that the Nb substitutes the Ti leading to an expansion of the lattice since the Nb^{5+} ions (radius 0.64 Å) is larger than the Ti^{4+} ions (radius 0.605 Å) [Sha76].

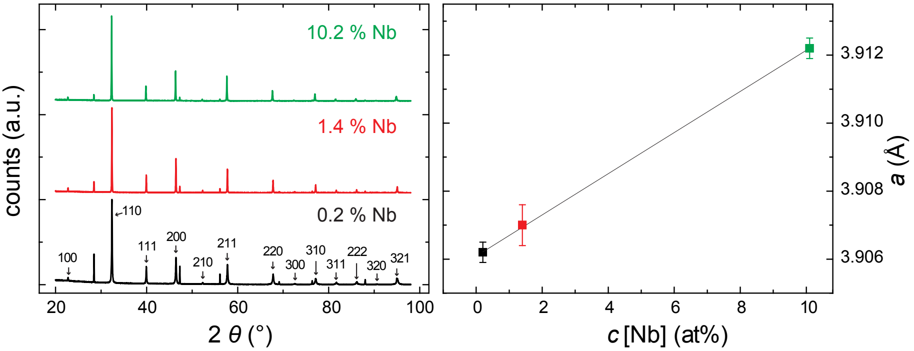

Figure 4.4.: The crystallographic structure. Left: Powder diffraction pattern of the crystals. Right: Lattice parameter as a function of doping concentration. Adapted from Rodenbücher *et al.* [RSB$^+$13].

4.2.2. Structural imperfections

Although the measured XRD pattern can be described by assuming a crystallization in a perfect perovskite lattice, a significant amount of imperfections was present influencing the crystallographic structure. In order to demonstrate the presence of such imperfections, the density of the crystals was measured by Archimedes method and compared to the theoretical density, which was calculated using the lattice parameter measured by XRD. Three models of different charge compensation mechanisms according to Sec. 2.3.1 were assumed. In the first model, only electronic compensation resulting in the composition SrTi$_{1-x}$Nb$_x$O$_3$ was taken into account. In the two other models, the charge compensation was realized by creation of Sr- or Ti-vacancies resulting in the compositions Sr$_{1-1/2x}\square_{1/2x}$Ti$_{1-x}$Nb$_x$O$_3$ and SrTi$_{1-5/4x}\square_{1/4x}$Nb$_x$O$_3$. As can be seen in Fig. 4.5, the experimental density of the lowest doped sample was in agreement with the theoretical values of all models within the error margin. At higher Nb concentration, the measured density decreased while the theoretical density of the most likely model of electronic compensation increased due to the higher mass of Nb atoms substituting Ti atoms. Particularly, the highest doped crystal revealed a large deviation from the theoretical values. Even the generation of Ti vacancies, which would balance the increase in the density caused by the higher mass of Nb, cannot explain the experimental data. This indicates that structural imperfections such as dislocations and three-dimensional defects were present reducing the density of the crystal.

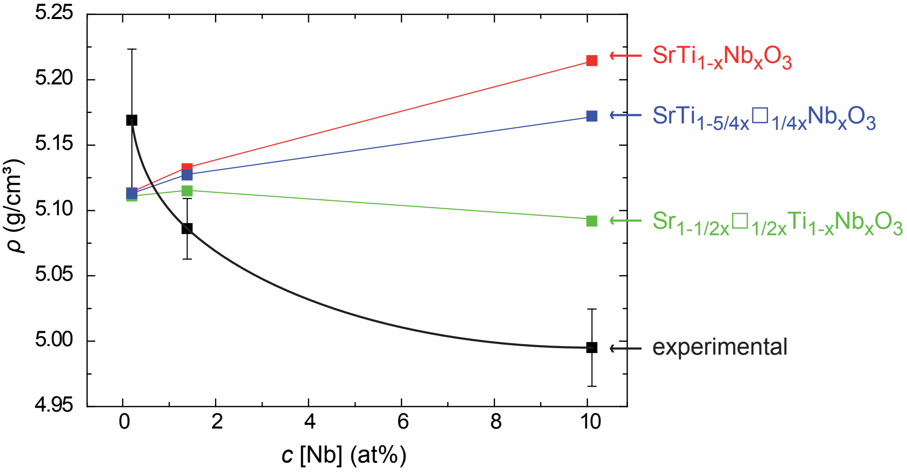

Figure 4.5.: Differences between theoretical density calculated for different structural models and experimental density measured by Archimedes method.

Mosaicity

The structural quality of the crystals was further investigated by X-ray topography in reflection mode providing an insight in the homogeneity of the crystal with respect to crystallographic orientation. The sample was irradiated by X-rays and the refracted images of the sample were recorded. In order to enhance the visibility of the topograms, an image processing with selected contrast enhancement was performed. In Fig. 4.6, characteristic topograms of crystals with different Nb content are shown. Although the investigated pieces of the crystals were rectangular, the images of the undoped crystal and of the crystals doped with 0.2 % and 1.4 % were distorted, thus indicating an inner inhomogeneity with respect to differences in phase orientation. Additionally, the region close to the upper right edges of the crystal doped with 1.4 % appeared displaced in the topogram indicating the presence of distinct deformations. The measurements on the highest doped crystal revealed a highly defective structure. The intensity of the topogram was relatively high, thereby showing that a strong mosaicity was present leading to a higher deflection of the primary beam into the diffracted images.

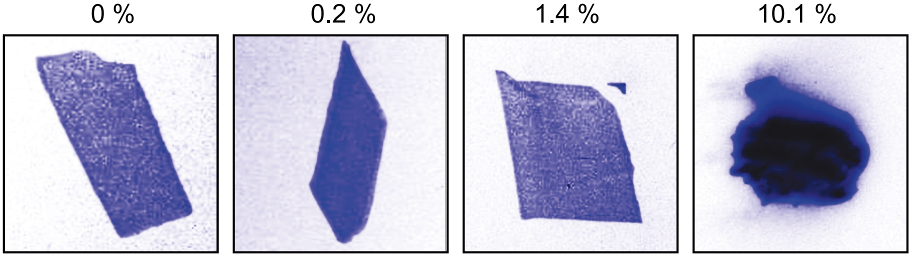

Figure 4.6.: Mosaicity measured by X-ray topography.

Dislocations

In order to investigate the influence of extended defects and particularly the dislocations on the crystallographic structure, transmission electron microscopy (TEM) was performed on a small piece of the single crystal doped with 10.1 at% cut by focused ion beam. The microscopy image obtained in bright field mode (Fig. 4.7) revealed the presence of various dislocation lines. By counting the dislocations in the field of view and relating them to the imaged area, it can be estimated that the density of dislocations is very high ($10^{12}/\mathrm{cm}^2$), a fact that underlines the poor structural quality of the highest doped crystal. By analysing the chemical composition close to the dislocations using energy electron loss spectroscopy

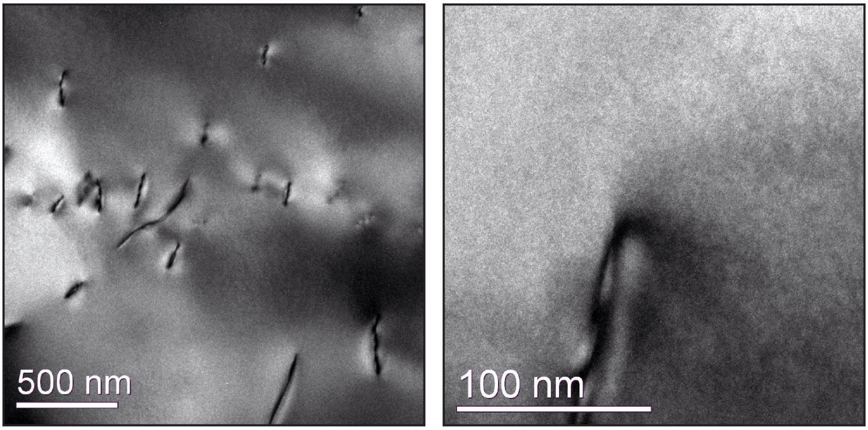

Figure 4.7.: Dislocation lines analysed by TEM in bright field mode.

(EELS) compared to the surrounding, no agglomeration effects could be detected, which indicates that the dislocation is only a structural defect in the stoichiometric matrix.

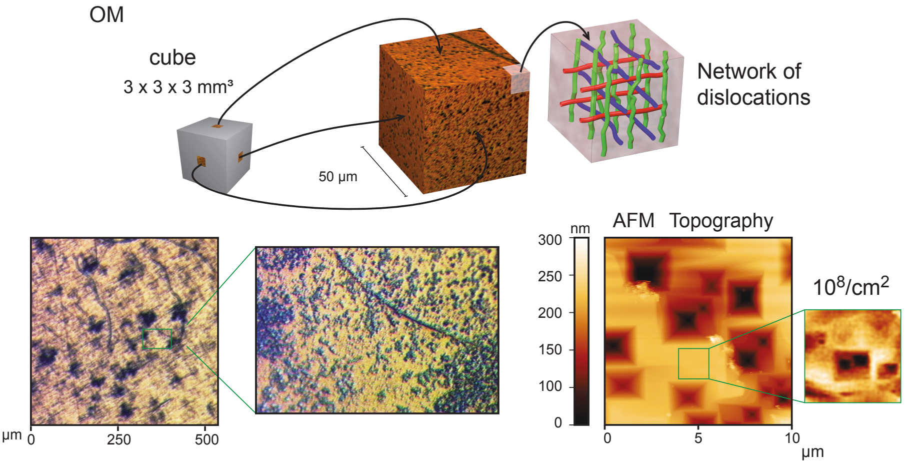

Figure 4.8.: Investigation of the exits of dislocations by etching method. Adapted from Rodenbücher *et al.* [RSB$^+$13].

The density of dislocations in the crystal doped with 1.4 at%, which was used to conduct most of the resistive switching experiments in this work, was determined by etching technique. A cubic piece of the crystal with an edge length of 3 mm orientated in (100) direction was etched in buffered hydrofluoric acid. After this procedure, etch pits had evolved at the exits of dislocations on the sides of the cube as can be seen in the projection of optical microscopy images in Fig. 4.8. Since all faces of the cube were decorated with etch pits, it can be assumed that the dislocations were orientated in all directions indicating the presence of a three-dimensional network of dislocations as has already be found in undoped $SrTiO_3$ [SSBW06].

A closer look at the etch pits on one surface of the crystal (optical microscopy image in Fig. 4.8) reveals that they were not distributed homogeneously on the microscale. In some regions of the surface, a rather small amount and in other regions agglomerations of etch pits can be seen, which can be explained by the existence of bundles of dislocations. In order to quantify the real density of dislocations, the etched surface was investigated by atomic force microscopy in contact mode revealing that further small pits had evolved besides the etch pits that were detected optically. Hence, the density of dislocations based on the AFM mapping method was estimated to $10^8/\mathrm{cm}^2$, which is lower than for the very defective crystal doped with 10.1 at% but still high enough to influence the properties of the material significantly.

4.3. Chemical imperfections

4.3.1. Admixtures

Nominal Nb content [%wt / %at]	0.1 / 0.2	0.7 / 1.4	5.0 / 10.1
Supplier	Crystec Berlin	Mateck Jülich	Surfacenet Rheine
Measured Nb content [wt%]	0.08	0.6	5.8
Additional elements [ppm]	–	–	Ba 1816 Zn 822 Cu 235 Na 203 Fe 152

Table 4.1.: Nb-content and presence of admixtures measured by ICP-MS.

In order to test the quality of the crystals with respect to the presence of additional elements, measurements by Laser Ablation Inductively Coupled Plasma Mass Spectrometry (LA-ICP-MS) were performed. In this technique, the sample is heated up locally by a laser resulting in the ablation and ionization of atoms which then form a plasma. The mass of the ions is then detected by a mass spectrometer. In Table 4.1, the results of the measurements are listed. It can be seen that the quality of the crystals doped with 0.1 %wt and 0.7 %wt was very high since no additional elements could be detected by LA-ICP-MS. In contrast to this, the measurements on the highly doped crystal (5.0 %wt) show that the surface region of the crystals was contaminated mainly with Pb (0.11 %) and also other elements like Zn, Cu, Ni and Gd could be detected. To check if this contamination was present in the bulk of the crystal as well, ICP-MS measurements were performed after chemical extraction of the sample in HNO_3. As presented in Table 4.1, the amount of admixtures was lower and especially Pb could not be found in this measurement. However, significant amounts of Ba, Zn and other elements were still present in the bulk. This shows that not only the surface of the crystal was contaminated during the preparation by sawing and polishing but that also the bulk of the crystal was contaminated during the crystal growth.

4.3.2. Carbon contamination

The carbon contamination of the crystals was investigated by thermal effusion measurements, in which the amount of molecules effused during heating up the sample under vacuum conditions was recorded by a mass spectrometer. The crystal doped with 1.4 at% Nb showed a distinct increase in the effusion above 300 °C as depicted in Fig. 4.9a. The main contributions to the effusion spectrum in this temperature range were related to CO and CO_2 molecules, indicating that preferentially physisorbed carbonates were released from the surface. While no significant amount of molecules with higher mass such as SrO could be detected even at higher temperature, an enhancement of effused molecules mainly having a mass of 28 u was observed above 800 °C. This mass corresponds to that of CO molecules implying a dissociation of strontium carbonate on the surface. This finding also corresponds to the XPS measurements in Sec. 4.5.5, in which carbon related components were not detectable any more above 800 °C. As a further source of the effused molecules, an opening of voids inside the crystal filled with carbon oxide molecules could be taken into account in order to explain the over-proportional increase in the effusion spectrum. Since the crystals were grown using the Verneuil technique in a hydrocarbon flame, a carbon contamination could have been incorporated easily during the growth process.

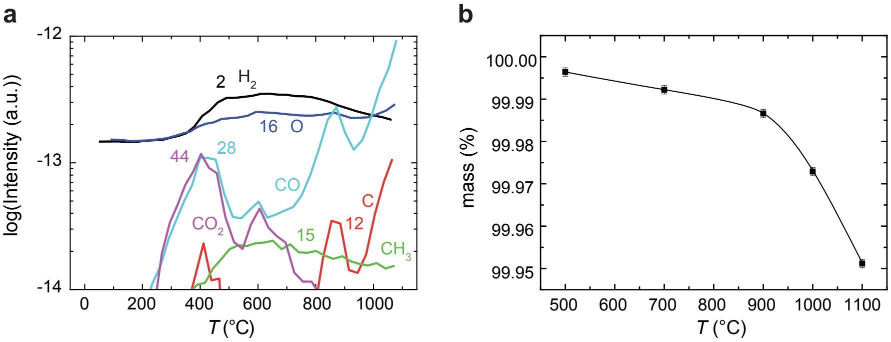

Figure 4.9.: Measurements of the thermal effusion (a) and thermogravimetric analysis (b) of the crystal doped with 1.4 at% Nb.

As illustration of the relevance of carbon effusion from the inside of the crystal, a thermogravimetric analysis performed. Using this technique, the mass of a piece of the crystal was measured during slow heating (20 °C/h) in reducing atmosphere consisting of 4 % H_2 in Ar. As shown in Fig. 4.9b, the mass decreased as a function of temperature. At 900 °C, a change in the slope can be seen, which could be a hint for the opening of voids filled with carbon oxides.

The crystal doped with 10.1 at% revealed a completely different effusion spectrum. Immediately after starting the heating procedure, a huge amount of carbon oxide related molecules was emitted from the sample. Above 400 °C, the effusion increased so much that the molecules could not be detected by the mass spectrometer making a further measurement impossible. This reveals that the quality of the highest doped crystal with respect to admixtures and carbon concentration was much lower than the quality of the lower doped ones.

4.4. Nb distribution

Depending on the conditions during crystal growth, inhomogeneities of the chemical compositions can be induced into the crystal. Particularly in Verneuil grown crystals, the presence of inhomogeneities is not unlikely, since the growth can take place far away from the thermodynamic equilibrium due to the substantial heat and mass flows during the crystallization process. In donor doped crystals, the investigation of the donor distribution is of extreme importance, since an inhomogeneous donor distribution would result in an inhomogeneous distribution of the electronic properties of the material. Hence, different methods of determine the Nb distribution of the used crystals are presented in the following.

4.4.1. Nb distribution on the microscale

In order to characterize the spatial Nb distribution on the microscale, two convenient complementary methods, namely fluorescence-lifetime imaging microscopy (FLIM) and confocal Raman microscopy (CRM), are presented in the following.

Fluorescence-lifetime imaging microscopy (FLIM)

Using FLIM, the distribution of the energy states involved in the process of fluorescence can be investigated with high spatial resolution (≈ 1 µm). Since Nb doping leads to the evolution of occupied Ti states having the valence 3+ in the band-gap as discussed in Sec. 2.4, the intensity and lifetime of the fluorescence can be used to estimate the Nb concentration. In order to correlate the Nb content to the measured fluorescence, at first a series of crystals with different Nb concentration was investigated using an excitation by a 325 nm HeCd laser with a power density of 0.1 W/cm^2.

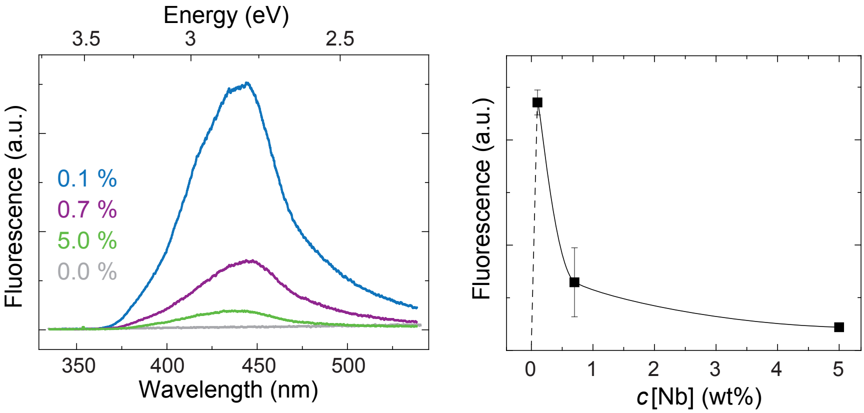

Figure 4.10.: Fluorescence spectra and intensity as function of the Nb concentration of the crystals. Adapted from Rodenbücher *et al.* [RGS$^+$13].

While undoped SrTiO$_3$ did not show fluorescence at this power density, an intense fluorescence signal was found in the crystal doped with 0.2 at% Nb with a maximum of the emission energy at 2.7-2.9 eV, which indicates that a band of Ti states with reduced valences 0.3 eV below the conduction band was involved in the fluorescence process. As shown in Fig. 4.10, the fluorescence intensity decreased again at higher Nb concentration revealing that the fluorescence was suppressed by competitive processes such as non-radiative Auger transitions related to the increasing occupation of the conduction band by the donor doping [YK08]. The observed correlation between the fluorescence and the Nb content only allows for a qualitative investigation of the local donor distribution since only crystals with three different Nb concentrations were available for investigation. In order to improve this method also with respect to practical application, a careful calibration between the fluorescence lifetime and the donor concentration should be performed in future by measuring a series of samples with different Nb content.

Spatially resolved measurements were performed on an upright scanning fluorescence microscope that uses a pulsed high repetition rate Ti:Sa-laser (100 fs, 80 MHz) for two-photon excitation and a photomultiplier in non-descanned configuration as a detector. The fluorescence intensity and lifetime were recorded while scanning the excitation laser in a raster of 350 x 350 µm. In Fig. 4.11, the colour-coded maps obtained at three different positions of the crystal doped with 1.4 at% Nb are shown. In all cases, an

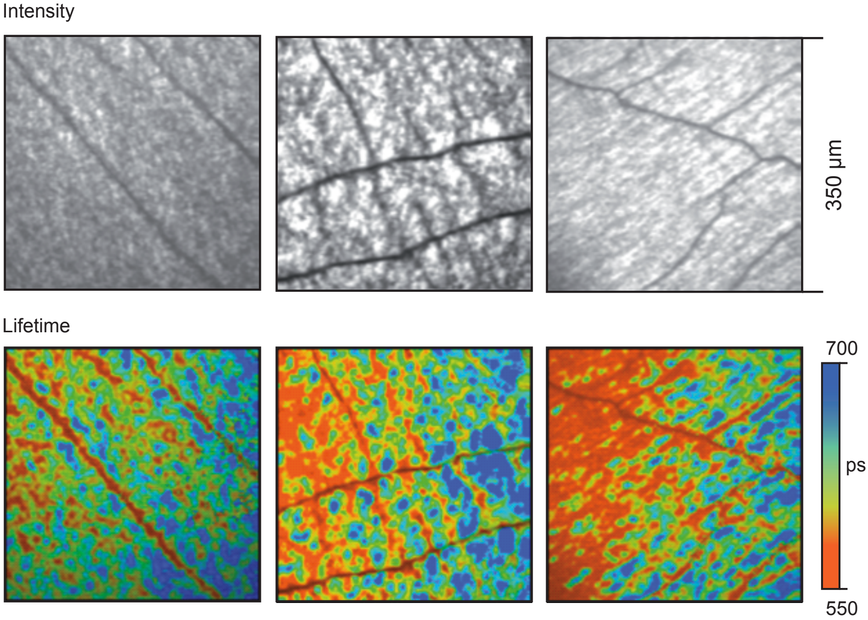

Figure 4.11.: Fluorescence intensity and lifetime measured by FLIM at three different positions of the crystal doped with 1.4 at% Nb.
Adapted from Rodenbücher *et al.* [RGS$^+$13].

inhomogeneous structure can be seen. The most remarkable features in the intensity maps are the extended lines with much lower intensity than the rest of the sample. With regard to the maps of the lifetime, it can be seen that also the lifetime inside the lines was significantly decreased. Apart from the extended lines, a grainy structure showing clusters with different fluorescence properties was recorded. Such an inhomogeneous structure can be assumed to be characteristic for the Verneuil-grown Nb-doped $SrTiO_3$ single crystals since it was found everywhere on the sample and even on crystals from different suppliers. According to the discussion above this indicates that an Nb clustering on the microscale was present. In all three lifetime maps, the left side of the image seems to correspond to a lower lifetime than the right side, which is however only an artefact of the used set-up.

At second, a crystal doped with 10.1 at% Nb was investigated by FLIM. The results presented in Fig. 4.12a reveal a significant different structure in the distribution of the fluorescence than in the lower doped crystal. While the fluorescence in large areas of the crystal barely could be detected, occasionally striped structures with higher intensity and

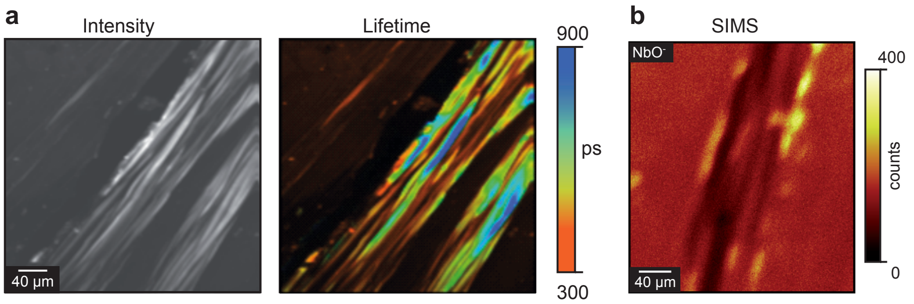

Figure 4.12.: Fluorescence measurements on the crystal doped with 10.1 at% Nb. (a) Intensity and lifetime maps measured by FLIM. (b) Mapping of the Nb concentration recorded by SIMS. Adapted from Rodenbücher *et al.* [RGS$^+$13].

lifetime were found. These structures had a total thickness of 50-100 µm and an additional sub-structure consisting of smaller stripes with a thickness of 3-10 µm. This measurement indicates that the Nb content inside the stripes was significantly lower than in the rest of the crystal since a higher fluorescence was related to a lower Nb concentration according to Fig. 4.10. In order to support this conclusion, the Nb content was measured additionally by SIMS. A map of the distribution of Nb in the striped region was recorded by counting the secondary NbO^- ions in a mass spectrometer as shown in Fig. 4.12b. In agreement with the FLIM mapping, it can be seen that the Nb content inside the stripes was lower, while at the rims of the stripes an agglomeration of Nb was present. The finding of this very inhomogeneous structure underlines the poor quality of the highest doped crystal and furthermore shows that donor segregation can easily evolve in doped $SrTiO_3$ crystals.

Confocal Raman microscopy (CRM)

As a complementary technique for the investigation of inhomogeneities of the Nb distribution, confocal Raman microscopy (CRM) was used that detects the presence of Nb by its influence on the lattice dynamics. In order to gain an insight into the change of the lattice vibrations of $SrTiO_3$ upon Nb doping, at first Raman spectra of crystals with different Nb concentration were measured.

As shown in Fig. 4.13, spectra with characteristic Raman peaks of $SrTiO_3$ were found. The peaks could be attributed to different vibrational modes according to the literature [SJ67, BE82] as listed in Table 4.2. It can be seen that the total intensity of the Raman spectra decreased as a function of the Nb concentration due to an increased optical ab-

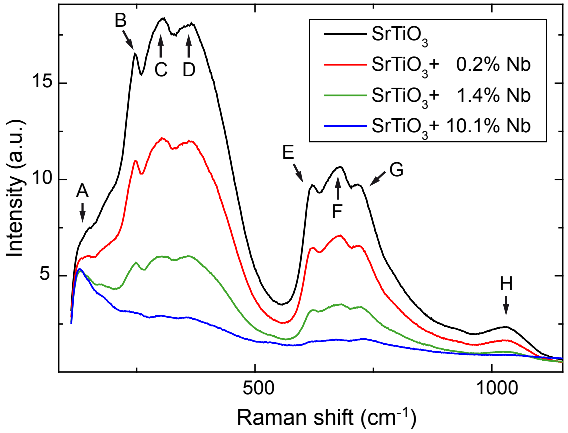

Figure 4.13.: Raman spectra of $SrTiO_3$ crystals with different Nb content.

Label	Raman shift (1/cm)	Vibrational modes
A	127	soft mode
B	244	2TA, 2TO1, TO1+TA, TA+LA
C	305	TO2+TA, TO2+TO1, TO4-TO2
D	366	TO1+LO1, TO2+LA, LO1+TA, TO4-TO1, TO4-TA, 2TO2
E	620	TO4+TA, TO4+TO1
F	678	2TO3, TA+LO3, TO1+LO3
G	720	TO4+TO2, LA+LO3
H	1028	2TO4, 2LO2, LO1+LO4

Table 4.2.: Correlation between measured Raman peaks and vibrational modes.

sorption. However, regarding only the first peak of the spectra around 127/cm potentially related to a soft mode, an increase in the relative intensity with the Nb concentration was observed. Hence, the intensity of this peak in relation to the intensity of the whole spectrum can be used as a measure of the Nb concentration when using a confocal Raman microscope.

In order to investigate the distribution of the intensity of lattice vibrations related to the Nb doping, Raman spectra were recorded while scanning the crystal (1.4 at% Nb) with

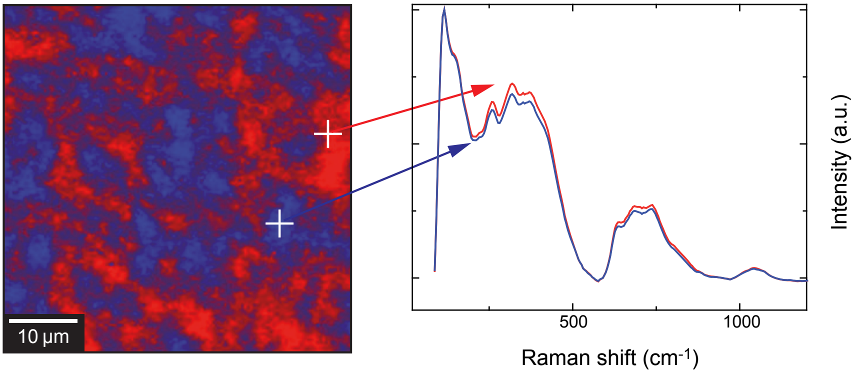

Figure 4.14.: Confocal Raman microscopy mapping obtained by base analysis.

the excitation laser beam. Two characteristic Raman spectra showing a significant difference in relative intensity in the higher frequency region were extracted from the spatial resolved measurements and were used for a base analysis. As result, a two-dimensional map of the relative amount of the two different spectra was obtained (Fig. 4.14) revealing an inhomogeneous cluster-like structure. The single spectra shown exemplarily for two positions reveal the differences in the intensity of the peaks. Since the intensity of the peaks of the spectrum plotted in red is higher than that of the blue one, the red colour of the map would correspond to a lower dopant concentration than the blue according to the arguments discussed above. In contrast to the FLIM results, no extended lines with different Nb content were found. This could be related to the fact that different pieces of crystals were used for the measurements, which would indicate that the lines were only present in some crystals. Beside this difference, in both cases, a similar grainy structure was found supporting the idea that FLIM as well as CRM are suited to monitor the inhomogeneous Nb distribution of the crystals.

4.4.2. Nb distribution on the nanoscale

The structure of the crystal on the nanoscale was analysed using high-resolution transmission electron microscopy. A piece of the crystal doped with 10.1 at% Nb was prepared by focused ion beam to obtain a sample, which was thin enough to examine it by transmitted electrons. On this sample, microscopic images were taken at two different scales. In Fig. 4.15a, an image obtained in the dark-field mode is shown revealing a distinct inhomogeneous structure. The observed inhomogeneities could be regarded as a hint for

Nb concentration on the nanoscale but also an intrinsic or extrinsic carbon contamination or a clustering of strontium vacancies can not be excluded as origin of the observed inhomogeneities.

In Fig. 4.15b, a high-resolution image of the crystal using Z-contrast, which allows the discrimination of different elements, is shown. The arrangement of the Sr atoms, which can be seen as bright spots reveals the presence of a perfect cubic perovskite lattice without any additional crystallographic phases. Furthermore, local fluctuations in the intensity on the nanometre scale were detected implying slight differences in the chemical composition.

In order to investigate the local variations of the lattice constant, a larger area (20 x 35 nm) of an $SrTiO_3$ single crystal doped with 1 % was recorded by HR-TEM as shown in Fig. 4.16a. Following the approach of Mlynarczyk *et al.* [MSP$^+$12], the obtained image was divided in squares of a size of 5 x 5 nm and for each of the squares the fast Fourier transform (FFT) was calculated using the Gwyddion program [NK12]. In Fig. 4.16b, the FFT of one square is shown exemplarily. By measuring the distance between the FFT spots of highest intensity, a relative value of the lattice parameter was estimated. The deviation of the lattice parameter from the mean value was calculated at every square and plotted in a colour graph (Fig 4.16c). It can be seen that locally differences of more than 1 % were calculated. Although the error of this value estimated by the described FFT method is of the same order and the observed local variations could also be related to inhomogeneities induced during sample preparation by focused ion beam, Nb segregation effects can also not be excluded since the difference in the lattice constant between the crystals doped with 0.2 % and 10.1 % is less than 0.2 % (cf. XRD measurements in Fig. 4.4) and thus

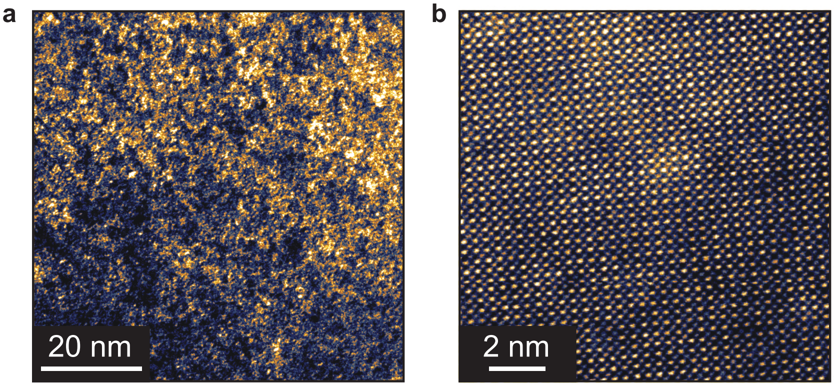

Figure 4.15.: TEM measurement of a crystal doped with 10.1 at%. (a) Image obtained in the dark field mode. (b) High resolution image obtained using Z-contrast.

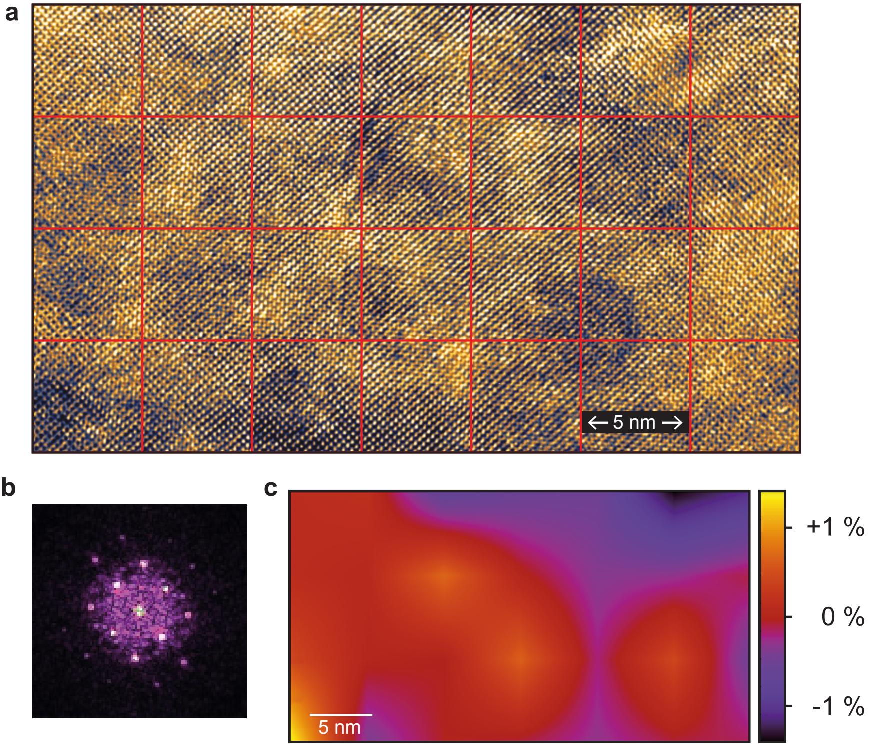

Figure 4.16.: TEM measurement of a crystal doped with 1.4 at%. (a) High resolution image obtained using Z-contrast. (b) Example of a fast Fourier transform of a 5 x 5 nm square. (c) Illustration of the estimated local variation of the lattice constant.

much smaller than local variations estimated here. Additionally, the Nb distribution of the lamella was investigated using EELS. In contrast to the distinct inhomogeneous Nb distribution on the microscale, a homogeneous distribution of Nb on the nanoscale was found. However, it has to be noted that the statistics of this investigation is too low to derive a reliable conclusion and hence a more systematic study of the Nb concentration on the nanoscale should be performed using HR-EELS, which was not in the scope of this thesis.

4.5. Surface layer

Since the surface is the place where a crystal is in contact with external gradients for example when applying a voltage sweep via deposited electrodes, the knowledge of the properties of the surface layer is the key factor for modelling the resistive switching effect. Hence in the following, investigations of the electronic structure and chemical composition of the surface layer and its reaction on different treatments are presented.

4.5.1. As-received surface layer

Using X-ray photoelectron spectroscopy (XPS), the electronic structure of the surface layer were investigated. Due to the information depth of 4-6 nm (for the K_α line), this technique is very well suited for the investigation of the surface layer. In Fig. 4.17a, a typical overview spectrum of $SrTiO_3$:Nb (1.4 at%) obtained by counting the emitted electrons with an energy-sensitive analyser is shown. All peaks of the spectrum were related to different energy states of the elements Sr, Ti, O, Nb and C. The absence of any additional peaks shows that no significant amount of admixtures was present besides the carbon contamination of the surface. In Fig. 4.17b, magnifications of the relevant core levels that were used for further analysis are shown. The characteristic background of the XPS spectrum was subtracted by the Shirley method [Shi72] and Gauss-Lorentz functions were fitted to the peaks using the Multipak program.

The signal of the O1s region was simulated by three peaks – a main peak at 530.5 eV related to the oxygen bound in the $SrTiO_3$ matrix and two peaks at higher binding energies that were attributed to OH^- and CO/CO_2 molecules adsorbed on the surface. The Ti2p region showed a doublet related to the states Ti$2p_{1/2}$ and Ti$2p_{3/2}$ around 430 eV due to the spin-orbit coupling in the electron orbital. It was simulated by only two peaks indicating that in the as-received surface layer the only Ti valence was 4+. In the C1s region, one major peak at 286 eV and two additional smaller peaks at higher binding energy were simulated showing that different organic molecules were present on the surface. The Nb3d region revealed a doublet at 208 eV similar as the Ti2p level. It could be fitted by two peaks related to the valence 5+. Since the amount of Nb is much smaller than that of the other elements because of the low doping level of 1.4 at%, the measurements had a lower signal-to-noise ratio compared to the other regions. The Sr3d level also had the form of a doublet due to the states Sr$3d_{5/2}$ and Sr$3d_{3/2}$. It was simulated by one major component at 134 eV related to Sr in $SrTiO_3$ and an additional component at higher binding energy, which could be attributed to the different surrounding of the Sr atoms at the surface. In the spectrum of the valence band, two main peaks at 7 and 5 eV can be seen that can

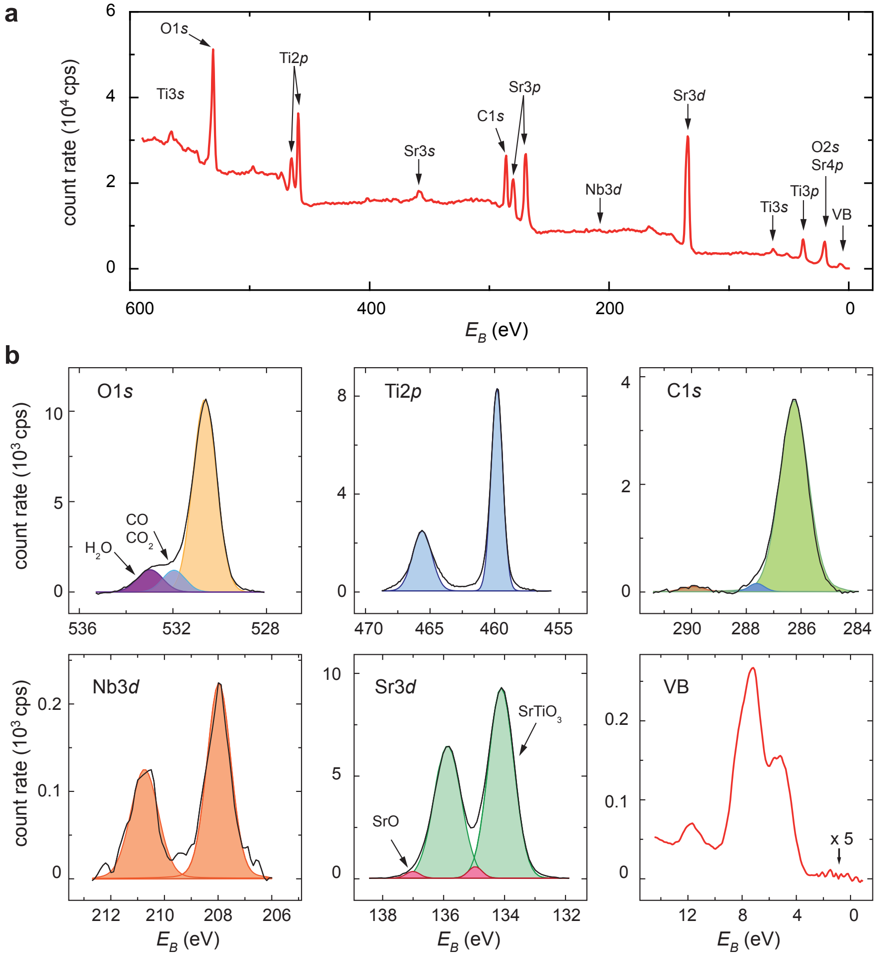

Figure 4.17.: XPS spectrum of the as-received crystal ($SrTiO_3$+1.4 at% Nb). (a) Overview spectrum. (b) Peaks of the core lines.

be attributed to O2p π and σ bonding orbitals according to Adachi *et al.* [AKWO98]. At higher binding energy around 11 eV, a further smaller peak was found that could be related to C2s emission from carbon impurities [RBM+84].

The most surprising finding in the investigation of the valence band of the as-received surface layer is however the absence of occupied electronic states close to the Fermi energy as is illustrated by a magnification (x 5) of the "VB" spectrum in this region in Fig. 4.17b.

Since Nb acts as a donor in $SrTiO_3$, metallic behaviour related to electronic states in the region of the Fermi energy would be expected. Furthermore, a valence change of Ti from 4+ to 3+ would have to occur if the charge of the Nb dopant is compensated by an electronic compensation mechanism according to Sec. 2.10, which was not observed by the XPS measurements. With regard to the chemical composition calculated from the XPS measurements, an Sr/Ti ratio of 1.3 was obtained, which also deviates from a perfect stoichiometry with an Sr/Ti ratio close to 1. This discrepancy between experimental result and expectation showed that the investigated surface layer did not have the expected properties of donor doped $SrTiO_3$.

4.5.2. Bulk properties

In order to gain an insight in the electronic structure and chemical composition of the bulk by using the surface sensitive method of XPS, an as-received crystal was introduced into a UHV chamber attached to the XPS measurement chamber and then the surface layer was removed *in situ* with a diamond scraper as illustrated in Fig. 4.18. After this procedure, a XPS spectrum was recorded and the chemical composition was calculated. The Sr/Ti ratio was much closer to the expected value and also hints for the presence of metallic states at the Fermi edge and the presence of the Ti valence 3+ were found in the spectrum.

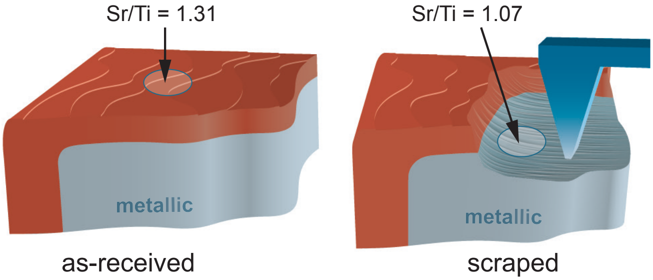

Figure 4.18.: Illustration of the *in situ* scraping of the crystal.
Adapted from Rodenbücher *et al.* [RSB+13].

After the measurement, the scraped crystal was exposed to air and then a further XPS spectrum was recorded. While the Sr/Ti ratio was slightly increased to 1.14, the metallic states at the Fermi edge could not be detected any more. This measurement revealed that on top of the metallic bulk which had the typical properties of Nb-doped $SrTiO_3$, an Sr-rich insulating surface layer with significant different properties from the bulk had evolved in air supporting the results obtained by Haruyama *et al.* [HAB$^+$97], who reported the suppression of metallic states due to the contact with oxygen.

4.5.3. Influence of different treatments on the surface layer

Crystallographic structure and chemical composition

Since the electronic properties of the surface layer could be changed easily by only exposing the freshly cleaved crystal to air, an extensive study of the influence of different treatments on the chemical composition and the electronic structure was conducted. In Fig. 4.19, the spectra of the core lines of Ti2p, Sr3d, Nb3d and the valence band are presented. The peaks were fitted as described above and the ratios of Sr/Ti and Nb/Ti were calculated. They are listed on the right of Fig. 4.19 together with the observed Ti and Nb valences and the presence of adsorbates as concluded from investigation of the C1s and O1s lines.

As presented above, the as-received surface layer had an excess of Sr and no additional Ti valences were observed while the scraped surface had a perfect stoichiometry and a small amount of Ti with the valence 3+ was observed. Upon reduction at 1000 °C under UHV conditions for several hours, the Sr/Ti ratio is decreased and additional valences of Ti and Nb were present. After heavy reduction at 1100 °C under UHV conditions for one day, the Sr/Ti ratio dropped to only 0.03, indicating that titanium oxides were formed in the surface layer. Simultaneously, metallic states at the Fermi edge appeared showing that reduction induced an insulator-to-metal transition in the surface layer. In contrast, oxidation in air at 1150 °C for one day led to an increase in the Sr/Ti ratio and a suppression of the metallic states indicating the formation of SrO on the surface, which is in agreement with previous findings [MWHB02, SPH$^+$96]. These measurements reveal that the Sr content can be influenced by the application of chemical gradients (reduction/oxidation) in that way that either additional phases of titanium oxides or strontium oxides evolve on the surface layer as illustrated in Fig. 4.20. Since during reduction no effusion of Sr was recorded by a mass spectrometer, it has to be assumed that movements of Sr or SrO complexes from the surface layer to the bulk and vice versa are the origin of the modification of the surface layer. Such a movement could take place along dislocations serving as easy diffusion paths as described in Sec. 2.3.5.

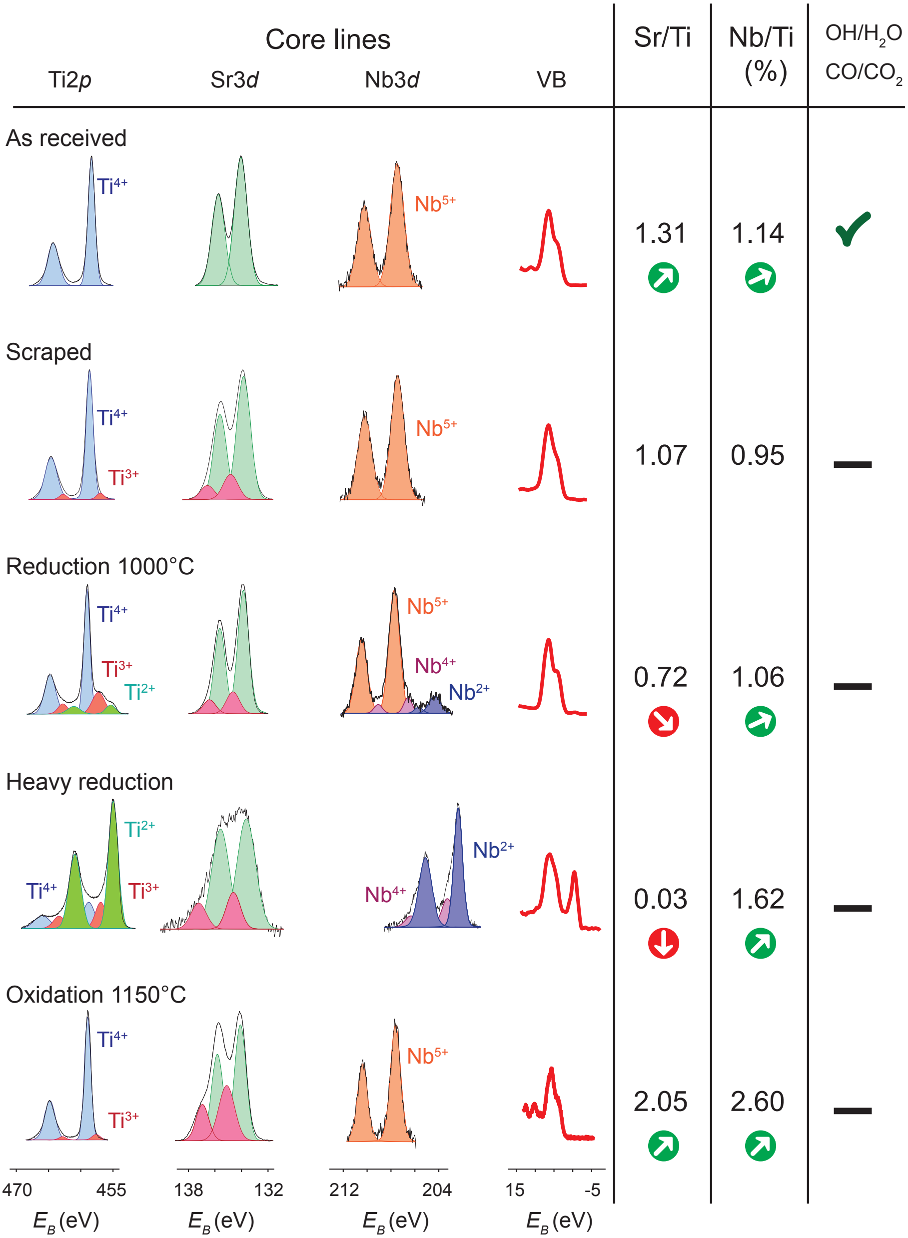

Figure 4.19.: XPS spectra, Sr/Ti and Nb/Ti ratios and indication of detected adsorbates of the $SrTiO_3$+1.4 at% crystal surface after application of different treatments.

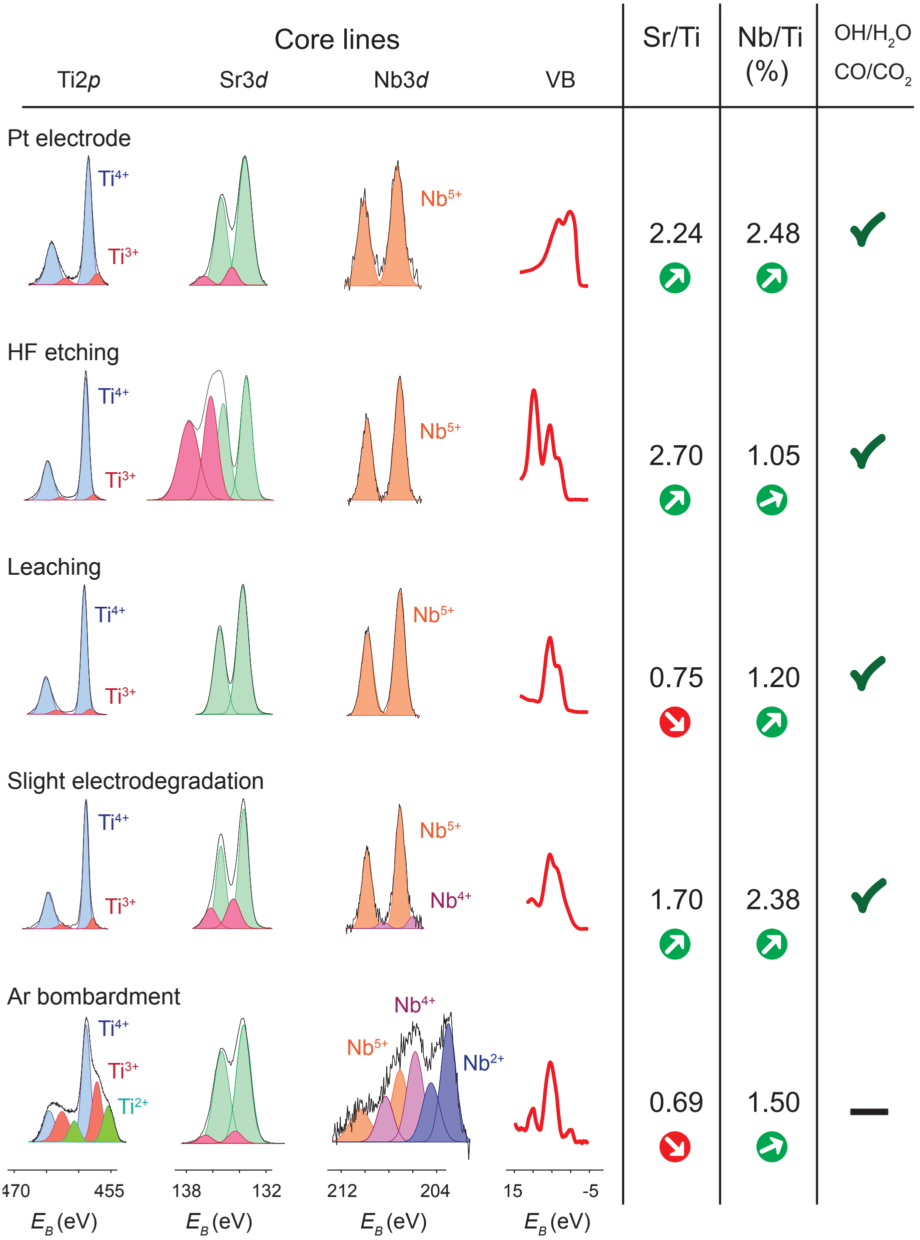
Core lines
Ti2p
Sr3d
Nb3d
VB
Sr/Ti
Nb/Ti (%)
OH/H2O CO/CO2
Pt electrode
Ti4+
Ti3+
Nb5+
2.24 ↗
2.48 ↗
✓
HF etching
Ti4+
Ti3+
Nb5+
2.70 ↗
1.05 ↗
✓
Leaching
Ti4+
Ti3+
Nb5+
0.75 ↘
1.20 ↗
✓
Slight electrodegradation
Ti4+
Ti3+
Nb5+
Nb4+
1.70 ↗
2.38 ↗
✓
Ar bombardment
Ti4+
Ti3+
Ti2+
Nb4+
Nb5+
Nb2+
0.69 ↘
1.50 ↗
—
470
455
138
132
212
204
15
-5
EB (eV)
EB (eV)
EB (eV)
EB (eV)

Upon covering the surface with 2 nm of Pt, which was thin enough to still get an access to the electronic properties of the crystal underneath, a huge increase in the Sr content and hints for the existence of the Ti valence 3+ were observed. This shows that the standard method of depositing a metal electrode to contact the crystal introduces fundamental changes in the surface layer, which has to be taken into account when interpreting electrical measurements. With regard to the spectra of the valence band in Fig. 4.19, a presence of metallic states at the Fermi energy can be seen, which is caused in this case by the metallic behaviour of the Pt film.

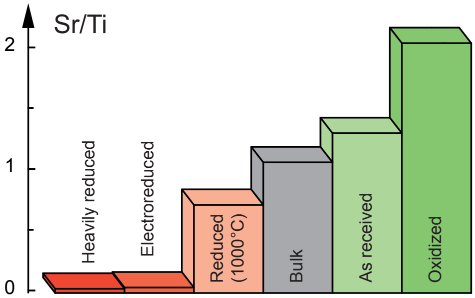

Figure 4.20.: Variability of the chemical composition of the surface layer under chemical gradients.

Etching the crystal in hydrofluoric acid, which was used to create etch-pits in order to investigate the exits of dislocations as shown in Fig. 4.8, also increased the Sr content on the surface layer. This was related to a change in the electronic structure of the Sr electrons. As can be seen in Fig. 4.19, a distinct second doublet at higher binding energy was recorded in the Sr3*d* region indicating significant changes in the surrounding of the Sr atoms. Additionally, a large fluorine peak was found in the total spectrum caused by the interaction of the acid with the crystal. Leaching of the crystal in water at 120 °C instead decreased the Sr excess from the surface and no second doublet of the Sr3*d* line was found.

To investigate the influence of electrical gradients on the surface layer, an as-received single crystal was scanned by a macroscopic Pt tip connected to a voltage source operated in a constant current mode (–50 mA) under UHV conditions. After this procedure, a significant increase in the Sr content of the surface layer was recorded showing that not only chemical but also electrical gradients can alter the properties of the surface layer. Since this is highly relevant for the understanding of the resistive switching effect, the influence of extremal gradients leading to modifications in the chemical composition and moreover to changes of the phase from $SrTiO_3$ to TiO_x are investigated in Sec 4.11.

Furthermore, bombarding the surface layer with Ar^+ ions introduced a change from an Sr-rich to a Ti-rich surface layer associated with an insulator-to-metal transition as presented in detail in Sec. 4.6.1.

With regard to the presence of adsorbates as derived from the XPS spectra, it can be seen that only scraping, reduction and ion bombardment were successful in removing the surface contamination, while in all other cases oxides of carbon and hydrogen could be identified in the core lines of C1*s* and O1*s*.

Morphology and crystallographic surface structure

The application of the treatments presented above not only changes the electronic structure and the stoichiometry but also influences the morphology and structure of the surface. In Fig. 4.21, LEED measurements of the crystallographic surface structure and AFM measurements of the topography are shown. In the LEED pattern, which were obtained using an electron energy of 95 eV corresponding to a wavelength of 1.26 Å, a cubic 1 x 1 symmetry can be seen, which is characteristic of the perovskite structure. Due to contamination of the surface of the as-received crystal by physisorbants, the LEED pattern was only detectable after heating to 275 °C. It is noteworthy that after all treatments presented here, a characteristic 1 x 1 LEED pattern was recorded showing that in average, the perovskite structure is very stable despite the huge changes of the stoichiometry discussed above. This is also supported by the fact that the lattice constants calculated from the spots of the LEED pattern only showed slight variations after the different preparation steps, which were within the error margin of approximately 0.04 Å.

The maps of the topography obtained by AFM reveal that the as-received surface was rather flat and unstructured due to the polishing procedure applied by the crystal manufacturer after cutting pieces from the Verneuil-grown crystal boule. After reduction, a bulged step-like structure with a step height around 3 nm had evolved. The oxidized surface, which was found to be Sr-rich, showed the presence of islands with a height of 10-20 nm on top of a step-like structure. As discussed above, these islands consisted of SrO, which segregated on the surface since the charge compensation mechanism of donor-doped $SrTiO_3$ changes under oxidizing conditions from electronic compensation to the compensation by strontium vacancies related to the evolution of SrO according to Eq. 2.22. As already shown in Fig. 4.8, etching in hydrofluoric acid led to the evolution of etch-pits while leaching did not change the topography significantly. This measurement illustrates that ionic movements in the surface layer can occur under external gradients that leading to distinct modifications of the structure of the surface layer on the nanoscale.

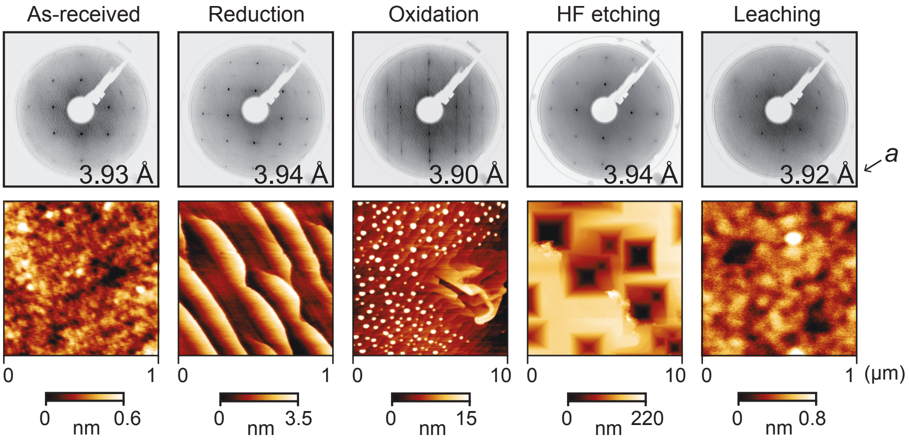

Figure 4.21.: Crystallographic surface structure and morphology after different treatments obtained by LEED and AFM. Adapted from Rodenbücher *et al.* [RSB+13].

4.5.4. Simulation of the surface layer

Having seen that an Sr-rich and insulating surface layer was present on the as-received crystals and that the Sr/Ti ratio of the surface layer can be modified easily by external gradients, the relation between the chemical composition and electronic structure was simulated by *ab initio* calculations. The local density of states (LDOS) was calculated for a symmetric, 13-layer TiO_2-terminated film with a $c(2 \times 2)$ in-plane unit cell. The Nb doping was taken into account by introducing one Nb atom in the centre substituting a Ti atom. In this study, the full-potential linearized augmented planewave method as implemented in the Fleur-code [Fle] was used. Two different models as illustrated in Fig. 4.22 were calculated - a fully stoichiometric system representing the bulk and an Sr-rich system, which was realized by introducing two Ruddlesden-Popper type SrO-SrO planes, representing the Sr-rich as-received surface layer.

In Fig. 4.22, the partial densities of states are presented for each layer of the simulated structures. In the upper left panel, a comparison of the total density of states of the stoichiometric (red) and the Sr-rich (green) case is shown. It can be seen that the metallic states at the Fermi edge, which are mainly related to Ti states, are present in the stoichiometric system but they are significantly suppressed by the introduction of Sr-rich layers. This simulation confirms that there is a strong correlation between the chemical composition and the electronic structure and that even slight changes in the Sr/Ti ratio can

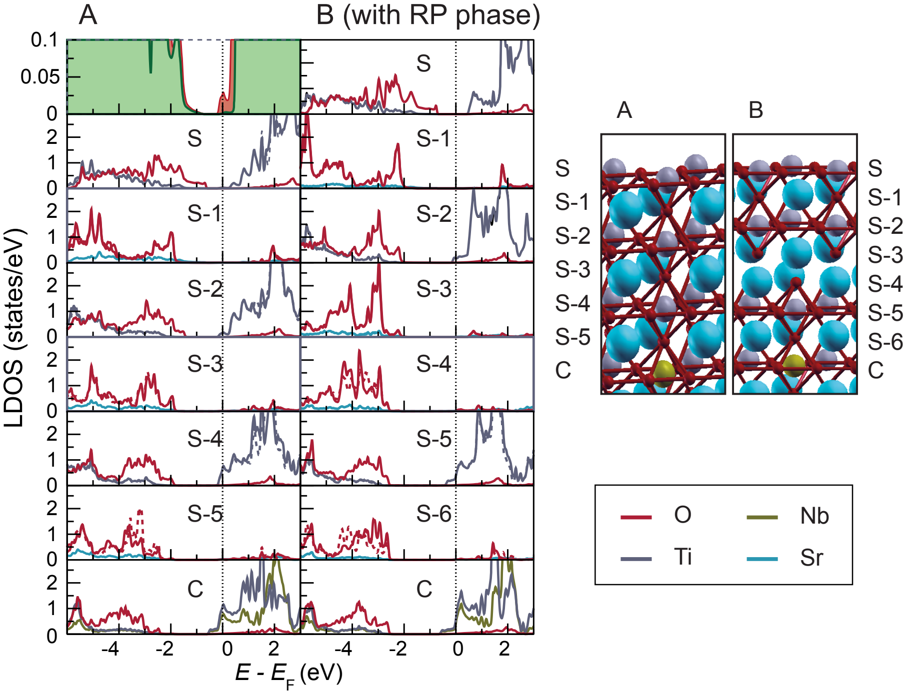

Figure 4.22.: Simulation of the LDOS of the stoichiometric bulk (A) and the Sr-rich surface layer (B). Adapted from Rodenbücher *et al.* [RSB⁺13].

significantly modify the electronic properties between insulating and metallic behaviour.

4.5.5. Insulator-to-metal transition upon reduction

In order to investigate the changes of chemical composition and electronic structure that induce an insulator-to-metal transition of the surface layer during reduction as shown above, a detailed XPS study was conducted during step-wise heating and cooling the sample under UHV conditions. In this way, crystals with two different doping concentrations were investigated as presented in the following. At first the results on $SrTiO_3$+1.4 at% Nb and at second on $SrTiO_3$+10.1 at% Nb are presented.

$SrTiO_3$+1.4 at% Nb

Starting with an as-received crystal, XPS spectra were recorded upon heating the sample *in situ* at 20 °C, 500 °C, 750 °C and 1000 °C. As shown in Fig. 4.23, the as-received surface layer was contaminated with adsorbates, which were detected by studying the O1*s* line showing two additional peaks related to OH/H_2O and CO/CO_2 molecules. The carbon contamination can also be seen with respect to the C1*s* line. Since the carbon peak is situated next to the Sr3*s* peak on the energy scale, the ratio of the carbon contamination could be estimated. At 500 °C, the amount of adsorbates was significantly reduced due to the removal of physisorbants taking place at approx. 250 °C. The O1*s* line showed only one additional peak from the carbon contamination but the characteristic peak of the hydroxides had vanished. In the C1*s* line, it can be seen that also the amount of the carbon oxides was reduced since the carbon peak was much smaller than the Sr3*s* peak. At 750 °C, the carbon peak in the C1*s* line was not detectable any more but the additional peak in the O1*s* line was still present. This indicates that the investigation of the O1*s* line, which reflects the change of the bond of the oxygen on the surface due to the interaction with carbon, is a more sensitive measure for the surface contamination than that of the C1*s* line. At 1000 °C, also the additional peak at the O1*s* line vanished and only one symmetric peak related to oxygen in the $SrTiO_3$ matrix was present. This shows that the binding of chemisorbed carbon oxides is very strong and that high temperatures have to be applied under reducing conditions in order to obtain a clean perovskite surface. As a second effect of the temperature increase, the width of the peaks of the core lines

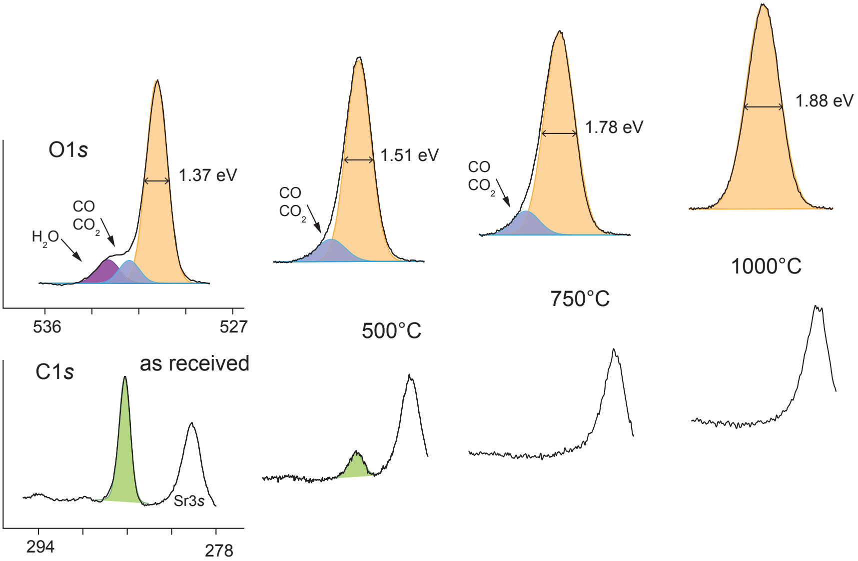

Figure 4.23.: XPS investigation of the removal of adsorbates upon reduction.

increased due to thermal broadening as can be seen from the values of the full width half maximum (FWHM) given in Fig. 4.23 for the O1*s* line.

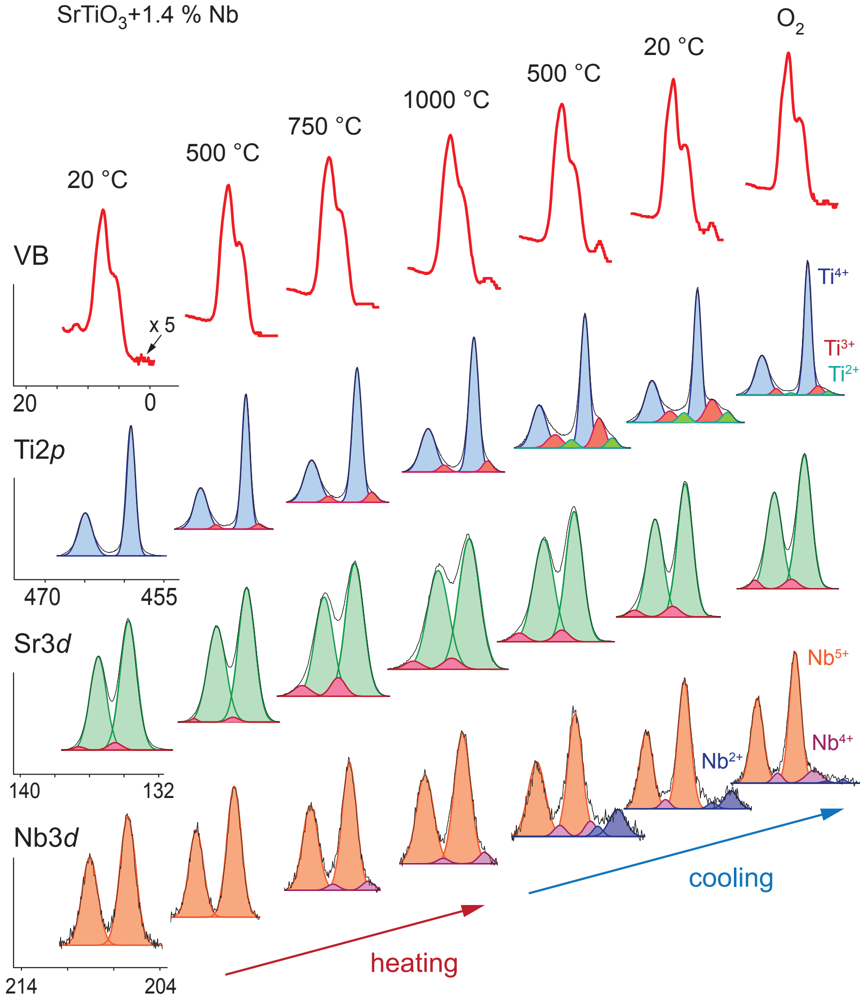

Figure 4.24.: XPS investigation of the influence of reduction on the surface layer ($SrTiO_3$+1.4 % Nb).

Heating the $SrTiO_3$:Nb crystal under UHV conditions not only leads to a desorption of additional molecules from the surface but also changes the properties of the surface layer significantly. As already presented above, the Sr content of the surface layer can be reduced until only a small amount of Sr is left, which indicates the formation of titanium oxides. In order to gain a detailed insight in this transformation, the evolution of the core lines of Ti, Sr and Nb as well as of the valence band during heating and subsequent cooling is shown in Fig. 4.24. In the valence band spectrum, the graph in the region close to the Fermi energy was multiplied by a factor of 5 in order to enhance the visibility of metallic states. It can be seen that above 500 °C, a distinct peak arose at the Fermi edge related to the evolution occupied of band-gap states indicating a transition from insulating to metallic behaviour. Simultaneously, additional valence states of Ti and Nb were detected. While a small amount of the Ti valence 3+ was detectable above 500 °C, the partial valence change of Nb to 4+ occurred not until 750 °C.

Upon reducing the temperature step-wise from 1000 °C to room temperature, a further change of the valences took place. In the Ti2*p* spectrum, an additional doublet related to the valence state 2+ was measured. Also in the Nb3*d* spectrum, an additional doublet evolved that was attributed to the Nb valence 2+ (the valence state 3+ is not expected to be present in the Nb-O system [Hal87, Bac09]). In Fig. 4.25, the ratios of the different valences as function of the temperatures are presented as extracted from the peak fitting of the XPS measurement in Fig. 4.24. It can be seen that the evolution of the additional valences of Nb and Ti was a real valence change since the amount of Ti^{4+} and Nb^{5+} was reduced simultaneously upon cooling. The Sr3*d* spectrum was composed of two doublets related to $SrTiO_3$ and a small amount of SrO in all measurements. The ratio of the main doublet decreased continuously during the thermal treatment under reducing conditions while the amount of the second Sr component only showed slight changes. It is quite surprising that the significant changes of the Ti and Nb valences did not occur during heating but during subsequent cooling, which reveals a new dimension of the valence change mechanism that had not been reported before. Hence, the details of the underlying mechanisms of this transformation are not completely understood and remain to be solved by future investigations.

After the crystal was cooled down to room temperature again, it was exposed to 10^5 L O_2, which led to an reversal of the insulator-to-metal transition. The metallic states at the Fermi edge were significantly suppressed and also the additional valence states of Ti and Nb were transformed into higher valences.

The analysis of the chemical composition by calculating the ratios of Sr/Ti, Ti/O and Nb/Ti shown in Fig. 4.26 revealed that during the insulator-to-metal transition of the surface layer not only a valence change but also a fundamental change of the stoichiometry took place. Starting from an Sr-rich as-received surface layer, the Sr/Ti ratio decreased

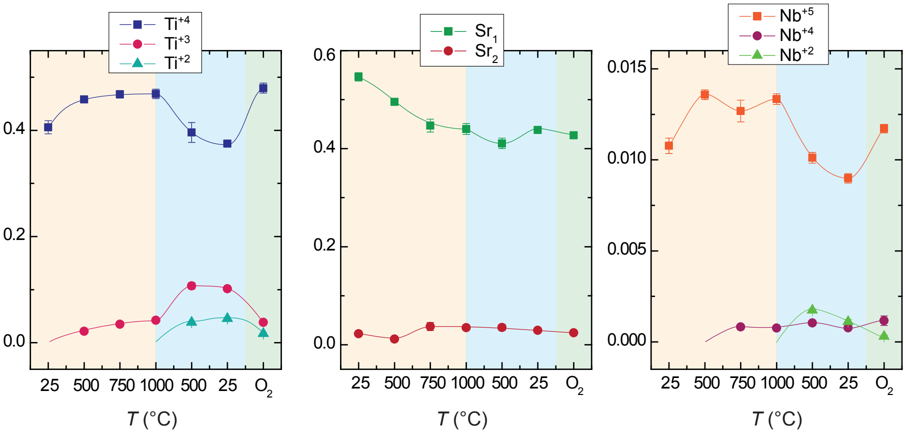

Figure 4.25.: Ratios of the valences as function of the reduction temperature ($SrTiO_3$+1.4 % Nb) extracted from the XPS measurement in Fig. 4.24.

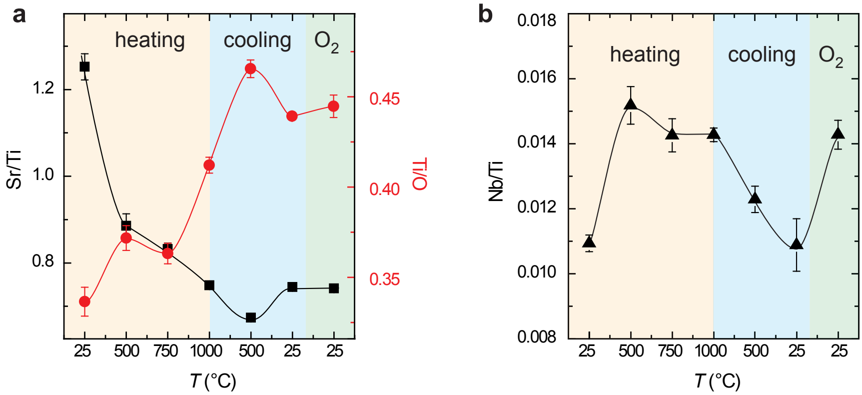

Figure 4.26.: Chemical composition as function of the reduction temperature ($SrTiO_3$+1.4 % Nb). (a) Ratio of Sr/Ti and Ti/O. (b) Ratios of Nb/Ti.

rapidly and reached a minimum around 0.7 after cooling from 1000 °C to 500 °C. This value is far away from the stoichiometric limit of $SrTiO_3$, which reveals that a phase separation in the surface layer with the formation of titanium oxides took place. Upon further cooling and subsequent re-oxidation, the Sr-content in the surface layer increased again showing that the transformation is partially reversible while in average, the new composition of the surface layer remained stable. The Ti/O ratio increased from the almost stoichiometric ratio of 0.34 up to 0.47 during the reduction implying a loss of oxygen. This could be related to either an effusion of oxygen leaving behind oxygen vacancies in the surface layer or to the movement of SrO complexes from the surface towards the bulk, which would decrease the Sr and O content of the surface layer simultaneously. It is noteworthy that the major increase in the Ti/O ratio reached its maximum after cooling from 1000 °C to 750 °C, indicating that not only a loss of oxygen towards the vacuum but also towards the bulk took place. This could be explained by the fact that the formation energy of surface vacancies is lower than that for a bulk vacancy [AKME09]. The Nb/Ti ratio increased during the first heating step at 500 °C from 0.011 to 0.015, which is close to the stoichiometric value of 0.014 showing that the Sr excess of the as-received surface layer also influenced the Nb distribution. Upon cooling, the Nb content decreased but increased again during re-oxidation. These changes could indicate that the transformation of the surface layer did not only involve a change in the Sr content and an evolution of titanium oxides but also Nb segregation effects.

In summary, the investigation of the surface layer under chemical gradients by XPS revealed that the surface layer of the $SrTiO_3$+1.4 % Nb crystal can be easily transformed between an Sr-rich and Ti-rich composition causing an insulator-to-metal transition under reducing conditions.

$SrTiO_3$+10.1 at% Nb

The crystal doped with 10.1 at% Nb was treated in a comparable way as the 1.4 at% crystal to investigate the influence of the reduction. XPS measurements were performed after a step-wise heating and subsequent cooling of the crystal *in situ* between 200 °C and 1000 °C. In Fig. 4.27, the spectra of the core lines and of the valence band are presented. In contrast to the measurement on the lower doped crystal, it was possible to simulate the core line regions of Ti2*p* and Nb3*d* at all temperatures by one component without any additional doublets, revealing that that no valence changes from Ti^{4+} and Nb^{5+} took place. Due to the high doping concentration, the signal-to-noise ratio of the Nb3*d* line is very high. Hence, the concluded absence of additional valence states is reliable. This finding shows that in the surface layer, an electronic charge compensation mechanism as expected according to the point defect chemistry for reducing conditions related to a high amount of Ti^{3+} was not present, thus illustrating once again the special role of the surface layer. Also the Sr3*d* line could be described by only one component showing the absence of a distortion in the surrounding of the Sr atoms. With regard to the valence band region, no occupied states in the band-gap and particularly no metallic states at the Fermi energy were observed showing that annealing under reducing conditions did not induce an insulator-to-metal transition. Even at 1000 °C, only slight changes in the main

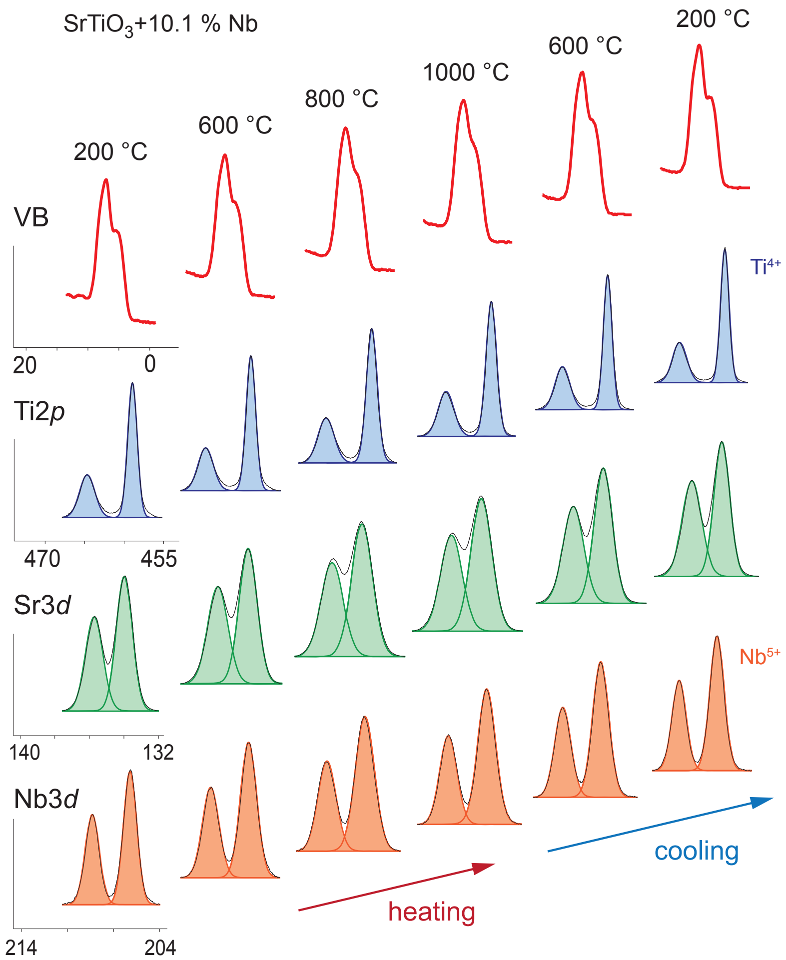

Figure 4.27.: XPS investigation of the influence of reduction on the surface layer (SrTiO$_3$+10.1 % Nb).

peaks of the valence band were detected but these changes did not lead to a permanent transformation of the surface layer.

The stability of the surface layer of the crystal doped with 10.1 % Nb gets more obvious by Fig. 4.28 showing the ratios of the valences as calculated from the peak fitting. It can be seen that in average, the values remain constant and are only altered slightly by the

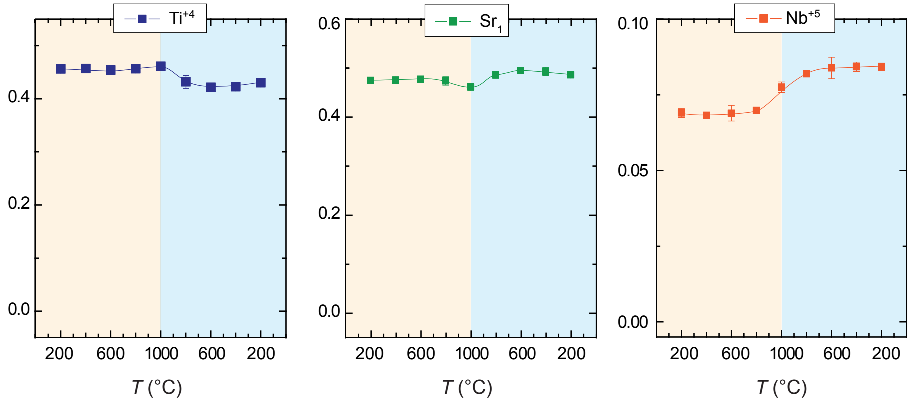

Figure 4.28.: Ratios of the valences as function of the reduction temperature ($SrTiO_3$+10.1 % Nb) extracted from the XPS measurement in Fig. 4.27.

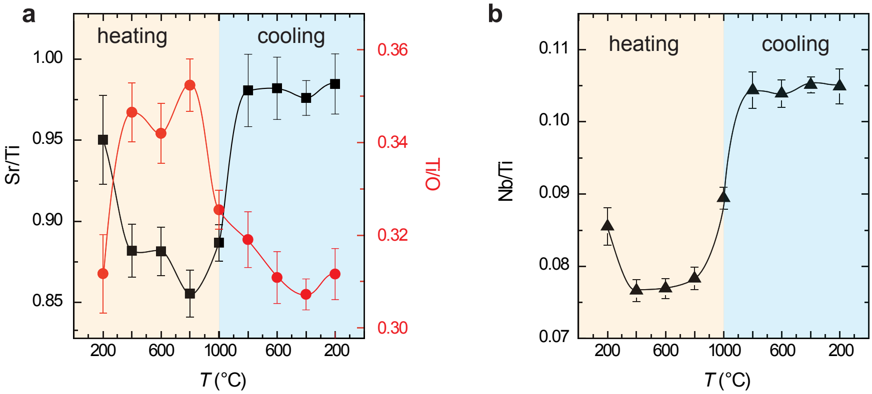

Figure 4.29.: Chemical composition as function of the reduction temperature ($SrTiO_3$+10.1 % Nb). (a) Ratio of Sr/Ti and Ti/O. (b) Ratios of Nb/Ti.

reduction procedure. After heating at 1000 °C, the amount of Ti^{4+} was decreased from 0.46 to 0.41 while the Nb^{5+} content was increased from 0.07 to 0.08.

The calculation of the chemical composition based on the XPS measurements revealed the same trend. Upon heating, at first the Sr/Ti ratio decreased slightly but increased again after starting the cooling from 1000 °C under UHV conditions. The Ti/O ratio showed an opposite behaviour with a first increase and a decrease after heating to 1000 °C. However, it is noteworthy that the changes in the chemical composition of the surface layer are much smaller than on the lower doped crystal. The Nb/Ti ratio decreased in the first heating step but increased at 1000 °C from 0.077 to 0.104, which is close to the expected value of 0.101. This indicates that Nb segregation processes took place at the surface layer, which could be related to the very inhomogeneous Nb concentration on the microscale as investigated by FLIM and SIMS measurements in Sec. 4.4.

Comparing the reaction of the $SrTiO_3$ crystals doped with 1.4 % and 10.1 % on the exposure to highly reducing conditions, it is striking that the surface layer of the lower doped crystal showed an insulator-to-metal transition related to a phase change from $SrTiO_3$ to TiO_x whereas the surface layer of the higher doped crystal was found to be stable. One reason of this different behaviour could be found in the different quality of the crystals. As presented in the beginning, the highest doped crystal had a lot of defects such as dislocations, voids, Nb agglomerations and contaminations by additional elements. The effusion measurement (Fig. 4.9) showed that during reduction, a large amount of gases such as oxygen is effused from the voids in the crystal. Hence, the bulk of the crystal itself and particularly the voids could have act as an oxygen source for the surface layer during the XPS measurements under reducing conditions, which prevented the surface layer from loosing oxygen and from starting the transformation to Ti-rich phases.

4.6. Influence of ion bombardment on the surface layer

Due to the high convertibility of the surface layer of $SrTiO_3$:Nb, the properties of the surface strongly depend on the preparation method that was applied to the crystal. When fabricating a functional electronic device, commonly methods involving ion bombardments are used such as sputtering or cutting by focused ion beam. In order to gain an insight into the transitions in the surface layer upon ion bombardment, the irradiation with Ar^+ ions and the cutting of a needle for 3D atom probe measurements by an ion beam are discussed in the following.

4.6.1. Ar^+ bombardment

The influence of bombardment by Ar^+ ions on the electronic structure and chemical composition of the surface layer was investigated by means of XPS. After bombarding the crystal surface *in situ* with ions for a defined time using an ion gun (Physical Electronics) with an energy of 2 keV and an emission current of 15 mA, the spectra of the core lines of Sr3*d*, Ti2*p*, Nb3*d* as well as the valence band were measured. In Fig. 4.30-4.32, the spectra after subtraction of the background signal by the Shirley method and peak-fitting analogue to the measurements in Sec. 4.5.5 are presented.

Three epi-polished as-received samples with different Nb concentration were investigated. Due to the low doping concentration of the crystal doped with 0.2 at% Nb, the Nb3*d* line could not be recorded precisely and is not shown here. Comparing the spectra of the three samples, a similar reaction on the Ar bombardment can be seen. With increasing bombardment time, additional occupied states in the band-gap and close to the Fermi energy were recorded in the spectra of the valence bands proving that an insulator-to-metal transition was induced in the surface layer. This gets more obvious when regarding the core levels of Ti2*p*. While the spectra of the as-received surfaces only displayed one doublet corresponding to the valence state 4+ (cf. Sec. 4.5.5), already a short bombardment of 10 s was sufficient to induce the additional presence of a small amount of the valence state 3+. After prolonged bombardment (70 s for the highest doped crystal and 150 s for the two lower doped ones), also the valence 2+ was observed. The measurements of the Nb3*d* core levels revealed a similar valence change for Nb. After a short bombardment time, the additional valences 4+ and 2+ became measurable and after a time of 310 s, the valence 2+ even became the main valence of Nb. Despite the huge changes of the electronic structure of Ti and Nb, the Sr3*d* line did not reveal comparable changes upon bombardment and was composed of one main doublet and one smaller doublet attributed to the surrounding of the Sr atoms at the surface.

The evolution of the additional valence change as function of the bombardment time is exemplarily illustrated in Fig. 4.33a for the crystal doped with 1.4 % Nb. It can be seen that the valence change of Ti and Nb occurred after a relatively short bombardment time and then reached a plateau region after approximately 10 min (600 s) of bombardment. Simultaneously with the valence changes, the chemical composition was also altered significantly. The ratio of Sr and Ti decreased from values close to 100 % to values below 70 % upon bombardment indicating that a preferential sputtering of Sr or SrO occurred leading to the evolution of a highly Ti-rich surface layer that could then be further reduced by a removal of oxygen. On the other hand, also the Ti/O ratio was altered upon bombardment starting from values close to 30 % to values above 50 % showing that ion bombardment is also related to a reduction process, which could lead to the evolution of additional Ti-rich phases in the surface layer similar to the effects of thermal reduction described in Sec. 4.5.5. The observed insulator-to-metal transition of the Nb-doped surface layer upon bombardment is rather similar to that of undoped $SrTiO_3$ [RB05, PSPS09, GBKO11] showing that the surface layer of doped $SrTiO_3$, which is nominally a metallic oxide, plays a very special role and can be altered easily in its properties.

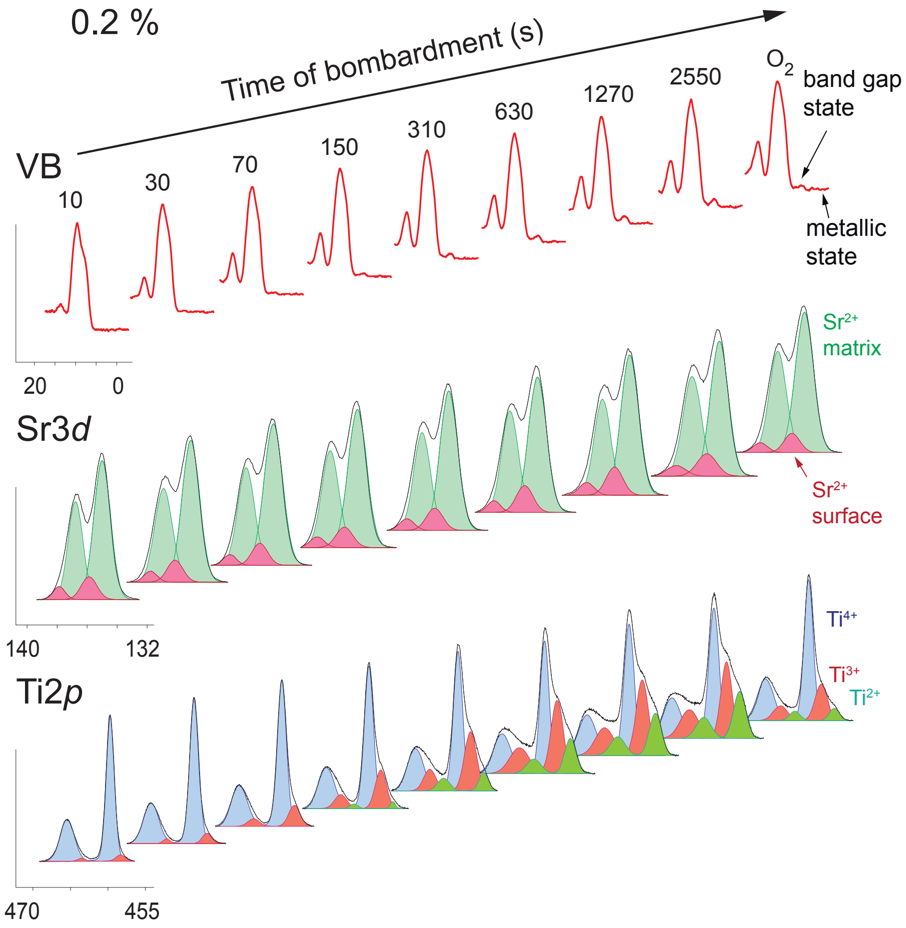

Figure 4.30.: Influence of Ar^+ bombardment on the electronic structure investigated by XPS ($SrTiO_3$+0.2 % Nb). Due to the low donor concentration the Nb3*d* line was not measurable.

After the crystal surfaces were bombarded by Ar^+ ions for 2550 s, the influence of re-oxidation on the evolved metallic surface layer was investigated. Therefore, the surfaces were exposed to a dose of 10^5 L O_2 at a pressure of $p_{O_2} = 1.3 \cdot 10^{-3}$ mbar. As can be seen in the spectra in Fig. 4.31 and 4.32, the amounts of additional valences of Ti and Nb were significantly reduced while the valences Ti^{4+} and Nb^{5+} were increased. Additionally also the metallic states and the occupied states in the band-gap were reduced but they

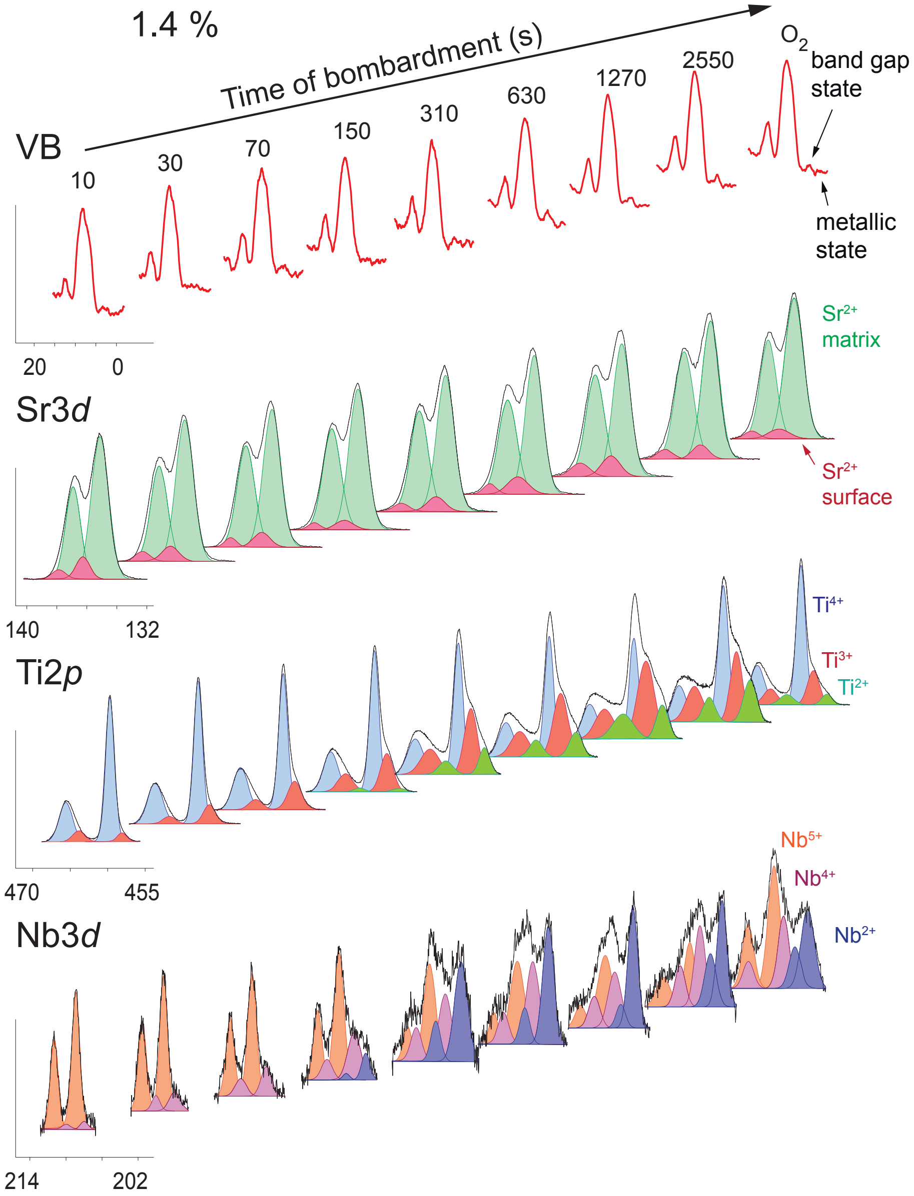

Figure 4.31.: Influence of Ar^+ bombardment on the electronic structure investigated by XPS ($SrTiO_3$+1.4 % Nb).

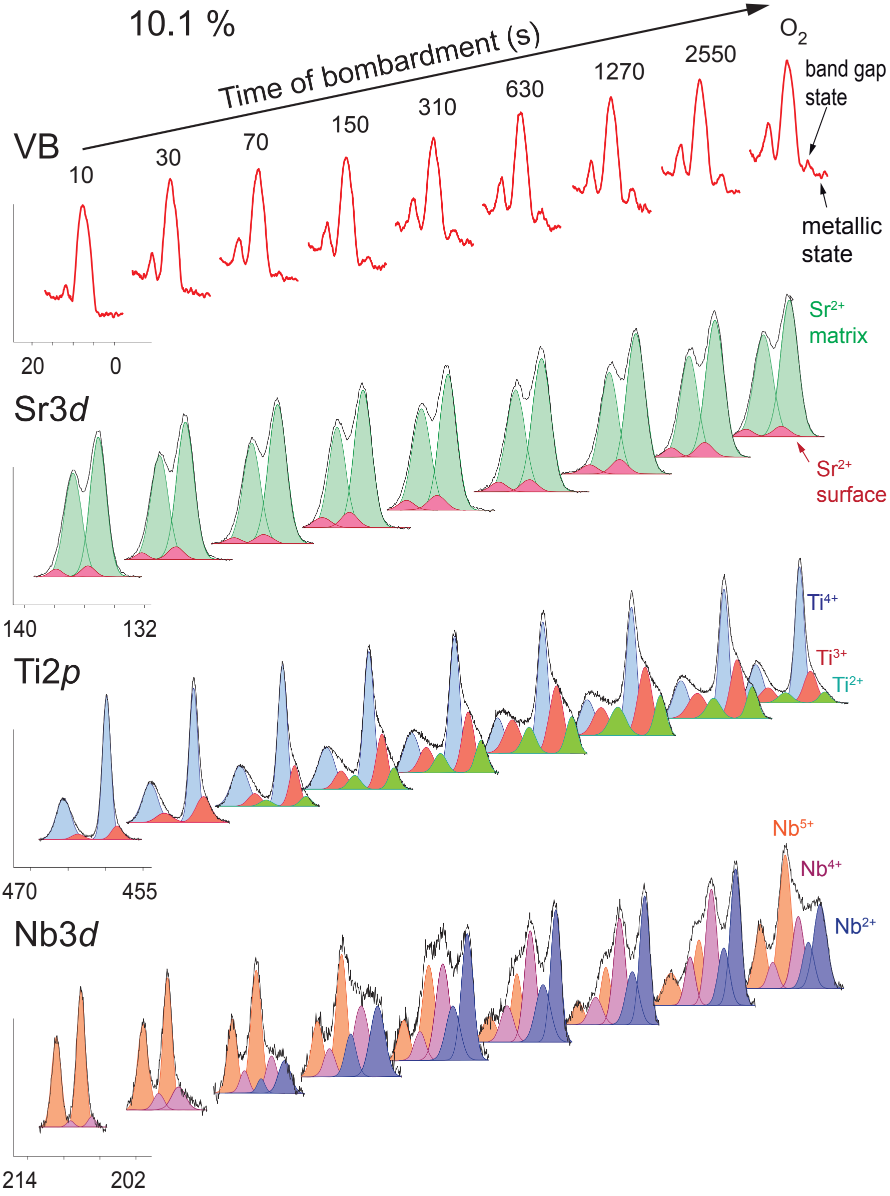

Figure 4.32.: Influence of Ar$^+$ bombardment on the electronic structure investigated by XPS (SrTiO$_3$+10.1 % Nb).

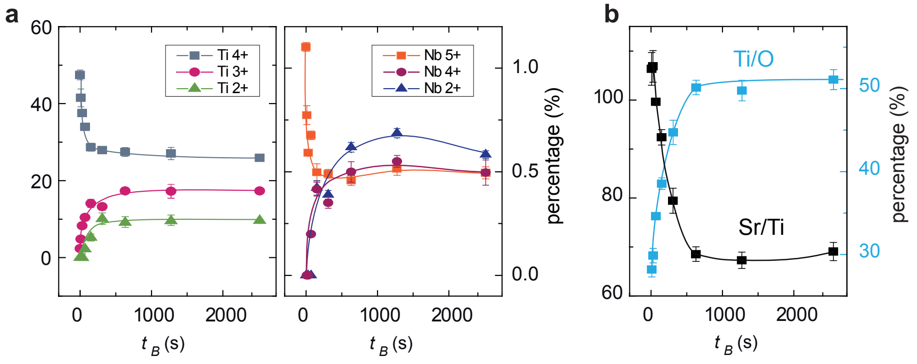

Figure 4.33.: Analysis of the valences of Ti and Nb (a) and of the chemical composition (b) as function of bombardment time extracted from the XPS measurement of the crystal doped with 1.4 % Nb shown in Fig. 4.31.
Adapted from Rodenbücher *et al.* [RWWS13].

could still be detected. The Sr/Ti ratio increased from 0.69 to 0.74 while the Ti/O ratio decreased from 0.51 to 0.39 upon re-oxidation. This shows that the insulator-to-metal transition was partially reversed but due to the huge changes of the chemical composition of the surface layer upon bombardment, the original stoichiometric $SrTiO_3$ surface could not be recovered.

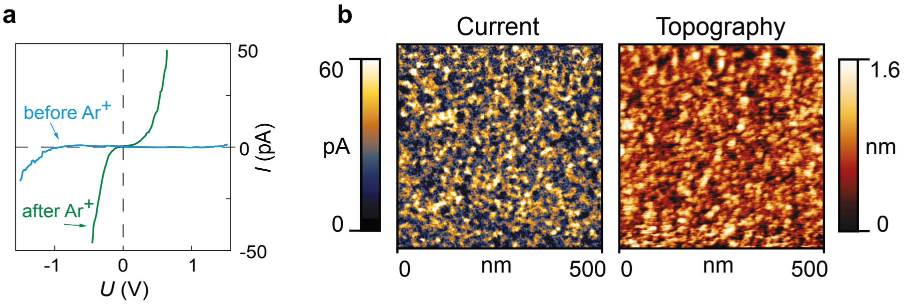

Figure 4.34.: LC-AFM investigation of the bombarded surface. (a) Local IV curves. (b) Maps of conductivity and topography. ($SrTiO_3$+1.4 % Nb).
Adapted from Rodenbücher *et al.* [RWWS13].

In order to gain an insight in the nature of the insulator-to-metal transition on the nanoscale, the conductivity and the topography after the bombardment was investigated *in situ* by LC-AFM. At first, local IV curves were measured using the Pt/Ir-coated AFM tip as top electrode. As shown in Fig. 4.34a, the as-received sample showed a flat IV curve typical of a highly insulating sample. The IV curve recorded after 30 min of bombardment in a good conducting spot of the surface revealed a distinct lower resistance with a semiconducting characteristic. While the topography remained rather flat and unstructured during bombardment with a slight increase in the RMS roughness parameter from 1.16 Å to 1.92 Å, the corresponding map of the conductivity presented in Fig. 4.34b was inhomogeneous and revealed an irregular cluster-like structure. This indicates that the insulator-to-metal transition was spatially inhomogeneous, which could be explained by the evolution of small Ti-rich phases where the transition already started whereas other parts of the surface layer remained insulating. This assumption was supported by LEED investigations showing a cubic 1 x 1 pattern for the as-received surface layer (cf. Fig. 4.21), which was not detectable following bombardment due to amorphization.

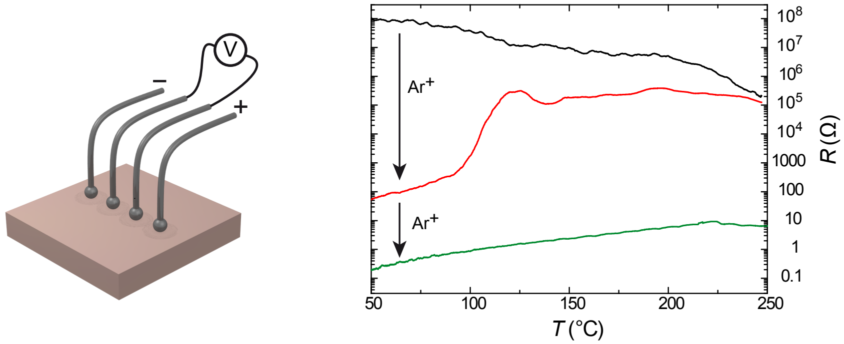

Figure 4.35.: Investigation of the resistance of the surface layer before and after ion bombardment using retractable probes aligned in four-point geometry ($SrTiO_3$+1.4 % Nb). Adapted from Rodenbücher *et al.* [RWWS13].

Having seen that Ar^+ bombardment induces an insulator-to-metal transition on the basis of investigations of the electronic structure, the changes in the electronic transport on the macroscale are focused in the following. In order to measure the macroscopic resistance of the surface layer after bombardment, a dedicated set-up with retractable probes in four-point geometry that could be lowered onto the crystal surface after bombardment *in situ* was developed (for details see Appendix A). This set-up was equipped with a heatable sample holder allowing the investigation of the temperature dependence of the resistance between room temperature and 250 °C.

In Fig. 4.35, an illustration of the arrangement of the retractable probes and measure-

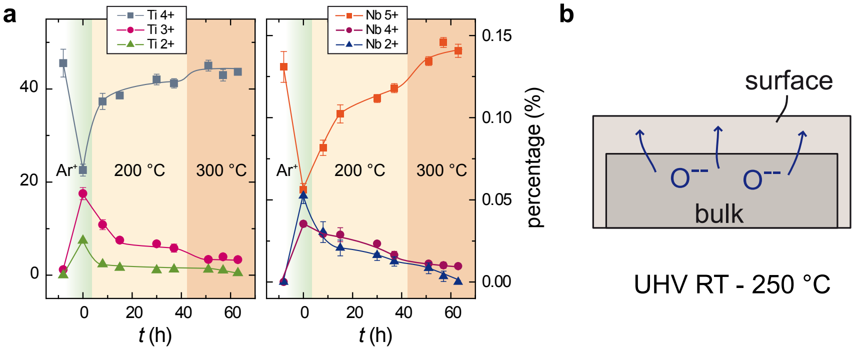

Figure 4.36.: (a) Amount of Ti and Nb valences upon ion bombardment and subsequent heating under UHV conditions ($SrTiO_3$+1.4 % Nb). (b) Model for the thermally induced re-oxidation with the bulk serving as an oxygen source for the surface layer. Adapted from Rodenbücher *et al.* [RWWS13].

ments of the resistance at the as-received and bombarded surface of the crystal doped with 1.4 % Nb are shown. It can be seen that the as-received surface (black curve) was semiconducting with a high resistance decreasing as function of temperature. After ion bombardment by using the same ion gun as used during the XPS and LC-AFM measurement for 30 min (red curve), the initial resistance dropped more than six orders of magnitude to values below 100 Ω reflecting the insulator-to-metal transition. Upon measuring the temperature dependence of the resistance, the resistance increased exponentially and then jumped to values of more than 10^5 Ω around 100 °C. At even higher temperatures, the value of the resistance returned almost completely to the semiconducting state. In the last step, the surface was bombarded by Ar^+ ions using a high-power ion gun operating with a beam current of 5 mA. After this treatment, a very low resistance state below 1 Ω was found (green curve). Up to 220 °C the resistance increased indicating metallic behaviour but at higher temperatures a slight decrease was observed. These measurements revealed that the insulator-to-metal transition of the surface layer upon bombardment is related to the evolution of an inhomogeneous surface layer having an different average resistance depending on the intensity of the bombardment.

Since after intermediate bombardment, a resistance state was found with low resistance at room temperature but showing a rapid increase in the resistance at elevated temperatures, the processes during heating of the bombarded surfaces were further investigated by means of XPS measurements. As presented in Fig. 4.36a, the amount of Ti and Nb valences obtained by peak fitting of Ti2*p* and Nb3*d* core-line spectra was monitored as function of time and temperature. An as-received crystal was at first bombarded by Ar^+ ions and then it was heated in two steps to 200 °C and 300 °C, while the electronic structure was measured. In agreement with the measurements discussed above, a valence change of Ti and Nb to lower valences took place during the bombardment. After the subsequent heating however, the amount of additional valences was reduced again revealing an inversion of the transformation. This behaviour is very similar to the changes in the electronic structure upon re-oxidation, which indicates that also heating the bombarded surface layer under UHV conditions leads to oxidation processes. In this case, the bulk of the crystal has to be regarded as the source of oxygen for the bulk as illustrated in Fig. 4.36b. Similar effects have already been found during the self-neutralization during photoemission experiments, in which the movement of oxygen along dislocations as easy diffusion paths was assumed to play an important role [SPP+09]. Hence, this explanation could also be a potential model for the observed increase in the resistance upon heating of bombarded surfaces.

4.6.2. Atom probe measurements

As a second method to investigate the effects of ion bombardment, 3D atom probe measurements were conducted. This technique allows monitoring the positions of the atoms inside a small needle by making use of the field evaporation effect. Using a time-of-flight detector, the mass and the origin of the evaporated atoms can be determined and thus, a three-dimensional map of the atom distribution can be calculated. Since at first, a small needle has to be fabricated out of the material under investigation by focused ion beam technique, the 3D atom probe is well suited to gain an insight into the influence of

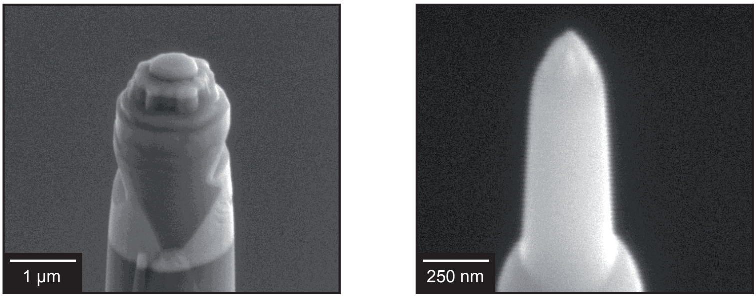

Figure 4.37.: SEM-images of the needle ($SrTiO_3$+1.4 % Nb) cut by focused ion beam for atom probe measurements during (left) and after (right) preparation.

ion bombardment on the nanoscale. In Fig. 4.37, images obtained by a scanning electron microscope (SEM) of the needle that was cut by focused ion beam are presented. In a first preparation step, a structured pillar was created that was then further thinned out until a sharp tip with a shape acceptable for atom probe measurements was obtained.

The ions of the tip were removed from the tip consecutively using field evaporation assisted by a laser (300 pJ). A dataset of about three millions of ions was recorded with a detection rate of 0.5 %. In order to obtain a measurement with sufficient data quality, the preparation and investigation of more than 25 needles was necessary [Bre13]. The measured mass spectra showed well defined peaks that were attributed to different ions and thus a mapping of the element distribution inside the needle was calculated. In Fig. 4.38, illustrations of the distribution of O, Ti, TiO, Sr and NbO_2 in the first 140 nm of the needle are presented. It can be seen that in the deeper parts of the needle, a

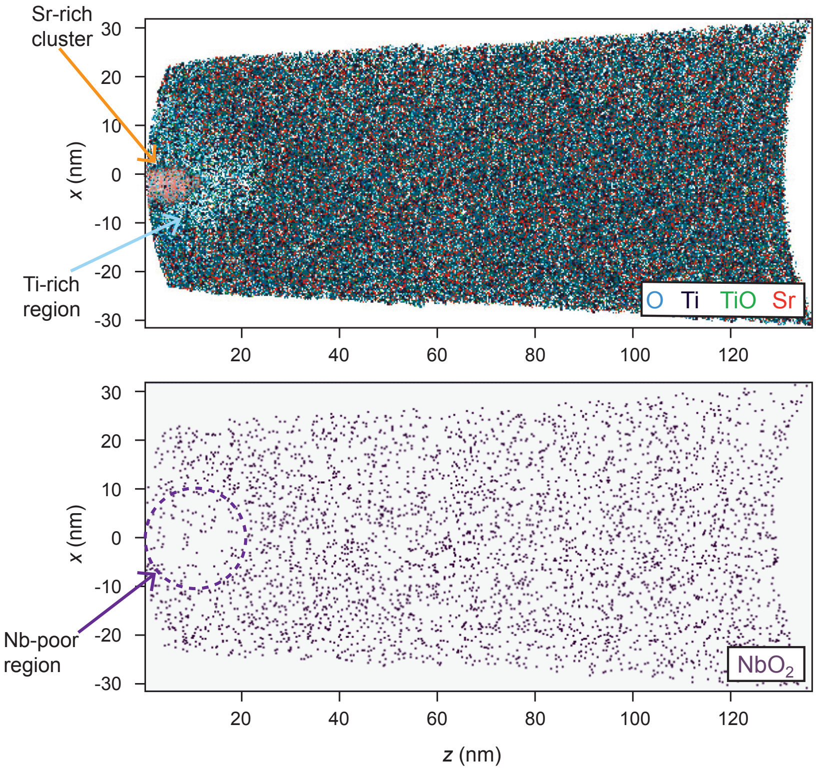

Figure 4.38.: Illustration of the element distribution obtained by atom probe ($SrTiO_3$+1.4 % Nb). Adapted from Rodenbücher *et al.* [RSB+13].

homogeneous distribution of the elements was present. In particular, in the distribution of NbO_2, no clear evidence for Nb segregation effects on the nanoscale could be found. On the top of the needle however, distinct segregation effects were recorded. In direct vicinity to the end of the tip, an Sr-rich cluster with a size about 10 nm was present while in the surrounding regions, the Sr content was decreased. This shows that during the preparation by focused ion beam, ionic movements were induced leading to distinct changes of the local stoichiometry. Corresponding to the region of Sr depletion that can be seen in the upper map of Fig. 4.38, also hints for an Nb depletion can be identified in this region. This reveals that the application of external gradients on $SrTiO_3$:Nb single crystals can strongly change the properties of the surface layer by inducing ionic movements leading to local phase separations.

4.7. Surface potential

Since Nb-doped $SrTiO_3$ is commonly used as prototypical conducting oxide substrate for the deposition of functional thin films, the homogeneity of the surface potential on the nanoscale is of high technological interest. As shown in the Sec. 4.4, Nb segregation effects were found in the Verneuil grown crystals that also influence the electrical properties of the crystal surface. In order to obtain an insight in the spatial distribution of the surface potential on the nanoscale, scanning Kelvin probe microscopy (SKPM) is used. In the following, at first the working principle of this technique and at second the results on $SrTiO_3$:Nb are presented.

4.7.1. Demonstration of the SKPM technique

As described in Sec. 3.2.7, SKPM is a scanning probe technique with the ability to measure the topography and the contact potential difference (CDP) between the AFM-tip and the surface simultaneously [NOW91]. Therefore, the AFM is operated in non-contact mode with the tip vibrating at its resonance frequency. Additionally, a AC and DC voltage V is applied between tip and sample to modulate the electrostatic Maxwell force [HHL$^+$96]. In this case, the electrostatic force F_e can be expressed as

$$
\begin{aligned}
F_e \quad &= \quad \frac{1}{2}\left(\left(V_{dc}-\frac{\Delta\Phi}{q}\right)^2+\frac{1}{2}V_{ac^2}\right)C' \qquad &(4.1)\\
&+ C'\left(V_{dc}-\frac{\Delta\Phi}{q}\right)V_{ac}\sin\left(\omega t\right) \qquad &(4.2)\\
&+ \frac{1}{4}C'\;V_{ac}\cos\left(2\omega t\right). \qquad &(4.3)
\end{aligned}
$$

$\Delta\Phi$ is the difference of the work functions of tip and sample, C is the capacity, ω is the frequency of the modulation voltage and t is the time. Since the second summand (4.2) is proportional to the modulation frequency ω, it can be evaluated using lock-in technique. The contact potential difference is then obtained by adjusting the DC voltage V_{dc} via a feedback-loop until it is equal to $\Delta\Phi$ thus minimizing this component of the electrostatic force.

Region	Resistivity ρ [Ωm]	Permittivity ε_r
Electrode	$4 \cdot 10^{-7}$	$1 \cdot 10^{7}$
Substrate	$1 \cdot 10^{-7}$	$1 \cdot 10^{7}$
$SrTiO_3$ layer	$1 \cdot 10^{11}$	200
Vacuum	$1 \cdot 10^{20}$	1
Tip	$1 \cdot 10^{-7}$	$1 \cdot 10^{7}$

Table 4.3.: Parameters used for the FEM simulation of the situation during SKPM measurement shown in Fig. 4.39. The high values of the permittivity of the metal were chosen to model the theoretically infinite permittivity numerically.

To illustrate the measurement of the potential difference by SKPM, the distribution of the potential of a test sample was modelled by the finite element method (FEM). As depicted in Fig. 4.39a, it was assumed that a metal electrode was deposited on an $SrTiO_3$ layer on top of a grounded substrate. The electrode was modelled to be on a fixed potential of 1 V. Using the ANSYS program, the potential distribution was then calculated for two situations using the parameters listed in Table 4.3. In the first one, only the distribution generated by electrode and substrate was modelled and in a second simulation, the influence of a conducting AFM-tip measuring the contact potential difference via the SKPM method was taken into account.

The calculated distribution of the potential shown in Fig. 4.39b revealed the bending of the equipotential lines close to the edge of the electrode and the propagation into the vacuum region. Inside the electrode and the grounded substrate, the potential was constant since these regions were modelled to be metallic by fixing the permittivity to a very high value. When measuring the potential distribution of this edge by SKPM, the introduction of the tip would also influence the shape of the potential lines as illustrated in Fig. 4.39c. Owing to the metallicity of the tip, an additional bending of the equipotential lines would occur around the tip. Hence, one should be aware that the SKPM measurements close to sharp structures may not necessarily reflect the true shape of the potential drop but may

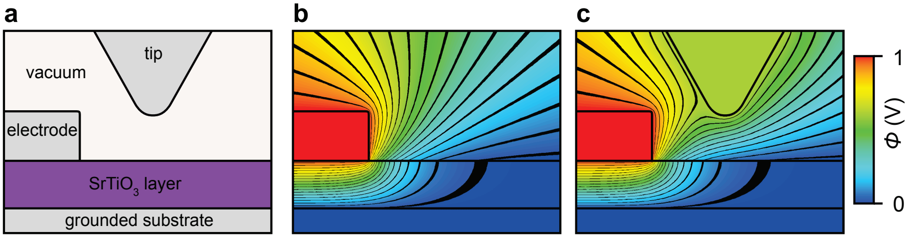

Figure 4.39.: FEM simulation of the situation during SKPM measurement. (a) Outline of the modelled system. (b) Potential distribution without and (c) with tip.

also depend on the size and the shape of the tip itself. In order to minimize the distortion of the potential in the vicinity of steps and edges, very sharp AFM tips of n-doped silicon especially designed for non-contact mode with an apex radius of less than 2 nm were used in the studies presented here.

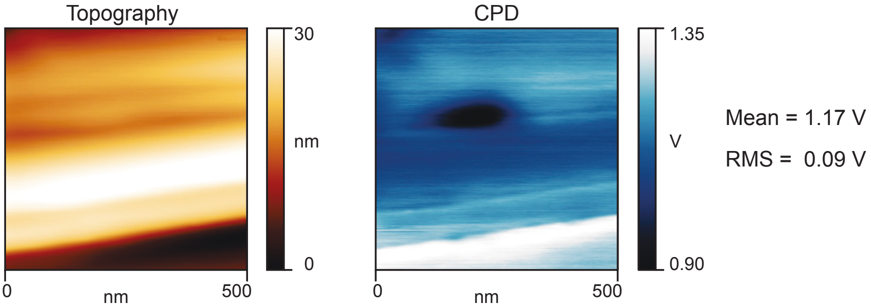

Figure 4.40.: Topography and CPD measurements of a highly oriented pyrolytic graphite (HOPG) reference sample obtained using a n-doped silicon SKPM tip.

In order to estimate the work function of the conducting n-doped silicon SKPM tip, which is needed for the calculation of absolute value of the surface potential, highly oriented pyrolytic graphite (HOPG) was used as a reference sample. In Fig. 4.40, a representative SKPM measurement of the topography and the contact potential difference (CPD) is shown. The mean value of the measurement was $\Delta\Phi/e = 1.17$ V. Using the literature value of the work function of HOPG $\Phi_{HOPG} = 4.6$ eV [MTO$^+$88], the work function of the tip was estimated:

$$\Phi_t = \Delta\Phi + \Phi_{HOPG} = 5.77 \text{ eV} \tag{4.4}$$

To demonstrate the performance of the SKPM method, two different test samples were inspected. Using a lithography process, Pt electrodes with a thickness in the nanometre

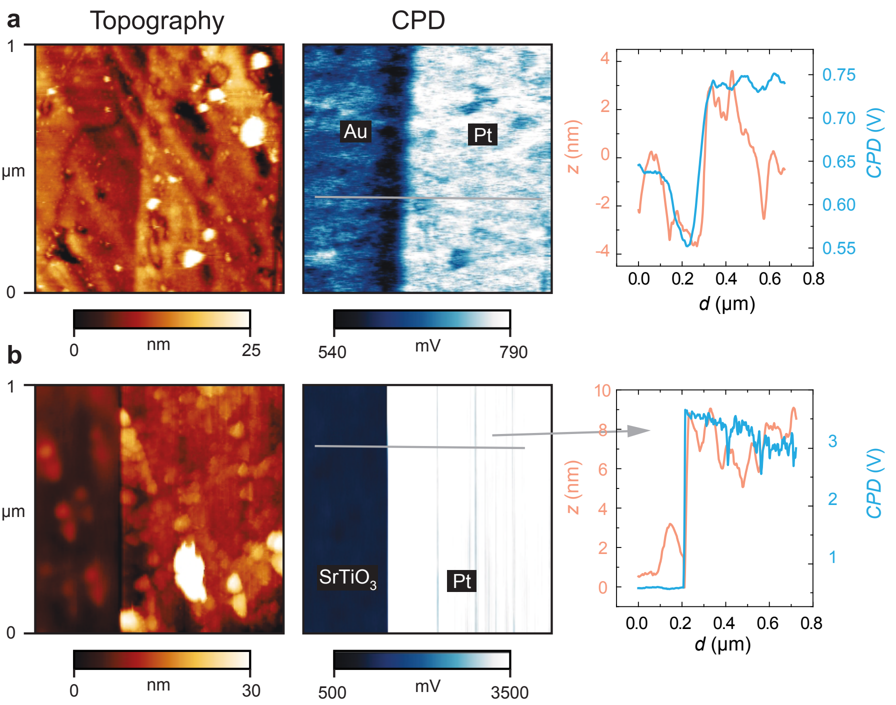

Figure 4.41.: Topography and CPD measurements of two test samples obtained by SKPM. (a) Au-Pt and (b) $SrTiO_3$-Pt.

range were deposited on Au and $SrTiO_3$ substrates. Under UHV conditions, the topography and contact potential difference was then recorded by SKPM, which was operated using an AC modulation voltage of $V_{ac} = 2$ V with a frequency of $f = 500$ Hz. In both cases, the edge of the electrode was clearly identifiable in the topography as well as in the CPD map as can be seen in Fig. 4.41. With regard to the Au-Pt structure, the contrast between the two materials in the topography map was not that pronounced due to the small thickness of the Pt electrode but in the CPD map, a clear contrast was present illustrating the advantages of the SKPM technique. In the region close to the edge of the electrode, a dip in topography and CPD map can be seen that could be related to segregation effects during sample preparation. The $SrTiO_3$-Pt sample instead revealed a sharp edge without segregation effects and a huge difference of the CPD signals.

Comparing the CPD values that were extracted from the measurements in Fig. 4.41 by averaging the value in the substrate region and the Pt region with literature data

[HL12, Göm05] as shown in Table 4.4 it can be seen that the literature values were not reproduced exactly but that the average trend was correct. However, it can be seen that the CPD value measured in the Pt region of both samples was significantly different although the same type of AFM tip was used and thus a comparable CPD value would be expected. This shows that the measured absolute CPD did not reflect the precise difference of the work functions of the materials, which indicates that the potential on the surface differed from that of the pure material. This difference could be explained by the fact that the interaction with gases from the atmosphere, which took place before the sample was transferred into the UHV chamber, induced the creation of an adsorbate layer on top of the surfaces. Particularly, Pt is well known to bind oxygen or hydrogen on the surface making it an excellent catalyst material. Since the samples were not annealed under vacuum conditions before measurement due to technical limitations, an adsorbate layer was still present on the surface influencing the measurement of the contact potential difference. Furthermore, the existence of electronic surface states could significantly influence the measurement of the CPD by forming a Bardeen barrier between AFM tip and surface layer due to pinning of the Fermi level.

4.7.2. Inhomogeneities in surface potential

Having seen that the SKPM method is well suited for the investigation of local variations of the surface potential, the surfaces of the Nb-doped $SrTiO_3$ single crystals were analysed. As shown in Fig. 4.42, topography and CPD were recorded (UHV, $V_{ac} = 2$ V, $f = 500$ Hz) on the nanometre scale on all three crystals with the doping concentrations 0.2 at%, 1.4 at% and 10.1 at%. While the investigation of the topography revealed a rather flat and unstructured surface, particularly for the crystal doped with 0.2 at% and 1.4 at%, in the CPD maps distinct inhomogeneities on the nanoscale related to the presence of clusters with a size of 20-80 nm showing different CPD contrast can be seen.

As a measure of the inhomogeneity of the surface and the surface potential, the root

Substrate	Pt thickness (nm)	CPD_{lit} (V)	CPD_{exp} (V)
Au	2	-0.17	-0.10 ± 0.02
$SrTiO_3$	10	-1.84	-2.70 ± 0.20

Table 4.4.: Nominal electrode thickness and comparison of the literature and measured CPD of the two test samples shown in Fig. 4.41.

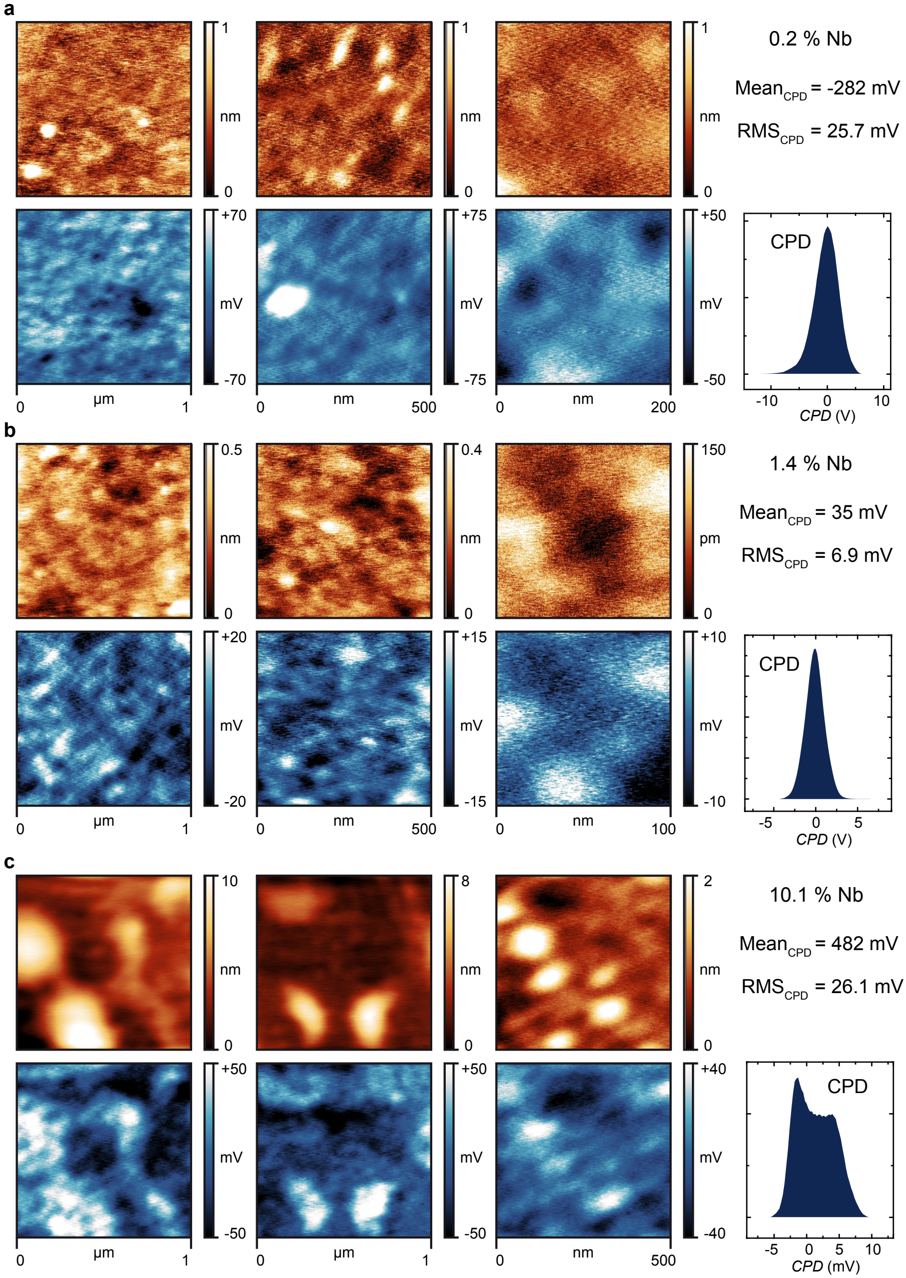

Figure 4.42.: Topography (red) and CPD (blue) maps of SrTiO$_3$:Nb crystals with different doping concentration. On the right, the corresponding CPD histograms are shown. The mean value of the measured CPD was defined as zero in order to emphasize the local variations.

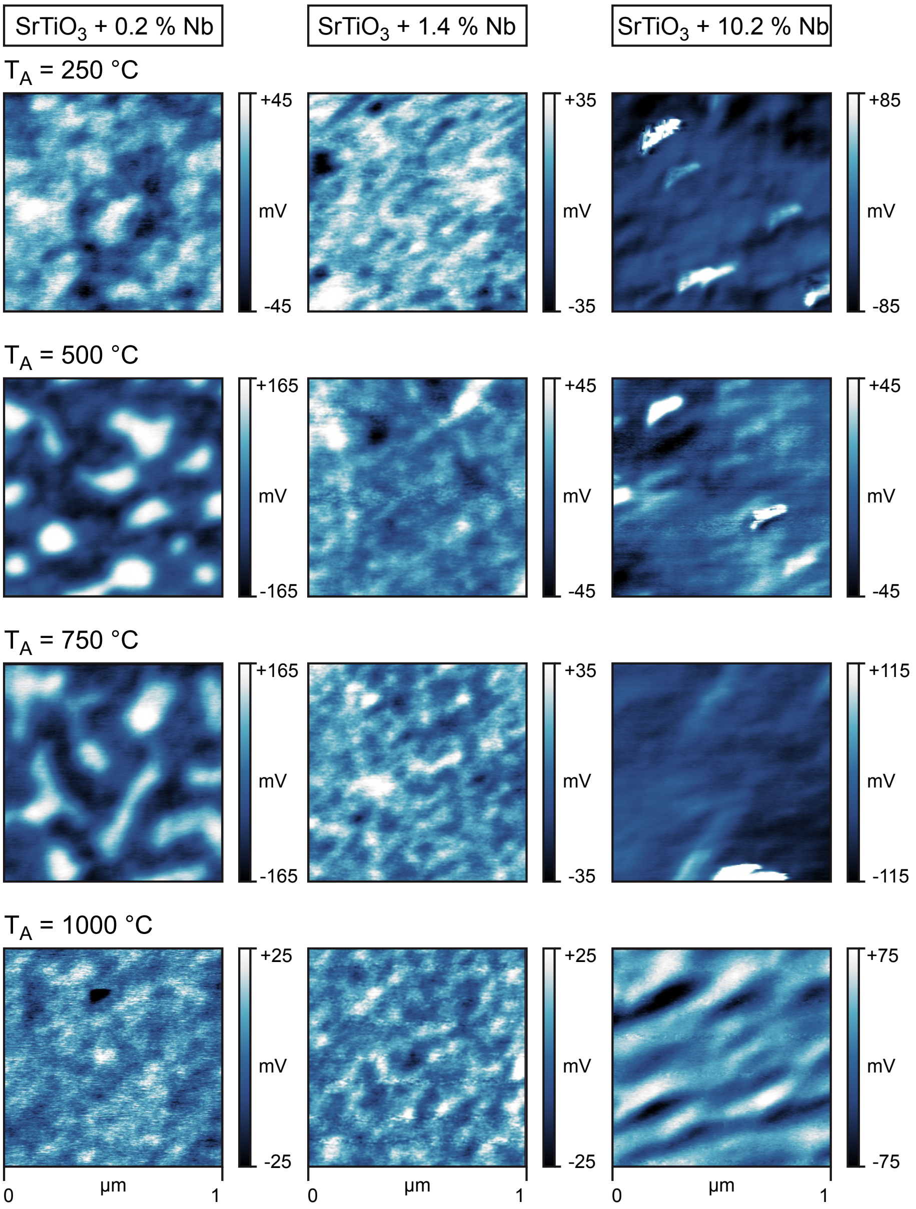

Figure 4.43.: CPD measurements of $SrTiO_3$:Nb crystals after annealing at different temperatures under UHV conditions. The mean value of the measured CPD was defined as zero in order to emphasize the local variations.

mean square (RMS) value of topography and CPD was calculated (Table 4.5). Comparing the three different crystals, the flat surface of the two lowest doped samples is also reflected by the RMS value, while the value of the highest doped crystal is above 10 nm indicating that it was not possible to obtain an atomically flat surface by the polishing procedure due to intrinsic inhomogeneities. The RMS value of the CPD maps is rather small for the crystal doped with 1.4 at% Nb but is increased to values above 20 µV for the 0.2 at% and 10.1 at% sample. Since these measurements revealed once again that the quality of the crystal doped with 1.4 at% was the highest, the major measurements of the resistive switching phenomena were conducted on this crystal. The inhomogeneous structure of the surface potential indicates the presence of segregation effects and could be related to Nb inhomogeneities as discussed in Sec. 4.4. Another explanation for the presence of the inhomogeneous surface potential could be a coverage of the surface with adsorbates, such as hydroxides or carbonates which is always present after the interaction with gases from atmosphere. The absolute CPD value showed distinct differences between the different measurements. For the lowest doped sample, the CPD mean value was negative (-282 mV), while it was positive for the sample doped with 1.4 % Nb (35 mV) and 482 % Nb (35 mV). Assuming a work function of 5.77 eV for the tip according to Eq. 4.4, the work function of the Nb-doped $SrTiO_3$ crystals would be in all cases higher than 5 eV, which is much higher than typical literature values. This indicates that the measurement of the CPD was influenced by additional parameters such as a contamination of the tip by adsorbates. Hence, the absolute value measured by the SKPM method in this thesis were not that significant as the relative measurement of the spatial fluctuations of the surface potential shown in the CPD maps.

4.7.3. Influence of annealing on the surface potential

In order to investigate how the surface potential is influenced by thermal treatment, SKPM measurements were performed after annealing the crystals under UHV conditions. After

Nb concentration (at%)	Topography RMS (Å)	CPD RMS (µV)
0.2	1.61 ± 0.68	25.7 ± 3.1
1.4	0.86 ± 0.23	6.9 ± 1.8
10.1	13.10 ± 7.67	26.1 ± 2.6

Table 4.5.: Roughness parameter of the CPD measurement shown in Fig. 4.42.

every one-hour temperature step, the sample was cooled down to room temperature and measured *in situ*. As shown in Fig. 4.43, the measurements of all samples revealed a comparable inhomogeneous cluster-like structure with fluctuations of several tens of mV. Since this structure was still present even after annealing under reducing conditions, it can be concluded that the inhomogeneities were more related to intrinsic segregation effects than to adsorbates.

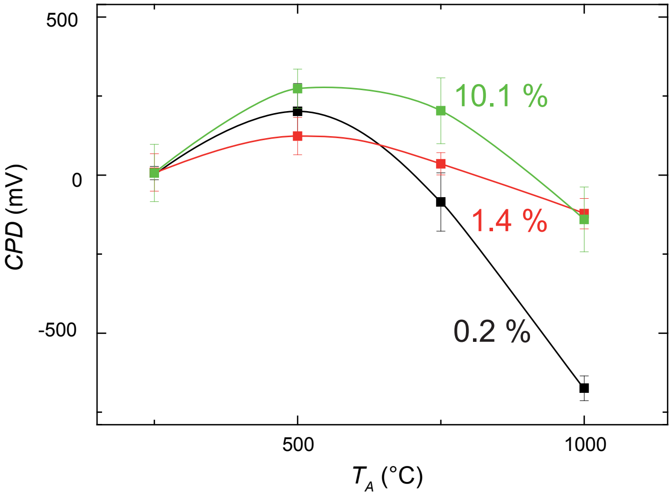

Figure 4.44.: Dependence of the relative CPD on the annealing temperature as extracted from Fig. 4.43. The CPD value measured on the as-received crystals was defined as zero.

In Fig. 4.44, the dependence of the average CPD on the annealing temperature T_A is shown. To generate this graph, the relative CPD maps of Fig. 4.43 were averaged and plotted as function of the temperature. All three crystals revealed a comparable trend. It can be seen that at first the CPD increased slightly but between 750 °C and 1000 °C a distinct drop in the potential difference occurred, which could be related on the one hand to the desorption of chemisorbed molecules such as carbonates or to a modification of the top of the surface layer by a loss of oxygen due to the presence of extremely reducing conditions according to the XPS analysis of the chemical composition during annealing (cf. Sec. 4.5.5).

After the sample was annealed at 1000 °C, it was investigated how the exposure to different gases change the surface potential. Therefore, the sample was exposed to different gases at a pressure of about $2 \cdot 10^{-8}$ mbar and the temporal change of the contact potential difference was measured by continuously performing SKPM scans of the same area. The obtained SKPM maps were averaged line-wise and the relative contact potential was plotted as function of the dose by taking into account the partial pressure of the gases and the scan velocity as shown in Fig. 4.45.

It can be seen that the exposure to oxygen changed the surface potential significantly. At first, a slight increase in the contact potential difference was observed up to 0.1 L that can be related to a physisorption of the oxygen molecules. Up to 1 L, a distinct increase in the contact potential difference occurred indicating the maximum acceleration of the reaction until full coverage of the surface was obtained. After the exposure, the sample was annealed in UHV conditions again at 1000 °C for 10 minutes and the original CPD value was recovered indicating that the interaction with oxygen is a reversible process. In contrast to the exposure to oxygen, the exposure to other gases such as CO_2, a mixture of 4 % H_2 in Ar and pure H_2 did not have such a big influence on the surface potential. Only after the exposure of higher doses of 10-100 L, a slow increase in the CPD was observed, which could be related to the contamination of the used gases with oxygen. The very sensitive reaction of the $SrTiO_3$:Nb surface with oxygen indicates that there is a strong influence of the oxygen content of the surface on the electronic properties, which is also highly relevant for the understanding of the transport phenomena.

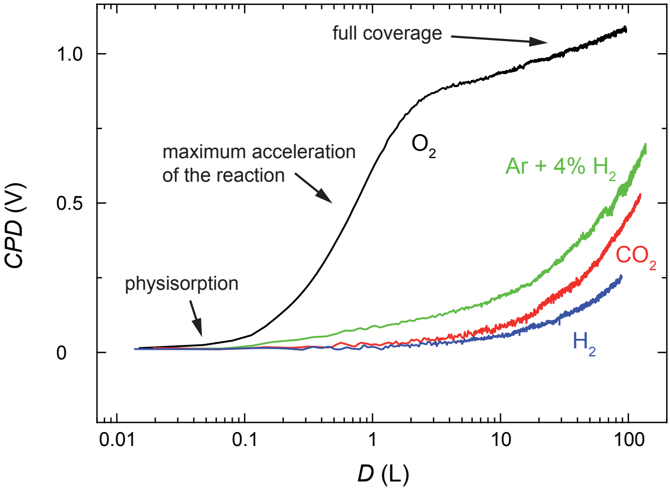

Figure 4.45.: Change of the CPD upon exposure to different gases. The CPD value measured on the as-received crystals was defined as zero.

4.8. Electronic transport phenomena of the surface layer

To understand the fundamental processes of electronic transport that are relevant when using $SrTiO_3$:Nb as functional oxide in a resistive switching device, the knowledge of the distribution of conducting paths on the nanoscale is highly important. For this purpose, local-conductivity atomic force microscopy (LC-AFM) is the method of choice since it offers the opportunity to investigate the topography and the conductivity by using a conducting Pt-Ir-coated tip in contact mode with highest spatial resolution due to the confined potential drop below the contact area of the tip (cf. Sec. 3.2.7) [WSW11]. Using this technique, the three crystals with different Nb concentrations were investigated at room temperature with respect to the influence of *in situ* annealing under reducing conditions.

4.8.1. Influence of annealing under reducing conditions

The crystals were measured after heating under UHV conditions at the annealing temperatures T_A of 250 °C, 500 °C, 750 °C, 1000 °C for one hour in each case. Below an annealing temperature of 500 °C, the surfaces of the crystals were found to be still highly insulating and no conductivity could be recorded.

$SrTiO_3$+0.2 at% Nb

In Fig. 4.46, the results obtained on the $SrTiO_3$ crystal doped with 0.2 at% Nb are presented starting from an annealing temperature of 500 °C. In the left panels, the topography map and in the center, the current map recorded simultaneously while applying a small voltage of 10 mV are shown. In the right panels, additionally magnified current maps are presented facilitating the identification of conducting paths. After annealing at 500 °C, the topography map revealed a striped pattern of frayed steps with a width of 100-150 nm. This striped pattern can also be seen in the current map, in which the conductivity close to the edges of the steps was decreased compared to the average of the map. On top of the steps, the conductivity revealed an inhomogeneous distribution, which was related to a cluster-like structure as can be seen in the magnification on the right of Fig. 4.46. The conducting clusters had a diameter of 10-20 nm and a significantly higher conductivity than the surrounding material. After the next heating step at 750 °C, the step-like structure of the surface was still detectable but was not as pronounced and regular as in the previous measurement. The distribution of the conductivity was more inhomogeneous with some clusters showing a conductivity, which was higher by a factor of 50 than the

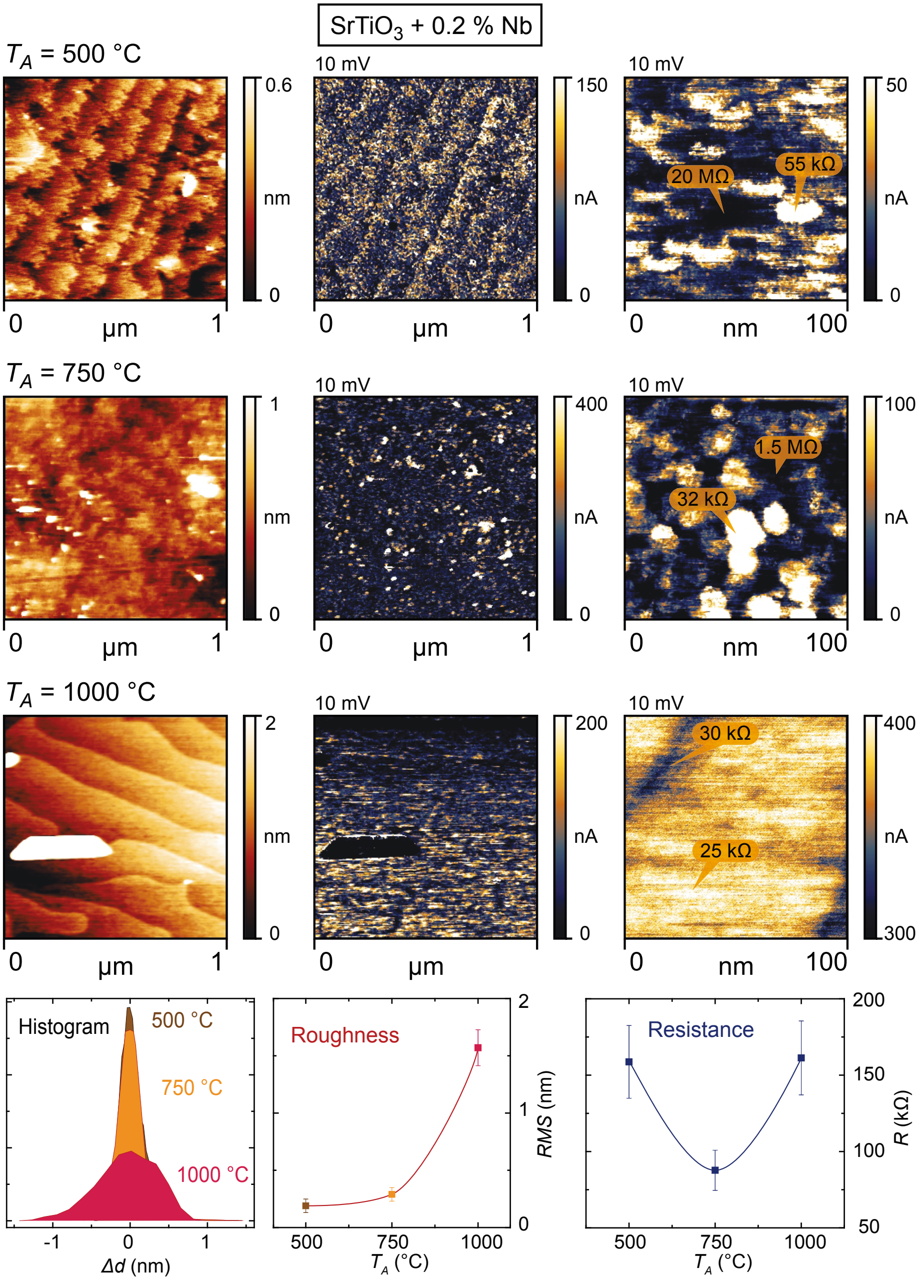

Figure 4.46.: Topography and local conductivity measured after annealing the crystal at different temperatures ($SrTiO_3$+0.2 % Nb). In the bottom row, a histogram of the height distribution, the measured roughness and the local resistance extracted from the LC-AFM measurements are shown.

rest.

During the last annealing step at 1000 °C, the most obvious changes of the surface occurred. The topography showed a rather flat terrace structure with well-defined atomic steps running in a curved shape. Besides this structure, occasionally some nano-crystallites with a height of 15-20 nm were detected. The distribution of the conductivity as can be seen in the current map was still inhomogeneous but the differences between conducting and non-conducting regions of the step-like structure were significantly smaller. In contrary, the newly evolved crystallites did not show a measurable conductivity indicating that they consisted of insulating material such as Sr-rich phases. In the magnification of the current obtained in a highly conducting region, an almost homogeneous conductivity can be seen. In particular, all regions of the scanned area were found to be conducting with a variation of about 30 % indicating that a homogenization of the surface layer took place during annealing. The fundamental transformation of the surface can also be seen by regarding the RMS roughness values extracted from histograms of the height distribution of the 1 x 1 µm AFM scans. While at 500 °C and 750 °C, a rather small roughness related to a sharp height distribution was found, the formation of the terrace structure with additional crystallites led to a broadening of the height distribution and an increase in the roughness. Despite the huge changes of the morphology, the average local resistance extracted from the current maps did not show a significant change with the annealing temperature showing that the conduction mechanism was unchanged.

$SrTiO_3$+1.4 at% Nb

In Fig. 4.47 the corresponding measurement on the crystal doped with 1.4 at% Nb is presented. After annealing at 500 °C, the surface remained flat and unstructured and did not show any terrace-like structure. The conductivity was much lower than that of the crystal doped with 1.4 at%, but the in-plane distribution of the conducting areas showed a comparable inhomogeneous cluster-like structure. However, a higher voltage had to be applied to the AFM-tip in order to record the magnified current map due to the high surface resistance. Also after the next annealing step at 750 °C, the behaviour had not changed significantly. The mapping of the topography revealed again an unstructured surface and the distribution of the conducting cluster in the similar in the current map although the average conductivity was increased compared to the measurement after annealing at 500 °C.

After the annealing at 1000 °C, the surface structure had changed from an unstructured surface to a terrace-like structure. In contrast to the lower doped crystal, this structure was not that regular and showed larger corrugations with step heights of 2-3 nm. Between

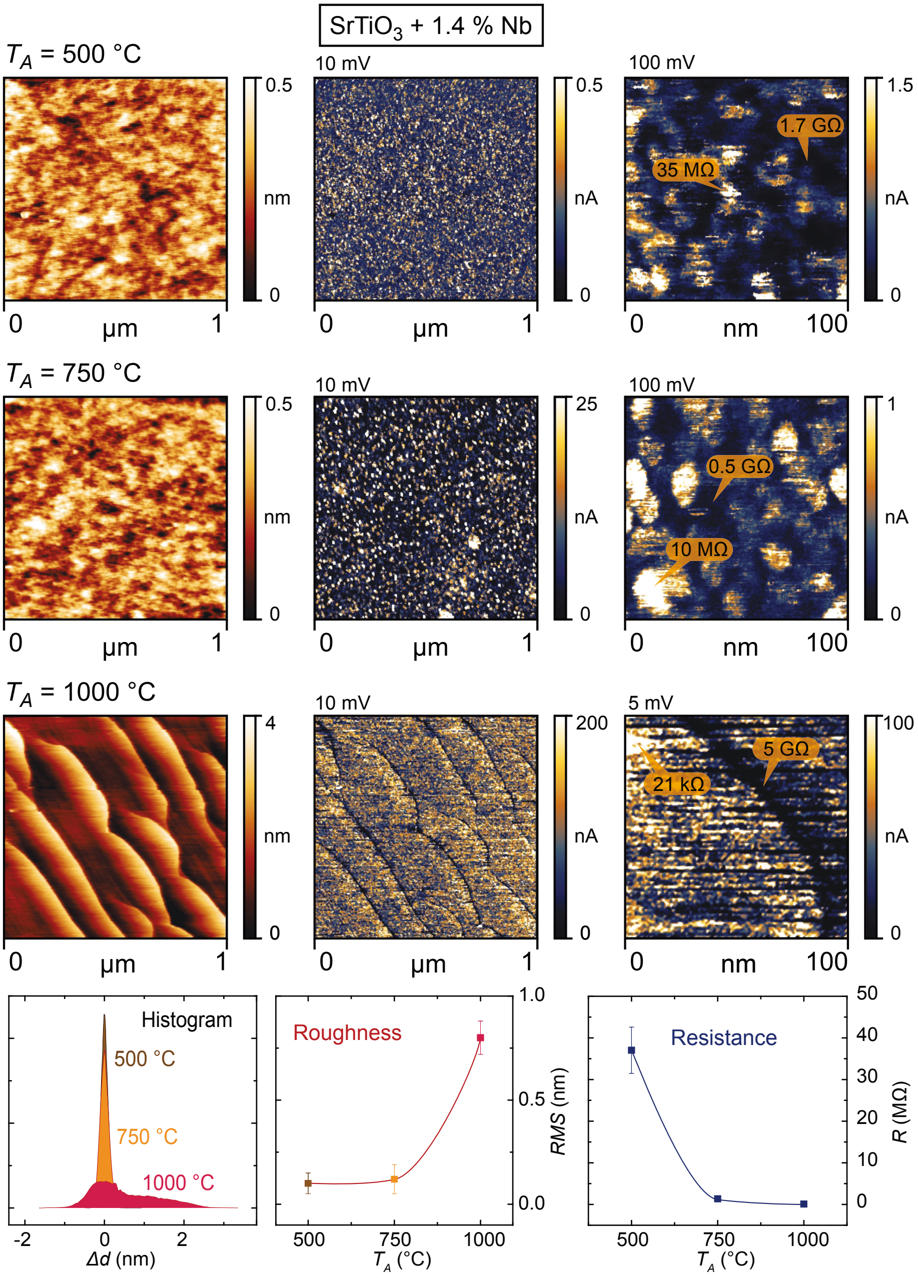

Figure 4.47.: Topography and local conductivity measured after annealing the crystal at different temperatures ($SrTiO_3$+1.4 % Nb).In the bottom row, a histogram of the height distribution, the measured roughness and the local resistance extracted from the LC-AFM measurements are shown.

these larger structures, an additional rippled pattern with atomic step heights was present. The conductivity was increased and more homogeneous but showed minima close to the steps of the larger structures, which becomes more obvious in the magnification of the current map, in which the edge was positioned in the centre of the scan.

The distinct change of the surface properties during the annealing step at 1000 °C was illustrated by extracting the average RMS roughness parameter and the local resistance, which are shown as function of the annealing temperature in the bottom row of Fig. 4.47. It can be seen that the roughness remained flat up to 750 °C and then increased overproportionally due to the formation of the high corrugations. The resistance revealed an exponential dependence on the annealing temperature as result of the insulator-to-metal transition of the surface layer. This also correlates with the evolution of metallic states and additional valences of Ti and Nb that were found after annealing under reducing conditions and subsequent cooling to room temperature by the XPS measurements presented in Sec. 4.5.5. After the conductivity of the annealed sample was investigated, it was exposed to 10^6 L O_2, whereupon the surface resistance increased immediately so that the current was below the detection limit of the LC-AFM set-up. This illustrates once again that the contact with oxygen can easily lead to the formation of a highly insulating surface layer on $SrTiO_3$:Nb, which has been discussed in detail in Sec. 4.5.5.

The distinct irreversible change of the morphology of the surface with the evolution of corrugation indicates that during the thermal treatment under reducing conditions considerable ionic movements and re-crystallization processes take place in the surface layer. This is also supported by the XPS results showing that during the reduction the Sr excess of the as-received surface layer is turned into a high Ti-excess. In order to further investigate the transformation of the surface, the crystal, which was first reduced and then re-oxidized, was heated again under UHV conditions to 1000 °C for one hour. After this, the surface revealed the rising of a new structure as shown in the centre of Fig. 4.48. The terrace-like structure, which already evolved during the first heating step, was still detectable but its height was decreased and it was superposed by a cluster-like distortion. This becomes particularly obvious when regarding the corresponding current map in the centre of Fig. 4.48 showing a distinct cluster-like pattern of the conductivity. After this measurement, the sample was once again oxidized and subsequently reduced at 1000 °C, which accomplished the transformation. As presented in the right panels of Fig. 4.48, the terrace-like structure had disappeared and instead a fully cluster-like structure can be seen. In average, the roughness of the surface decreased to a RMS value of 0.17 nm, with a maximum difference between the highest and lowest clusters of about 1 nm. The mapping of the current correlates perfectly to the cluster-like structure of the topography revealing that the conductivity inside the clusters was more than a factor of 2 higher than in the regions between the clusters. The diameter of the clusters was in the range of 30-50 nm, which corresponds to the size of the conducting clusters that were found after low-temperature reduction at 500 °C and 750 °C shown in Fig. 4.47. This could imply that the shape of the clusters was predetermined by structural inhomogeneities in the as-received crystal serving as a template for the evolution of the clusters on the surface, which will be discussed in detail below. The conductivity of the newly evolved cluster-like structure was very high with a maximum local surface resistance below 6 kΩ and IV-curves measured by the LC-AFM showed an ohmic behaviour indicating metallic conductivity. Exposing this surface to oxygen atmosphere did not reduce the conductivity significantly showing that a stable metallic surface layer had evolved during the prolonged preparation. This transformation is probably related to the formation of titanium suboxides as already concluded during the discussion of the XPS measurements shown above.

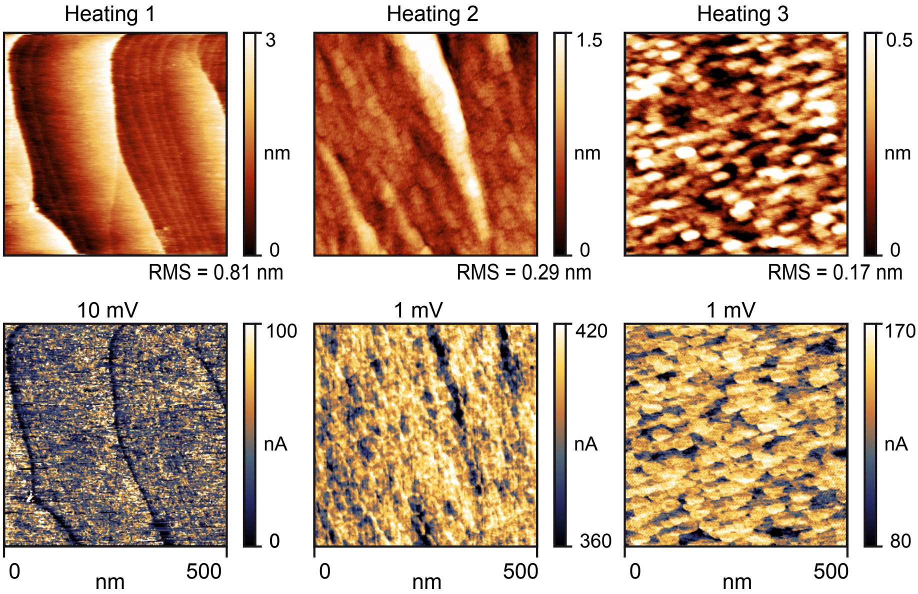

Figure 4.48.: Surface transformation during subsequent annealing and oxidation steps ($SrTiO_3$+1.4 % Nb).

$SrTiO_3$+10.1 at% Nb

In Fig. 4.49, the investigation of the changes of the topography and the local conductivity upon reduction for the highest doped crystal are presented. As already discussed previously, the quality of the crystal and especially of the surface was not as good compared to the lower doped ones. This was also reflected by the measurement of the topography after moderate reduction at 500 °C, which revealed an unstructured and inhomogeneous surface with a RMS roughness parameter of 0.6 nm and maximum differences between the surface features of more than 10 nm. The conductivity was relatively low and even upon the application of a voltage of 100 mV, the majority of the surface did not conduct. Only a few spots with increased conductance within an otherwise insulating matrix could be detected. After reduction at 750 °C, the topographic structure did not change significantly but an increase in the conductivity was observed. In some areas of the surface, the LC-AFM measurements revealed the existence of conducting clusters with a size and shape comparable to the crystals with lower donor concentrations.

The last annealing step at 1000 °C however led to a different surface structure than on the other crystals. Instead of a flat and step-like structure, a rough topography consisting of irregular arranged blocks with a size of 30-60 nm was measured. This structure shows rather some similarities to that obtained on the crystal doped with 1.4 % Nb after repeated reduction and oxidation steps shown in Fig. 4.48, which supports the idea that the clusters are related to structural inhomogeneities induced by the crystal growth serving as a template for the evolution of the characteristic cluster-like pattern. Also the mapping of the conductivity of the highest doped crystal after annealing at 1000 °C revealed the existence of conducting clusters although they were not that regularly aligned. In some regions of the scans, agglomerations of clusters with higher conductivity than the rest can be seen showing a modulation of the conductivity on larger scales. This could be related to the very inhomogeneous donor distribution in this crystal that was revealed by FLIM and SIMS measurements shown in Fig. 4.12.

The measurement of an inhomogeneous cluster-like conductivity on the nanoscale revealed that the nature of the electronic transport phenomena and the related resistive switching phenomena are very complex. Hence, the resistive switching phenomena cannot be explained by only taking into account a homogeneous diffusion of point defects modulating the Schottky barrier of an oxide-metal interface but structural intrinsic inhomogeneities related to extended defects have to be taken into account when modelling resistive switching of the system as will be presented at the end of this thesis.

Comparing the absolute value of the current measured on the epi-polished surface of the three crystals with different doping concentration, a clear correlation between the Nb

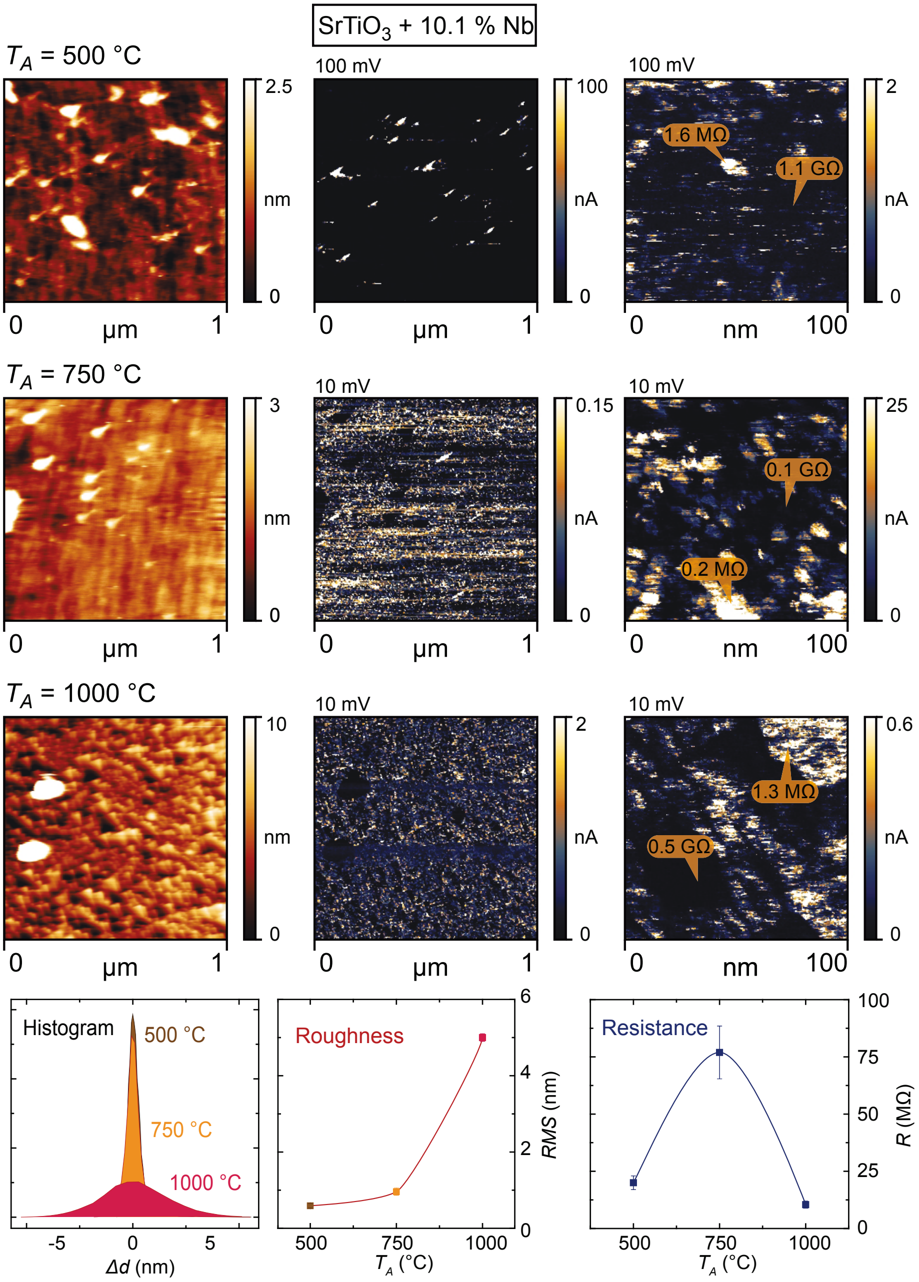

Figure 4.49.: Topography and local conductivity measured after annealing the crystal at different temperatures ($SrTiO_3$+10.1 % Nb). In the bottom row, a histogram of the height distribution, the measured roughness and the local resistance extracted from the LC-AFM measurements are shown.

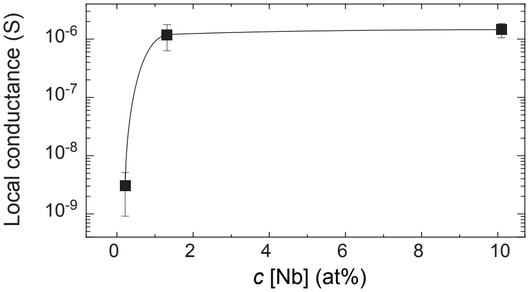

Figure 4.50.: Local conductance measured by LC-AFM on freshly cleaved $SrTiO_3$:Nb crystals as function of the donor concentration.
Adapted from Rodenbücher *et al.* [RGS$^+$13].

concentration and the conductivity of the surface cannot be extracted. In contrast to this, measurements on the freshly cleaved sample revealed a distinct increase in the local conductance with the donor concentration as shown in Fig. 4.50, which illustrates once again that the properties of the real surface layer can differ significantly from those of the bulk.

4.8.2. Investigation of the conducting clusters by different surface preparations

Since the local conductivity of all crystals revealed an inhomogeneous structure consisting of conducting clusters with an average diameter of 30-60 nm, the nature of these conducting clusters is focused in the following. In order to determine whether the clusters are only a feature of the surface layer, the local conductivity of the bulk had to be investigated on the nanoscale.

Etched surface

As first step for the investigation of the nanoscale distribution of the bulk conductivity, LC-AFM was applied on a crystal surface (1.4 at% Nb) that was etched in buffered hydrofluoric acid as described in Sec. 3.1.2. As already presented in Fig. 4.8, the etching procedure led to the evolution of etch-pits propagating from the surface towards the bulk. Hence, a measurement of the local conductivity inside the etch-pits may provide a “quasi-tomographic” insight into the properties of the bulk. However, it is obvious that due to the use of the surface sensitive LC-AFM technique only the newly evolved surface of the pits and not the pristine bulk itself is investigated.

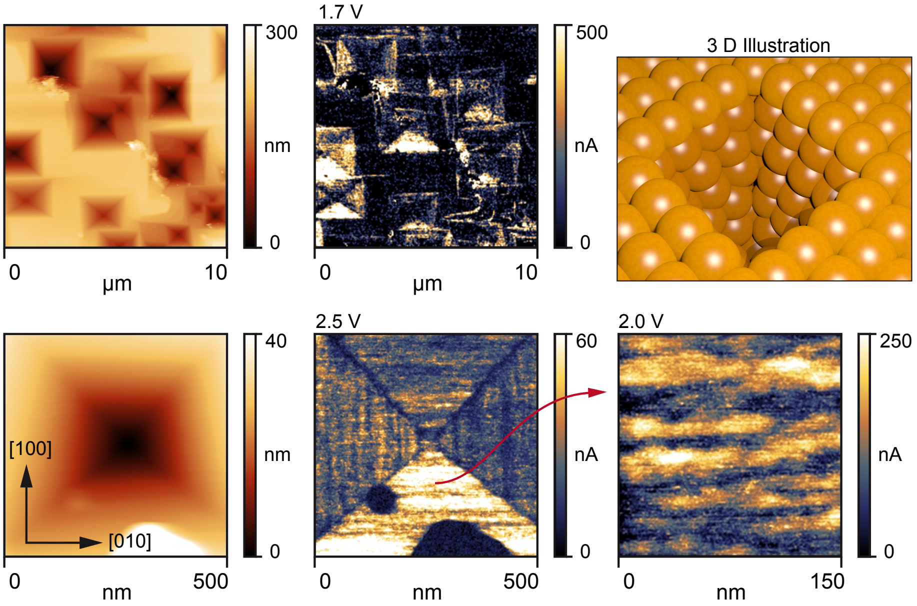

Figure 4.51.: Topography and local conductivity of the etched surface ($SrTiO_3$+1.4 % Nb).
Adapted from Rodenbücher *et al.* [RSB+13].

In Fig. 4.51, the topography and conductivity measured on an etched surface are shown. In the upper row the overview maps of an area of 10 x 10 µm reveal that the conductivity was enhanced at the sides of the etch-pits. The magnifications of one etch-pit shown in the lower row provide a clear insight in the structure of the conductivity on the nanoscale. It can be seen that along the sides of the etch pits, a striped structure was recorded following the edges of the etch-pits, which evolved along the crystallographic axes. A comparable structure was already been found by Guisinger *et al.* [GSG+09] on fractured $SrTiO_3$:Nb by scanning tunnelling microscopy showing that the measurements inside the etch-pits have possibly the potential to gather information about the inside of the crystal. The magnification of one side of the etch pits revealed that within the striped structure, a cluster-like pattern was present. This shows that the conducting clusters are not only an effect of the epi-polished surface but that they could be also present in the bulk of the crystal as illustrated in the 3D graphic in Fig. 4.51.

Cleaved surface

As a second method for the analysis of the local conductivity inside the bulk, LC-AFM measurements on a freshly cleaved crystal were performed. In the maps of topography and conductivity presented in Fig. 4.52, an inhomogeneous cluster-like structure can be seen. This structure was found on some areas of the cleaved surface besides those areas showing a pronounced conchoidral structure as shown in Fig. 4.2. The clusters had a comparable size as those measured on the epi-polished surface proving that the existence of clusters is not related to the surface preparation but rather is an intrinsic property of Verneuil-grown $SrTiO_3$:Nb crystals.

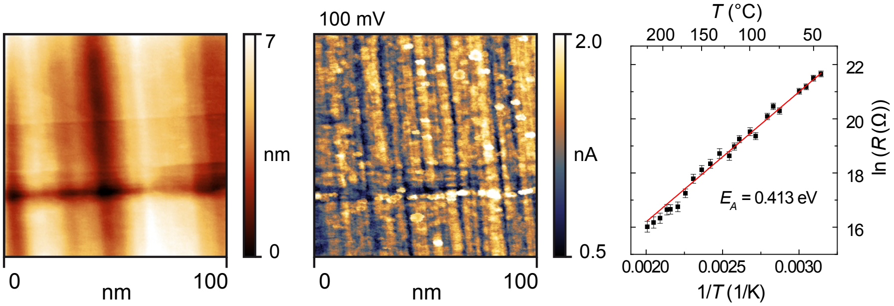

Figure 4.52.: Topography and local conductivity of freshly cleaved surface and Arrhenius plot of the average surface resistance ($SrTiO_3$+1.4 % Nb). Adapted from Rodenbücher *et al.* [RSB$^+$13].

Furthermore, it can be seen that the clusters were very regularly aligned along the breaking edge indicating that there are preferential orientations for the evolution of clusters along the crystal axes. This corresponds to the measurements inside of the etch-pits, in which a regular alignment parallel to the edges of the pits was found as well. In the right panel of Fig. 4.52, an Arrhenius plot of the average local resistance calculated from LC-AFM maps measured at different temperatures is presented. The linear dependence between the logarithm of the resistance and the reciprocal of the temperature clearly reveals semiconducting behaviour with and activation energy of 0.41 eV. This is reasonable since the crystal was cleaved ex situ thus being in contact with oxygen. Hence, the metallic behaviour of the bulk was suppressed according to the discussion in Sec. 4.5.2 and instead the surface was found to be semiconducting.

In summary, the investigation of the conductivity on the nanoscale clearly revealed that a cluster-like pattern of the local conductivity is present on epi-polished as well as on etched and cleaved crystal surfaces showing that the existence of conducting clusters is an intrinsic property of the Verneuil-grown crystals.

4.8.3. LC-AFM with atomic resolution

In order to investigate the origin of the existence of the conducting clusters, the shape of the distribution of the conductivity was recorded with high magnification and it was possible to map the local conductivity using an AFM operated in contact mode with atomic resolution. As discussed in Sec. 3.2.7, the contact area between the tip and the surface was below one nanometre although the radius of the tip was in the range of 20 nm, which allowed the measurement of the current on the atomic scale. Since the high-resolution (HR)-LC-AFM is a novel technique under development at the PGI-7, not all technical details are given here due to secrecy and will be presented in future publications. In Fig. 4.53, maps of the local conductivity obtained on an $SrTiO_3$:Nb crystal (1.4 %) reduced at 750 °C are shown. Starting with a measured area of 40 x 40 nm, the conducting clusters were clearly visible. The clusters that can be seen in the map have an

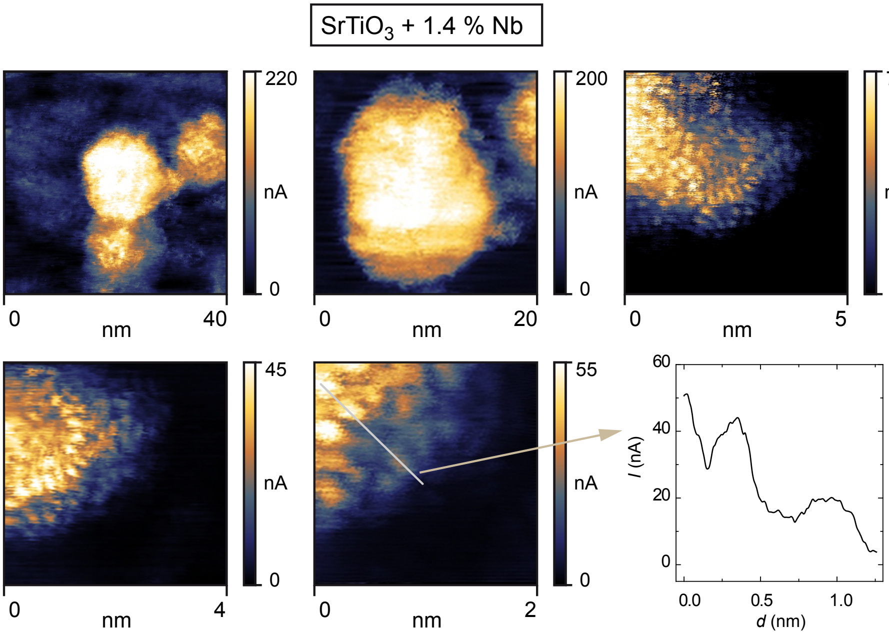

Figure 4.53.: Local conductivity of the clusters measured with atomic resolution ($SrTiO_3$+1.4 % Nb).

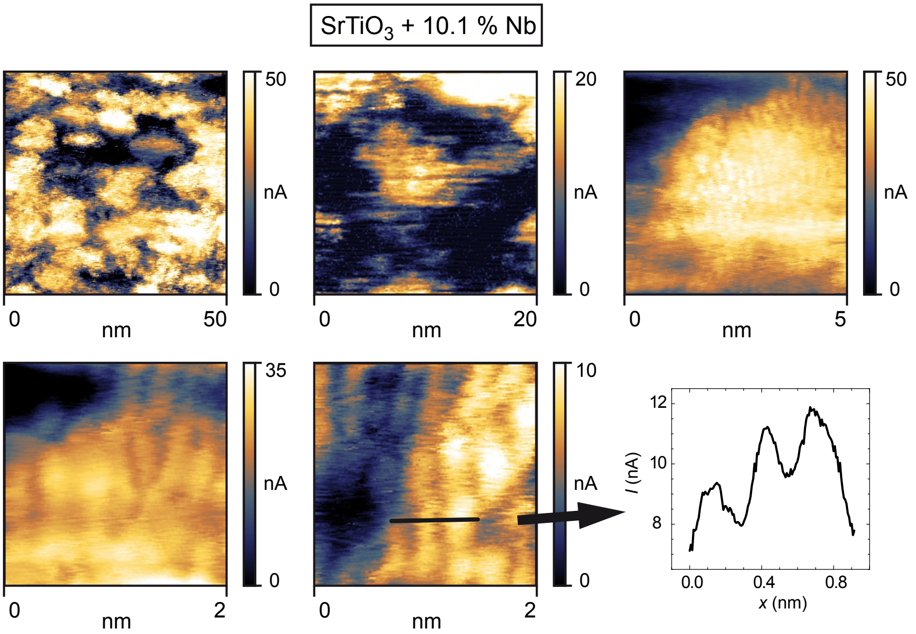

Figure 4.54.: Local conductivity of the clusters measured with atomic resolution ($SrTiO_3$+10.1 % Nb).

almost constant conductivity inside each cluster but display rather different conductivities among each other. This is related to the chosen reduction temperature, which only led to a partial enhancement of the conductivity and not to a complete insulator-to-metal transition of the surface layer. The cluster in the centre of the first scan, which showed the highest conductivity, was then monitored with higher magnification. When measuring a 5 x 5 nm area of the lower right edge of the conducting cluster, a clear modulation of the conductivity on the atomic length scale was detectable. Using this technique, the edge of the cluster was clearly identified in a 2 x 2 nm scan. Across the edge, a line-plot was extracted as shown on the right of Fig. 4.53. It can be seen that the conductivity drops in the region between the conducting cluster and the insulating surrounding by more than a factor of 10 within only a few lattice constants. This indicates that the properties of the cluster region are rather different to that of the surrounding matrix.

On the crystal doped with 10.1 % Nb, it was also possible to obtain LC-AFM measurement with atomic resolution after reduction at 750 °C. As shown in Fig. 4.54, the map of the local conductivity of an area of 50 x 50 nm revealed the existence of a conducting clusters that were with a diameter of 10-20 nm slightly smaller and more asymmetric than those observed on the lower doped crystal. According to the measurements in Fig. 4.53, a good conducting cluster was chosen to monitor it with highest magnification. The line-plot extracted from the LC-AFM scan at the edge of the cluster clearly reveals the drop of the conductivity. The structure of the atomic scale revealed the existence of long-range lines following the rows of the crystal lattice.

These measurements show that the conductivity on the nanoscale is highly confined to conducting clusters. Hence, two regions with rather different properties have to be distinguished, namely the highly conducting clusters and the insulating matrix of the crystal. As an explanation for the evolution of the conducting clusters in the entire crystal during the Verneuil growth, a segregation of defects should be taken into account. These defects could either be strontium vacancies that are known to form agglomerations as discussed in Sec. 2.3 or Nb dopants. Since the concentration of strontium vacancies should be relatively low under reducing condition according to Eq. 2.22, it seems to be more likely to assume an Nb segregation. Such a segregation in a cluster-like shape could also explain why the conductivity inside the clusters is enhanced compared to the matrix. Furthermore, this assumption is supported by the fact that indications for Nb segregation effects were found on the microscale as presented in Sec. 4.4. However, a Nb clustering on the nanoscale could not be observed by the techniques used in this thesis, which indicates that there could be alternative reasons for the observed conducting clusters in the surface layer.

4.8.4. Theoretical investigation of Nb segregation

Since the atomically resolved LC-AFM measurements only provided information about the conductivity and the chemical composition on the nanoscale was inaccessible for measurement, theoretical LDOS calculations were performed to determine the correlation between measured conductivity and a potential Nb segregation. Therefore, the same 5-layer structure with a $p(3 \text{ x } 3)$ in-plane unit cell as in Fig. 4.22 was analysed. Within a stoichiometric arrangement of Sr, Ti and O atoms, one centre Ti atom was substituted by one Nb atom to simulate the effect of doping. The local density of states 20 meV below the Fermi level was then calculated at a distance of 1.3 Å from the surface. In Fig. 4.55a, the projection of the distribution displayed d_{yz}, d_{zx} type orbitals located at the Ti atom in the centre, which was situated on top of the Nb atom. This resulted in a ring-like structure in the centre of the projection. Besides this contribution, some induced charge density can be seen also at the neighbouring Ti atoms but with significantly reduced intensity. From the results of thicker films it could be extrapolated that the intensity can be reduced by two orders of magnitude within three lattice constants.

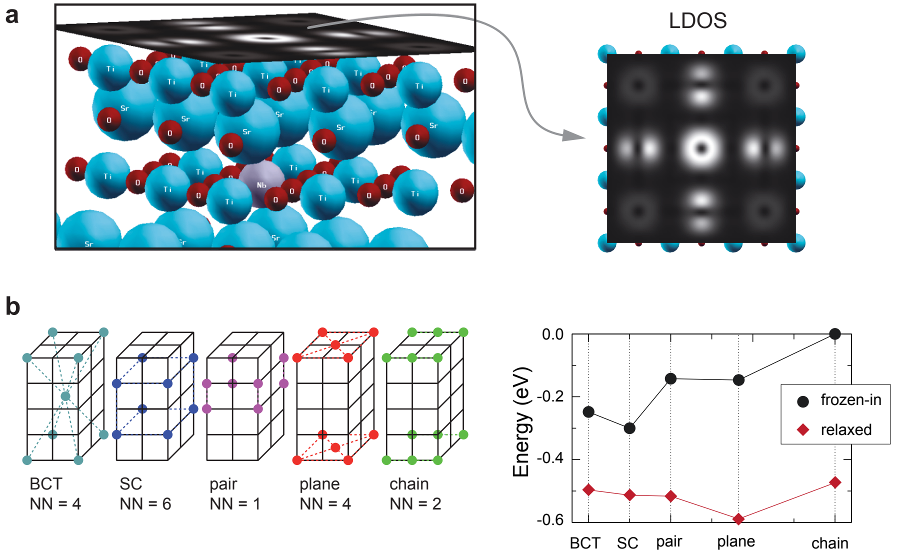

Figure 4.55.: (a) Two-dimensional projection of the LDOS of an $SrTiO_3$ cell with one Nb dopant in the centre. (b) Calculation of the energy for different inhomogeneous arrangements of Nb. Adapted from Rodenbücher *et al.* [RSB^+13].

In comparison with the measured LC-AFM measurements it can be seen that the abrupt reduction of the conductivity at the edges of the conducting clusters was reproduced by the LDOS calculation, which supports the assumption that the Nb content inside the clusters was higher than in the surrounding matrix. As a second hint for the existence of Nb segregation processes on the nanoscale, the formation energy of different inhomogeneous distributions of Nb was calculated by density functional theory (DFT) calculations at 0 K following the approach of Shanthi and Sarma, who calculated the effect of vacancy clustering in oxygen deficient $SrTiO_{3-\delta}$ and $Sr_{1-x}La_xTiO_3$ [SS98]. Six different structures in a 2 x 2 x 4 unit cell were simulated as shown in Fig. 4.55b. In the body centred tetragonal (BCT) structure, eight edges and the centre of the tetraeder were occupied. In the simple cubic structure (SC), eight sites of the tetraeder were symmetrically occupied. In the pair structure, two adjacent sites of the tetraeder were always filled with Nb atoms. In the plane structure, the Nb atoms were positioned on the top and bottom faces of the tetraeder and the chain structure was realized by occupying three adjacent sites. The six structures differ in the number of nearest neighbours (NN) and the Nb density. The calculation of the formation energy presented on the right of Fig. 4.55b revealed that configurations with many Nb atoms on nearest-neighbour position were highest in energy with a difference of more than 300 eV to spatially separated arrangement, which corresponds to expectations based on electrostatic arguments predicting a homogeneous distribution of Nb atoms in $SrTiO_3$. This calculation is however only valid for a frozen-in system. When taking into account relaxation processes of the atoms around the impurities, highly clustered structures can gain several hundreds of meV, while this effect is significantly smaller for more homogeneous Nb distributions. This can be understood by considering that the strain-field around an Nb cluster is smaller than the accumulated strain-fields of the same amount of isolated Nb atoms. In total, the combination of these effects leads to a rather flat dependence between formation energy and Nb concentration as symbolized by the diamonds in the graph of Fig. 4.55b. This indicates that in principle, many different types of inhomogeneous Nb distributions on the nanoscale can be achieved without the need for additional energy.

In conclusion, the theoretical calculations of the possibility of Nb doping together with the similarities of the calculated LDOS and the measured atomically resolved LC-AFM maps may act as helpful support for the assumption of Nb segregation on the nanoscale. However, the presented calculations were conducted for 0 K and did not take into account that at the high temperatures of the crystal growth the entropy term may become much larger than the formation entropy which would result in a minimum of the total free enthalpy for a homogeneous Nb distribution. Also from the experimental point of view, a definite proof of the assumption of Nb clustering cannot be provided on the bases of the available set-ups since only a three-dimensional mapping of the chemical composition and crystallographic structure with atomic resolution could solve this problem. This emphasizes the demand for the development of novel experimental techniques and methods in order to gain a closer insight into the origin of electronic transport phenomena.

4.9. Resistive switching on the macroscale

After the analysis of the properties of the $SrTiO_3$:Nb single crystals and the influence of external gradients on the surface layer presented so far, the actual resistive switching, namely the modification of the resistance by an applied voltage is focused on the following. Since it turned out that on top of the single crystals a surface layer with significantly different properties than the bulk exists, particularly the role of the surface layer during the resistive switching process is analysed.

4.9.1. Four-point measurements

V-I curves

Four-point measurements are very well suited for the investigation of the influence of the surface layer on the electrical characteristics since they offer the opportunity to determine the resistance of surface and bulk separately. As illustrated in Fig. 4.56a, four Pt electrodes were deposited by sputtering on top of an epi-polished $SrTiO_3$:Nb (1.4 %) crystal in so-called modified Valdes geometry, in which a sufficient distance between the electrodes and the edges of the samples prevents perturbation effects. The larger outer electrodes A and B were then connected by retractable metal needles to a voltage source operating in constant-current mode. Using electrometers, the potential drop between all four electrodes was recorded as function of the current. In this way, V-I curves were obtained at different temperatures under vacuum conditions. While most of the recorded curves revealed semiconducting behaviour of the sample, occasionally a switching of the resistance was observed as presented exemplarily in Fig. 4.56a. The upper left graph displays the total voltage drop of the entire sample recorded between electrodes A and B. The three graphs shown below display the voltage drop between each electrodes. It can be seen that a switching behaviour could only be observed between the electrodes A and 1 while the potential drop between the electrodes B and 2 was relatively small. This indicates that an asymmetry was introduced into the sample since the arrangement of the electrodes was symmetrically. Such an asymmetry could be related to inhomogeneities that were intrinsically present in the surface layer of the single crystal or they could be induced by the first application of a voltage leading to electrodegradation effects as will be discussed in detail in Sec. 4.11. In comparison to the voltage drop at the outer electrodes, the recorded potential between the inner electrodes 1 and 2 was very small and revealed Ohmic behaviour as function of the current. Since the voltage measurement between the inner electrodes reflects the properties of the bulk, it can be concluded that resistive switching only took place in the surface layer of the crystal.

To analyse the differences between bulk and surface layer, V-I curves were recorded at different temperatures and the resistance was calculated from the linear part of the curves. The results for the total resistance and the contributions derived from the measurements between the inner electrodes are presented in Fig. 4.56b. In average, the total resistance representing the properties of the surface layer decreased with the temperature while the bulk resistance (1-2) was significantly lower and increased with temperature. This shows that the bulk of the $SrTiO_3$:Nb single crystals was metallic as it would be expected for a donor-doped oxide but that the surface layer was semiconducting, which supports the

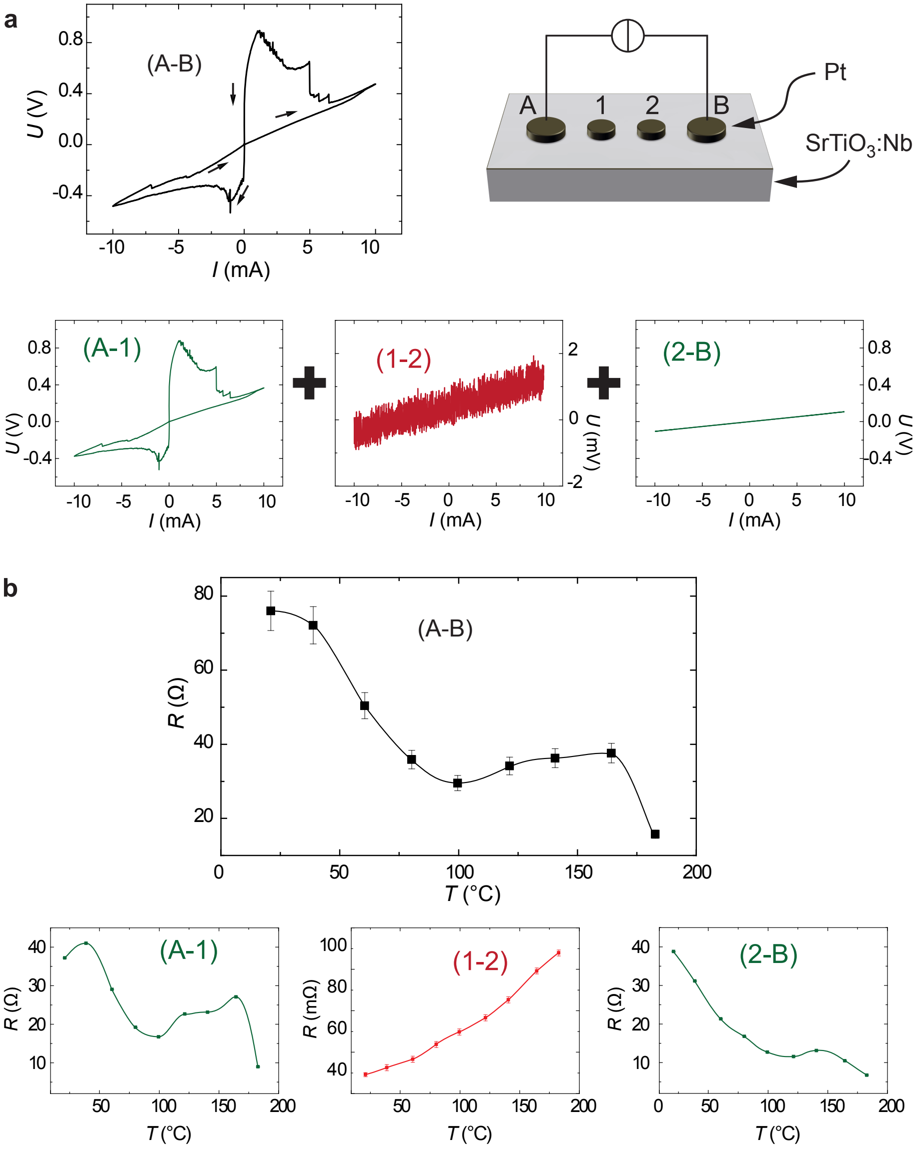

Figure 4.56.: (a) Electrical V-I curves obtained in four-point Valdes geometry. (b) Temperature dependence of the resistance extracted from V-I curves measured at different temperatures ($SrTiO_3$+1.4 % Nb).
Adapted from Rodenbücher *et al.* [RSB$^+$13].

conclusions drawn from the investigations of the electronic structure revealing that the metallic states of $SrTiO_3$:Nb are suppressed upon the contact with oxygen.

Simulation

To illustrate the method of electrical measurements in four-point geometry and to show that it is a well suited method for the characterization of surface layer and bulk, simulations were performed. At first, a finite element simulation of the potential distribution inside the bulk of the crystal was conducted using the ANSYS program. A single crystal of $SrTiO_3$:Nb with a size of 10 x 10 x 0.5 mm that was contacted by two electrodes with a potential difference of 1 V positioned on the surface was modelled.

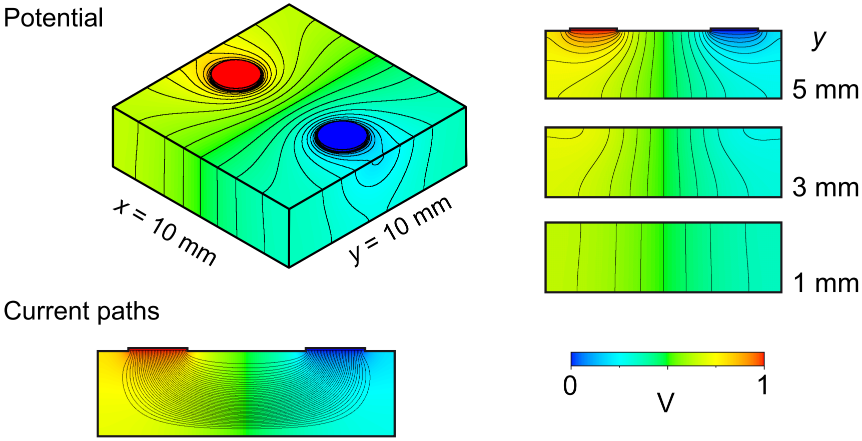

Figure 4.57.: Simulation of the potential distribution and current paths of a crystal contacted with two top electrodes obtained by finite element method. Adapted from [WSW+13].

The potential distribution is illustrated in Fig. 4.57 as colour-coded graphic with equipotential lines drawn in black. On the right-hand side of the graphic, the potential inside the bulk at different distances from the electrodes is presented. It can be seen that the potential penetrates from the electrodes into the bulk and forms a symmetric distribution. Hence, the current does not only flow at the surface but fills the entire volume between the electrodes as shown by the illustration of the current paths in Fig. 4.57. This shows that in the four-point measurements, also the bulk was affected by the applied potential allowing the investigation of its characteristics. With regard to the four-point measurements in Fig. 4.56, it was concluded that the existence of a semiconducting surface layer on top of the metallic bulk caused the differences of the potential measured between inner and outer electrodes. In order to simulate this effect, an electric circuit simulation was carried out using SPICE (Simulation Program with Integrated Circuit Emphasis). As illustrated in Fig. 4.58, a network of resistors was analysed. For the resistors representing the surface layer, a higher resistance (10 Ω) than for the resistors representing the bulk (10 mΩ) was chosen to take into account the different conductivity in these two regimes. Furthermore, the arrangement of the resistors in a three-dimensional structure is a first model for the cluster-like conductivity that was found to be present on the nanoscale by LC-AFM investigations. According to the four-point measurements, the application of a specified voltage between the points A and B was simulated and the potential difference between the points 1 and 2 representing the inner electrodes was calculated. The simulated values reproduced the different measured resistance values between the individual electrodes qualitatively showing that also from the electrical point of view, the assumption of the existence of a switching surface layer with higher resistance than the metallic bulk was justified.

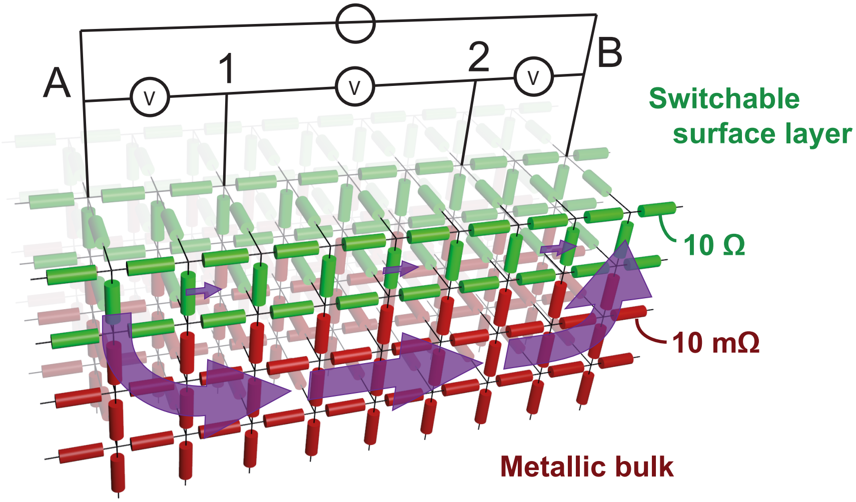

Figure 4.58.: Illustration of a network of resistors used for the simulation of the measured potential in the four-point measurements shown in Fig. 4.56. The arrows illustrate the current flow.
Adapted from Rodenbücher *et al.* [RSB$^+$13].

High temperature electroreduction

Using the four-point geometry, the influence of reduction and electroreduction on the surface layer at high temperatures was investigated. A single crystal was contacted with electrodes deposited using Pt paste to avoid a modification of the surface layer due to the bombardment during sputtering. A relatively high constant current was send through the sample via the outer electrodes while the whole set-up was heated to 1000 °C under vacuum conditions. In the beginning of the experiment, a very high resistance of the surface layer of more than 100 MΩ was measured, which dropped to values of several tens of ohms upon heating while the current was constantly flowing. Starting from a maximum temperature of 1000 °C, the potential between the four electrodes was recorded by electrometers. The calculated resistances are shown in Fig. 4.59 as function of temperature. At higher temperatures, the total resistance measured between electrodes A and B decreased with decreasing temperature indicating metallic behaviour until it reached a minimum around 250 °C. At lower temperatures, the resistance increased again indicating semiconducting

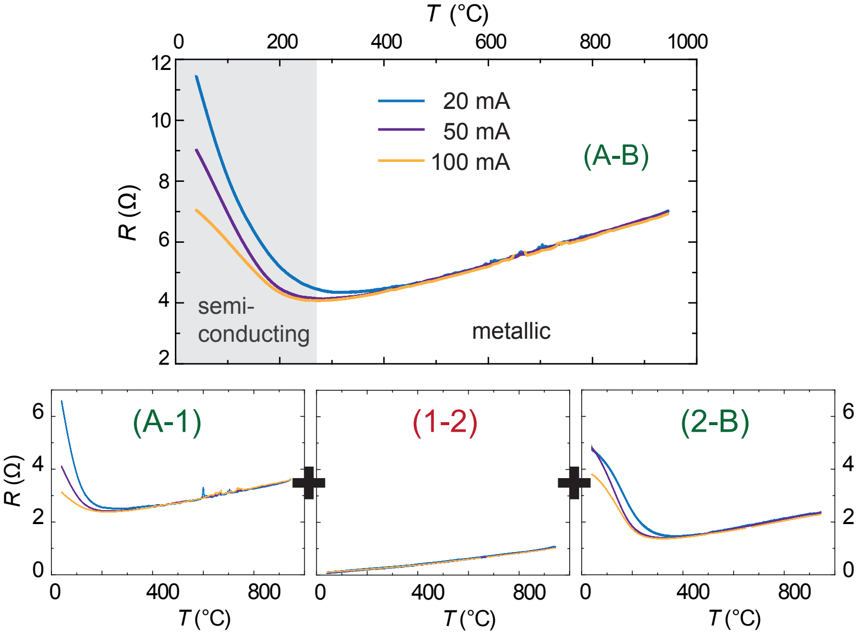

Figure 4.59.: Resistance after high temperature electroreduction measured upon cooling by four-point measurements ($SrTiO_3$+1.4 % Nb). Adapted from Rodenbücher *et al.* [RSB$^+$13].

behaviour. The individual resistances of the different regions of the sample calculated from the potential measurements between the four electrodes revealed that the characteristic minimum of the resistance was only obtained from the measurements of the surface layer. The resistance of the bulk, which was measured between electrodes 1 and 2 was significantly lower than that of the surface layer and showed a metallic behaviour throughout the whole temperature range. While the metallic resistance at high temperature did not depend on the current flowing between the outer electrodes, the resistance of the semiconducting part at lower temperatures decreased with higher current. This indicates that during the high temperature electroreduction, the surface layer was transformed to a material showing an insulator-to-metal transition around 250 °C, while the bulk was not affected by this transformation. Since the substoichiometric titanium oxide Ti_2O_3 also shows such a characteristic insulator-to-metal transition at this temperature [SRS+11], one possible explanation for the measured temperature dependence of the resistance could be that a local phase change took place in some parts of the surface layer during the high temperature electroreduction as will be discussed in detail in Sec. 4.11.

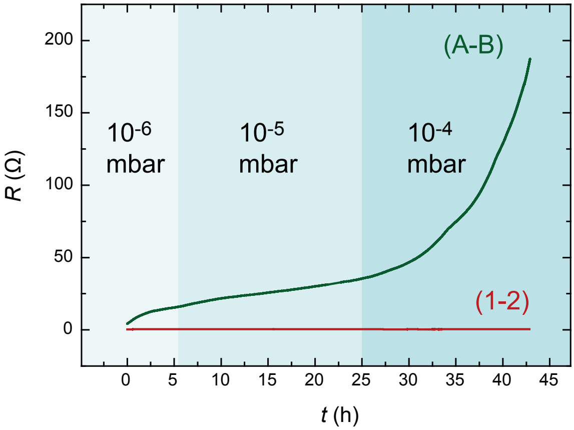

Figure 4.60.: Temporal change of the resistances of surface layer and bulk during reoxidation. ($SrTiO_3$+1.4 % Nb).

The special role of the surface layer was further investigated by re-oxidation experiments. After performing high temperature electroreduction at 1000 °C, the sample was cooled down to 400 °C under vacuum conditions. Then a constant voltage of 0.2 V was applied to the outer electrodes and the temporal change of the resistances of bulk and surface layer was recorded while increasing the oxygen partial pressure. Starting at 10^{-6} mbar, the pressure was increased to 10^{-5} mbar after 6 hours and to 10^{-4} mbar after 25 hours. It can be seen from Fig. 4.60 that the resistance of the bulk remained constant at a small value during the oxidation but the resistance of the surface layer increased exponentially as function of time. This shows that the properties of the surface layer are very sensitive to oxygen supporting once again the assumption that the high resistive surface layer found on the as-received crystals evolved due to the contact with oxygen from air.

4.9.2. Influence of oxidation

As revealed by the XPS measurements in Sec. 4.5, annealing of the sample under oxidizing conditions leads to an increase in the Sr-content in the surface layer, which was assumed suppress the metallic states thus creating an insulating layer. In order to investigate the consequence of the evolution of an Sr-rich surface layer on the electronic transport properties and the resistive switching effect, electrical measurements on samples oxidized at different temperatures T_A were conducted.

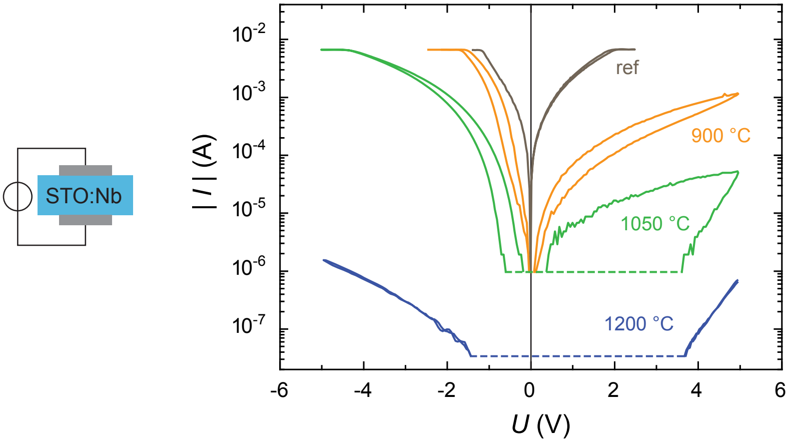

Figure 4.61.: Resistive switching on crystals annealed under oxidizing conditions at different temperatures. The dotted lines indicate the respective noise level. ($SrTiO_3$+1.4 % Nb). Adapted from Rodenbücher *et al.* [RSB$^+$13].

Unpolished samples with a size of 5 x 5 x 0.5 mm were cut from the same piece of a single crystal and annealed in air for five hours at different temperatures. After this procedure, the top and the bottom of the samples were contacted using Pt paste and I-V curves were recorded under ambient conditions while applying a voltage sweep. In the logarithmic plot of the current presented in Fig. 4.61, distinct differences between the samples can be seen. While the non-annealed reference sample showed the highest current, the conductivity systematically decreased with the annealing temperature. Besides the sample annealed at 1200 °C, all crystals revealed bipolar resistive switching. Since resistive switching can only occur in an asymmetrical configuration but the arrangement of the electrodes was nominally symmetrical, it can be concluded that some internal asymmetry was introduced in the crystal for example during the crystal preparation or by electroforming effects during the application of the first voltage sweep. This measurement confirms that the thermal treatment under oxidizing conditions significantly influences the electrical characteristics.

In order to gain an insight into the change of the surface layer during the oxidation, the capacitance of the samples was recorded simultaneously with the I-V curves. Therefore, a small AC voltage (0.1 V) with a frequency of 10 kHz was superposed with a DC voltage and the serial Maxwell-Wagner capacitance was determined by recording the real and imaginary part of the AC current using a lock-in amplifier. On the left-hand side of

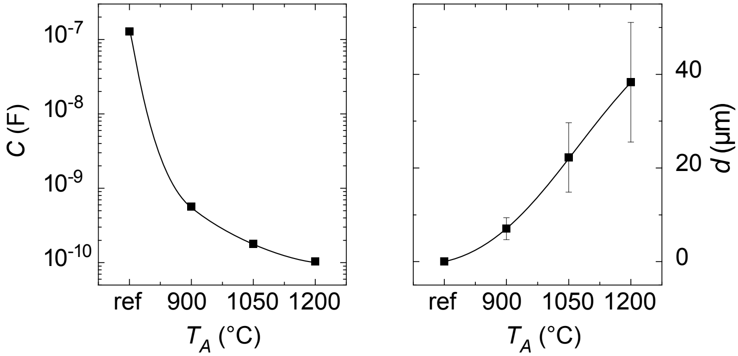

Figure 4.62.: Capacitance and calculated thickness of the surface layer as function of the annealing temperature ($SrTiO_3$+1.4 % Nb).
Adapted from Rodenbücher *et al.* [RSB+13].

Fig. 4.62, the measured serial capacitance is shown as function of the annealing temperature T_A. It can be seen that the capacitance decreased systematically with the annealing temperature. The value of the capacitance was relatively high indicating that not the whole sample but only the surface layer contributed to the displacement of the phase of the current, which was used to calculate the capacitance. This assumption provided the opportunity to estimate the thickness of the surface layer d when fixing the permittivity to $\varepsilon_r = 300$, which is a typical value of $SrTiO_3$, and taking into account the electrode area A according to Eq. 3.12 As shown on the right-hand side of Fig. 4.62, the calculated thickness of the surface layers of the as-received sample was in the range of several nanometres increasing to values of several tens of micrometres at higher annealing temperatures. This indicates that under oxidizing conditions, the thickness of the insulating Sr-rich surface layer increases, which is in complete agreement with the conclusions drawn from the XPS measurements.

4.9.3. Influence of electrode preparation

Since the composition and structure of the surface layer was found to be highly sensitive on external gradients influencing resistive switching characteristics, the impact of the electrode deposition is focused in the following. Two different geometries were investigated. At first, Pt electrodes were deposited by painting with Pt past and by sputtering on top of epi-polished samples cut from the same piece of the crystal. Between each two top-electrodes, the voltage was recorded while performing a current sweep. As can be seen in Fig. 4.63, the two pieces of the crystal revealed distinctly different electrical behaviour. Only on the painted sample, a hysteresis loop indicating the presence of resistive switching could be observed, but the sputtered sample showed an ohmic dependence between current and voltage indicating metallic behaviour.

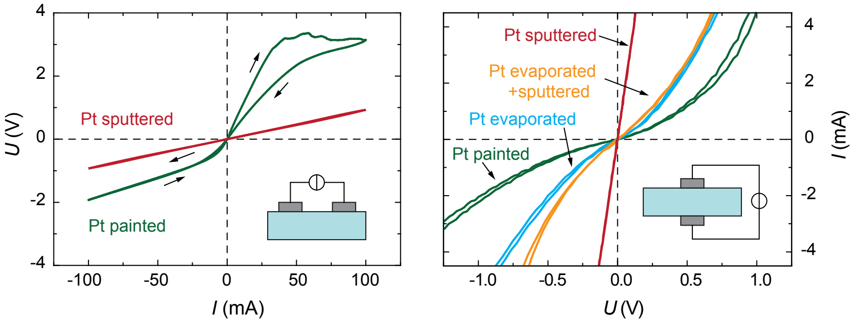

Figure 4.63.: Dependence between current and voltage measured using differently prepared electrodes in two geometries ($SrTiO_3$+1.4 % Nb).

As a second geometry, pieces of the single crystals were contacted by a top and a bottom electrode. In this configuration four different preparations were compared. The first sample was contacted by painted electrodes and the second by evaporated electrodes. On the third sample, the top electrode was evaporated and the bottom electrode was sputtered while on the fourth sample both electrodes were sputtered. In the I-V curves shown on the right of Fig. 4.63, it can be seen that the conductivity increased systematically between sample one to four. The painted electrodes led to a S-shaped I-V curve showing bipolar resistive switching. The curves of the samples that were evaporated and mixed evaporated and sputtered were relatively similar to each other showing still an S-shaped form with small hysteresis but with higher conductivity than the painted sample. The fourth sample which had sputtered electrodes on both sides revealed a linear I-V curve without hysteresis indicating metallic behaviour.

This different behaviour could be explained by considering the impact of the Pt deposition. While contacting with Pt past is a relatively soft method, which does not change the sample that much, evaporation and particularly sputtering lead to a penetration of high-energy particles into the surface layer [PSPS09]. Hence, it can be assumed that during sputtering the surface layer was penetrated by the Pt electrodes thus enabling an access to the metallic bulk, while the evaporation only led to a partial change of the surface layer. The finding that the resistance state of the sample is dependent on the technique used for electrode preparation is also relevant for the modelling of resistive switching. It reveals that models taking into account only the modulation of the Schottky barrier between oxide and metal as origin of resistive switching as discussed in Sec. 2.6.4 are not suitable since in this case, the electrical characteristics should only depend on the work function of the two materials and not on how the contact was formed. This illustrates that only a careful investigation of the special properties of the surface layer on the macro and the nanoscale can give a closer insight into the nature of the resistive switching phenomenon.

4.10. Resistive switching on the nanoscale

The analysis of resistive switching on the nanoscale is the decisive step in order to build up a model of the resistive switching mechanism. Especially, an answer to the question if an interfacial or filamentary type of switching is present in $SrTiO_3$:Nb can only be given based on nanoscale switching experiments performed by LC-AFM.

4.10.1. Switching at a point-like contact

Analogue to the investigations of undoped $SrTiO_3$, which revealed a filamentary type of switching along single dislocations [SSBW06], local switching experiments were performed on $SrTiO_3$:Nb single crystals (1.4 at%) using LC-AFM. At first, the as-received surface was scanned in a region of 250 x 250 nm with a reading voltage of 10 mV as shown in Fig. 4.64a. During this scan, no current was recorded proving the highly isolative behaviour of the as-received surface layer. Then, the AFM tip was positioned in the centre

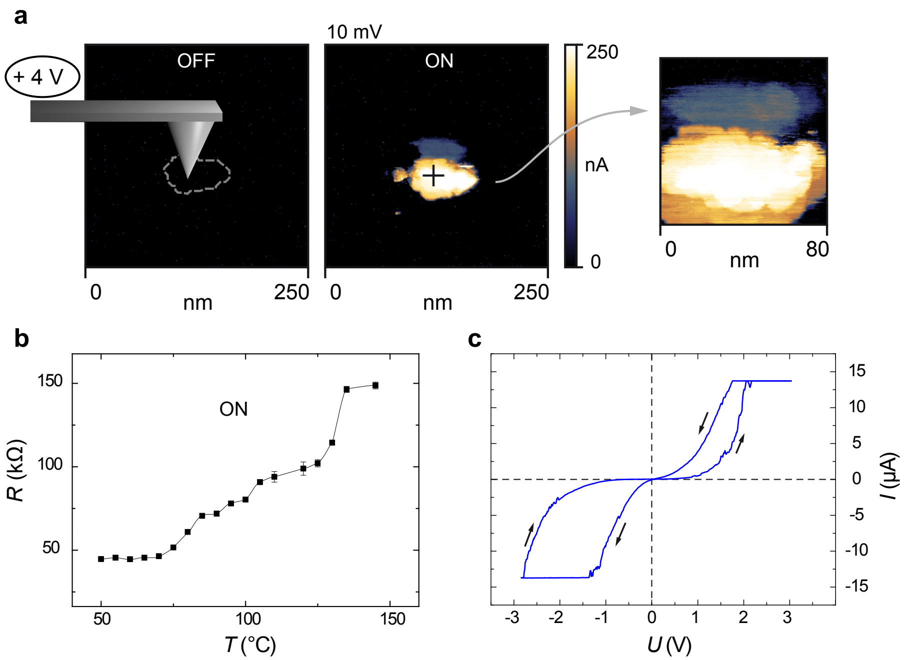

Figure 4.64.: Resistive switching of one conducting cluster. (a) LC-AFM measurement before and after switching. (b) Temperature dependence of the local resistance in the ON state. (c) Local I-V curve. ($SrTiO_3$+1.4 % Nb). Adapted from Rodenbücher *et al.* [RSB$^+$13].

of the scanned area and a voltage of +4 V was applied for several seconds. After this, the same area was scanned again with a reading voltage of 10 mV. As can be seen in the right panels of Fig. 4.64a, a whole conducting cluster with a diameter of 30-70 nm had switched to the ON state although the contact between tip and sample was only a few nanometres in diameter can thus be regarded as point-like contact. Since the dimension of this cluster is comparable to the conducting clusters detected on the nanoscale after reduction (cf. Sec. 4.8), it can be concluded that the presence of the conducting clusters in $SrTiO_3$:Nb single crystals change the switching mechanism from a purely filamentary to a cluster-like mechanism. By performing LC-AFM scans of the conducting cluster in the ON state at different temperatures, the local resistance of the cluster as function of the temperature was determined. As presented in Fig. 4.64b, the resistance increased with the temperature indicating metallic behaviour, which shows that during the switching process a local insulator-to-metal transition took place confined to the region of the conducting cluster.

This transition was found to be reversible as can be seen in the local I-V curve, which was measured while the tip was in contact with the surface at one fixed point (Fig. 4.64c). The curve revealed bipolar switching with an eight-wise sense of rotation showing that the conducting clusters can be regarded as intrinsic channels for resistive switching. The relevance of the conducting clusters for the switching was further confirmed by applying the switching voltage via the AFM tip to different positions within the area of one conducting cluster, which always resulted in an increase in the conductivity of the whole cluster with the same shape. Since the contact area between tip an surface is only a few nanometres in size, this also shows that the detection of a cluster-like switching mechanism was not an artefact related to the tip geometry but rather that the conducting clusters are intrinsically present in Verneuil-grown $SrTiO_3$:Nb single crystals due to segregation effects. The fact that a whole cluster is switching when applying a voltage via the AFM tip indicates the presence of a complex switching mechanism. As discussed in detail at the end of this section, such a behaviour could be modelled by the formation of a switchable bridge acting as nano-filament between the conducting clusters.

4.10.2. Switching of an area

Having seen that the application of the switching voltage to one point resulted in the switching of one single cluster, in the next step, an area of 500 x 500 nm was scanned while the switching voltage of +4 V was permanently applied to the AFM-tip. After this, a larger area of 750 x 750 nm was scanned with the smaller reading voltage of 10 mV in order to investigate the result of the switching procedure. As presented in Fig. 4.65, the whole area previously scanned with the writing voltage had switched to the ON state. Within this area, the conductivity was not homogeneous but revealed the presence of an array of conducting clusters. The clusters were aligned in rows predominantly along the <100> crystal axes. By performing LC-AFM switching scans with different angles to the crystal axes, it was excluded that the regular alignment of the clusters was an artefact of the scanning procedure, showing that the clusters were related to the structure of the crystal itself. The observed alignment along the crystal axes corresponds to the alignment along the faces of the etch pits presented in Sec. 4.8.2, which indicates that the conducting clusters found on the nanoscale investigations of the conductivity and the clusters found after switching under electrical gradients were the same. This conclusion is supported by the fact that the diameter of the clusters of around 50 nm, which was calculated by averaging the distance of the rows of the array, is in agreement with the dimension found in the previous LC-AFM measurements in Sec. 4.8.

After the array of conducting clusters was switched to the ON state, the stability of

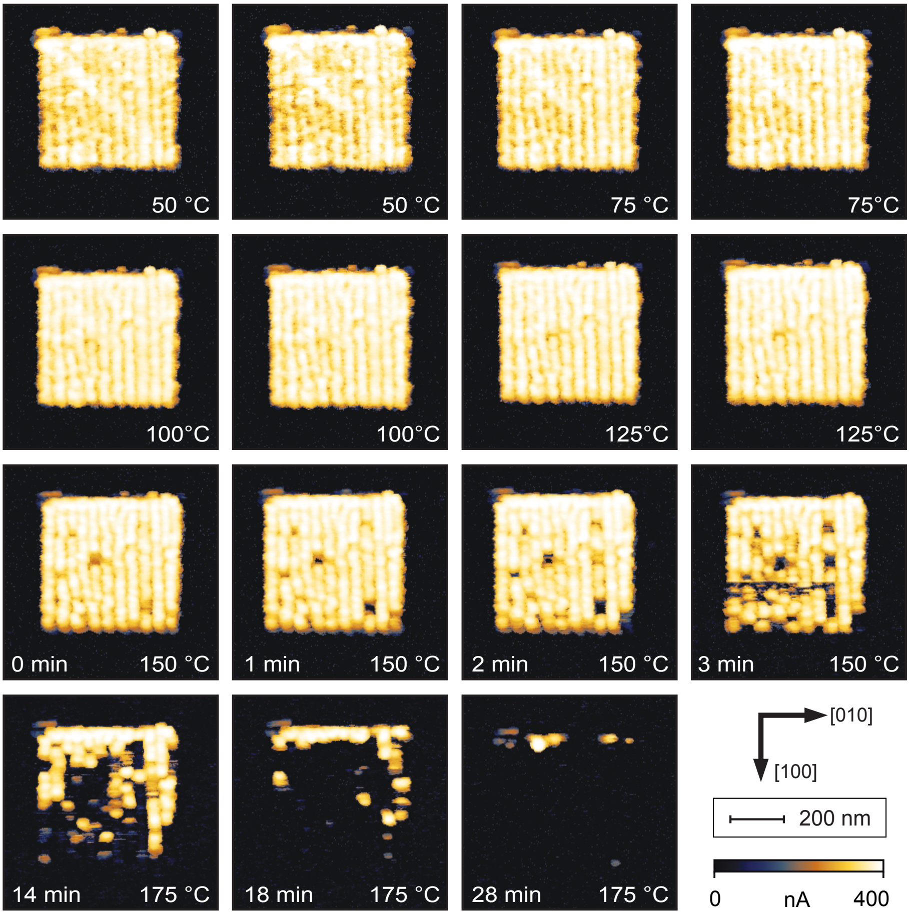

Figure 4.65.: Resistive switching of an array of clusters. The behaviour of the ON state was recorded as function of time and temperature by LC-AFM. ($SrTiO_3$+1.4 % Nb). Adapted from Rodenbücher *et al.* [RSB$^+$13].

the ON state was analysed by increasing the temperature. Starting at 50 °C, LC-AFM measurements of the same area were performed as function of temperature and time as presented in Fig. 4.65. Up to 125 °C, the array of clusters did not change significantly showing that the ON state was stable in this temperature regime. Above 150 °C, a few individual clusters of the array switched back to the OFF state and at 175 °C, the majority of the clusters returned to the OFF state after some time. Only the clusters of the upper row, which was switched at first by the initial writing scan were very stable and remained in the ON state even after 30 minutes at the 175 °C.

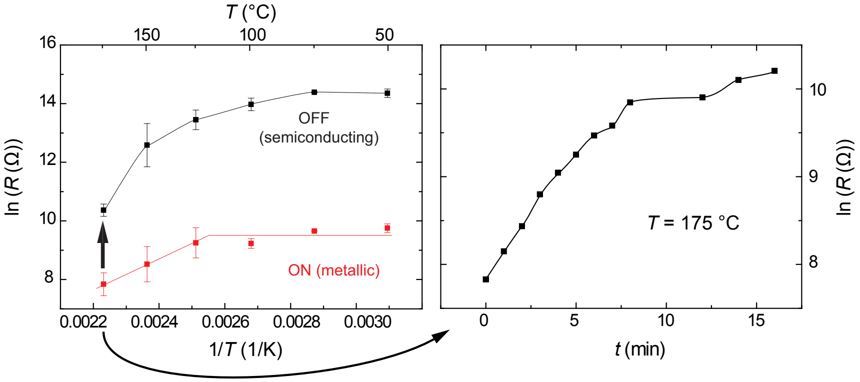

Figure 4.66.: Arrhenius graph of the resistance of ON and OFF state as function of the temperature extracted from Fig. 4.65. ($SrTiO_3$+1.4 % Nb). Adapted from Rodenbücher *et al.* [RSB$^+$13].

In Fig. 4.66, the resistance of ON and OFF state is presented as function of the temperature calculated by averaging the current in the switched and non-switched regions of the LC-AFM maps in Fig. 4.65. At low temperatures, the resistance of the ON state was constant indicating metallic behaviour while the resistance of the OFF state decreased with increasing temperature indicating semiconducting behaviour. Above 125 °C, the resistance of the ON state decreased as well due to the inset of the switching of the some clusters back to the OFF state. Since almost all clusters switched back to the OFF state at 175 °C after several time, the resistance of the initially switched area is presented as function of time on the right of Fig. 4.66 showing a significant increase in the resistance in the first 5-7 minutes at this temperature.

In general, it can be seen from the LC-AFM maps of the switching back to the OFF state at higher temperatures that the cluster always switched as a whole and rather independently from the other clusters. This implies that the switching mechanism of $SrTiO_3$:Nb is not of purely filamentary nature with switchable conducting paths confined to a few nanometres as in undoped $SrTiO_3$ [SSBW06]. On the other hand, resistive switching in $SrTiO_3$:Nb can also not be explained by an interfacial switching related to the modulation of a Schottky barrier as described in Sec. 2.6.3 since the LC-AFM clearly revealed that it is possible to retain the ON state locally without the presence of a permanent electrode. If the Schottky model would be right, the charge carriers that would have been trapped at the barrier between metal and oxide while applying the switching voltage would be released when removing the electrode leading to a vanishing of the band bending. However, it was possible to detect the clusters, which were switched to the ON state, even after retracting the metal AFM tip from the surface completely showing that during switching a fundamental transformation of the surface layer of the crystal itself took place. Furthermore, the area switched to the ON state by a writing scan was found to have an inhomogeneous conductivity consisting of conducting clusters. Hence, it can be concluded that resistive switching in $SrTiO_3$:Nb single crystals is a local phenomenon with a cluster-like switching mechanism. A potential model for this mechanism will be discussed below.

4.10.3. Multi-level switching

In order to demonstrate the reversibility of resistive switching on the nanoscale induced by LC-AFM, reiterate switching was performed. At first, an area of 1 x 1 µm was scanned with a writing voltage of +4 V corresponding to the measurements shown in Fig. 4.65. In a second step, a smaller scan with a size of 500 x 500 nm was performed in the centre of the switched area while an erasing voltage of –3 V was applied to the tip. Then, an inner area with a size of 300 x 300 nm was scanned again with the switching voltage of +4 V. At last, an area of 1.5 x 1.5 nm was measured by LC-AFM with a reading voltage of 1 mV as presented by in Fig. 4.67 revealing that this procedure resulted in an evolution of different resistive states. The outer area, which was only scanned once with the writing voltage, had a resistance state comparable to that presented by the measurements in Fig. 4.65. The inner area, which was scanned with the writing and then with the erasing voltage, had a lower conductivity than the outer area but still had a higher conductivity than the as-received one. This shows that resistive switching induced by LC-AFM was only partially reversible. The centre area, which was treated by writing, erasing and re-writing scans, showed the highest conductivity of all three areas, thereby indicating that different resistance states can be achieved based on subsequent switching scans illustrating the possibility of multi-level switching.

4.10.4. Simulation of the cluster-like switching

Outline of a potential model

In the following, the basic principle of a model of the cluster-like resistive switching on the nanoscale is discussed. It is extremely simplified since it only considers one conduction path as will be explained below. Since the LC-AFM measurements revealed that the conducting clusters always switched as a whole and independently from each others, one reasonable assumption is that the switching does not occur inside the conducting clusters

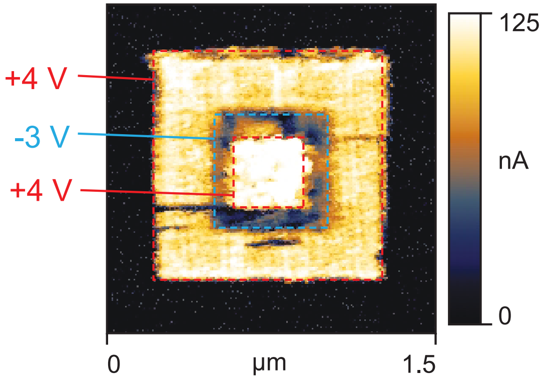

Figure 4.67.: Current map measured by LC-AFM after switching an area several times between ON and OFF state with different voltages. ($SrTiO_3$+1.4 % Nb).

but in the higher resistive region between them. In an electroforming process, a conducting bridge in the form of a nano-filament could be formed acting as a switch, which would change the conductivity of the whole cluster.

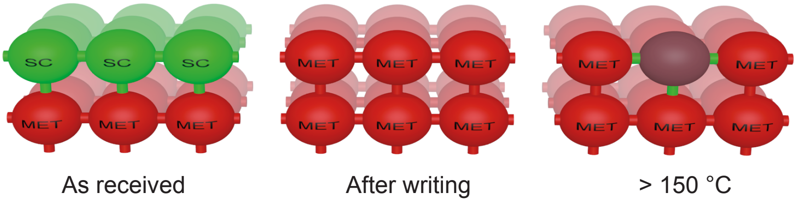

Figure 4.68.: Phenomenological model of the cluster-like resistive switching on the nanoscale.

In Fig. 4.68, the potential processes during switching induced by LC-AFM are illustrated. In the beginning, the clusters of the as-received surface layer are in a semiconducting state with high resistivity while the bulk, which also was found to consist of conducting clusters, is metallic. During a writing scan, also the clusters and bridges of the surface layer would be transformed into the metallic state. If this configuration once is reached, the switching of individual clusters above 150 °C back to the OFF state could be explained by a switching of the bridges connecting the cluster of the surface with the clusters of the bulk. If such a connection would be lost, the whole conducting surface cluster would be measured to be in the OFF state by an LC-AFM scan. As mentioned, this is an extremely simplified model because it disregards the electronic conduction between the walls in the entire area outside of the bridges. This is all the same single crystalline material $SrTiO_3$, even if slight clustering of the Nb doping is postulated as discussed in Sec. 4.8.3.

Temperature conductivity

In order to understand the processes that are present during the application of the writing voltage, finite element simulations of the electrical potential and the temperature of two conducting clusters connected by a bridge with higher resistivity were performed. In preparation for these simulations, at first the thermal diffusivity of $SrTiO_3$:Nb single crystals doped with 1.4 at% and 10.1 at% was measured using the laser-flash method. As reference an undoped $SrTiO_3$ single crystal was measured as well. The front side of the samples were heated by a laser pulse with a wavelength of 1064 nm and the temperature increase in the back side was measured by a detector under vacuum conditions. As presented in the left panel of Fig. 4.69, the thermal diffusivity of all three samples showed a decrease with the temperature.

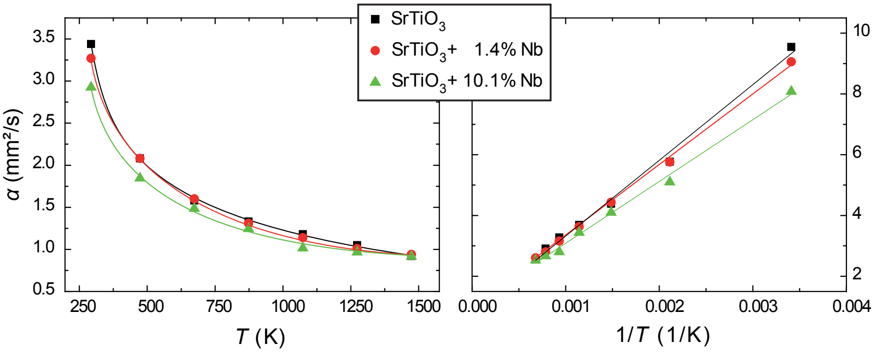

Figure 4.69.: Temperature conductivity measured by the laserflash method and calculated thermal conductivity of $SrTiO_3$ single crystals with different Nb content.

The thermal conductivity λ was calculated from the thermal diffusivity α by using literature values for the density ϱ and the temperature dependent specific heat c_p using Eq. 3.3. The result presented using a logarithmic scale in the right panel of Fig. 4.69 reveals that the thermal conductivity of all three samples decreased exponentially with the temperature, which is in agreement with previous findings on Nb-doped $SrTiO_3$ [ONOK05, MKY05]. Comparing the three investigated samples, it can be seen that the undoped crystal had the highest thermal conductivity while the highest doped one had the lowest. This implies that an influence of the electronic thermal conductivity induced by donor doping can be neglected since this would lead to an increase in the thermal conductivity with Nb content. Instead, the effect of the higher mass of the Nb atoms dampening the lattice oscillations could be taken into account in order to explain the systematic decrease in the thermal conductivity with the Nb content.

Simulation of the situation during switching

The obtained results of the thermal conductivity were used as parameter for the calculation of the temperature during local switching induced by LC-AFM using the finite element method. Since it was assumed that not the conducting clusters themselves are switching but rather that a switchable nano-filament is formed connecting the individual clusters, the situation during forming of such a filament was simulated using the ANSYS program. As illustrated in Fig. 4.70, it was assumed that a writing voltage of +4 V was applied to one cluster of the surface via the AFM tip. The simulation was performed in the region between one cluster of the surface layer and one cluster of the bulk that were connected by a small bridge. The clusters were modelled to have a higher electrical conductivity than the surrounding matrix. According to simulations of $SrTiO_3$ thin films [MWM+11], the assumed values for the resistivity were $\rho_c = 1 \cdot 10^{-6}$ Ωm for the clusters and $\rho_m = 1 \cdot 10^{2}$ Ωm for the matrix. Thereby it is assumed that the clusters are metallic and a conduction through the walls of the clusters is disregarded. The resistivity of the bridge was set to $\rho_b = 1.3 \cdot 10^{-2}$ Ωm corresponding to the current of 1 µA measured by LC-AFM during local switching.

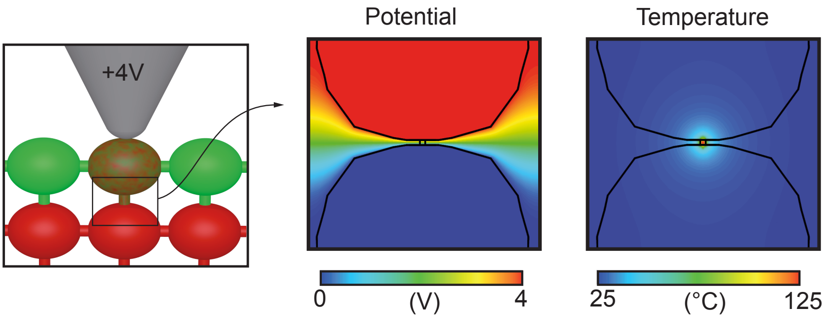

Figure 4.70.: Simulated potential and temperature distribution during switching in a bridge between two conducting clusters within a highly insulating matrix. Adapted from Rodenbücher *et al.* [RSB+13].

The calculated electrical potential and temperature distribution are shown on the right of Fig. 4.70. It can be seen that almost the entire applied potential drops in the region of the bridge between the conducting clusters, which was modelled to be only a few nanometres in size. This would lead to the presence of very high electric fields inside the bridge. The temperature increase during the application of the writing voltage was calculated to be relatively small with a maximum temperature around 125 °C suggesting that thermal effects only play a minor role in the switching process on the nanoscale. Hence, it should be assumed that the high electric field between the conducting clusters causes ionic movements, which would lead to the formation of a switchable bridge with very small dimension.

4.11. Emulation of switching

Since a direct investigation of the crystallographic structure or chemical composition of a nano-filament that was assumed to be formed as switchable bridge between the conducting clusters is not possible on the nanoscale, the influence of large electrical gradients was emulated on the macroscale by performing electrodegradation experiments. Although this experiment cannot be compared directly to the situation on the nanoscale, it will show that under extreme conditions a phase transformation from $SrTiO_3$ towards TiO_x is possible and that thus such transformation could play a role during the electroforming and resistive switching as will be discussed in the following.

4.11.1. Electrodegradation

Temperature evolution during electrodegradation

To generate comparable electrical gradients as were assumed to be present during resistive switching on the nanoscale, a relatively small voltage of 7-8 V was applied to a macroscopic single crystal (7 x 3 x 0.5 mm) via pasted Pt electrodes under vacuum conditions. The dissipated power in the range of 10-15 W was sufficient to heat up the sample up to orange glow as can be seen in Fig. 4.71a. Comparing the distribution of the glow when applying an AC or a DC voltage, significant differences can be recognized. While in the AC case, the glowing area was situated in the centre of the sample symmetrically between the electrodes, in the DC case, the glowing area was shifted towards the anode revealing an asymmetrical temperature distribution. Using a pyrometer, a maximum temperature about 1200 °C was found close to the anode whereas the temperature in the region close to the cathode was below 600 °C.

In order to illustrate this asymmetric temperature distribution, a finite element simu-

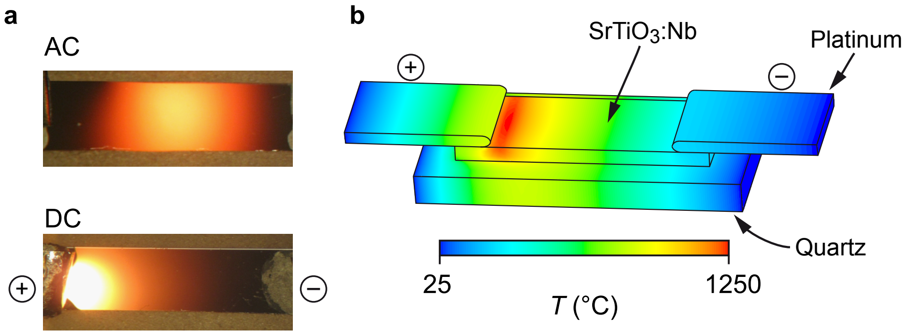

Figure 4.71.: (a) Photographs of a single crystal while applying an AC or DC voltage ($SrTiO_3$ + 1.4 % Nb). (b) Simulated temperature distribution during electodegradation.

lation using the ANSYS program was performed. An $SrTiO_3$:Nb single crystal positioned on a quartz plate and contacted with two Pt clamps acting as large-area electrodes was modelled. As boundary condition, the potential of the left clamp was held as 7 V, while the right clamp was grounded. To take into account the observed asymmetry in the glow, the volume of the sample was divided into a high resistive anode region and a low resistive cathode region. The simulated temperature distribution shown in Fig. 4.71b thus shows a good agreement with the measurement. To justify the assumption of volumes with different resistivity in the single crystal, the potential distribution between anode and cathode was measured using an electrometer while applying a DC current. It was found that almost the entire potential dropped close to the anode, indicating the presence of higher resistivity in this region. This shows that the directed electric field during the application of a DC voltage induced an internal transformation of the single crystal.

During the application of an AC and DC voltage, the effusion of molecules from the sample was recorded by a mass spectrometer as presented in Fig. 4.72 as colour-coded graph as function of time. While mass spectra were recorded continuously, the voltage was switched on after 30 s of measuring and after 400 s the voltage was switched off again. Before starting the electrodegradation, the base pressure of the vacuum chamber was in the range of 10^{-7} mbar and mainly molecules with a mass of 28 u corresponding to CO were detected. After switching on an AC voltage, no immediate changes were recorded. Only after several minutes of treatment, an increase in the amount of molecules with masses between 25 u and 32 u was detected, which can be explained by thermal effusion due to direct heating of the sample. After applying a DC voltage, a different

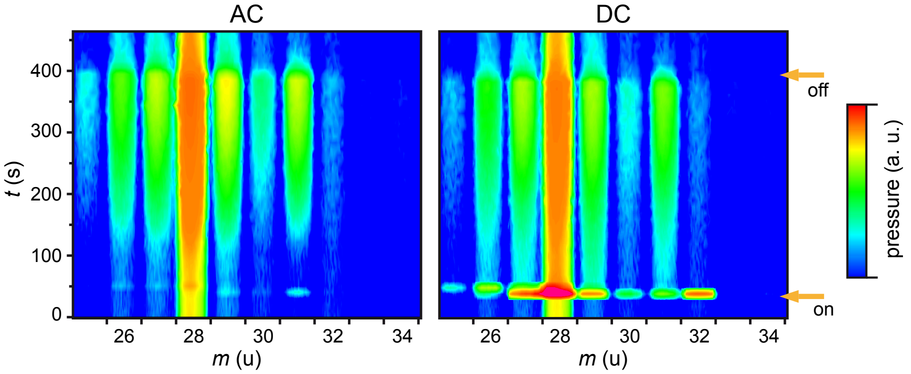

Figure 4.72.: Mass spectra of effused molecules during electrodegradation presented as colour-coded graph as a function of time.

behaviour was observed. Immediately after switching on the voltage, a distinct effusion of molecules was recorded before the onset of the thermal effusion. Particularly, an effusion of molecules with a mass of 32 u was present indicating the effusion of O_2 molecules during electrodegradation, which could change the stoichiometry of the crystal significantly. In order to investigate the effusion of molecules with higher masses such as SrO, detailed spectra were recorded up to a mass of 120 u, but no effusion was found in this region.

Investigation of the surface layer after short electrodegradation

In order to determine the changes in the surface layer induced by the application of a DC voltage under vacuum conditions, the chemical composition and electronic structure was measured by XPS. Spectra were recorded at different positions along a line between the anode and the cathode. At first, the surface layer of a crystal electrodegraded for only 10 minutes was investigated. In Fig. 4.73b, the Sr/Ti and Ti/O ratios measured by XPS are presented. Close to the anode region, where the temperature had reached the maximum, a depletion of Sr was observed. Since this corresponds to the measurements of the surface layer after thermal reduction also showing a decrease in the Sr content in the surface layer, it can be concluded that the changes after short electrodegradation were mainly induced by chemical gradients due to direct heating. In order to monitor the ionic movements in the anode region during the treatment, a SIMS depth profile was recorded and the SrO/TiO ratio was calculated (cf. Fig. 4.73b). Within the first 100 nanometres building up the surface layer, a depletion of Sr was found while in the deeper parts of the bulk, an Sr segregation was present showing that an ionic movement of Sr or SrO took

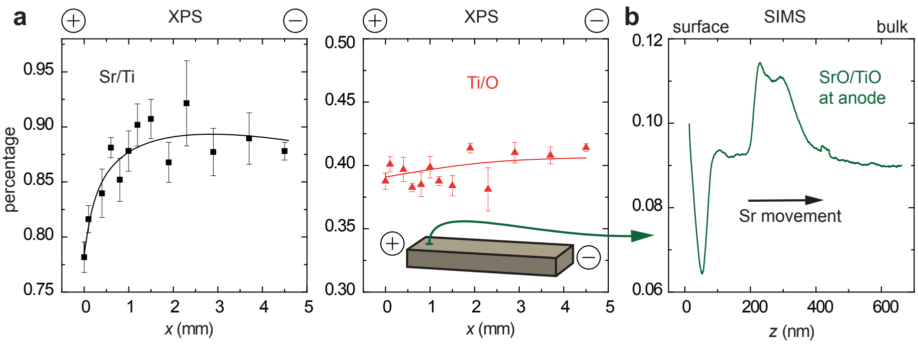

Figure 4.73.: (a) Ratios of Sr/Ti and Ti/O measured by XPS between anode and cathode after short electrodegradation. (b) SIMS depth profile of the Sr/Ti ratio in the anode region ($SrTiO_3$+1.4 % Nb).

place from the surface layer towards the bulk in agreement with the conclusions discussed in Sec. 4.5.5. With regard to the spectra of the core lines Ti2*p*, Sr3*d* and Nb3*d*, the similarities to the annealing under reducing conditions becomes even more obvious. It can be seen in the illustration of the peaks fitted to the measured spectra shown in Fig. 4.74 that close to the anode, two additional components for Ti and Nb were present revealing a partial valence change in this region. In the rest of the surface layer closer to the cathode, no changes in the electronic structure were detected supporting the assumption that the transformation of the surface layer in the anode region was induced by the increase in the temperature under reducing conditions.

Investigation of the surface layer after long electrodegradation

Since a short time electrodegradation only transformed the anode region due to the chemical gradients related to the direct heating, the degradation time was extended to one day in order to observe additional effects induced by electrical gradients. After this treatment, distinct changes in the surface layer were detectable even with the bare eye as illustrated in the photograph of the sample shown in Fig. 4.75. Close to the cathode, a striped region with greyish to reddish colour can be seen while the colour in the anode region remained black. This already indicates that fundamental transformations had taken place in the surface layer close to the cathode, which is quite surprising since the temperature in this region was the lowest during the electrodegradation.

In order to correlate the observed changes in the colour with changes in the chemical compositions, the Sr/Ti and Ti/O ratio were calculated from XPS measurements analogue

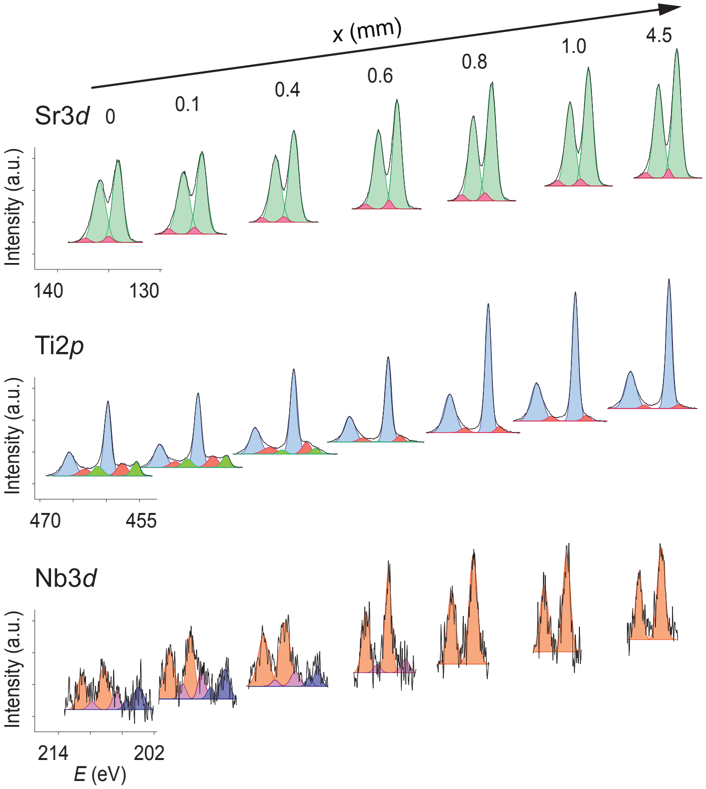

Figure 4.74.: Spectra of the core lines measured by XPS after short electrodegradation between anode and cathode. ($SrTiO_3$+1.4 % Nb)

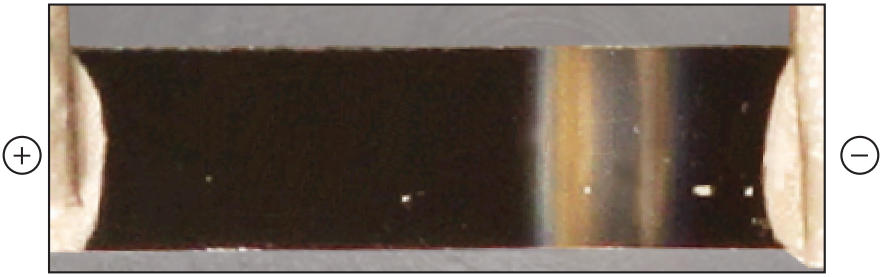

Figure 4.75.: Photograph of the crystal after long electrodegradation. (1.4 % Nb)

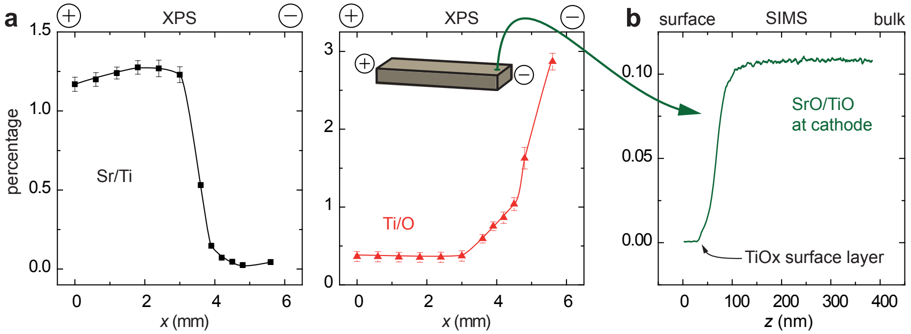

Figure 4.76.: (a) Ratios of Sr/Ti and Ti/O measured by XPS between anode and cathode after long electrodegradation. (b) SIMS depth profile of the Sr/Ti ratio in the cathode region ($SrTiO_3$+1.4 % Nb).

to the investigations after short electrodegradation. As can be seen in Fig. 4.76a, distinct changes in the stoichiometry occurred close to the cathode. While the Sr/Ti ratio in the anode region was still above 1 implying the same chemical composition as in the as-received surface layer, it had dropped to values below 0.1 in the cathode region revealing the evolution of a highly Sr-deficient surface layer. The Ti/O ratio differed distinctly between anode and cathode. In the anode region, values around 0.3 were found, which are the typical values of $SrTiO_3$, but in the cathode region the Ti/O ratio reached values close to 3. Since these values are far away from the stoichiometric range of $SrTiO_3$, it can be concluded that a series of substoichiometric titanium oxides was formed close to the cathode. By performing a SIMS depth profile in the cathode region (Fig. 4.76b), it was revealed that the transformation only affected the surface layer, since in a depth of more than 100 nm, an SrO/TiO ratio typical for $SrTiO_3$ was recorded. In order to confirm this by a second method, the greyish surface layer in the cathode region was scraped away with a sapphire file whereupon the bulk with black colour and a stoichiometry typical for $SrTiO_3$ as measured by XPS became visible. This shows that the long time electrodegradation led to a phase transformation to TiO_x phases in the surface layer of Nb-doped $SrTiO_3$.

By investigating the electronic structure, the consequence of the phase transformation were illustrated. As shown in Fig. 4.77, the XPS spectra of the core lines of Ti2p, Sr3d, Nb3d as well as of the valence band region were recorded. In the anode region, the spectra revealed the presence of the valences Ti^{4+} and Nb^{5+} but no metallic states close to the Fermi energy corresponding to the electronic structure of the as-received surface layer of $SrTiO_3$:Nb (cf. Sec. 4.5). In the Ti-rich cathode region instead, a valence change of Ti

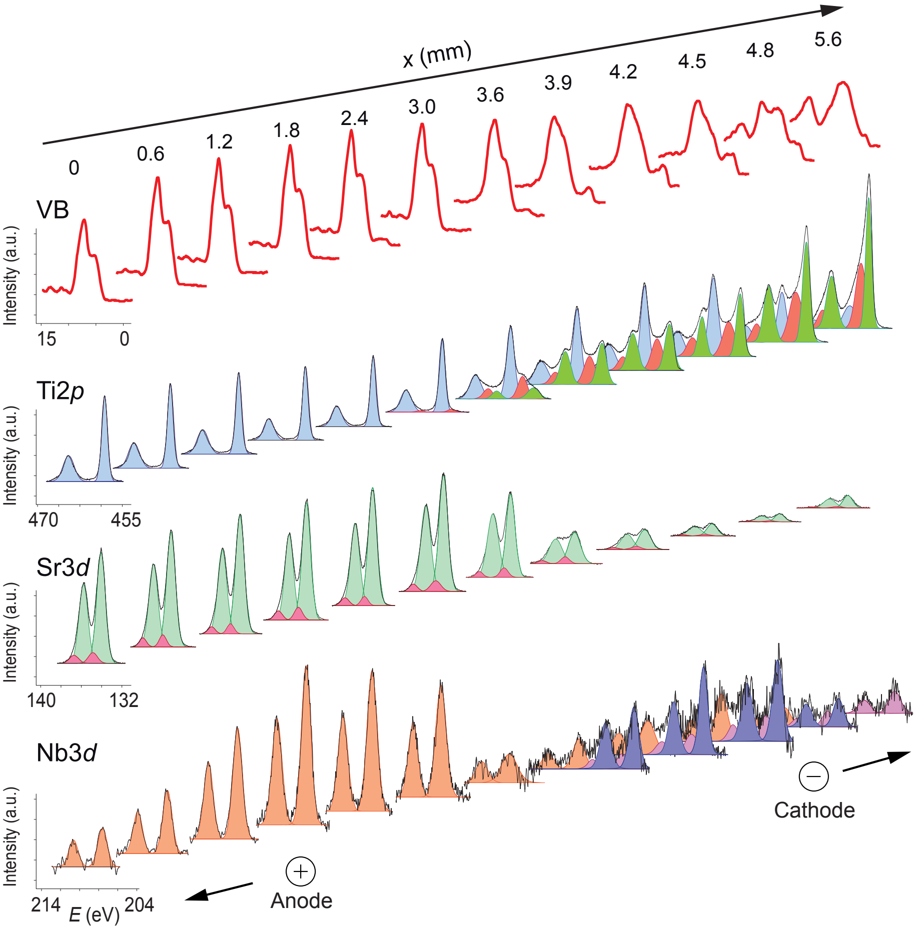

Figure 4.77.: Spectra of the core lines measured by XPS after long electrodegradation between anode and cathode. ($SrTiO_3$+1.4 % Nb)

and Nb to lower valences was found associated with a distinct change of the electronic structure of the valence band region showing a significant amount of occupied states in the band-gap related to the Ti3*d* band and close to the Fermi energy. Furthermore, a distinct change of the O1*s* peaks of the valence band around 8 eV in the cathode region can be seen. This illustrates that the fundamental transformation of the surface layer is also related to a complex insulator-to-metal transition from a band insulator to a correlated system and finally to a metal.

In order to investigate the crystallographic structure of the evolved Ti-rich surface layer,

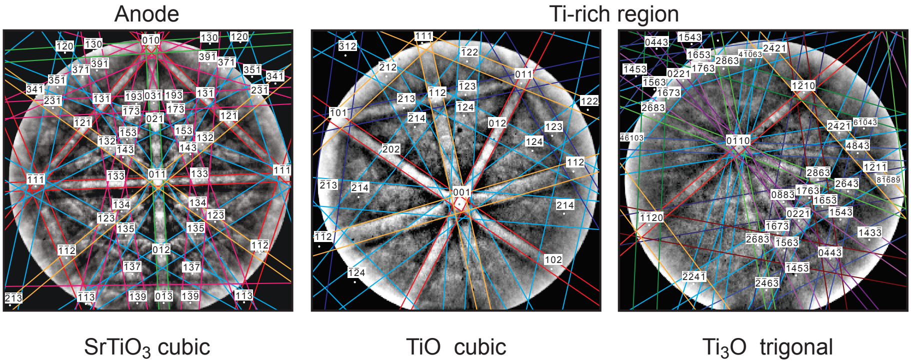

$SrTiO_3$ cubic TiO cubic Ti_3O trigonal

Figure 4.78.: Kikuchi pattern recorded by EBSD in the anode and cathode region after long electrodegradation.

measurements by electron backscatter diffraction (EBSD) were performed. As presented in Fig. 4.78, so-called Kikuchi pattern [Kik28] were recorded at different positions between anode and cathode using an electron beam energy of 10 keV and a current of approx. 25 nA. The lines of the pattern were attributed to different scattering planes and compared to data from a NIST database. The pattern found in the anode region corresponds to a typical diffraction pattern of $SrTiO_3$ with a cubic perovskite lattice proving that the structure of the surface layer close to the anode was unchanged during the electrodegradation although the temperature was the hottest in this region. In the Ti-rich cathode region, different pattern were recorded that could not be described as a perovskite pattern as shown in the right of Fig. 4.78. Instead, they were attributed to the cubic structure of TiO (NIST 47537) and the trigonal structure of Ti_3O (NIST 47547), which is in agreement with the XPS result showing a Ti/O ratio close to 3 while almost no Sr could be detected on the surface. This proves that a fundamental phase transformation from $SrTiO_3$ to substoichiometric titanium oxide took place in the cathode region.

The measurement of two different diffraction pattern in the cathode region indicated that the evolved Ti-rich layer was inhomogeneous. Hence, the morphology of the surface was investigated by scanning electron microscopy (SEM) at different positions between anode and cathode as shown in Fig. 4.79. In the anode region, the flat and unstructured surface of an epi-polished crystal was found confirming once again that this region did not change during electrodegradation. In the cathode region however, a grainy and porous structure with a grain size of 100-500 nm was present. Between the grains, expanded holes had evolved proving that the migration of Sr away from the cathode during the electrodegradation caused a decomposition and rearrangement of the material.

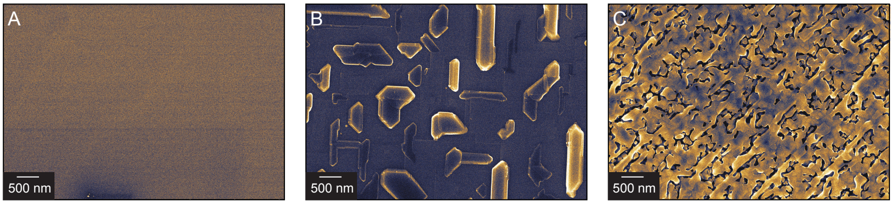

Figure 4.79.: Morphology of the surface on the nanoscale measured by SEM after long electrodegradation in the anode region (A), the intermediate region (B) and the cathode region (C).

In the intermediate region between the flat and the porous regions, an evolution of island on the flat surface can be seen from Fig. 4.79. The islands form geometrical figures with edges aligned along the crystal axes. Using EBSD, the crystallographic structure of these island was investigated. While most of the island showed a diffraction pattern that could not be related to a single crystallographic structure indicating a superposition of different cubic phases, some islands were found with a diffraction pattern corresponding to the trigonal structure of Ti_3O. This illustrates that the transformation between the original surface and the nano- or mesoporous Ti-rich surface was not abrupt but was related to an inhomogeneous phase change process on the nanoscale.

The inhomogeneity of the porous Ti-rich layer also influenced the electrical properties as can be seen from LC-AFM measurements of topography and current ($U = 0.25$ V) at three different positions of the cathode region presented in Fig. 4.80. In the topography, a grainy structure with differences in the height up to hundreds of nanometres was found in agreement to the observation by SEM. Within the porous cathode region, a systematic decrease in the grain size starting with bigger islands at the anode side to an arranged structure of smaller grains at the cathode side was observed.

In order to understand the phase transformation from $SrTiO_3$ to titanium oxides, which was observed after long time electrodegradation with a DC voltage, ionic movements in the surface layer due to the extremal chemical and electrical gradients leading to a kinetic demixing have to be taken into account. As first step of the transformation, a movement of oxygen towards the anode due to the applied electric field could be assumed. This would lead to a local oxidation of the anode region changing the charge compensation mechanism of the Nb donors from electronic compensation to the compensation by Sr vacancies and the segregation of SrO (cf. Sec. 2.3.1). This would cause a movement of SrO complexes directed towards the anode leaving behind a TiO_2 layer in the cathode region. In a second step, an electroreduction of TiO_2 could take place resulting in the evolution of different

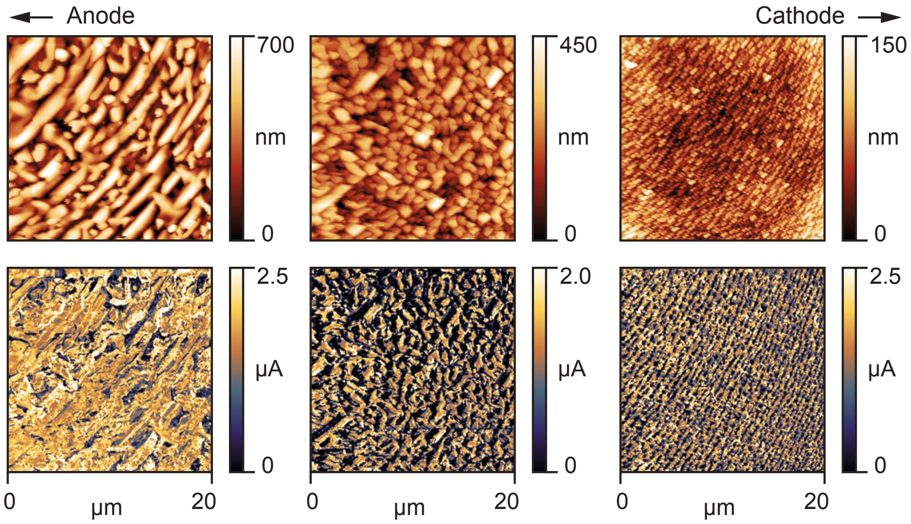

Figure 4.80.: Topography (top) and current (bottom) maps measured by LC-AFM at three positions in the cathode region after electrodegradation.

substoichiometric TiO_x phases up to TiO and Ti_3O.

Self-delamination of the surface layer

In order to check if the phase transformation of the surface layer can be extended, a comparable electrodegradation experiment was conducted with higher power of 17-20 W. After the crystal was treated in this way for one day, a similar colour change close to the cathode was observed. However, the surface layer in the cathode region had delaminated itself from the rest of the crystal as can be seen from the SEM images in Fig. 4.81. In the upper right image, an overview of the cathode side of the sample is shown. While a part of the crystal below the electrode had broken off due to the mechanical and thermal stress in the sample holder during electrodegradation, the evolution of a foil-like surface layer can be identified in a distance of approx. 1 mm from the cathode. The magnifications of this foil reveal that parts of the surface layer had delaminated and rolled up themselves while a comparable mesoporous layer as after the electrodegradation with lower power was present underneath the foil. By performing SIMS depth profiling it was found that the delaminated layer as well as the porous structure were highly Sr deficient indicating that they consisted of titanium oxide phases up to a depth of 60-100 nm. As origin for the delamination different thermal conductivities and thermal expansion coefficients of the new surface layer and the bulk can be regarded leading to a

The self-delamination of the new Ti-rich surface layer with a low thickness opened up the opportunity to investigate the structure on the nanoscale by transmission electron microscopy without further preparation. In Fig. 4.82, an image of one flake of the delaminated layer obtained in the high angle annular darkfield (HAADF) mode is shown. It can be seen that the flake was not homogeneous but consisted of grains showing different contrast in the image indicating phase separations on the nanoscale. Using energy electron loss spectroscopy (EELS), the spectrum at the Ti $L_{2,3}$ edge was recorded at different positions marked with numbers in Fig. 4.82. Inside the dark grains at the positions 1,3 and 5, the energy loss spectrum of Ti revealed one doublet corresponding to the valence 2+ [SLSN07], while outside of the grains at positions 2, 4 and 6 an additional valence was present proving the coexistence of different titanium oxide phases on the nanoscale.

The segregation on the nanoscale was not only related to Ti but also to Sr and Nb as shown by measurements using energy dispersive X-ray spectroscopy (EDX). The mapping of the elements presented in Fig. 4.83a, reveals that an agglomeration of Ti to grains with a size of 100-200 nm took place. In between these grains, a small amount of Sr was detected showing that not the entire Sr moved away from the surface layer during electrodegradation. With regard to the distribution of Nb within the flake, it can be seen that some irregularly spread clusters with significant higher Nb content and a size of 20-50 nm

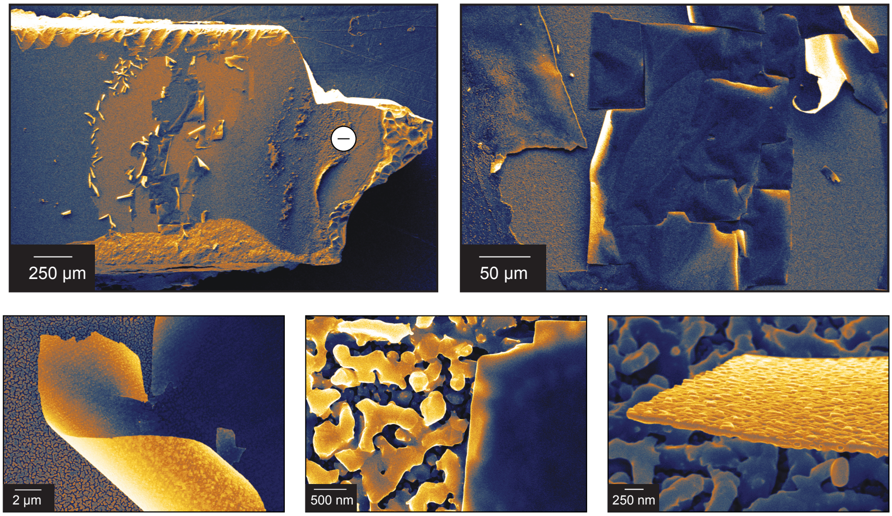

Figure 4.81.: SEM images of the cathode region after high-power electrodegradation.

had evolved. This shows at first that also the Nb was involved in the electrodegradation process in the surface layer and at second that in principle an Nb segregation on the nanoscale can take place as suggested during the discussion of the conducting clusters found in $SrTiO_3$:Nb (cf. Sec. 4.8).

In order to gain an insight in the crystallographic structure of the Ti-rich grains of the self-delaminated layer, a high-resolution transmission electron microscopy (HR-TEM) image was recorded shown in Fig. 4.83b. It can be clearly seen that a Moiré pattern was present indicating the superposition of two lattices with different lattice constants. Taking into account the spacing of the Moiré pattern of 2.7 nm, a superposition of the cubic structures of $SrTiO_3$ and TiO could explain the evolution of this pattern. This indicates that on the nanoscale, it was possible to generate a layer with a coexistence of different phases such as $SrTiO_3$, TiO and Ti_3O, which is not expected from the classical phase diagram of the Sr-Ti-O system. Hence, it can be concluded that during the application of electrical gradients to the surface layer of $SrTiO_3$:Nb, complex processes leading to

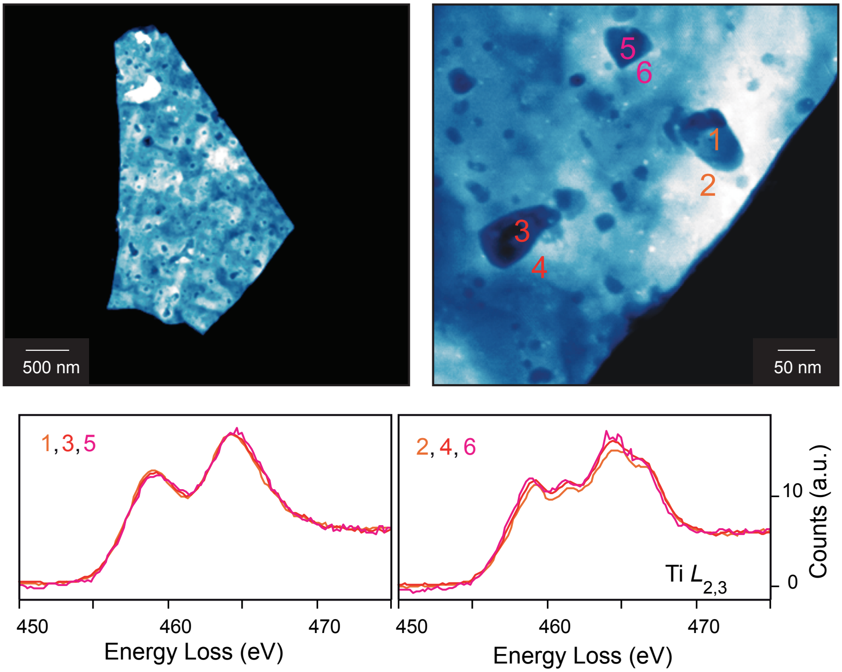

Figure 4.82.: HAADF and EELS measurements of the self-delaminated layer obtained by TEM.

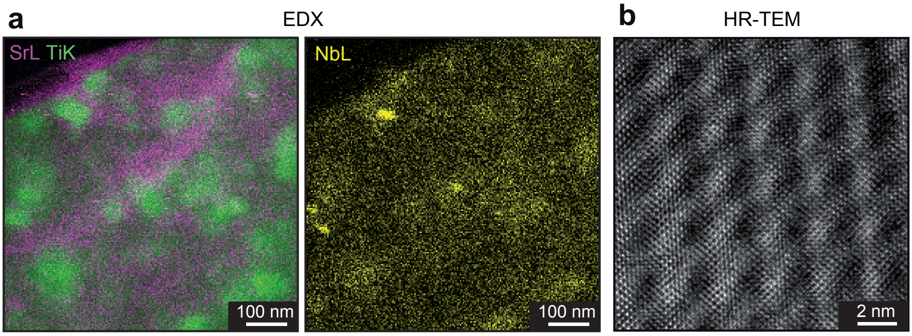

Figure 4.83.: (a) Distribution of the elements inside the delaminated layer measured by EDX. (b) HR-TEM image obtained inside a Ti-rich grain.

segregation and phase transformations can occur.

4.11.2. Potential phase change model of resistive switching

Based on the investigations of resistive switching on the nanoscale by LC-AFM and the observation of the phase transition between $SrTiO_3$ and TiO_x during electroreduction, a physical model of the cluster-like resistive switching process in the surface layer is presented in the following. Therefore, the following findings presented in this thesis were taken into account

- On top of the metallic bulk, a semiconducting surface layer exists.
- Ab-initio calculations demonstrated a correlation between an Sr excess and the suppression of metallic states.
- The chemical composition of the surface layer can be altered easily by external gradients.
- On the nanoscale, a cluster-like switching mechanism is present.
- Electrical gradients in combination with Joule heating can induce a phase transformation from $SrTiO_3$ to TiO_x

As already discussed in Sec. 4.10.4, it is reasonable to assume that resistive switching of the individual conducting clusters as seen by LC-AFM is realized by a switching of bridges between the clusters acting as nano-filaments. Finite element simulations revealed that during the switching or forming process the entire potential would drop in such a bridge leading to the presence of high electric fields. Hence, this situation is comparable to that during electrodegradation on the macroscale, which was found to induce a phase transformation from $SrTiO_3$ to various substoichiometric titanium oxides related to ionic movements under electrical gradients. In consideration of all these findings, a two-step model of resistive switching under electrical gradients applied via a conducting LC-AFM tip was developed as illustrated in Fig. 4.84.

In this model, it is assumed that the entire crystal consists of conducting clusters connected by bridges while the conduction through the surrounding matrix is neglected. Since the bulk of the crystal was found to be metallic irrespective of external gradients by means of electrical four-point measurements and investigations of the electronic structure and chemical composition using XPS, it is assumed that the clusters and bridges of the bulk are always in the metallic state. The as-received surface layer instead was found to be semiconducting and Sr-rich. Hence, resistive switching itself would take place between the topmost clusters forming the semiconducting as-received surface layer and the bulk. If a voltage is applied to one cluster of the semiconducting surface layer, a first electroforming step would be needed to reduce the Sr content of this cluster in order to reconstruct the same stoichiometry as in the clusters of the bulk. Since it was presented that Sr or SrO complexes are highly mobile under electrical gradients on the macroscale, it can be taken into account that such a movement directed from the surface layer towards the bulk also occurs during resistive switching on the nanoscale. After the Sr excess of the cluster in the surface layer would be reduced, it would have metallic properties. In this case the entire potential would drop in the region between the topmost cluster and the bulk cluster, which would induce such a high electric field that it may be conceivable that a phase transformation occurs resulting in the formation of a TiO_2 bridge connecting the two clusters.

In order to transform this bridge to the metallic state as well, which would be necessary to observe metallic conductivity at the topmost cluster when measuring the current by LC-AFM, a second step of electroformation would have to take place changing the crystallographic phase of the bridge from TiO_2 to a metallic substoichiometric titanium oxide such as the Magnéli phase Ti_4O_7. Since this would be a phase transition between different titanium oxides, it can be explained by a movement of oxygen ions towards the bulk serving as oxygen sink. After these electroforming steps the clusters as well as the bridge would be in the metallic state opening up a metallic conductance path between the AFM tip and the bulk connected to the bottom electrode.

Within the framework of this model, resistive switching itself between the metallic ON state and the semiconducting OFF state due to the application of a negative voltage to

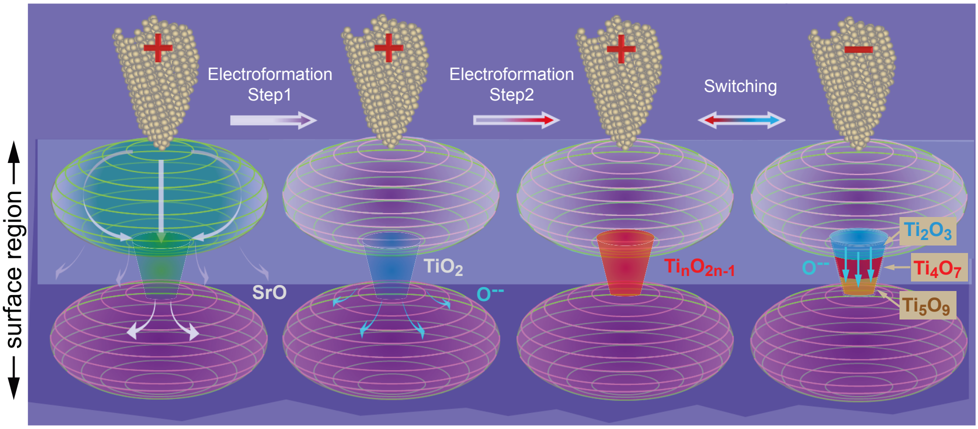

Figure 4.84.: Phase change model of the cluster-like resistive switching via the formation of a TiO_x nano-filament.

the tip would be then explained by a switching of the bridge. If only the bridge would be highly resistive again, the whole surface cluster would be measured to be in the OFF state since it lost its connection to the bulk. As illustrated on the right of Fig. 4.84, an internal movement of oxygen ions in the electric field from the bottom to the top of the bridge could then form semiconducting substoichiometric titanium oxides such as Ti_2O_3 and Ti_5O_9. Since this process would be reversible, an alternating switching between ON and OFF state would be possible by changing the polarity of the applied voltage.

In summary, a phenomenological model of the cluster-like resistive switching mechanism of $SrTiO_3$:Nb on the nanoscale was presented introducing bridges as nano-filaments between conducting clusters as decisive element for the resistance change. Due to the high electrical gradients inside these filaments, phase transformation processes were taken into account resulting in a model describing resistive switching as a phase transformation mechanism between the $SrTiO_3$ and several titanium oxides. Since the switching region itself would be confined to the bridge, this model indicates that in principle resistive switching can occur in very small volumes of only a few cubic nanometre in size. This indicates that memory devices with extremely high storage density could be designed if it would be possible to build structures with comparable properties as present in the bridges artificially.

	Paper	Electrodes	Methods	Proposed model
1	Sim H et al. (2005) In IEDM Tech. Dig. 758	Pt, Pd, Ti 0.01-10^4 µm²	I-V	Modulation of Schottky barrier by charge trapping
2	Seong D J et al. (2007) Elec. Solid-State Lett. **10** H168	Pt 30 x 30 µm²	I-V, XPS after H_2 annealing	Modulation of Schottky barrier improvement of RS by oxygen vacancies
3	Lee J et al. (2010) Curr. Appl Phys. **10** e68	Pt 50 x 50 µm²	I-V, impedance T-dependence	Modulation of Schottky barrier, generation of electrons from oxygen vacancies
4	Rana K G et al. (2012) Appl. Phys. Lett. **100** 213502	Au 250 x 650 µm²	I-V, 4 probe, Hall T-dependence	Redistribution of oxygen vacancies or defects at the interface
5	Seong D J et al. (2008) Jpn. J. Appl. Phys., Part 2 **47** 8749	Pt 30 x 30 µm²	I-V, C-V	Accumulation of oxygen vacancies and formation of tunneling paths
6	Shang D S et al. (2008) Appl. Phys. Lett. **93** 102106	Au 400 µm Ø	I-V, photoresponse	Presence of *active regions* being sensitive to external field at interface
7	Kan D et al. (2010) Thin Solid Films **518** 3246	Pt 50-100 µm Ø	I-V, C-V, time dependence	Intrinsical local conduction channels due to inhomogeneities responsible for RS
8	Zhang X T et al. (2010) Appl. Phys. Lett. **97** 222117	Pt, Ag 800 µm Ø	I-V, C-f, time dependence	Tunneling through depletion layer at interface leading to formation of filaments
9	Chen Y L et al. (2012) J. Appl. Phys. **112** 023703	Pt-Ir tip	STM, STS	Switching of blocks with 10-30 nm Ø due to oxygen migration
10	Yang M et al. (2014) J. Appl. Phys. **115** 134505	Pt 300 µm Ø	I-V, C-V, C-f time dependence	Switching of conducting filaments by oxygen vacancies
11	Mikheev E et al. (2014) Nat. Comm. **5** 3990	Pt 30 x 30 µm²	I-V, C-V, SIMS	Presence of interface layer leads to RS
12	This work	Pt 500 µm Ø Pt-Ir tip	I-V, C-V, SIMS, FLIM, XRD, 3D atom probe HR-LC-AFM, after degradation: XPS, EBSD, OM, SEM, EDX, EELS, HR-TEM	Phase transformation in bridges (nano-filaments) between clusters

Figure 4.85.: Models of resistive switching in $SrTiO_3$:Nb single crystals presented in literature.

Comparison to literature models

In comparison to other models of the resistive switching in $SrTiO_3$:Nb, the hypothetical model presented in this work stresses that ionic movement in the surface layer may play a bigger role than assumed by the majority of previous models. In particular, the observed conducting clusters in combination with eightwise switching polarity show that switching in $SrTiO_3$:Nb is a complex phenomenon which is not purely filamentary and also not purely interfacial. However, the presented model gives only a rough idea how the switching on the nanoscale could work and some fundamental assumptions should be reviewed if improved experimental methods are able to provide a more detailed insight into the properties of the surface layer on the atomic scale. Hence, the presented model does not exclude the potential applicability of other models, which however also did not succeed so far to describe all details of the switching process. As can be seen in Fig. 4.85 and already discussed in Sec. 2.6.4, the models proposed in literature can be distinguished between interfacial models taking into account a global modulation of the Schottky barrier between the oxide and the electrode (Fig. 4.85, 1-5) and local models proposing the formation of conducting and switchable filaments (Fig. 4.85, 6-10). However, most of those models are only based on electrical measurements obtained on devices with rather large electrodes as listed in Fig. 4.85. Investigations using scanning probe methods such as STM measurements performed by Chen et at. [CWX+12] (Fig. 4.85, 9) and LC-AFM measurements as shown in this work clearly reveal that the conductivity of the surface is inhomogeneous on the nanoscale related to switching blocks with a diameter of 10-50 nm, which gives favour to local filamentary models. Using various characterization techniques, in this work (see also [RWWS13, RSB+13, RGS+13, RJH+14]), a surface region with different properties than the bulk was identified as region where the switching related to an insulator-metal transition takes place. The surface region was found to be highly sensitive on external gradients such as reduction, oxidation and ion bombardment. This is in agreement with the investigations of Mikheev et al. [MHSS14] (Fig. 4.85, 10), who also attributed the switching to the formation of a surface layer depending on the conditions during electrode deposition. Furthermore, distinct inhomogeneities on the nanoscale were found by means of the surface-sensitive techniques LC-AFM and SKPM, which would support the suggestion of Kan et al. [KIS10] (Fig. 4.85, 7) that intrinsic inhomogeneities facilitate the formation of conducting filaments. As a new aspect, it was demonstrated in this thesis using various high-resolution techniques that the stoichiometry of the surface region can be altered significantly using chemical or electrical gradients until phase transformations from $SrTiO_3$ to TiO_x or SrO take place. Since this fact was not yet taken into account in literature, the proposed hypothetical formation of a switching bridge consisting of titanium suboxides could give inspiration to improve and enhance the present models leading to a deeper understanding of the resistive switching on the nanoscale. Since the process of the resistive switching itself is modelled by a movement of oxygen or oxygen vacancies within the bridge leading to the formation of metallic or insulating Magnéli phases it can be noted that the main idea of the presented model is in agreement with the majority of models from the literature claiming that the redistribution of oxygen vacancies under an electric field is the decisive step for switching the resistance. However, it is obvious that although the hypothetical model is based on a variety of investigations, two essential questions remain open at the end of this thesis. First of all, the nature of the cluster observed on the surface of $SrTiO_3$:Nb is still not completely understood. It was discussed that a potential clustering of Nb could be made responsible for the enhanced conductivity inside the clusters but by means of the available methods, it is not possible to give a direct proof for a Nb clustering on the nanoscale due to limited spatial or chemical resolution. Alternatively, it could be assumed that Nb is distributed homogeneously on the nanoscale which would demand for a different explanation for the observed cluster-like switching mechanism. Second, the formation of TiO_x nano-filaments that was proposed to take place in a electroforming step between the conducting clusters could not be observed in situ. Since such a transformation was unambiguously observed after electrodegradation on the macroscale, the assumption of the presence of phase transformations on the nanoscale is to some extend reasonable, but a direct evidence for the formation of nano-filaments in $SrTiO_3$:Nb remains a challenging task for future research.

5. Conclusions

The present thesis focused on the phenomenon of resistive switching in oxides. In order to understand the insulator-to-metal transition occurring during the switching between a high resistive OFF state and a low resistive ON state, the model material $SrTiO_3$, donor-doped with Nb was chosen serving as a reference material for many other oxides. Single crystals were investigated due to two reasons. On the one hand, the analysis of the properties of single crystals and their reaction on external gradients provides an insight into the fundamental physical phenomena taking place during an insulator-to-metal transition, which is needed in order to design and produce functional logic or memory devices based on the resistive switching effect. On the other hand, the characterization of the basic properties of $SrTiO_3$:Nb single crystals is by itself highly relevant from a technological point of view since they are commonly used as conducting substrates for the growth of perovskite thin films.

As a guideline for the investigations presented in this thesis, the question "How is it possible to switch a metallic material?" was regarded, since the observation of resistive switching in donor-doped $SrTiO_3$ is in principle a paradoxical phenomenon. Due to the charge compensation mechanism, the substitution of Ti^{4+} by Nb^{5+} leads to a valence change of the neighbouring Ti atoms, which should result in metallic behaviour at sufficiently high donor concentration. Although a number of researchers studied resistive switching in $SrTiO_3$:Nb single crystals and thin films, thereby presenting various models for the switching mechanism, the fundamental problem of observing an insulator-to-metal transition in a system, which already should have metallic properties was not discussed in literature so far. In this thesis, it was presented on the basis of careful characterizations of the properties of the single crystal under influence of external gradients that an intrinsic surface layer with different properties than the bulk is present, which is responsible for the unusual properties of $SrTiO_3$:Nb and resistive switching as summarized in the following.

Structure and quality of the crystals

$SrTiO_3$ single crystals grown by the Verneuil method with three different doping concentrations were investigated. By X-ray diffraction measurements it was revealed that all samples were crystallized in the perovskite structure and no evidence for the existence of significant amounts of secondary phases were found indicating that in principle the crystal growth was successful. However, the comparison of the measured density with the theoretical density extracted from the XRD results showed distinct deviations that cannot be explained by the existence of point defects, which is hint for the existence of structural defects. Additionally, X-ray topography measurements demonstrated that the investigated crystals had a distinct mosaicity related to the existence of differently orientated crystallographic phases.

In order to characterize the imperfections of the crystallographic structure, various methods were applied showing that a significant number of dislocations was present in the crystals. In comparison of crystals with different doping concentrations, which were grown and polished by different manufacturers, the highest doped one (10.1 at%) was found to have the highest amount of structural defects and furthermore was contaminated by additional elements. But also the crystal doped with 1.4 at% of Nb, which is frequently used as conducting substrate for the deposition of oxide thin films, had a high dislocation density of $10^8/\mathrm{cm}^2$.

Nb distribution

Since the electronic properties of the material strongly depend on the donor concentration, great care was taken in order to determine the spatial distribution of Nb in the crystals. Using optical methods such as optical microscopy, confocal Raman microscopy and fluorescence-lifetime imaging microscopy distinct modulations of the optical properties were found on the microscale that were correlated to the Nb content by comparison to reference sample as well as by direct mapping of the Nb distribution by SIMS. This involves that also the electronic properties vary on the microscale, which has to be taken into account when estimating the suitability of the Verneuil grown crystals for future applications.

Surface layer

As mentioned above, the evidence of the existence of a surface layer with different properties that expected was the key for the understanding of resistive switching of a nominally metallic material. Using X-ray photoelectron spectroscopy (XPS) before and after removal of the surface layer of the crystals under UHV conditions it was revealed that in contrast to the bulk the as-received surface layer had a slight Sr excess and did not show electronic states close to the Fermi edge. Based on *ab-initio* calculations, it was concluded that the presence of an Sr excess disturbs the electronic structure of $SrTiO_3$:Nb thus suppressing the metallicity.

By exposing the surface layer to different external gradients it was found that the surface layer is highly variable and an insulator-to-metal transition can be induced easily by electrical and chemical gradients. Such a transition not only changes the electronic properties but involves ionic movements leading to a change of the stoichiometry. Particularly, heating under oxidizing or reducing conditions can alter the ratio of the elements Sr and Ti to values far away from the stoichiometry range of $SrTiO_3$, which indicates the possibility of inducing phase change mechanisms from $SrTiO_3$ to strontium oxide or substoichiometric titanium oxides in the surface layer due to the small stoichiometric limit of $SrTiO_3$.

Besides the global inhomogeneity of the crystal between surface layer and bulk, an additional inhomogeneity on the nanoscale was found to be present in $SrTiO_3$:Nb single crystals. By scanning Kelvin probe microscopy it was revealed that a cluster like structure was present in the distribution of the surface potential. A similar structure was also found in the local conductivity by AFM measurements in contact mode. This shows that the electronic transport phenomena and particularly resistive switching can only be understood by taking into account the complex inhomogeneous structure on the nanoscale.

Resistive switching

Resistive switching phenomena were investigated by electrical measurements on the macro- and nanoscale. By electrical four-point measurements in Valdes geometry being capable to characterize surface layer and bulk during the application of electrical gradients independently it was found out that only the surface layer is affected during resistive switching while the bulk always has metallic properties. Hence, the consideration of an intrinsic semiconducting surface layer with different stoichiometry than the bulk as location of resistive switching can sufficiently resolve the contradiction of observing resistive switching in a nominally metallic system.

In order to understand the resistive switching mechanism itself, switching experiments on the nanoscale were performed by LC-AFM. By scanning the surface with a writing voltage of around 4 V and subsequent measuring of the switched area with lower reading voltage of around 10 mV it was revealed that resistive switching is related to the conducting clusters determine the conductivity on the nanoscale. Using the novel technique of HR-LC-AFM allowing the observation of the local conductivity with atomic resolution, the structure of the clusters were investigated in detail. They were found to have a diameter of 30-60 nm and can be switched independently from each other between ON and OFF state thus serving as intrinsic resistive switching block. This finding illustrates that doping $SrTiO_3$ with Nb significantly changes the switching mechanism from a purely filamentary as was found in undoped $SrTiO_3$ to a cluster-like switching mechanism. Hence, Nb segregation effects were suggested as origin of the conducting clusters.

The observation of a cluster-like switching mechanism by LC-AFM illustrates that the switching mechanism itself is very complex and cannot be described in terms of models taking only into account the modulation of the Schottky barrier between oxide and electrode under an electric field as origin of the switching as presented in literature. Hence, an alternative model of the nanoscale nature of resistive switching in $SrTiO_3$:Nb was developed in the present thesis. Since the conducting cluster always switched as a whole and independently of each other, it was suggested that not the clusters themselves but small bridges connecting the clusters are switching as nano-filaments. Since in the region between the clusters high electric fields are present during the application of a switching voltage, it can be concluded that ionic movements within this region could take place forming the nano-filament. In order to gain an insight into these potential ionic movements under electrical gradients, resistive switching on the nanoscale was emulated on the macroscale by electrodegradation experiments. Under vacuum conditions, a DC voltage was applied to a macroscopic crystal resulting in a transformation of the surface layer with time. Close to the cathode, a new porous Ti-rich surface layer evolved consisting of several substoichiometric titanium oxides, which even delaminated itself under heavier electroreduction. This experiment, which may furthermore serve as a template for the production of functional titanium oxide structures needed in various future technologies, clearly revealed that Sr or SrO complexes are highly mobile in the surface layer under electrical gradients leading to a phase transformations. By adapting this result to the situation during resistive switching on the nanoscale, a hypothetical model was suggested describing the electroforming of the nano-filaments between the conducting clusters as a phase change mechanism between $SrTiO_3$ to TiO_x and the subsequent resistive switching as a change between different metallic and insulating substoichiometric titanium oxides.

Outlook

The proposal of a model of resistive switching in $SrTiO_3$ taking into account phase change mechanisms introduces a new dimension in the understanding of the resistive switching effect in materials, which were supposed to belong to the class of valence change materials. The additional consideration of significant ionic movements as driving force for the evolution of switchable filaments may have the potential to bridge the gap between the theory of the valence change mechanism and other mechanisms such as the electrochemical metallization mechanism, which could lead to a more fundamental and general understanding of the resistive switching effect. In order to judge if the presented hypothetical phase-transformations model or other models are more applicable to describe the processes during resistive switching, a closer insight into the physical processes on the atomic scale would be needed such as a direct prove for the formation of nano-filaments. Regarding the enormous progress in high-resolution techniques such as HR-TEM or 3D atom probe, it can be expected that in future appropriate techniques will be available, which could lead to a more fundamental model of resistive switching.

The investigations presented in this thesis revealed the existence of inhomogeneities in different scales influencing the properties of the material and showing the challenges for the design and development of potential functional devices. On the one hand, one could take effort in order to avoid such effects by improving the crystal growth and sample preparation techniques. On the other hand, the intrinsic inhomogeneities found on the nanoscale may also serve as a template for self-structuring effects, which may be exploited in future by controlling the evolution of structural defects thus building up materials with bespoke properties on the nanoscale.

From the experimental point of view, the main challenge for the understanding the mechanisms during resistive switching is the investigation of the properties of the switching blocks on the nanoscale with highest precision. The standard method for the inspection of small structures on the nanoscale with atomic resolution is transmission electron microscope (HR-TEM), which is related to a preparation of a thin sample by focused ion beam. As shown in this thesis, such a preparation by ion bombardment can significantly change the properties of oxide materials complicating the investigation of switching blocks or filaments. In order to avoid this preparation step, the observed delamination of a self-supporting surface layer under electrical gradients can be used as a potential guideline for the creation of specimens for TEM investigations without further external preparation.

Furthermore, HR-LC-AFM measurements with atomic resolution are presented in this thesis in order to investigate the electronic transport of switching clusters in $SrTiO_3$ on the atomic lengthscale for the first time. In future, this novel technique has the potential to uncover the conduction and switching mechanisms in many different classes of materials, which may open up a new chapter in surface science.

Bibliography

[AAJC95] M. J. Akhtar, Z.-U.-N. Akhtar, R. A. Jackson, and C. R. A. Catlow. Computer-simulation studies of Strontium-Titanate. *J. Am. Ceram. Soc.*, 78(2):421–428, 1995.

[AB02] R. Astala and P. Bristowe. First principles calculations of niobium substitution in strontium titanate. *J. Phys. Condens. Mat.*, 14(6):L149–L156, 2002.

[ABBN] J. W. Anthony, R. A. Bideaux, K. W. Bladh, and M. C. Nichols, editors. *Handbook of Mineralogy.* Mineralogical Society of America, http://www.handbookofmineralogy.org/.

[AKME09] V. E. Alexandrov, E. A. Kotomin, J. Maier, and R. A. Evarestov. First-principles study of bulk and surface oxygen vacancies in $SrTiO_3$ crystal. *Eur. Phys. J. B Condens. Matter.*, 72(1):53–57, 2009.

[AKWO98] Y. Adachi, S. Kohiki, K. Wagatsuma, and M. Oku. Intrinsic and extrinsic surface states of single crystalline $SrTiO_3$. *J. Appl. Phys.*, 84(4):2123–6, 1998.

[Alb] J.-M. Albina. Atomistic simulations of (111) stacking faults in $SrTiO_3$. *HPC Europa-2 Project report*, www2.epcc.ed.ac.uk/˜europa/HPCE2/Reports/0080_Albina.pdf.

[AM56] S. Andersson and A. Magnéli. Diskrete Titanoxydphasen im Zusammensetzungsbereich $TiO_{1,75}$-$TiO_{1,90}$. *Naturwissenschaften*, 43:495–496, 1956.

[Arg68] F. Argall. Switching phenomena in titanium oxide thin films. *Solid-State Electron.*, 11(5):535–541, 1968.

[Ask94] B. M. Askerov. *Electron Transport Phenomena in Semiconductors.* World Scientific, 1994.

[AvDvLvT08] S. Amelinckx, D. van Dyck, J. van Landuyt, and G. van Tendeloo, editors. *Electron Microscopy: Principles and Fundamentals.* John Wiley & Sons, 2008.

[Bac09] D. Bach. *EELS investigations of stoichiometric niobium oxides and niobium-based capacitors.* PhD thesis, Universität Karlsruhe, 2009.

[Bal74] A. A. Balchin. X-ray topography. *Phys. Educ.*, 9(2):97, 1974.

[Bar47] J. Bardeen. Surface States and Rectification at a Metal Semi-Conductor Contact. *Phys. Rev.*, 71(10):717–727, 1947.

[BBG+00] A. Beck, J. G. Bednorz, C. Gerber, C. Rossel, and D. Widmer. Reproducible switching effect in thin oxide films for memory applications. *Appl. Phys. Lett.*, 77(1):139–41, 2000.

[BBP07] C. Bernard, E. Blanquet, and M. Pons. Chemical vapor deposition of thin films and coatings: Evaluation and process modeling. *Surf. Coat. Technol.*, 202(4-7):790–797, 2007.

[BBS+78] D. Bäuerle, W. Braun, V. Saile, G. Sprüssel, and E. E. Koch. Vacuum Ultraviolet Reflectivity and Band-structure of $SrTiO_3$ and $BaTiO_3$. *Z. Phys. B*, 29(3):179–184, 1978.

[BCK05] H. Butt, B. Cappella, and M. Kappl. Force measurements with the atomic force microscope: Technique, interpretation and applications. *Surf. Sci. Rep.*, 59(1-6):1–152, 2005.

[BE81] U. Balachandran and N. G. Eror. Electrical conductivity in strontium titanate. *J. Solid State Chem.*, 39(3):351 – 359, 1981.

[BE82] U. Balachandran and N.G. Eror. Raman Spectra of Strontium Titanate. *J. Am. Ceram. Soc.*, 65(4):C54–C56, 1982.

[BGG+12] R. Buzio, A. Gerbi, A. Gadaleta, L. Anghinolfi, F. Bisio, E. Bellingeri, A. S. Siri, and D. Marrè. Modulation of resistance switching in Au/Nb:$SrTiO_3$ Schottky junctions by ambient oxygen. *Appl. Phys. Lett.*, 101(24):243505, 2012.

[BHH+08] P. Blennow, A. Hagen, K. K. Hansen, L. R. Wallenberg, and M. Mogensen. Defect and electrical transport properties of Nb-doped $SrTiO_3$. *Solid State Ion.*, 179(35-36):2047–2058, 2008.

[BHWM09] P. Blennow, K. K. Hansen, L. R. Wallenberg, and M. Mogensen. Electrochemical characterization and redox behavior of Nb-doped $SrTiO_3$. *Solid State Ion.*, 180(1):63+, 2009.

[BK99] D. Brandon and W. D. Kaplan. *Microstructural Characterization of Materials.* John Wiley & Sons, 1999.

[BK13] E. M. Bourim and D. W. Kim. Conductance spectroscopy of resistive switching Pt/Nb:STO single crystal Schottky junctions in air and vacuum. *Curr. Appl. Phys.*, 13(3):505–509, 2013.

[BMK+11] A. Brandao, J. F. Monteiro, A. V. Kovalevsky, D. P. Fagg, V. V. Kharton, and J. R. Frade. Guidelines for improving resistance to CO_2 of materials for solid state electrochemical systems. *Solid State Ion.*, 192(1):16–20, 2011.

[BMM+96] A. E. Bocquet, T. Mizokawa, K. Morikawa, A. Fujimori, S. R. Barman, K. Maiti, D. D. Sarma, Y. Tokura, and M. Onodas. Electronic structure of early 3d-transition-metal oxides by analysis of the 2p core-level photoemission spectra. *Physical Review B*, 53(3):1161–1170, 1996.

[Böe92] K. W. Böer. *Survey of Semiconductor Physics Volume II.* Springer, 1992.

[BQG86] G. Binnig, C.F. Quate, and C. Gerber. Atomic force microscope. *Phys. Rev. Lett.*, 56(9):930–933, 1986.

[Bre13] U. Breuer. Private communication. 2013.

[BS77] J. G. Bednorz and H. J. Scheel. Growth of $SrTiO_3$ Crystals using Verneuil Method. *Z. Kristall.*, 146(1-3):91–91, 1977.

[BS81] G. Barbosa and J. Dos Santos. Relaxation Mode in $SrTiO_3$ - a Mode to Test Melting Models? *J. Raman Spectrosc.*, 10:100–102, 1981.

[BSW36] L. P. Bouckaert, R. Smoluchowski, and E. Wigner. Theory of Brillouin Zones and Symmetry Properties of Wave Functions in Crystals. *Phys. Rev.*, 50:5867, 1936.

[BZBH08] M. Bäurer, L. F. Zagonel, N. Barrett, and M. J. Hoffmann. Changes in macroscopic behaviour through segregation in Niobium doped Strontium Titanate. In *Symposium on Interfacial Nanostructures in Ceramics held at the 2007 E-MRS Spring Meeting, Strasbourg, FRANCE*, pages 12015/1–6. Interfacial Nanostructures in Ceramics: a Multiscale Approach, 2008.

[Car65] M. Cardona. Optical Properties and Band Structure of $SrTiO_3$ and $BaTiO_3$. *Phys. Rev.*, 140(2A):A651, 1965.

[Car08] F. Cardarelli. *Materials handbook : a concise desktop reference.* Springer, 2008.

[CF89] J. Chen and D. A. Feng. Crystallographic shear planes and stacking disorders in perovskites $KNbO_3$ and $NaNbO_3$. *phys. stat. sol. (a)*, 116(1):231–235, 1989.

[Cho65] K. L. Chopra. Avalanche-induced negative resistance in thin oxide films. *J. Appl. Phys.*, 36:184–187, 1965.

[Chu10] D. D. L. Chung. *Functional Materials: Electrical, Dielectric, Electromagnetic, Optical and Magnetic Applications.* World Scientific, 2010.

[CKD02] S. Y. Chung, S. J. L. Kang, and V. P. Dravid. Effect of sintering atmosphere on grain boundary segregation and grain growth in niobium-doped $SrTiO_3$. *J. Am. Ceram. Soc.*, 85(11):2805–2810, 2002.

[CLS+06] D. Choi, D. Lee, H. Sim, M. Chang, and Hwang H. Reversible resistive switching of $SrTiO_x$ thin films for nonvolatile. *Appl. Phys. Lett.*, 88:082904, 2006.

[CM63] A. Cocco and F. Massazza. Microscopic study of the system SrO-TiO_2. *Ann. Chim. (Rome)*, 53:892, 1963.

[CMY+11] X. G. Chen, X. B. Ma, Y. B. Yang, L. P. Chen, G. C. Xiong, G. J. Lian, Y. C. Yang, and J. B. Yang. Comprehensive study of the resistance switching in $SrTiO_3$ and Nb-doped $SrTiO_3$. *Appl. Phys. Lett.*, 98(12):122102/1–3, 2011.

[COPS96] F. A. Chudnovskii, L. L. Odynets, A. L. Pergament, and G. B. Stefanovich. Electroforming and switching in oxides of transition metals: the role of metal-insulator transition in the switching mechanism. *J. Solid State Chem.*, 122(1):95–9, 1996.

[Cow64] R. A. Cowley. Lattice dynamics and phase transitions of strontium titanate. *Phys. Rev.*, 134:A981–A997, 1964.

[Cox95] P. A. Cox. *Transition Metal Oxides: An Introduction to Their Electronic Structure and Properties.* Clarendon Press, 1995.

[CSS06] H. Czichos, T. Saito, and L. Smith, editors. *Springer Handbook of Materials Measurement Methods.* Springer, 2006.

[CWX+12] Y. L. Chen, J. Wang, C. M. Xiong, R. F. Dou, J. Y. Yang, and J. C. Nie. Scanning tunneling microscopy/spectroscopy studies of resistive switching in Nb-doped $SrTiO_3$. *J. Appl. Phys.*, 112(2):023703, 2012.

[DBPD10] G. Dhanaraj, K. Byrappa, V. Prasad, and M. Dudley, editors. *Springer Handbook of Crystal Growth.* Springer, 2010.

[DFC+13] T. Ding, Y. Fang, L. Chen, S. Huang, and Y. Chen. Electric-pulse-controlled Schottky-like/Ohmic contact for Ag/Nb-doped $SrTiO_3$ junctions. *Mater. Sci. Semicond. Process.*, 16(4):1105–1108, 2013.

[DHT11] T. Dieing, O. Hollricher, and J. Toporski, editors. *Confocal Raman Microscopy.* Springer, 2011.

[dR96] D. de Ligny and P. Richet. High-temperature heat capacity and thermal expansion of $SrTiO_3$ and $SrZrO_3$ perovskites. *Physical Review B*, 53(6):3013–3022, 1996.

[DSDV77] V. Dekanenko, Z. Samoilenko, E. Darovskikh, and V. Vavilova. Stabilization of Ti_3O structure by niobium. *Inorg. Mater.*, 13(1):75–78, 1977.

[DSW90] W. Denk, J. Strickler, and W. Webb. Two-photon laser scanning fluorescence microscopy. *Science*, 248(4951):73–76, 1990.

[EK10] R. I. Eglitis and E. A. Kotomin. Ab initio calculations of Nb doped $SrTiO_3$. *Physica B*, 405(15):3164–3166, 2010.

[EWH78] S. Ellialtioğlu, T. Wolfram, and V. Henrich. Surface-states on n-type $SrTiO_3$. *Solid State Comm.*, 27(3):321–324, 1978.

[FBKS07] W. Frammelsberger, G. Benstetter, J. Kiely, and R. Stamp. C-AFM-based thickness determination of thin and ultra-thin SiO_2 films by use of different conductive-coated probe tips. *Appl. Surf. Sci.*, 253(7):3615–3626, 2007.

[FG03] P. Fang and H. Gu. Dopant distribution in microstructure of Nb_2O_5-doped $SrTiO_3$ ceramics. *Key Eng. Mat.*, 247:323–326, 2003.

[Fle] The Juelich FLEUR project: www.flapw.de.

[FW85] M. Fujimoto and M. Watanabe. Ti_nO_{2n-1} Magnéli phase formation in $SrTiO_3$ dielectrics. *J. Mater. Sci.*, 20(10):3683–3690, 1985.

[GBF$^+$03] A. Gunhold, L. Beuermann, M. Frerichs, V. Kempter, K. Gomann, G. Borchardt, and W. Maus-Friedrichs. Island formation on 0.1 at.% La-doped $SrTiO_3$(100) at elevated temperatures under reducing conditions. *Surf. Sci.*, 523(1-2):80–88, 2003.

[GBKO11] H. Gross, N. Bansal, Y. Kim, and S. Oh. In situ study of emerging metallicity on ion-bombarded $SrTiO_3$ surface. *J. Appl. Phys.*, 110:073704, 2011.

[GCS$^+$03] X. G. Guo, X. S. Chen, Y. L. Sun, L. Z. Sun, X. H. Zhou, and W. Lu. Electronic band structure of Nb doped $SrTiO_3$ from first principles calculation. *Phys. Lett. A*, 317(5-6):501–506, 2003.

[GGB$^+$02] A. Gunhold, K. Gomann, L. Beuermann, M. Frerichs, G. Borchardt, V. Kempter, and W. Maus-Friedrichs. Geometric structure and chemical composition of $SrTiO_3$ surfaces heated under oxidizing and reducing conditions. *Surf. Sci.*, 507:447–452, 2002.

[GHH85] R. K. Goodall, R. J. Higgins, and J. P. Harrang. Capacitance measurements of a quantized two-dimensional electron-gas in the regime of the quantum hall-effect. *Physical Review B*, 31(10):6597–6608, 1985.

[GLS$^+$10] M. Gwon, E. Lee, A. Sohn, E. M. Bourim, and D. W. Kim. Doping-level Dependences of Switching Speeds and the Retention Characteristics of Resistive Switching Pt/$SrTiO_3$ Junctions. *J. Kor. Phys. Soc*, 57(6):1432–1436, 2010.

[GLSS$^+$07] T. Glatzel, M.C. Lux-Steiner, E. Strassburg, A. Boag, and Y. Rosenwaks. Principles of Kelvin Probe Force Microscopy. In Sergei Kalinin and Alexei Gruverman, editors, *Scanning Probe Microscopy*, pages 113–131. Springer New York, 2007.

[GM80] R. Gruehn and W. Mertin. Die hochauflösende Transmissionselektronenmikroskopie – eine noch junge Untersuchungsmethode der Festkörperchemie. *Angewandte Chemie*, 92:531–546, 1980.

[GMG98] P. Ghosez, J. P. Michenaud, and X. Gonze. Dynamical atomic charges: The case of ABO_3 compounds. *Phys. Rev. B*, 58(10):6224–6240, 1998.

[Göm05] A. Gömann. *Das Verhalten von donatordotierten $SrTiO_3$-Oberflächen unter Hochtemperaturbehandlung.* PhD thesis, Technische Universität Clausthal, 2005.

[GSG$^+$09] N. P. Guisinger, T. S. Santos, J. R. Guest, T. Y. Chien, A. Bhattacharya, J. W. Freeland, and M. Bode. Nanometer-Scale Striped Surface Terminations on Fractured $SrTiO_3$ Surfaces. *ACS Nano*, 3(12):4132–4136, 2009.

[HAB$^+$97] Y. Haruyama, Y. Aiura, H. Bando, H. Suzuki, and Y. Nishihara. Surface electronic structure of electron-doped $SrTiO_3$. *Physica B*, 237:380–382, 1997.

[Hal87] J. Halbritter. On the Oxidation and on the Superconductivity of Niobium. *Appl. Phys. A Mater. Sci. Process.*, 43(1):1–28, 1987.

[Ham09] A. S. Hamid. Atomic and electronic structure of oxygen vacancies and Nb-impurity in $SrTiO_3$. *Appl. Phys. A Mater. Sci. Process.*, 97(4):829–833, 2009.

[Hay02] P. C. S. Hayfield. *Development of a New Material.* Royal Society of Chemistry, 2002.

[HB11] D. Hull and D. J. Bacon. *Introduction to Dislocations, Fifth Edition.* Elsevier, 2011.

[HCG$^+$10] G. Herranz, O. Copie, A. Gentils, E. Tafra, M. Basletic, F. Fortuna, K. Bouzehouane, S. Fusil, E. Jacquet, C. Carretero, M. Bibes, A. Hamzic, and A. Barthelemy. Vacancy defect and carrier distributions in the high mobility electron gas formed at ion-irradiated $SrTiO_3$ surfaces. *J. Appl. Phys.*, 107(10):103704, 2010.

[HDZ78] V. Henrich, G. Dresselhaus, and H. Zeiger. Surface defects and the electronic structure of $SrTiO_3$ surfaces. *Phys. Rev. B*, 17(12):4908–4921, 1978.

[HEK$^+$02] E. Heifets, R. Eglitis, E. Kotomin, J. Maier, and G. Borstel. First-principles calculations for $SrTiO_3$(100) surface structure. *Surf. Sci.*, 513(1):211–220, 2002.

[HH65] W. R. Hiatt and T. W. Hickmott. Bistable switching in niobium oxide diodes. *Appl. Phys. Lett.*, 6:106–108, 1965.

[HHL$^+$96] T. Hochwitz, A. Henning, C. Levey, C. Daghlian, and J. Slinkman. Capacitive effects on quantitative dopant profiling with scanned electrostatic force microscopes. *J. Vac. Sci. Technol. B*, 14(1):457–462, 1996.

[Hic69] T.W. Hickmott. Electroluminescence, Bistable Switching, and Dielectric Breakdown of Nb_2O_5 Diodes. *J. Vac. Sci. Technol.*, 6(5):828–833, 1969.

[HIC$^+$03] L. Q. Han, N. Iizawa, Y. Chiba, T. Yoneta, A. Kaimai, K. Yashiro, H. Yugami, Y. Nigara, T. Kawada, and J. Mizusaki. Electrical properties of the surface layer formed on the Nb-doped $SrTiO_3$ single crystal. In K. Uematsu and H. Yokokawa, editors, *5th International Workshop on Interfaces of Ceramic Materials, Tsukuba, Japan*, pages 29–41, 2003.

[HL12] W. M. Haynes and D. R. Lide, editors. *CRC handbook of chemistry and physics.* CRC Press, 93 edition, 2012.

[Hof10] S. Hoffmann-Eifert. Point defects – disorder thermodynamics and kinetics. In S. Blügel, T. Brückel, R. Waser, and C. M. Schneider, editors, *Electronic oxides - Correlation Phenomena, Exotic Phases and Novel Functionalities.* Forschungszentrum Jülich GmbH, 2010.

[HTK$^+$00] T. Higuchi, T. Tsukamoto, K. Kobayashi, Y. Ishiwata, M. Fujisawa, T. Yokoya, S. Yamaguchi, and S. Shin. Electronic structure in the band gap of lightly doped $SrTiO_3$ by high-resolution x-ray absorption spectroscopy. *Phys. Rev. B*, 61(19):12860–12863, 2000.

[HY03] K. Hung and W. Yang. X-ray photoelectron spectroscopy and electrical properties studies of nonstoichiometric Nb_2O_5-doped strontium titanate ceramics prepared by sol-precipitation process. *Mater. Sci. Eng. A-Struct. Mater. Prop. Microstruc*, 351(1-2):70–80, 2003.

[ISW96] J. T. S. Irvine, P. R. Slater, and P. A. Wright. Synthesis and Electrical Characterisation of the Perovskite Niobate-Titanates, $Sr_{1-x/2}Ti_{1-x}Nb_xO_{3-\delta}$. *Ionics*, 2(3-4):213–216, 1996.

[JTK$^+$12] D. Jeong, R. Thomas, R. Katiyar, J. Scott, H. Kohlstedt, A. Petraru, and C. Hwang. Emerging memories: Resistive switching mechanisms and current status. *Rep. Prog. Phys.*, 75(7), 2012.

[JTU05] C. L. Jia, A. Thust, and K. Urban. Atomic-scale analysis of the oxygen configuration at a $SrTiO_3$ dislocation core. *Phys. Rev. Lett.*, 95(22):225506/1–4, 2005.

[Kän55] W. Känzig. Space charge layer near the surface of a ferroelectric. *Phys. Rev.*, 98:549–550, 1955.

[Kar] Fachinformationszentrum (FIZ) Karlsruhe. ICSD - Inorganic crystal structure database https://icsd.fiz-karlsruhe.de.

[Kik28] S. Kikuchi. Diffraction of Cathode Rays by Mica. *Jpn. J. Phys*, 5:8396, 1928.

[KIS10] D. Kan, K. Ito, and Y. Shimakawa. Local conduction in junctions composed of Pt and single-crystalline Nb-doped $SrTiO_3$. *Thin Solid Films*, 518(12):3246–3249, 2010.

[Kit04] C. Kittel. *Introduction to Solid State Physics, 8th Edition.* John Wiley & Sons, 2004.

[KL64] A. H. Kahn and A. J. Leyendecker. Electronic Energy Bands in Strontium Titanate. *Phys. Rev.*, 135(5A):1321, 1964.

[KML+77] S. Kowalczyk, F. McFeely, L. Ley, V. Gritsyna, and D. Shirley. Electronic-structure of $SrTiO_3$ and some simple related oxides (MgO, Al_2O_3, SrO, TiO_2). *Solid State Comm.*, 23(3):161–169, 1977.

[KP10] M. S. Kim and C. H. Park. GW Calculation of the Electronic Structure of Cubic Perovskite $SrTiO_3$. *J. Kor. Phys. Soc*, 56(1):490–493, 2010.

[KTA+06] K. Kinoshita, T. Tamura, M. Aoki, Y. Sugiyama, and H. Tanaka. Bias polarity dependent data retention of resistive random access memory consisting of binary transition metal oxide. *Appl. Phys. Lett.*, 89(10):103509–1–3, 2006.

[KTK+05] D. Kan, T. Terashima, R. Kanda, A. Masuno, K. Tanaka, S. Chu, H. Kan, A. Ishizumi, Y. Kanemitsu, Y. Shimakawa, and M. Takano. Blue-light emission at room temperature from Ar^+-irradiated $SrTiO_3$. *Nat. Mater.*, 4(11):816–819, 2005.

[KV56] F. A. Kröger and H. J. Vink. Relations between the concentrations of imperfections in crystalline solids. *Solid State Physics*, 3:307 – 435, 1956.

[KWYZ09] R. F. Klie, W. Walkosz, G. Yang, and Y. Zhao. Aberration-corrected Z-contrast imaging of $SrTiO_3$ dislocation cores. *J. Electron Microsc. (Tokyo)*, 58(3):185–191, 2009.

[LBS+10] J. Lee, E. M. Bourim, D. Shin, J. S. Lee, D. j. Seong, J. Park, W. Lee, M. Chang, S. Jung, J. Shin, and H. Hwang. Analysis of interface switching for Nb doped $SrTiO_3$ single crystal device using complex impedance spectroscopy. *Curr. Appl. Phys.*, 10(1):E68–E70, 2010.

[LGF82] R. D. Leapman, L.A. Grunes, and P.L. Fejes. Study of the L_{23} edges in the 3d transition-metals and their oxides by electron-energy-loss spectroscopy with comparisons to theory. *Phys. Rev. B*, 26(2):614–635, 1982.

[LH11] M. H. Lee and C. S. Hwang. Resistive switching memory: observations with scanning probe microscopy. *Nanoscale*, 3(2):490–502, 2011.

[Lif56] E. M. Lifshitz. The Theory of Molecular Attractive Forces between Solids. *Sov. Phys. JETP*, 2(1):73–83, 1956.

[LM66] J. Levine and P. Mark. Theory and observation of intrinsic surface states on ionic crystals. *Phys. Rev.*, 144(2):751–, 1966.

[LPK10] S. Lee, S. H. Phark, and D. W. Kim. Influences of Interface States on the Electrical Properties of Pt/$SrTiO_3$ Junctions. *J. Kor. Phys. Soc*, 56(1):362–365, 2010.

[LPSR05] S. B. Lee, F. Phillipp, W. Sigle, and M. Rühle. Nanoscale TiO island formation on the $SrTiO_3$ (001) surface studied by in situ high-resolution transmission electron microscopy. *Ultramicroscopy*, 104(1):30–38, 2005.

[LSP05] S. Lee, M. Saito, and F. Phillipp. Dynamic observation of nanometer-sized island formation on the $SrTiO_3$(001) and (011) surfaces by in situ high-resolution transmission electron microscopy. *Z. Metallk.*, 96(5):452–454, 2005.

[LSR11] A. Leonarska, K. Szot, and A. Ratuszna. Temperature evolution of the crystal structure in $SrTiO_3$ doped by W6+, Ni3+, Fe3+ and La3+. *Phase Transit.*, 84(11-12):1015–1024, 2011.

[Lüt10] H. Lüth. *Solid Surfaces, Interfaces and Thin Films.* Springer, 2010.

[LWW+05] C. Y. Liu, P. H. Wu, A. Wang, W. Y. Jang, J. C. Young, K. Y. Chiu, and T. Y. Tseng. Bistable resistive switching of a sputter-deposited Cr-doped $SrZrO_3$ memory film. *IEEE Electron Device Lett.*, 26(6):351–353, 2005.

[Mal03] J. Malzbender. Comment on hardness definitions. *J. Eur. Ceram. Soc.*, 23:1355–1359, 2003.

[Mar09] A. Marques. *Advanced Si pad detector development and $SrTiO_3$ studies by emission channeling and hyperfine interaction experiments.* PhD thesis, Universidade de Lisboa, 2009.

[MC09] M. S. J. Marshall and M. R. Castell. Shape Transitions of Epitaxial Islands during Strained Layer Growth: Anatase TiO_2(001) on $SrTiO_3$(001). *Phys. Rev. Lett.*, 102(14):146102/1–4, 2009.

[MDS+06] H. L. Marsh, D. S. Deak, F. Silly, A. I. Kirkland, and M. R. Castell. Hot STM of nanostructure dynamics on $SrTiO_3$(001). *Nanotechnology*, 17(14):3543–3548, 2006.

[MDS+08] R. Muenstermann, R. Dittmann, K. Szot, S. Mi, C.-L. Jia, P. Meuffels, and R. Waser. Realization of regular arrays of nanoscale resistive switching blocks in thin films of Nb-doped $SrTiO_3$. *Appl. Phys. Lett.*, 93(2):23110/1–3, 2008.

[Meh07] H. Mehrer, editor. *Diffusion in Solids: Fundamentals, Methods, Materials, Diffusion-Controlled Processes.* Springer, 2007.

[MH97] R. Moos and K. H. Haerdtl. Defect Chemistry of Donor-Doped and Undoped Strontium Titanate Ceramics between 1000° and 1400°C. *J. Am. Ceram. Soc.*, 80(10):2549–62, 1997.

[MHSS14] E. Mikheev, B. D. Hoskins, D. B. Strukov, and S. Stemmer. Resistive switching and its suppression in Pt/Nb:$SrTiO_3$ junctions. *Nat. Comm.*, 5:3990, 2014.

[MJ04] E. A. Moore and R. Janes. *Metal-Ligand Bonding.* The Royal Society of Chemistry, 2004.

[MKY05] H. Muta, K. Kurosaki, and S. Yamanaka. Thermoelectric properties of reduced and La-doped single-crystalline $SrTiO_3$. *J. Alloys Compd.*, 392(1-2):306–309, 2005.

[MMD$^+$09] T. Menke, P. Meuffels, R. Dittmann, K. Szot, and R. Waser. Separation of bulk and interface contributions to electroforming and resistive switching behavior of epitaxial Fe-doped $SrTiO_3$. *J. Appl. Phys.*, 105:066104, 2009.

[MMDW10] R. Muenstermann, T. Menke, R. Dittmann, and R. Waser. Coexistence of Filamentary and Homogeneous Resistive Switching in Fe-doped $SrTiO_3$ Thin-Film Memristive Devices. *Adv. Mat.*, 22(43):4819, 2010.

[MNP$^+$11] M. S. J. Marshall, D. T. Newell, D. J. Payne, R. G. Egdell, and M. R. Castell. Atomic and electronic surface structures of dopants in oxides: STM and XPS of Nb- and La-doped $SrTiO_3$(001). *Phys. Rev. B*, 83(3):35410/1–6, 2011.

[Moo94] R. Moos. *Donatordotierung im Strontiumtitanat: Elektrische Eigenschaften und modellhafte Beschreibung.* PhD thesis, Universität Karlsruhe, 1994.

[Moo98] G. E. Moore. Cramming more components onto integrated circuits (Reprinted from Electronics, pg 114-117, April 19, 1965). *PROCEEDINGS OF THE IEEE*, 86(1):82–85, 1998.

[MRFB76] R. Migoni, K. H. Rieder, K. Fischer, and H. Bilz. Lattice-dynamics and Raman-spectra of $SrTiO_3$. *Ferroelectrics*, 13(1-4):377–379, 1976.

[MRS] O. Madelung, U. Rössler, and M. Schulz, editors. *Landolt-Börnstein - Group III Condensed Matter Numerical Data and Functional Relationships in Science and Technology*, chapter $SrTiO_3$ crystal structure, lattice parameters. SpringerMaterials - The Landolt-Börnstein Database.

[MSP$^+$12] M. Mlynarczyk, K. Szot, U. Poppe, U. Breuer, S. Mi, B. Psiuk, E. A. Goerlich, K. Tomala, and R. Waser. Structural stratification of $Sr_{1-x}Ca_xRuO_3$ thin films: Influence of aging process. *Phys. Status Solidi A*, 210(2):239–254, 2012.

[MSSB95] J.F. Moulder, W.F. Stickle, P.E. Sobol, and K.D. Bomben. *Handbook of X Ray Photoelectron Spectroscopy.* Physical Electronics, 1995.

[MTO$^+$88] F. Maeda, T. Takahashi, H. Ohsawa, S. Suzuki, and H. Suematsu. Unoccupied-electronic-band structure of graphite studied by angle-resolved secondary-electron emission and inverse photoemission. *Phys. Rev. B*, 37(9):4482–4488, 1988.

[MWHB02] R. Meyer, R. Waser, J. Helmbold, and G. Borchardt. Cationic surface segregation in donor-doped $SrTiO_3$ under oxidizing conditions. *J. Electroceram.*, 9(2):101–10, 2002.

[MWM$^+$11] S. Menzel, M. Waters, A. Marchewka, U. Böttger, R: Dittmann, and R. Waser. Origin of the Ultra-nonlinear Switching Kinetics in Oxide-Based Resistive Switches. *Adv. Funct. Mater.*, 21(23):4487–4492, 2011.

[MWR69] G. J. McCarthy, W. B. White, and R. Roy. Phase Equilibria in the 1375°C Isotherm of the System Sr-Ti-O. *J. Am. Ceram. Soc.*, 52:463–467, 1969.

[Nel63] C. W. Nelson. Ferroelectricity and the Chemical Bond in Perovskite-Type Oxides. Technical report, MIT, L.I.R. Tech. Rept. 179, 1963.

[NK12] D. Necas and P. Klapetek. Gwyddion: an open-source software for SPM data analysis. *Cent. Eur. J. Phys.*, 10(1):181–188, 2012.

[Nog96] C. Noguera. *Physics and Chemistry at Oxide Surfaces*. Cambridge University Press, 1996.

[Nog00a] C. Noguera. Polar oxide surfaces. *J. Phys. Condens. Mat.*, 12(31):R367–R410, 2000.

[Nog00b] C. Noguera. Theoretical investigation of the Ruddlesden-Popper compounds $Sr_{n+1}Ti_nO_{3n+1}$ (n = 1 - 3). *Philos. Mag. Lett.*, 80(3):173 – 180, 2000.

[NOW91] M. Nonnenmacher, M. P. OBoyle, and H. K. Wickramasinghe. Kelvin probe force microscopy. *Appl. Phys. Lett.*, 58(25):2921–3, 1991.

[NS68] W. G. Nilsen and J. G. Skinner. Raman Spectrum of Strontium Titanate. *J. Chem. Phys.*, 48(5):2240–2248, 1968.

[ONOK05] S. Ohta, T. Nomura, H. Ohta, and K. Koumoto. High-temperature carrier transport and thermoelectric properties of heavily La- or Nb-doped $SrTiO_3$ single crystals. *J. Appl. Phys.*, 97(3):034106, 2005.

[PG92] V. Prisedsky and V. Golubitsky. A novel type of extended defects in the perovskite oxides of the PbO-La_2O_3-TiO_2 system. *Ferroelectrics*, 131(1-4):283–287, 1992.

[PHEB04] S. Piskunov, E. Heifets, R. I. Eglitis, and G. Borstel. Bulk properties and electronic structure of $SrTiO_3$, $BaTiO_3$, $PbTiO_3$ perovskites: an ab initio HF/DFT study. *Comput. Mater. Sci.*, 29(2):165–78, 2004.

[Phi91] J. Philibert. *Atom movements: diffusion and mass transport in solids*. Les Ulis, France : Editions de Physique, 1991.

[PS76] R. Powell and W. Spicer. Photoemission investigation of surface states on strontium-titanate. *Phys. Rev. B*, 13(6):2601–2604, 1976.

[PS12] M. Pilch and K. Szot. Resistive switching in $Sr_{1-0.05}La_{0.05}TiO_3$. In *2012 International Symposium On Applications of Ferroelectrics Held Jointly With 11th IEEE ECAPD and IEEE PFM (ISAF/ECAPD/PFM)*, 2012.

[PSJK08] C. Park, Y. Seo, J. Jung, and D. Kim. Electrode-dependent electrical properties of metal/Nb-doped $SrTiO_3$ junctions. *J. Appl. Phys.*, 103(5):54106, 2008.

[PSPS09] B. Psiuk, J. Szade, M. Pilch, and K. Szot. XPS studies of perovskites surface instability caused by Ar^+ ion and electron bombardment and metal deposition. In *8th International Conference on Ion Implantation and Other Applications of Ions and Electrons, Kazimierz Dolny, POLAND*, pages S69–S72. Vacuum, 2009.

[PV98] J. Padilla and D. Vanderbilt. Ab initio study of $SrTiO_3$ surfaces. *Surf. Sci.*, 418(1):64–70, 1998.

[Rah04] B. Rahmati. *Microstructural Studies on the Reoxidation Behavior of Nb-doped $SrTiO_3$ Ceramics.* PhD thesis, Universität Stuttgart, 2004.

[RB05] D. Reagor and V. Butko. Highly conductive nanolayers on strontium titanate produced by preferential ion-beam etching. *Nat. Mater.*, 4(8):593–596, 2005.

[RB11] G. Radtke and G. A. Botton. Energy Loss Near-Edge Structures. In *Scanning Transmission Electron Microscopy.* Sp, 2011.

[RBM+84] B. Reihl, J. Bednorz, K. Müller, Y. Jugnet, G. Landgren, and J. Morar. Electronic structure of strontium-titanate. *Phys. Rev. B*, 30(2):803–806, 1984.

[RC08] B. C. Russell and M. R. Castell. Surface of sputtered and annealed polar $SrTiO_3(111)$: TiOx-rich (n x n) reconstructions. *J. Phys. Chem. C*, 112(16):6538–6545, 2008.

[RFS+05] B. Rahmati, J. Fleig, W. Sigle, E. Bischoff, J. Maier, and M. Rühle. Oxidation of reduced polycrystalline Nb-doped $SrTiO_3$: Characterization of surface islands. *Surf. Sci.*, 595:115–126, 2005.

[RGS+13] C. Rodenbücher, T. Gensch, W. Speier, U. Breuer, M. Pilch, H. Hardtdegen, M. Mikulics, E. Zych, R. Waser, and K. Szot. Inhomogeneity of donor doping in $SrTiO_3$ substrates studied by fluorescence-lifetime imaging microscopy. *Appl. Phys. Lett.*, 103(16):162904, 2013.

[RIS04] M. J. Rozenberg, I. H. Inoue, and M. J. Sanchez. Nonvolatile memory with multilevel switching: a basic model. *Phys. Rev. Lett.*, 92(17):178302/1–4, 2004.

[RJH+14] C. Rodenbücher, A. Jauß, V. Havel, R. Waser, and K. Szot. Fast mapping of inhomogeneities in the popular metallic perovskite Nb:$SrTiO_3$ by confocal Raman microscopy. *Phys. Status Solidi RRL*, 1-4:DOI: 10.1002/pssr.201409221, 2014.

[RK28] C. V. Raman and K. S. Krishnan. A new type of secondary radiation. *Nature*, 121:501–502, 1928.

[RKB12] K. G. Rana, V. Khikhlovskyi, and T. Banerjee. Electrical transport across Au/Nb:$SrTiO_3$ Schottky interface with different Nb doping. *Appl. Phys. Lett.*, 100(21):213502, 2012.

[RKR+13] M. Rogala, Z. Klusek, C. Rodenbücher, R. Waser, and K. Szot. Quasi-two-dimensional conducting layer on TiO_2 (110) introduced by sputtering as a template for resistive switching. *Appl. Phys. Lett.*, 102(13):131604, 2013.

[RP57] S. Ruddlesden and P. Popper. New compounds of the K_2NiF_4 type. *Acta Crystallogr.*, 10:538–540, 1957.

[RP58] S. N. Ruddlesden and P. Popper. The compound $Sr_3Ti_2O_7$ and its structure. *Acta Crystallogr.*, 11:54–55, 1958.

[RS10] F. Rustichelli and J. Skrzypek, editors. *Innovative Technological Materials.* Springer, 2010.

[RSB+13] C. Rodenbücher, W. Speier, G. Bihlmayer, U. Breuer, R. Waser, and K. Szot. Cluster-like resistive switching of $SrTiO_3$:Nb surface layers. *New J. Phys.*, 15:103017, 2013.

[RWWS13] C. Rodenbücher, S. Wicklein, R. Waser, and K. Szot. Insulator-to-metal transition of $SrTiO_3$:Nb single crystal surfaces induced by Ar^+ bombardment. *Appl. Phys. Lett.*, 102(10):101603, 2013.

[Sar99] Sartorius AG, Handbuch wägetechnischer Applikationen, 1999.

[Saw08] A. Sawa. Resistive switching in transition metal oxides. *Mater. Today*, 11(6):28–36, 2008.

[SBD76] H. J. Scheel, J. G. Bednorz, and P. Dill. Crystal growth of strontium titanate $SrTiO_3$. *Ferroelectrics*, 13(1):507–509, 1976.

[SBS14] K. Szot, G. Bihlmayer, and W. Speier. Nature of the Resistive Switching Phenomena in TiO_2 and $SrTiO_3$: Origin of the Reversible Insulator-Metal Transition. *Solid State Physics*, 65:353–559, 2014.

[SC11] H. J. Scheel and P. Capper, editors. *Crystal Growth Technology: From Fundamentals and Simulation to Large-scale Production.* John Wiley & Sons, 2011.

[Sch00] H. Scheel. Historical aspects of crystal growth technology. *J. Cryst. Growth*, 211(1-4):1–12, 2000.

[SCL⁺05] H. Sim, H. Choi, D. Lee, M. Chang, D. Choi, Y. Son, E. Lee, W. Kim, Y. Park, I. Yoo, and H. Hwang. Excellent resistance switching characteristics of Pt/$SrTiO_3$ Schottky junction for multi-bit nonvolatile memory application. In *IEEE International Electron Devices Meeting, Washington, DC*, pages 777–780, 2005.

[SDSW07] K. Szot, R. Dittmann, W. Speier, and R. Waser. Nanoscale resistive switching in $SrTiO_3$ thin films. *Phys. Status Solidi-Rapid Res. Lett.*, 1(2):R86–R88, 2007.

[SFKT05] A. Sawa, T. Fujii, M. Kawasaki, and Y. Tokura. Colossal electro-resistance memory effect at metal/La_2CuO_4 interfaces. *Jpn. J. Appl. Phys.*, 44(37-41):1241–3, 2005.

[Sha76] R. D. Shannon. Revised effective ionic radii and systematic studies of interatomic distances in halides and chalcogenides. *Acta Crystallogr. Sect. A*, A32:751–67, 1976.

[SHC64] J. F. Schooley, W. Hosler, and M. Cohen. Superconductivity in semiconducting $SrTiO_3$. *Phys. Rev. Lett.*, 12(17):474, 1964.

[Shi72] D. A. Shirley. High-Resolution X-Ray Photoemission Spectrum of Valence Bands of Gold. *Physical Review B*, 5(12):4709–4714, 1972.

[SJ67] R.F. Schaufele and M. J.Weber. First- and Second-Order Raman Scattering of $SrTiO_3$. *J. Chem. Phys.*, 46(7):2859, 1967.

[SJB94] R. A. Schultz, M. C. Jensen, and R. C. Bradt. Single-crystal cleavage of brittle materials. *Int. J. Fract.*, 65(4):291–312, 1994.

[SJLH07] D. J. Seong, M. Jo, D. Lee, and H. Hwang. HPHA effect on reversible resistive switching of Pt/Nb-doped $SrTiO_3$ Schottky junction for nonvolatile memory application. *Electrochem. Solid State Lett.*, 10(6):H168–H170, 2007.

[SJLZ12] J. Sun, C. H. Jia, G. Q. Li, and W. F. Zhang. Control of normal and abnormal bipolar resistive switching by interface junction on In/Nb:$SrTiO_3$ interface. *Appl. Phys. Lett.*, 101(13):133506, 2012.

[SKS12] M. Schmidbauer, A. Kwasniewski, and J. Schwarzkopf. High-precision absolute lattice parameter determination of $SrTiO_3$, $DyScO_3$ and $NdGaO_3$ single crystals. *Acta Crystallogr. Sect. B*, 68(1):8–14, 2012.

[SL81] H. Schmalzried and W. Laqua. Multicomponent oxides in oxygen potential gradients. *Oxid. Met.*, 15(3-4):339–353, 1981.

[SLP⁺08] D. J. Seong, D. Lee, M. Pyun, J. Yoon, and H. Hwang. Understanding of the Switching Mechanism of a Pt/Ni-Doped $SrTiO_3$ Junction via Current-Voltage and Capacitance-Voltage Measurements. *Jpn. J. Appl. Phys.*, 47(12):8749–8751, 2008.

[SLSN07] E. Stoyanov, F. Langenhorst, and G. Steinle-Neumann. The effect of valence state and site geometry on Ti $L_{3,2}$ and O K electron energy-loss spectra of Ti_xO_y phases. *Am. Miner.*, 92(4):577–586, 2007.

[SMPW12] R. A. De Souza, V. Metlenko, D. Park, and T. E. Weirich. Behavior of oxygen vacancies in single-crystal $SrTiO_3$: Equilibrium distribution and diffusion kinetics. *Physical Review B*, 85(17):174109, 2012.

[Smy84] D. M. Smyth. The role of impurities in insulating transition metal oxides. *Prog. Solid State Chem.*, 15(3):145–71, 1984.

[SN98] C. Suryanarayana and M. Grant Norton. *X-Ray Diffraction: A Practical Approach.* Plenum Press, 1998.

[SPH+96] K. Szot, M. Pawelczyk, J. Herion, C. Freiburg, J. Albers, R. Waser, J. Hulliger, J. Kwapulinski, and J. Dec. Nature of the surface layer in ABO_3-type perovskites at elevated temperatures. *Appl. Phys. A*, 62(4):335–43, 1996.

[SPP+09] J. Szade, B. Psiuk, M. Pilch, R. Waser, and K. Szot. Self-neutralization via electroreduction in photoemission from $SrTiO_3$ single crystals. *Appl. Phys. A Mater. Sci. Process.*, 97(2):449–454, 2009.

[SQW+13] J. X. Shen, H. Q. Qian, G. F. Wang, Y. H. An, P. G. Li, Y. Zhang, S. L. Wang, B. Y. Chen, and W. H. Tang. Temperature-dependent resistive switching behavior in the structure of Au/Nb:$SrTiO_3$/Ti. *Appl. Phys. A Mater. Sci. Process.*, 111(1):303–308, 2013.

[SRS+11] K. Szot, M. Rogala, W. Speier, Z. Klusek, A. Besmehn, and R. Waser. TiO_2 - a prototypical memristive material. *Nanotechnology*, 22(25):254001/1–21, 2011.

[SS98] N. Shanthi and D.D. Sarma. Electronic structure of electron doped $SrTiO_3$: $SrTiO_{3-\delta}$ and $Sr_{1-x}La_xTiO_3$. *Phys. Rev. B: Condens. Matter*, 57(4):2153–2158, 1998.

[SS99] K. Szot and W. Speier. Surfaces of reduced and oxidized $SrTiO_3$ from atomic force microscopy. *Physical Review B*, 60(8):5909–26, 1999.

[SSB+00] K. Szot, W. Speier, U. Breuer, R. Meyer, J. Szade, and R. Waser. Formation of micro-crystals on the (100) surface of $SrTiO_3$ at elevated temperatures. *Surf. Sci.*, 460(1-3):112–28, 2000.

[SSBW06] K. Szot, W. Speier, G. Bihlmayer, and R. Waser. Switching the electrical resistance of individual dislocations in single-crystalline $SrTiO_3$. *Nat. Mater.*, 5(4):312–20, 2006.

[SSC+96] K. Szot, W. Speier, S. Cramm, J. Herion, C. Freiburg, R. Waser, M. Pawelczyk, and W. Eberhardt. Surface layer on $KNbO_3$ and the hysteresis loop anomaly. *J. Phys. Chem. Solids*, 57(11):1765–75, 1996.

[SSCK+11] A. F. Santander-Syro, O. Copie, T. Kondo, F. Fortuna, S. Pailhes, R. Weht, X. G. Qiu, F. Bertran, A. Nicolaou, A. Taleb-Ibrahimi, P. Le Fevre, G. Herranz, M. Bibes, N. Reyren, Y. Apertet, P. Lecoeur, A. Barthelemy, and M. J. Rozenberg. Two-dimensional electron gas with universal subbands at the surface of $SrTiO_3$. *Nature*, 469(7329):189–193, 2011.

[SSHF97] K. Szot, W. Speier, J. Herion, and C. Freiburg. Restructuring of the surface region in $SrTiO_3$. *Appl. Phys. A*, A64(1):55–9, 1997.

[SSSS08] D. S. Shang, J. R. Sun, L. Shi, and B. G. Shen. Photoresponse of the Schottky junction $Au/SrTiO_3$: Nb in different resistive states. *Appl. Phys. Lett.*, 93(10):102106/1–3, 2008.

[Szo10] K. Szot. Extended defects of perovskite materials of ABO_3 type. In S. Blügel, T. Brückel, R. Waser, and C. M. Schneider, editors, *Electronic oxides - Correlation Phenomena, Exotic Phases and Novel Functionalities.* Forschungszentrum Jülich GmbH, 2010.

[SZS+10] H. Stoecker, M. Zschornak, J. Seibt, F. Hanzig, S. Wintz, B. Abendroth, J. Kortus, and D. C. Meyer. Formation of Schottky-type metal/$SrTiO_3$ junctions and their resistive properties. *Appl. Phys. A Mater. Sci. Process.*, 100:437–445, 2010.

[Tas79] P. Tasker. Stability of ionic-crystal surfaces. *J. Phys. C Solid State Phys.*, 12(22):4977–4984, 1979.

[TBC+04] S. Tsui, A. Baikalov, J. Cmaidalka, Y. Y. Sun, Y. Q. Wang, Y. Y. Xue, C. W. Chu, L. Chen, and A. J. Jacobson. Field-induced resistive switching in metal-oxide interfaces. *Appl. Phys. Lett.*, 85(2):317–19, 2004.

[TC67] O. N. Tufte and P. W. Chapman. Electron mobility in semiconducting strontium titanate. *Phys. Rev.*, 155(3):796–802, 1967.

[TF04] T. Trautmann and C. Falter. Lattice dynamics, dielectric properties and structural instabilities of $SrTiO_3$ and $BaTiO_3$. *J. Phys. Condens. Mat.*, 16(32):5955–5977, 2004.

[TG11] N. Tomczak and K. E. J. Goh, editors. *Scanning Probe Microscopy.* World Scientific, 2011.

[TI62] H. Toyoda and M. Itakura. The Surface Effect on Electrical Properties of $BaTiO_3$ Single Crystals. *J. Phys. Soc. Jpn.*, 17(6):924–931, 1962.

[TKO+11] Y. Tokuda, S. Kobayashi, T. Ohnishi, T. Mizoguchi, and N. Shibata. Strontium vacancy clustering in Ti-excess $SrTiO_3$ thin film. *Appl. Phys. Lett.*, 99:033110, 2011.

[TLAM91] J. Torrance, P. Lacorre, C. Asavaroengchai, and R. Metzger. Why are some oxides metallic, while most are insulating. *Physica C*, 182(4-6):351–364, 1991.

[vBEF01] K. van Benthem, C. Elsässer, and R. H. French. Bulk electronic structure of $SrTiO_3$: Experiment and theory. *J. Appl. Phys.*, 90(12):6156–6164, 2001.

[VG09] J. C. Vickerman and I. Gilmore, editors. *Surface Analysis - The Principal Techniques*. John Wiley & Sons, 2009.

[VZB10] G. M. Vanacore, L. F. Zagonel, and N. Barrett. Surface enhanced covalency and Madelung potentials in Nb doped $SrTiO_3$ (100), (110) and (111) single crystals. *Surf. Sci.*, 604(19-20):1674–1683, 2010.

[WA07] R. Waser and M. Aono. Nanoionics-based resistive switching memories. *Nat. Mater.*, 6(11):833–840, 2007.

[WBB+01] Y. Watanabe, J. G. Bednorz, A. Bietsch, Gerber-Ch, D. Widmer, A. Beck, and S. J. Wind. Current-driven insulator-conductor transition and nonvolatile memory in chromium-doped $SrTiO_3$ single crystals. *Appl. Phys. Lett.*, 78(23):3738–40, 2001.

[WD94] D. P. Woodruff and T. A. Delchar. *Modern Techniques of Surface Science*. Cambridge University Press, 1994.

[WDSS09] R. Waser, R. Dittmann, G. Staikov, and K. Szot. Redox-Based Resistive Switching Memories - Nanoionic Mechanisms, Prospects, and Challenges. *Adv. Mater.*, 21(25-26):2632–2663, 2009.

[WE77] T. Wolfram and S. Ellialtioğlu. Surface Enhanced Covalency and its Effect on Surface-States of d-Band Metal Oxides. *Appl. Phys.*, 13(1):21–24, 1977.

[WK08] C. Wang and M. H. Kryder. Epitaxial growth and resistive switching properties of $BaTiO_3$ on (001) Si by RF sputtering. *J. Phys. D Appl. Phys.*, 41(24):245301/1–, 2008.

[WSP84] S. Witek, D. M. Smyth, and H. Pickup. Variability of the Sr/Ti Ratio in $SrTiO_3$. *J. Am. Ceram. Soc.*, 67(5):372–375, 1984.

[WSW11] M. Wojtyniak, K. Szot, and R. Waser. The thermal stability of Pt/Ir coated AFM tips for resistive switching measurements. *Appl. Surf. Sci.*, 257(17):7627–7632, 2011.

[WSW+13] M. Wojtyniak, K. Szot, R. Wrzalik, C. Rodenbücher, G. Roth, and R. Waser. Electro-degradation and resistive switching of Fe-doped $SrTiO_3$ single crystal. *J. Appl. Phys.*, 113(8):83713/1–6, 2013.

[WZS98] R. Wang, Y. Zhu, and S. M. Shapiro. Structural defects and the origin of the second length scale in $SrTiO_3$. *Phys. Rev. Lett.*, 80(11):2370–3, 1998.

[WZS+13] Y. H. Wang, K. H. Zhao, X. L. Shi, G. L. Xie, S. Y. Huang, and L. W. Zhang. Investigation of the resistance switching in Au/$SrTiO_3$:Nb heterojunctions. *Appl. Phys. Lett.*, 103(3):031601, 2013.

[XJG+12] Z. Xu, K. Jin, L. Gu, Y. Jin, C. Ge, C. Wang, H. Guo, H. Lu, R. Zhao, and G. Yang. Evidence for a Crucial Role Played by Oxygen Vacancies in $LaMnO_3$ Resistive Switching Memories. *Small*, 8(8):1279–1284, 2012.

[YCHL11] K. H. Yang, T. Y. Chen, N. J. Ho, and H. Y. Lu. In-Gap States in Wide-Band-Gap $SrTiO_3$ Analyzed by Cathodoluminescence. *J. Am. Ceram. Soc.*, 94(6):1811–1816, 2011.

[YK08] H. Yasuda and Y. Kanemitsu. Dynamics of nonlinear blue photoluminescence and Auger recombination in $SrTiO_3$. *Phys. Rev. B*, 77(19):193202/1, 2008.

[YYK00] J. Yamanaka, J. Yoshimura, and S. Kimura. Characterization of lattice defects in strontium titanate single crystals by X-ray topography and transmission electron microscopy. *J. Electron Microsc.*, 49(1):89–92, 2000.

[ZC13] S. Zhong and Y. Cui. Metal and annealing atmospheres dependence of resistive switching in metal/Nb-0.7wt%-$SrTiO_3$ interfaces. *Curr. Appl. Phys.*, 13(5):913–918, 2013.

[ZML+05] Y. Zhu, X. Ma, D. Li, H. Lu, Z. Chen, and G. Yang. Microstructural analyses of a highly conductive Nb-doped $SrTiO_3$ film. *Acta Mater.*, 53(5):1277–1284, 2005.

[ZML+12] P. Zhang, Y. Meng, Z. Liu, D. Li, T. Su, Q. Meng, Q. Mao, X. Pan, D. Chen, and H. Zhao. Impact of interfacial resistance switching on thermoelectric effect of Nb-doped $SrTiO_3$ single crystalline. *J. Appl. Phys.*, 111:063702, 2012.

[ZSA86] J. Zaanen, G. A. Sawatzky, and J. W. Allen. The electronic-structure and band-gaps in transition-metal compounds. *J. Magn. Magn. Mater.*, 54-7:607–611, 1986.

[ZSR02] Z. Zhang, W. Sigle, and M. Rühle. Atomic and electronic characterization of the a[100] dislocation core in $SrTiO_3$. *Physical Review B*, 66(9):94108/1–8, 2002.

[ZWL+08] C. Zhang, C. L. Wang, J. C. Li, K. Yang, Y. F. Zhang, and Q. Z. Wu. Substitutional position and insulator-to-metal transition in Nb-doped $SrTiO_3$. *Mater. Chem. Phys.*, 107(2-3):215–219, 2008.

[ZYYL10] X. T. Zhang, Q. X. Yu, Y. P. Yao, and X. G. Li. Ultrafast resistive switching in $SrTiO_3$:Nb single crystal. *Appl. Phys. Lett.*, 97(22):222117/1–3, 2010.

Acknowledgements

At the end of the thesis, I would like to express my gratitude to everyone, who made this work possible by their contributions, support and encouragement.

First of all, I would like to thank Prof. Dr. Rainer Waser for giving me the opportunity to perform my work in the fascinating environment of his research group at the Forschungszentrum Jülich, for many inspiring discussions and for reviewing this thesis.

Furthermore, I would like to thank Prof. Dr. Joachim Mayer for supporting and agreeing to be the physical reviewer of the thesis.

A very big thank you goes to my supervisor Prof. Dr. Kristof Szot who is greatly involved in the accomplishment of this work. He introduced me to the world of surface science, gave me the opportunity to learn a lot about measurement engineering, was always open for discussions, and encouraged me to pursue new ideas and alternative concepts.

I am grateful to the whole team of the project A4 of the SFB 917 "Nanoswitches", particularly to Dr. Wolfgang Speier and Dr. Gustav Bihlmayer, who also performed many *ab initio* calculations facilitating the understanding of the complex nature of the $SrTiO_3$:Nb surface layer.

Some of the results presented in this thesis were obtained in cooperation with colleagues who I would like to thank for sharing with me their expertise in different fields of physics. I am especially grateful to Dr. Helmut Klapper and Cong Zhang (Institut für Kristallographie der RWTH-Aachen) for XRT measurements, Dr. Jürgen Malzbender (FZJ, Institut für Energie- und Klimaforschung 2) for hardness measurements, Dr. Wolfhard Beyer (FZJ, Institut für Energie- und Klimaforschung 5) for effusion measurements, Dr. Hilde Hardtdegen and Dr. Martin Mikulics (FZJ, Peter-Grünberg-Institut 9) for fluorescence measurements, Dr. Thomas Gensch (FZJ, Institute of complex systems 4) for FLIM measurements, Dr. Astrid Besmehn and Dr. Uwe Breuer (FZJ, Zentralinstitut für Engineering, Elektronik und Analytik 3) for XRD, atom probe and SIMS measurements, Dr. Jan Wördenweber (FZJ, Institut für Energie- und Klimaforschung 5) for Raman spectroscopy, Andrea Jauß (WITec GmbH) for CRM measurements, Prof. Dr. Chun-Lin Jia, Dr. Martina Luysberg, Dr. Eva Würtz and Dr. Hongchu Du (FZJ, Peter-Grünberg-Institut 5) for electron microscopy, Dr. Gerald Pintsuk and Friedel Gormann (FZJ, Hot materials lab) for laser flash measurements and Dr. Alexander Schwedt (Gemeinschaftslabor für Elektronenmikroskopie der RWTH Aachen) for EBSD measurements.

I would like to thank all my colleagues from the Peter-Grünberg-Institut 7 for their support and the great working atmosphere. I would especially like to thank Jochen Friedrich and Stephan Masberg for building many excellent measurement set-ups which formed the basis for this work.

Furthermore, I am grateful to René Borowski, Manfred Gebauer, Marcel Gerst, Mirka Grates, Cerstin Makovicka, Georg Pickartz and Thomas Pössinger for technical support, to Maria Garcia and Michaela Ott for administrative support, as well as to Dr. Paul Meuffels for fruitful discussions.

For helpful advice and assistance in the lab, special thanks go to my colleagues Marcin Wojtyniak, Dr. Maciek Rogala, Annemarie Köhl, Katharina Skaja and Dr. Sebastian Wicklein.

Finally, I would like to thank my family for their encouragement and unflinching support.

Appendix

A. Four-probe set-up

In order to measure the influence of ion bombardment on the resistance of the samples, a special set-up was designed and constructed. The basic idea of this set-up was to integrate the four-probe method as well as the ion bombardment device into one UHV chamber which allows the determination of the resistance *in situ* without exposing the sample to ambient conditions. Furthermore, the sample must not come into contact with electrodes deposited directly on the surface because this might lead to intermixing of the atoms of the electrodes with the sample. To fulfil these requirements, the sample has to be mounted on a rotatable holder as shown in Fig. A.1. During the ion bombardment, the sample is positioned in the focus of the ion beam. After this, the sample holder is rotated by 90° and a lowerable four-probe measuring head is driven towards the sample. In Fig. A.2a, a drawing of the designed measuring head is shown. The four probes are aligned at a distance of 1.3 mm from each other. To ensure sufficient electrical contact with the surface of the sample, small metal spheres are attached at the end of the probes and a slight pressure is applied by flexible springs. As shown in the picture in Fig. A.2b, the measuring head is attached to a positioning system which allows the approach to the surface as well as the adjustment of the probes to the centre of the sample. Since the sample has to be grounded during the ion bombardment but has to be isolated during the electrical measurements, it is mounted on an isolating quartz plate using silver paste connected via a cable to the outside of the chamber where it can be grounded manually. In order to measure the temperature-dependent resistivity of the sample, the sample holder which can be seen in Fig. A.2c is heated up to 300° C. The control of the heater is connected to a computer which automatically records the current and the voltages between the four probes as function of the temperature. An overview of the entire set-up is shown in Fig. A.2d. It is installed next to a LEED set-up which can be seen in the background on the left. On the right, the ion gun using Ar^{+} ions with energies up to 5 keV and in the centre the four-probe chamber can be seen.

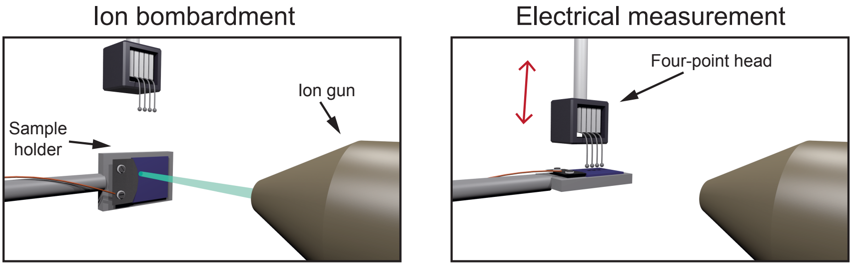

Figure A.1.: Illustration of the four-probe set-up enabling an investigation of the resistance of a bombarded surface by using a rotatable sample holder and a retractable four-point measurement head.

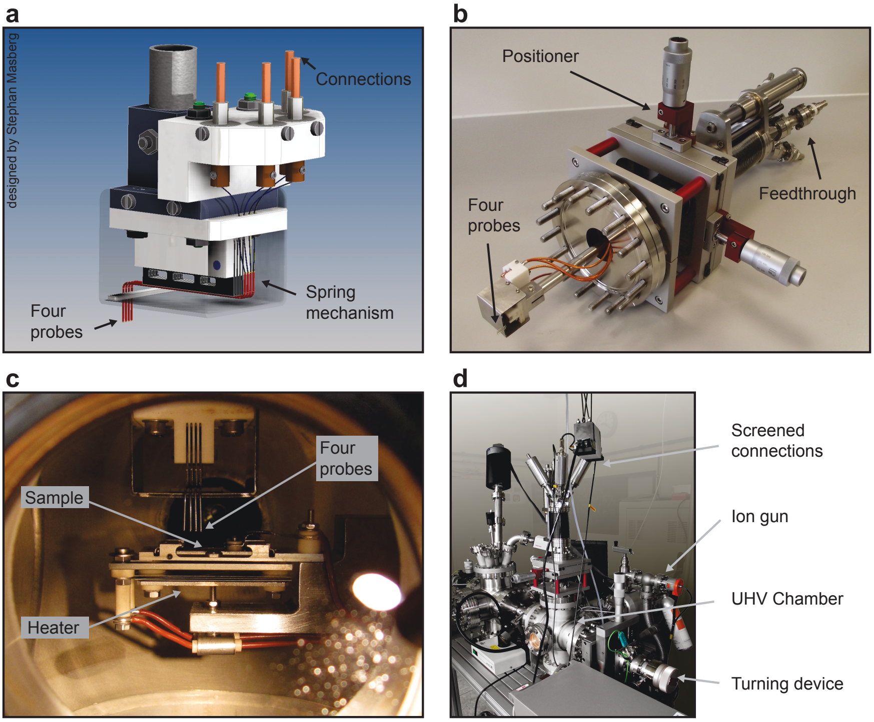

Figure A.2.: The four-probe set-up. a) Drawing of the measuring head. b) The measuring head before mounting on the vacuum chamber. c) A look inside the vacuum chamber. d) Overview of the entire set-up.

B. Photographs of used setups

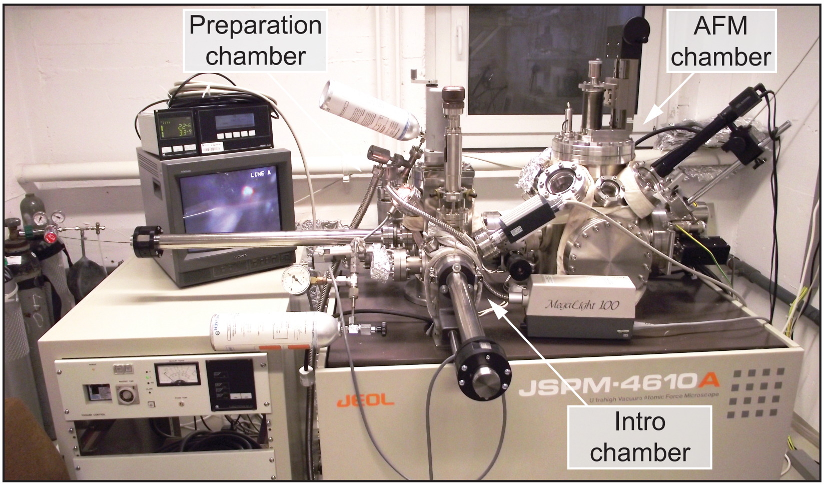

Figure B.1.: The UHV-AFM system JEOL 4610A.

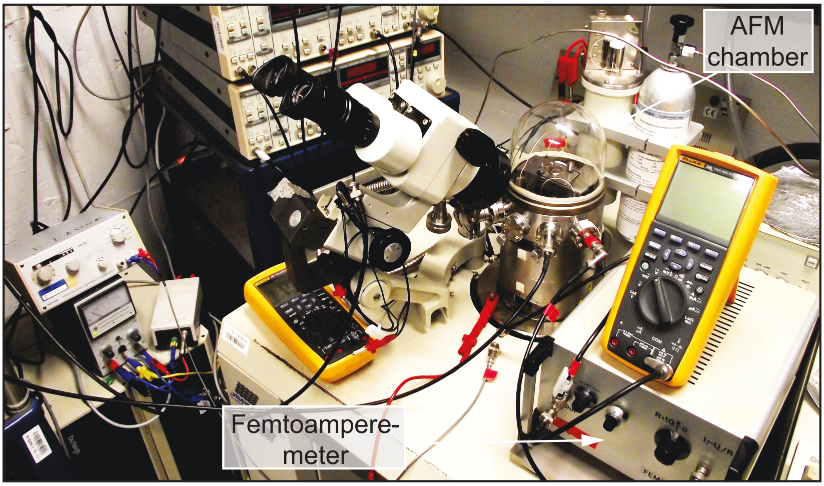

Figure B.2.: The HV-AFM system JEOL 5200.

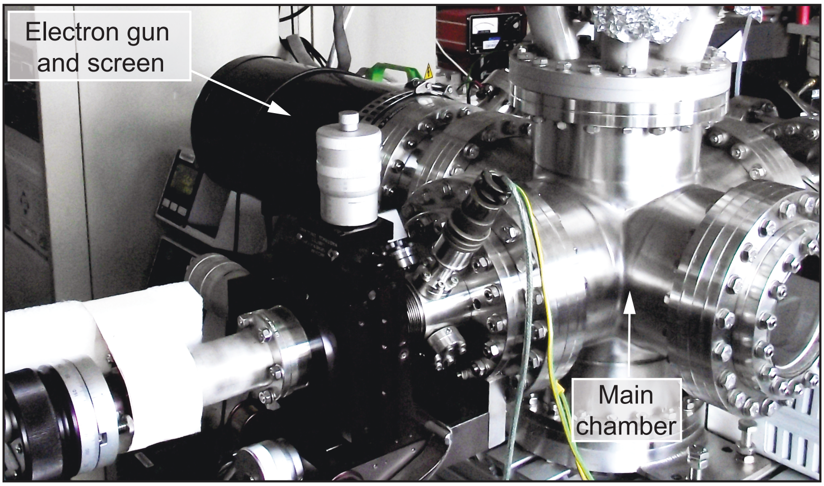

Figure B.3.: The LEED system Omicron SPECTALEED.

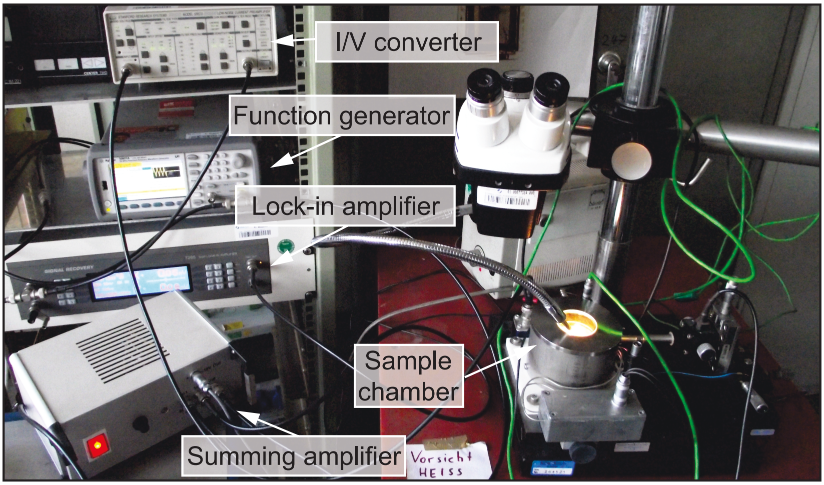

Figure B.4.: System for the simultaneous measurement of resistance and capacitance.

Band / Volume 24
Ultrathin Gold Nanowires - Chemistry, Electrical Characterization and Application to Sense Cellular Biology
A. Kisner (2012), 176 pp
ISBN: 978-3-89336-824-2

Band / Volume 25
Interaction between Redox-Based Resistive Switching Mechanisms
C. R. Hermes (2012), iii, 134 pp
ISBN: 978-3-89336-838-9

Band / Volume 26
Supported lipid bilayer as a biomimetic platform for neuronal cell culture
D. Afanasenkau (2013), xiv, 132 pp
ISBN: 978-3-89336-863-1

Band / Volume 27
15th European Workshop on Metalorganic Vapour Phase Epitaxy (EWMOVPE XV) June 2-5, 2013, Aachen, Germany
A. Winden (Chair) (2013)
ISBN: 978-3-89336-870-9

Band / Volume 28
Characterization, integration and reliability of HfO_2 and $LaLuO_3$ high-κ/metal gate stacks for CMOS applications
A. Nichau (2013), xi, 177 pp
ISBN: 978-3-89336-898-3

Band / Volume 29
The role of defects at functional interfaces between polar and non-polar perovskite oxides
F. Gunkel (2013), X, 162 pp
ISBN: 978-3-89336-902-7

Band / Volume 30
Parallelisation potential of image segmentation in hierarchical island structures on hardware-accelerated platforms in real-time applications
S. Suslov (2013), xiv, 211 pp
ISBN: 978-3-89336-914-0

Band / Volume 31
Carrier mobility in advanced channel materials using alternative gate dielectrics
E. Durğun Özben (2014), 111 pp
ISBN: 978-3-89336-941-6

Band / Volume 32
Electrical characterization of manganite and titanate heterostructures
A. Herpers (2014), ix, 165 pp
ISBN: 978-3-89336-948-5

Band / Volume 33
Oxygen transport in thin oxide films at high field strength
D. Weber (2014), XII, 115 pp
ISBN: 978-3-89336-950-8

Band / Volume 34
Structure, electronic properties, and interactions of defects in epitaxial GaN layers
P. H. Weidlich (2014), 139 pp
ISBN: 978-3-89336-951-5

Band / Volume 35
Defect Engineering of $SrTiO_3$ thin films for resistive switching applications
S. Wicklein (2014), xi, 144 pp
ISBN: 978-3-89336-963-8

Band / Volume 36
Integration and Characterization of Atomic Layer Deposited TiO_2 Thin Films for Resistive Switching Applications
M. Reiners (2014), xiv, 166 pp
ISBN: 978-3-89336-970-6

Band / Volume 37
Resistive switching in ZrO_2 based metal-oxide-metal structures
I. Kärkkänen (2014), xviii, 125 pp
ISBN: 978-3-89336-971-3

Band / Volume 38
Resistive switching phenomena of extended defects in Nb-doped $SrTiO_3$ under influence of external gradients
C. Rodenbücher (2014), xiii, 200 pp
ISBN: 978-3-89336-980-5

Weitere ***Schriften des Verlags im Forschungszentrum Jülich*** unter
http://wwwzb1.fz-juelich.de/verlagextern1/index.asp

Information / Information
Band / Volume 38
ISBN 978-3-89336-980-5

JÜLICH
FORSCHUNGSZENTRUM